

AFRL-SN-HS-TR- 2002-001

**PROCEEDINGS OF THE 2000 ANTENNA APPLICATIONS
SYMPOSIUM –VOLUME I**

**Daniel H. Schaubert, et al
Electrical and Computer Engineering Department
University of Massachusetts
Amherst MA 01002**

**Electromagnetics Laboratory
University of Illinois
Urbana-Champaign**

FINAL REPORT : September 20 – 22, 2000

APPROVED FOR PUBLIC RELEASE: DISTRIBUTION UNLIMITED

20020716 058



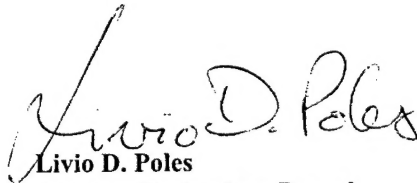
**AIR FORCE RESEARCH LABORATORY
Sensors Directorate
Electromagnetics Technology Division
80 Scott Dr
Hanscom AFB MA 01731-2909**

TITLE OF REPORT:
2000 Antenna Applications Symposium

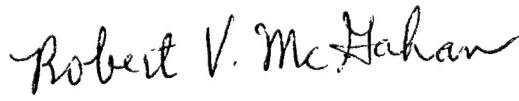
PUBLICATION REVIEW

This report has been reviewed and is approved for publication.

APPROVED:


Livio D. Poles
Antenna Technology Branch
Electromagnetics Technology Division

FOR THE DIRECTOR


Robert V. McGahan,
Division Technical Advisor
Electromagnetics Technology Division

REPORT DOCUMENTATION PAGE				Form Approved OMB No. 0704-0188	
<p>The public reporting burden for this collection of information is estimated to average 1 hour per response, including the time for reviewing instructions, searching existing data sources, gathering and maintaining the data needed, and completing and reviewing the collection of information. Send comments regarding this burden estimate or any other aspect of this collection of information, including suggestions for reducing the burden, to Department of Defense, Washington Headquarters Services, Directorate for Information Operations and Reports (0704-0188), 1215 Jefferson Davis Highway, Suite 1204, Arlington, VA 22202-4302. Respondents should be aware that notwithstanding any other provision of law, no person shall be subject to any penalty for failing to comply with a collection of information if it does not display a currently valid OMB control number.</p> <p>PLEASE DO NOT RETURN YOUR FORM TO THE ABOVE ADDRESS.</p>					
1. REPORT DATE (DD-MM-YYYY) 11 February 2002		2. REPORT TYPE FINAL		3. DATES COVERED (From - To) 20-22 September 2000	
4. TITLE AND SUBTITLE PROCEEDINGS OF THE 2000 ANTENNA APPLICATION SYMPOSIUM				5a. CONTRACT NUMBER GS01K99BKM0012	
				5b. GRANT NUMBER Task Order Number R1570132D	
				5c. PROGRAM ELEMENT NUMBER	
6. AUTHOR(S) Daniel H. Schaubert et, al				5d. PROJECT NUMBER	
				5e. TASK NUMBER	
				5f. WORK UNIT NUMBER	
7. PERFORMING ORGANIZATION NAME(S) AND ADDRESS(ES) Air Force Research Laboratory 80 Scott Rd Electromagnetics Technology Division Sensors Directorate Hanscom AFB, MA 01731				8. PERFORMING ORGANIZATION REPORT NUMBER Volume I	
9. SPONSORING/MONITORING AGENCY NAME(S) AND ADDRESS(ES) Air Force Research Laboratory 80 Scott Rd Electromagnetics Technology Division Sensors Directorate Hanscom AFB, MA 01731				10. SPONSOR/MONITOR'S ACRONYM(S)	
				11. SPONSOR/MONITOR'S REPORT NUMBER(S) AFRL-SN-HS-TR-2002-001	
12. DISTRIBUTION/AVAILABILITY STATEMENT Approved for Public Release; Distribution Unlimited					
13. SUPPLEMENTARY NOTES SNHA Project Engineer Volume I contains Pages 1-245, Volume II contains Pages 246-414					
14. ABSTRACT The Proceedings of the 2000 Antenna Applications Symposium is a collection of state-of-the-art papers relating to phased array antennas, multibeam antennas, satellite antennas, microstrip antennas, reflector antennas, HF, VHF, UHF, and various other antennas.					
15. SUBJECT TERMS Antennas, Satellite Antennas, Broadband Antennas, Microstrip Antennas, Reflectors, HF, VHF, UNF, Multibeam Antenna, Array Antennas					
16. SECURITY CLASSIFICATION OF:			17. LIMITATION OF ABSTRACT SAR	18. NUMBER OF PAGES 245	19a. NAME OF RESPONSIBLE PERSON Livio D. Poles AFRL/SNHA
a. REPORT U	b. ABSTRACT U	c. THIS PAGE U			19b. TELEPHONE NUMBER (Include area code) 781-377-4087

2000 ANTENNA APPLICATIONS SYMPOSIUM

Systems

Recent Advances in Space-Time Adaptive Processing M. C. Wicks	1
Ranking and Selection for Training Data Selection in Multi-Channel Radar P. Chen and M. C. Wicks	23
Efficient Architectures for Implementing Adaptive Algorithms D. C. Ricks and J. S. Goldstein	29
Design Considerations for the Reflector Antenna System of the High Altitude MMIC Sounding Radiometer (HAMSR) V. Jamnejad, A. L. Riley, R. T. Swindlehurst	42

Arrays I

Transmitter/Receiver Pulse-Driven Antenna Array with Near-Field Beam-Forming for UWB Subsurface Imaging Radar	55
A. Boryssenko, E. Boryssenko, V. Ivashuck, V. Prokhorenko	
Antenna Time-Domain Effects on Waveforms and Advanced Signal Processing	83
D. A. Leatherwood, D. D. Aalfs, L. E. Corey, R. B. Cotton, B. S. Mitchell	
Wideband Digital Subarray Beamforming Using True Time Delay Steering at the Element Level	103
M. G. Parent, J. J. Alter, R. Pickles, J. B. L. Rao, J. O. Coleman and D. P. Scholnik	
Mutual Coupling Between Electrically Small Genetic Antennas	128
E. E. Altshuler and T. O'Donnell	
The Cellular Scanning Concept and its Applications	134
P. K. Bondyopadhyay	

Measurements/Reconfigurable

Determination of Array Feeding Coefficients using Limited Angle FarField Measurements	142
H. Tobin and P. Franchi	
Spacecraft Communications System Verification Using On-Axis NearField Measurement Techniques	154
T. Keating, M. Baugh, R. B. Gosselin, M. C. Lecha	
SAC-C Satellite Antenna Gains	171
V. Trainotti, N. D. DiGiovanni, J. S. Skora, D. A. Schweitzer	
Error Compensation for Very Large Inflatable Reflector Antennas	193
W. H. Weedon, W. C. Chew, T. J. Cui, L. Poles	
A Dual Feed REConfigurable Leaky-Wave/Patch APerture	201
J. Sor, Y. Qian and T. Itoh	
Stripline Feed Networks for Reconfigurable Patch Antennas	211
W. J. Payne and W. H. Weedon	
Program to Plot Touchstone Antenna Circuit Files	218
W. R. Pickles	

Elements

Using Multiple Resonant Radiators for Increasing the Impedance Bandwidth of Electrically Small Antennas	246
P. E. Mayes and W. Gee	
Miniaturized Shorting Post Microstrip Antenna for Mobile Handsets	270
D. McNeil, T. A. Denidni, G. Y. Delisle	
A Coaxial Cavity Antenna Exhibiting Low Dispersion Over a Wide Field of View	281
T. Holzheimer	
A Canted Sector Antenna with Broad Impedance Bandwidths for High Performance Arrays	311
J. T. Bernhard, N.-W. Chen, R. Clark, P. Mayes, E. Michielssen	
Planar Inverted F Antenna Covered with a Dielectric Layer	323
J. W. He and K. S. Chung	
Strip-Slot-Air-Mercury Patch Microwave Antennas	338
Y. P. Kosta and S. Kosta	

Arrays II

PAGES 360 - 372 INTENTIONALLY LEFT BLANK	360
Space Based Lens Vs Corporate Antenna Distortion Comparison D. Davis and J. A. Moellers	373
Uplink C/I-Simulations of Mulit-Beam Antennas in an LMDS System U. Engstrom, M. Johansson, A. Derneryd, B. Johannisson, G. Masini	390
Affordable Antenna Array for Multiple Satellite Links S. S. Bharj, A. Merzhevskiy, P. Oleski, B. Tomasic, S. Liu	401

Identifiers for Proceedings of Symposia

The USAF Antenna Research and Development Program

Year	Symp. No.	Identifier
1951	First	
1952	Second	C054 520
1953	Third	AD63794
1954	Fourth	AD63139
1955	Fifth	AD90397
1956	Sixth	AD114702
1957	Seventh	AD138500
1958	Eighth	AD301151
1959	Ninth	AD314721
1960	Tenth	AD244388 (Vol. 1) AD319613 (Vol. 2)
1961	Eleventh	AD669109 (Vol. 1) AD326549 (Vol. 2)
1962	Twelfth	AD287185 (Vol. 1) AD334484 (Vol. 2)
1963	Thirteenth	AD421483
1964	Fourteenth	AD609104
1965	Fifteenth	AD474238L
1966	Sixteenth	AD800524L
1967	Seventeenth	AD822894L
1968	Eighteenth	AD846427L
1969	Nineteenth	AD860812L
1970	Twentieth	AD875973L
1971	Twenty-First	AD888641L
1972	Twenty-Second	AD904360L
1973	Twenty-Third	AD914238L

Antenna Applications Symposium

		TR#	ADA#
1977	First	None	955413
1978	Second	None	955416
1979	Third	_____	077167
1980	Fourth	_____	205907
1981	Fifth	_____	205816
1982	Sixth	_____	129356
1983	Seventh	_____	142003; 142754
1984	Eighth	85-14	153257; 153258
1985	Ninth	85-242	166754; 165535
1986	Tenth	87-10	181537; 181536
1987	Eleventh	88-160	206705; 206704
1988	Twelfth	89-121	213815; 211396
1989	Thirteenth	90-42	226022; 226021
1990	Fourteenth	91-156	237056; 237057
1991	Fifteenth	92-42	253681; 253682
1992	Sixteenth	93-119	268167; 266916
1993	Seventeenth	94-20	277202; 277203
1994	Eighteenth	95-47	293258; 293259
1995	Nineteenth	96-100	309715; 309723
1996	Twentieth	97-189	341737
1997	Twenty First	1998-143	
1998	Twenty Second	1999-86	
1999	Twenty Third		

Recent Advances in Space-Time Adaptive Processing

Michael C. Wicks, Ph.D.
Air Force Research Laboratory
Radar Signal Processing Branch
26 Electronic Parkway
Rome, NY 13441-4514

Abstract: STAP algorithms are often developed under many simplifying assumptions. Adaptive weights are computed statistically, based on an estimated interference covariance matrix. This estimation process requires a large number of homogeneous data in order to provide for adequate sample support. In the real world, the received data is often not homogeneous, and the required sample support is not available. New techniques must be used to counter non-homogeneous interference. In addition, STAP must also compensate for mutual coupling and near field scattering effects.

Our research addresses the issues of sample support and array effects. The sample support required is directly proportional to the number of adaptive weights to be computed. Joint Domain Localized (JDL) processing in the angle-Doppler domain yields excellent interference suppression with few degrees of freedom and low sample support. Array effects may be addressed in a generalized JDL algorithm via the use of measured spatial steering vectors. We use a Non-Homogeneity Detector (NHD) to select training data, and a Direct Data Domain (D^3) least squares based STAP beamforming algorithm to suppress clutter discretely in the cell under test. In this research, we apply a hybrid algorithm which combines NHD and D^3 least squares processing with the generalized JDL algorithm, in order to achieve the benefits of each. Our hybrid algorithm provides effective suppression of discrete and spatially distributed, correlated interference.

1.0 Introduction

Airborne surveillance radar systems operate in a severe and dynamic interference environment. This interference is a sum of clutter, electronic counter measures (ECM), and electromagnetic interference (EMI). Extensive research into STAP for the airborne moving target indication (AMTI) mission has proven its superiority over non-adaptive techniques. Looking to the future, the advantages of STAP for the AMTI mission need to be extended to weak, slow moving target detection, as well as to ground moving target indication (GMTI). Here, targets are masked in Doppler by clutter from the antenna mainbeam and near-in sidelobes.

In airborne or space-based radar, the clutter in a given range cell has a structure determined in part by the motion of the sensor (Figure 1). The slope of the clutter ridge in angle-Doppler space is determined by the velocity of the platform. In AMTI, the threat target is often widely spaced from mainlobe clutter in Doppler. As such, it is possible to use conventional STAP algorithms to suppress sidelobe returns. For slower airborne threats, and in GMTI, the detection problem is more difficult since the target is closer to mainbeam clutter in Doppler.

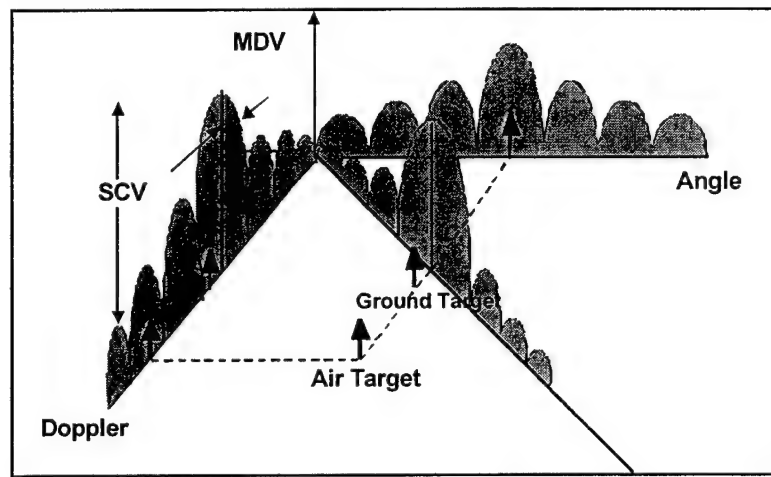


Figure 1. Angle-Doppler structure of clutter.

The goal of our adaptive processing research is to solve practical STAP problems and to improve AMTI/GMTI performance. Our efforts address issues of sample support and array effects, including mutual coupling. In the real world, measured data is often not homogeneous, and the required sample support may not be available. For non-homogeneous test cells, new techniques are required to separate mainlobe targets from sidelobe discretes. In our research, we apply a hybrid algorithm, which combines environmental assessment via the NHD for training data selection, with a least squares beamformer to suppress sidelobe discretes. The JDL algorithm then provides for additional clutter suppression in the angle-Doppler domain, using only limited degrees of freedom. This hybrid algorithm provides effective suppression of discrete and spatially distributed, correlated interference.

2.0 Background

The goal of adaptive processing is to weight the received space-time data vectors to maximize the output signal-to-interference plus noise ratio (SINR). Traditionally, weights are computed using estimates of the interference statistics

averaged over range. These weights maximize the gain in a desired look direction, while nulling interference. Traditionally, fully adaptive STAP procedures determine adaptive weights using an estimated covariance matrix, as given by Equation (1)

$$\mathbf{w} = \hat{\mathbf{R}}^{-1} \mathbf{s}. \quad (1)$$

In this equation, \mathbf{s} sets the “look direction”, the direction in angle and Doppler being tested for the presence of a target. The covariance matrix, $\hat{\mathbf{R}}$, is estimated by averaging over *secondary data* chosen from range cells close to the cell under test (the primary range cell) as given by:

$$\hat{\mathbf{R}} = \frac{1}{K} \sum_{k=1}^K \mathbf{x}_k \mathbf{x}_k^H. \quad (2)$$

Equations (1) and (2) illustrate the two main challenges in applying a fully adaptive procedure: the degrees of freedom and the homogeneity of the radar data. Underlying several STAP approaches is a third problem, array effects. In Equation (1) the number of unknowns and size of the covariance matrix directly determines the degrees of freedom. The total computation load rises as the third power of the number of unknowns. Choosing this parameter is therefore crucial to a practical implementation of STAP. In the fully adaptive approach, the number of unknowns is the number of elements (N) times the number of pulses (M). This requires estimation of the NM dimensional covariance matrix of the interference. In practice, an accurate estimate requires $2NM$ to $3NM$ independent and identically distributed (i.i.d.) secondary data samples [Reed 74]. This number may be very large, making it impossible to evaluate the covariance matrix and the adaptive weights in a reasonable computation time. One goal of STAP research has therefore been to reduce the number of adaptive unknowns, while maintaining performance. Equation (2) estimates the covariance matrix using K secondary data vectors from range bins close to the range cell under test. The inherent assumption is that the statistics of the interference in the secondary data are the same as that within the primary range cell, i.e. the data is assumed homogeneous. K should be greater than twice the number of unknowns in any adaptive processor. Practically speaking, it is impossible to obtain a large number of i.i.d. homogeneous secondary data vectors (large K). No clutter scene is perfectly homogeneous and most, if not all, land clutter is sufficiently non-homogeneous to impact performance. Traditionally, STAP algorithms were developed for proof-of-concept assuming the receive antenna is a linear array of isotropic point sensors. In practice, building such an array is not feasible and the elements must be of some physical size. This implies that the array not only receives, but also scatters incident fields, leading to mutual coupling between elements.

2.1 Joint Domain Localized Processing in the Ideal Case

To overcome the drawbacks of the fully adaptive algorithm, researchers have limited the number of adaptive weights to reduce problems associated with sample support and computation. Wang and Cai [Wang 94] introduced the JDL algorithm, a post-Doppler beam-space approach, that adaptively processes the radar data after transformation to the angle-Doppler domain. Adaptive processing is restricted to a localized processing region (LPR) in the transform domain, thereby significantly reducing the number of unknowns while retaining maximal gain against thermal noise. The lower degrees of freedom leads to a corresponding reductions in required sample support and computational load.

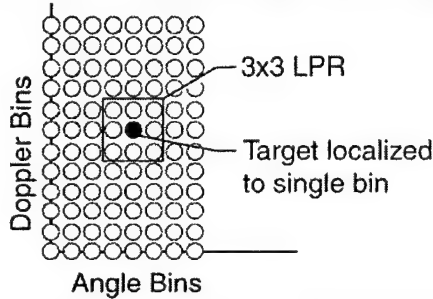


Figure 2. Localized Processing Regions in JDL for $\eta_a = \eta_d = 3$.

As shown in Figure 2, a LPR centered about the look angle-Doppler point is formed and interference is suppressed in this angle-Doppler region only. The LPR covers η_a angle bins and η_d Doppler bins. The choice of η_a and η_d is independent of the number of elements, N , and the number of pulses, M , and “decouples” the adaptive degrees of freedom from the size of the data cube. The covariance matrix corresponding to this LPR is estimated using secondary data from neighboring range cells. The adaptive weights are then calculated using Equation (1). The estimated covariance matrix $\hat{\mathbf{R}}$ is replaced with $\tilde{\mathbf{R}}$, the estimated 9 dimensional *angle-Doppler* domain covariance matrix corresponding to the LPR of interest. The steering vector \mathbf{s} is replaced with the angle-Doppler steering vector $\tilde{\mathbf{s}}$, and

$$\tilde{\mathbf{w}} = \tilde{\mathbf{R}}^{-1} \tilde{\mathbf{s}}. \quad (3)$$

Here, the number of adaptive unknowns is equal to $\eta_a \eta_d = 9$. The steering vector for the adaptive process is the space-time steering vector \mathbf{s} of Equation (1) transformed to the angle-Doppler domain and truncated. Under the two conditions listed above, $\tilde{\mathbf{s}}$ is given by the $\eta_a \eta_d$ length vector

$$\tilde{\mathbf{s}} = [0, 0, \dots, 0, 1, 0, \dots, 0, 0]^T. \quad (4)$$

2.2 Accounting for Array Effects

This section addresses a second major concern: the impact of mutual coupling between the elements of the array as well as scattering off the aircraft body [Adve 00]. When applying the JDL algorithm to measured data, a crucial assumption in the discussion above is invalid. The elements of an array cannot be point sensors. Owing to their physical size, the elements of the array are subject to mutual coupling. In a physical array, the spatial steering vectors must be measured or obtained using numerical electromagnetic analysis. These steering vectors must be used to transform from the spatial domain to the angle domain. This transformation is necessarily non-orthogonal with a corresponding spread of target information in the angle-Doppler domain.

In this section, we replace the DFT-based transformation described above with a generalized transformation matrix. The key contribution of this approach is in accounting for array effects, thereby eliminating two stipulations on the original JDL algorithm. This formulation can now be applied to physical arrays of arbitrary configuration.

In the JDL algorithm, only data from within the LPR is used for adaptive processing. The transformation from the space-time domain to the angle-Doppler domain is an inner product with a space-time steering vector, an argument that holds true for ideal linear arrays and physical arrays. Mathematically therefore, the relevant transformation to within the LPR is a pre-multiplication with a $(NM \times \eta_a \eta_d)$ transformation matrix. The transformation process is

$$\tilde{\mathbf{x}}_{LPR} = \mathbf{T}^H \mathbf{x}. \quad (5)$$

In [Wang 94], to achieve the simple form of the angle-Doppler steering vector given by Equation (4), the use of a low sidelobe window to lower transform sidelobes is discouraged. However, the use of such a window may be incorporated by modifying the transformation matrix \mathbf{T} . The angle-Doppler steering vector used to solve for the adaptive weights in Equation (1) is the space-time steering vector, transformed to the angle-Doppler domain via the same transformation matrix \mathbf{T} , i.e.

$$\tilde{\mathbf{s}} = \mathbf{T}^H \mathbf{s}. \quad (6)$$

The transformation matrix is defined for the chosen Doppler frequencies and angles without any restrictions on their values.

2.2.1 Multi-Channel Airborne Radar Measurements (MCARM)

The discussion above dealt with applying the JDL algorithm to real arrays by accounting for mutual coupling and airframe effect. The performance

improvements over the original JDL algorithm are presented here using data from the MCARM program. The MCARM program had as its objective the collection of multiple spatial channel airborne radar data for the development and evaluation of STAP algorithms. The Air Force Research Laboratory contracted with Northrop Grumman to develop the measurement capability and to accomplish flight tests [Fenner 96]. Under the MCARM program, monostatic data was collected during flights along the east coast of the United States.

The array antenna is mounted in an aerodynamic cheek-mounted radome, located just forward of the port wing of the aircraft. The L-band (1.24GHz) active array consists of 16 columns, with each column having two 4-element subarrays. The elements are vertically polarized, dual-notch reduced-depth radiators. These elements are located on a rectangular grid with horizontal spacing of 4.3 inches and vertical spacing of 5.54 inches. There is a 20 dB Taylor weighting across the 8 elevation elements resulting in a 0.25 dB elevation taper loss on both transmit and receive. The total average radiated power for the array is approximately 1.5 kW. A 6 dB modified trapezoid weighting on the azimuth transmit illumination function is used to produce a 7.5° beamwidth boresight pattern with -25 dB rms sidelobes.

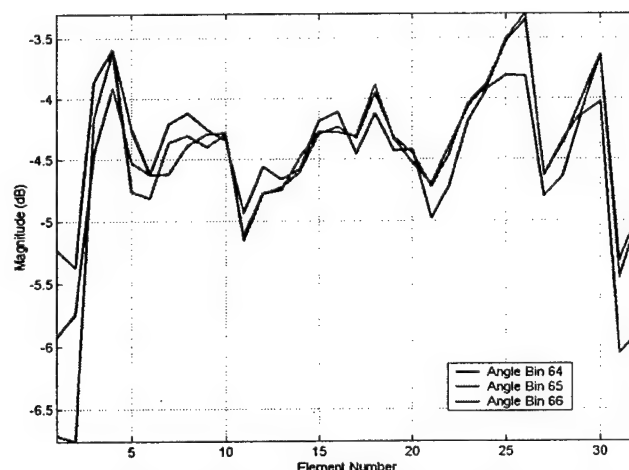


Figure 3. Magnitude of MCARM steering vectors.

Of the 32 possible channels, only 24 receivers were available for data recording. Two of the receivers were used for analog sum and azimuthal difference beams. There are 22 ($N=22$) digitized channels which, in this work, are arranged as a rectangular 2×11 array. Each coherent processing interval (CPI) comprises 128 ($M=128$) pulses at a pulse repetition frequency (PRF) of 1984Hz. In the ideal case of a linear array, the magnitude of the steering vector is a constant. Figure 3 shows the variation in magnitude for the MCARM array. The magnitude varies by as much as 4dB over the 32 elements.

2.2.2 Example: MTS Tones

Flight 5, acquisition 152 includes clutter and tones from a moving target simulator (MTS) radiating at pre-selected Doppler frequencies. Five tones are received at approximately -800 Hz (0 dB), -600 Hz (-14 dB), -400 Hz (-20 dB), -200 Hz (-26 dB) and 0 Hz (-31 dB). The data in this acquisition are returns from 128 pulses measured across 22 channels. The PRF for this flight was 1984 Hz, hence the separation of 200 Hz corresponds to nearly 13 Doppler bins.

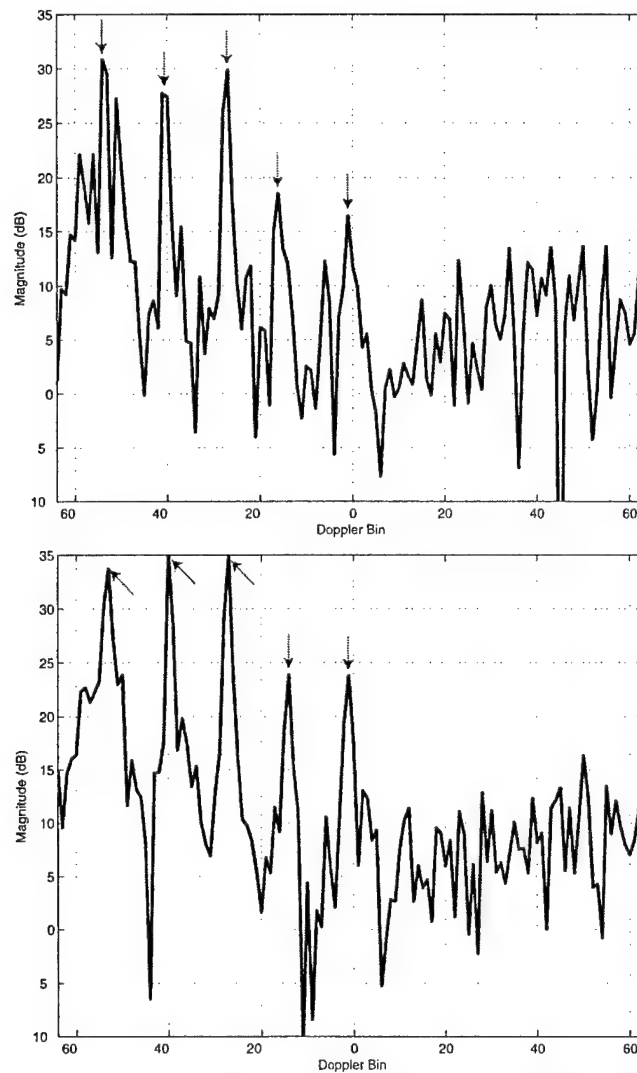


Figure 4. JDL before and after accounting for array effects (MTS Tones).

Figure 4 plots the modified sample matrix inversion (MSMI) test statistic versus Doppler bin for the two cases considered. A target at the primary range cell is declared if the MSMI statistic,

$$\eta_{MSMI} = \frac{|\hat{\mathbf{w}}^H \tilde{\mathbf{x}}|^2}{\tilde{\mathbf{s}}^H \hat{\mathbf{R}}^{-1} \tilde{\mathbf{s}}} \underset{H_0}{\overset{H_1}{>}} \eta_0, \quad (7)$$

is above a chosen threshold. In the first plot, the five tones are clearly visible with the strongest tone at bin -53 spread over Doppler space. A few spurious tones are also visible. The second plot shows the results of the JDL algorithm modified to account for array effects. The five tones are clearly visible and the spurious tones are suppressed.

2.3 Non-Homogeneity Detection

This section presents the third key issues that limits adaptive processing in real world applications: the non-homogeneous and dynamic environments typically observed from airborne radars. Non-homogeneous data is the most significant of the three issues discussed herein. Significant processing losses result from the mismatch between the environment and the algorithm. Recent work has shown that it is essential to sense the actual environment, and then to match adaptive processing to the environment [Antonik 97].

In the filtering stage of the radar processing chain, training data are selected about the cell under test, and that training data is used to estimate the interference. Conventional STAP algorithms use a symmetric sliding window about the cell under test in order to select training data. This assumes that the data are homogeneous and i.i.d. Improved methods are needed to more carefully implement processing based on the environment. For detection, this means better selection of training data, requiring non-symmetric, non-contiguous secondary data samples be selected. As shown in the literature, [Chang 97], these secondary data samples must best represent the interference, or at least the homogeneous component of the interference, in a statistical sense. The non-homogeneity detector (NHD) must be matched to the processing at hand.

Recent developments in non-homogeneity detection allow for better selection of training data. We have been investigating a variety of non-homogeneity detection techniques including application of the Generalized Inner Product and multi-pass STAP. In multi-pass STAP techniques, a first filtering stage serves as the NHD. A second stage then performs the filtering function.

Using the NHD provides a significant performance improvement over conventional methods. However, once non-homogeneous cells have been identified, how are these cells handled in the filtering and detection processes?

By definition, the non-homogeneous cells are not like neighboring cells, so it is not appropriate to use traditional statistical techniques. To address this case, we developed a hybrid STAP technique that combines non-statistical and statistical adaptive processing methods.

2.4 Direct Least Squares Approach

The inability of traditional statistical algorithms to counter the non-homogeneous components of interference motivates research in non-statistical direct data domain or D^3 algorithms. One researcher [Sarkar 89] developed an algorithm that optimizes the signal to interference ratio in a least squares sense for signals in a constrained look-direction. This method minimizes the error between the received voltages (signal plus interference) and a signal from the assumed direction. This approach does not employ data from outside the range cell under test, and therefore does not require secondary data. This makes the D^3 an attractive alternative in non-homogeneous clutter.

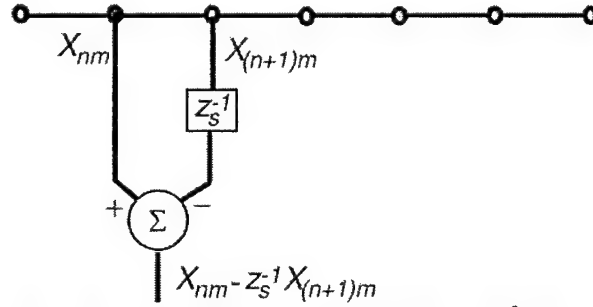


Figure 5. Principle of Direct Data Domain (D^3) Processing.

Consider the N -element uniformly spaced array shown in Figure 5. For a look direction of ϕ , the signal advances from one element to the next by the same phase factor $z_s = [\exp(j2\pi\sin(\phi))]$. The term obtained by the subtraction operation in Figure 5 is therefore free of the target signal and contains only interference terms. The D^3 algorithm minimizes the power in such interference terms while maintaining gain in the direction of the target.

To best present the D^3 algorithm, the data from the N elements due to the M pulses in a CPI is written as a $N \times M$ matrix \mathbf{X} whose m^{th} column corresponds to the N returns from the m^{th} pulse, represented by $\mathbf{x}(m)$. The data matrix is a sum of target and interference terms

$$\mathbf{X} = \xi \mathbf{S}(\phi_t, f_t) + \mathbf{C} + \mathbf{N}. \quad (8)$$

Define the $M \times (N-1)$ matrix \mathbf{A} to be:

$$\mathbf{A} = \begin{bmatrix} \mathbf{X}_{00} - z_s^{-1}\mathbf{X}_{10} & \mathbf{X}_{10} - z_s^{-1}\mathbf{X}_{20} & \cdots & \mathbf{X}_{(N-2)0} - z_s^{-1}\mathbf{X}_{(N-1)0} \\ \mathbf{X}_{01} - z_s^{-1}\mathbf{X}_{11} & \mathbf{X}_{11} - z_s^{-1}\mathbf{X}_{21} & \cdots & \mathbf{X}_{(N-2)1} - z_s^{-1}\mathbf{X}_{(N-1)1} \\ \vdots & \vdots & \vdots & \vdots \\ \mathbf{X}_{0(M-1)} - z_s^{-1}\mathbf{X}_{1(M-1)} & \mathbf{X}_{1(M-1)} - z_s^{-1}\mathbf{X}_{2(M-1)} & \cdots & \mathbf{X}_{(N-2)(M-1)} - z_s^{-1}\mathbf{X}_{(N-1)(M-1)} \end{bmatrix}, \quad (9)$$

where z_s is the phase progression of the *target signal* from one element to the next. Theoretically, the entries of \mathbf{A} are interference terms only. Consider the following scalar functions of a vector of spatial weight \mathbf{w}_s , where $\|\cdot\|$ represents the 2-norm of a vector and $\mathbf{a}_{(0:N-2)}$ represents the first $N-1$ entries of the spatial steering vector. The term G in Equation (10) represents the gain of the weight vector \mathbf{w}_s at the look angle ϕ , while the term I represents the residual interference power after the data is filtered by the same weights. Hence, the term C is the difference between the gain of the antenna at the look angle and the residual interference power. The term κ in the definition of C is an emphasis parameter that will be described later.

$$\begin{aligned} G_{\mathbf{w}_s} &= \left| \mathbf{w}_s^H \mathbf{a}_{(0:N-2)} \right|^2 = \mathbf{w}_s^H \mathbf{a}_{(0:N-2)} \mathbf{a}_{(0:N-2)}^H \mathbf{w}_s, \\ I_{\mathbf{w}_s} &= \left\| \mathbf{A}^* \mathbf{w}_s \right\|^2 = \mathbf{w}_s^H \mathbf{A}^T \mathbf{A}^* \mathbf{w}_s, \\ C_{\mathbf{w}_s} &= G_{\mathbf{w}_s} - \kappa^2 I_{\mathbf{w}_s}, \end{aligned} \quad (10)$$

Mathematically, the D^3 algorithm finds weights that maximize the difference:

$$\begin{aligned} \max_{\|\mathbf{w}_s\|_2=1} [C_{\mathbf{w}_s}] &= \max_{\|\mathbf{w}_s\|_2=1} [G_{\mathbf{w}_s} - \kappa^2 I_{\mathbf{w}_s}] \\ &= \max_{\|\mathbf{w}_s\|_2=1} \mathbf{w}_s^H [\mathbf{a}_{(0:N-2)} \mathbf{a}_{(0:N-2)}^H - \kappa^2 \mathbf{A}^T \mathbf{A}^*] \mathbf{w}_s, \end{aligned} \quad (11)$$

where the constraint $\|\mathbf{w}_s\|_2 = 1$ is chosen to obtain a finite solution. Using the method of Lagrange multipliers, it can be shown that the desired weight vector is the eigenvector corresponding to the maximum eigenvalue of the $(N-1) \times (N-1)$ matrix $[\mathbf{a}_{(0:N-2)} \mathbf{a}_{(0:N-2)}^H - \kappa^2 \mathbf{A}^T \mathbf{A}^*]$. This formulation yields a weight vector of length $(N-1)$. The loss of one degree of freedom represents the subtraction operation in defining the matrix \mathbf{A} . Analogous to the spatial adaptive weights, the temporal weight vector \mathbf{w}_t is also computed. The length NM space-time adaptive weight vector, for look angle ϕ_t and look Doppler f_t is then given by

$$\mathbf{w}(\phi_t, f_t) = \begin{bmatrix} \mathbf{w}_t \\ 0 \end{bmatrix} \otimes \begin{bmatrix} \mathbf{w}_s \\ 0 \end{bmatrix} \quad (12)$$

The parameter κ above sets a trade off between main beam gain and interference suppression. By changing the value of this parameter, it is possible to emphasize one or the other term. In determining the spatial weights, choosing $\kappa = 0$ eliminates the interference term. Therefore, as $\kappa \rightarrow 0$ the D^3 weight vector approaches the non-adaptive steering vector used in pulse-Doppler processing. On the other hand, if κ is chosen to be large, the role of the gain term G is negligible and the weight vector is dependent on the interference term only. This leads to emphasis on the suppression of interference at the expense of main beam gain. Note that the adaptive weight vector in Equation (12) is obtained using data from the primary range cell (test cell) only.

2.4.1 Performance of D^3 Processing in Non-homogeneous Interference

In this section, the advantages and disadvantages of D^3 processing are illustrated. This simulation includes the effects of clutter, barrage noise jammers, white noise and a discrete interferer. Table 1 lists the parameters used in the example.

Table 1: Parameters for example using simulated data.

<i>Parameter</i>	<i>Value</i>	<i>Parameter</i>	<i>Value</i>
Elements (N)	18	Pulses (M)	18
Element Spacing	0.5λ	Pulse Repetition Frequency	300 Hz
Array Transmit Pattern	Uniform	Uncompressed Pulse Width	$400\mu s$
Mainbeam Transmit Azimuth	0°	Transmit Power	400kw
Backlobe Attenuation	30	Land Reflectivity	-3.0dB
Jammer Azimuth Angles	$[-20^\circ 45^\circ]$	Jammer Power	40 dB each
Target Doppler (f_t)	1/3	Jammer Elevation Angles	$[0^\circ 0^\circ]$
Doppler of Interferer	1/3	Interferer Power	40 dB
Angle of Interferer	-51°	Thermal Noise Power	Unity
β (Clutter slope)	1	Number of Clutter Patches	361

The jammer power and discrete interferer power are both referenced to the noise level. The clutter power is fixed by the transmit power. The clutter and jammers represent correlated interference because these two interference sources are homogeneous across all range cells. Note that the discrete interferer is contained in the test cell, with an offset from the look direction in angle but not Doppler.

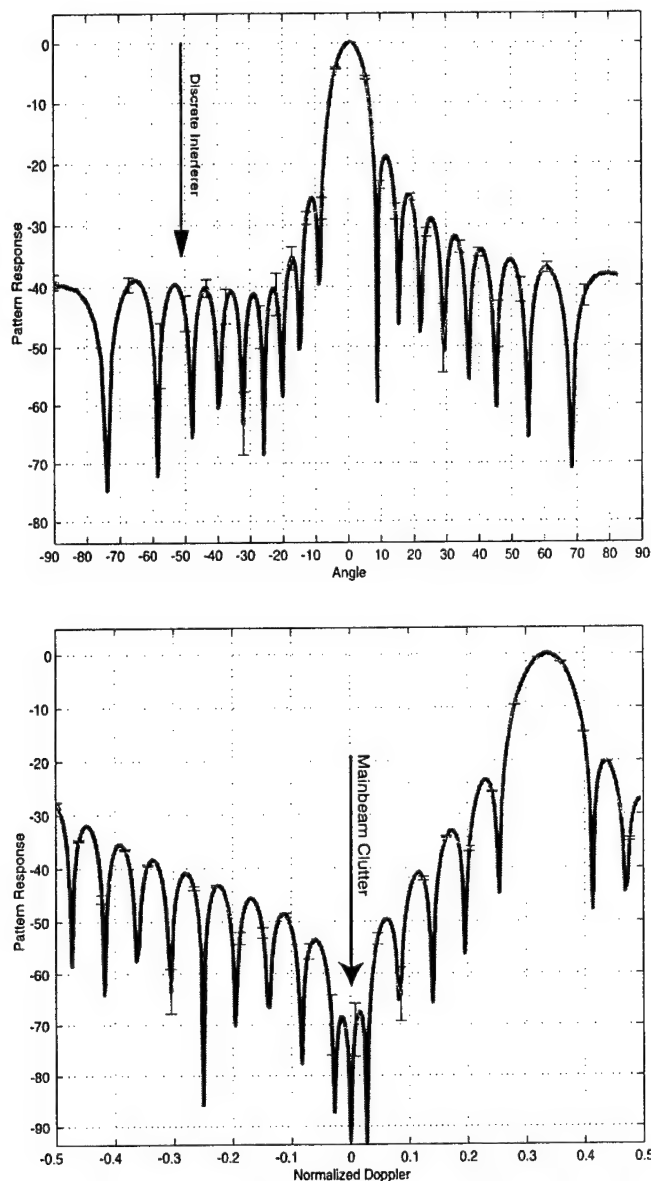


Figure 6: JDL Antenna Patterns at Target Doppler and Azimuth
(a) Angle Pattern (b) Doppler Pattern.

Figure 6 plots antenna patterns along the target azimuth and Doppler for the JDL algorithm. In the angle pattern, note the high sidelobe in the direction of the discrete interferer. This discrete interferer is within the primary range cell and *cannot* be nulled by the JDL algorithm. However, JDL does place deep nulls in the direction of the white noise jammers at -20° and 45° .

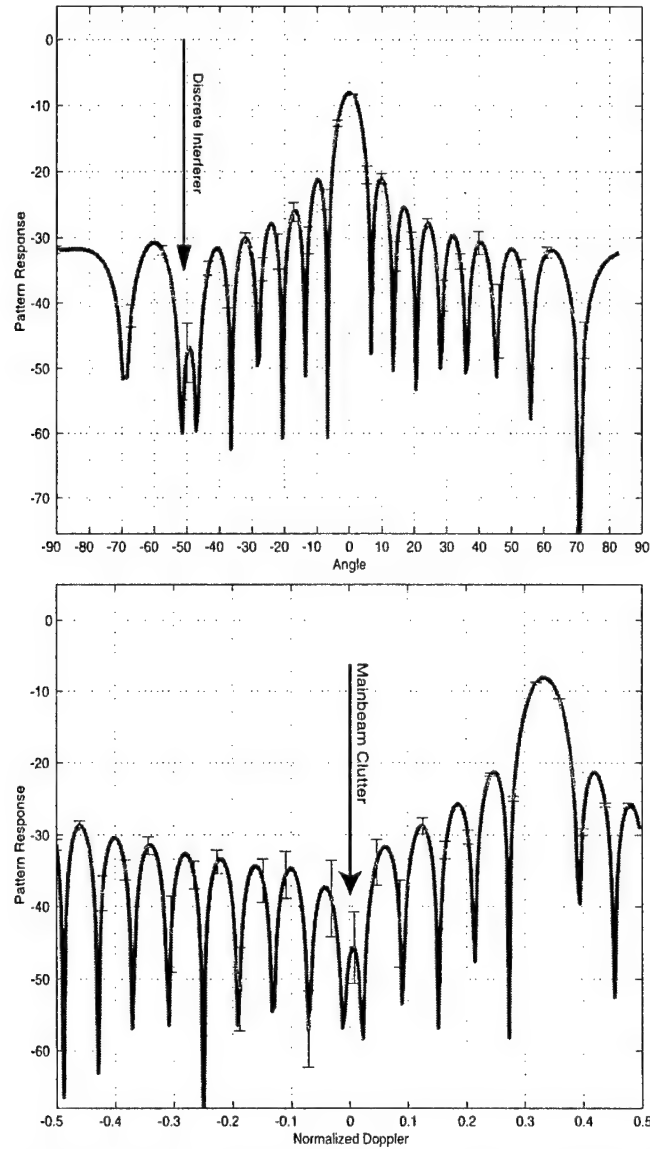


Figure 7: Direct Data Domain Patterns at Target Doppler and Azimuth
(a) Angle Pattern (b) Doppler Pattern.

The Doppler plot in Figure 6 shows a deep null at zero Doppler frequency corresponding to mainbeam clutter. These two plots illustrate the effectiveness of the JDL algorithm in suppressing distributed interference such as jamming and clutter. However, they also illustrate the inability of a purely statistical algorithm to suppress point non-homogeneities (discretes) in the cell under test. The adapted beam patterns presented in this paper are mean averaged over 200 independent realizations. Vertical bars represent the standard deviation over these 200 trials. This method was required because the D^3 algorithm is non-statistical and based solely on one realization. Operating with the a known covariance matrix to obtain an ideal pattern, as possible in statistical algorithms, is not an option.

Figure 7 above plots the antenna patterns resulting from the implementation of the two-dimensional D^3 algorithm. The angle plot demonstrates the effectiveness of the D^3 algorithm in placing a null in the direction of a discrete interferer. The adapted spatial beam pattern shows a distinct null in the direction of the interferer at -51° , i.e. the algorithm is effective in countering the discrete within the range cell under test. However, this figure also illustrates the limitations of the D^3 algorithm. The nulls in the direction of the jammers are not as deep as in the case of JDL. The Doppler plot shows a shallow null in the direction of mainbeam clutter as well. In summary, D^3 algorithms do not suppress distributed interference as well as statistical algorithms, however they offer an excellent approach to deal with discrete "point" non-homogeneities.

3.0 GMTI-STAP

The research presented in this section continues the work described above, while also addressing some of the critical issues raised earlier. We present a hybrid algorithm combining non-statistical and statistical adaptive processing, and use this algorithm to develop the simplest formulation for a comprehensive, practical, approach to STAP. This formulation accounts for the many of the real world effects listed above.

Section 2.4 discusses non-statistical adaptive processing in non-homogeneous environments, pointing out both the advantages and drawbacks of such an approach. Here we present a unique formulation combining the benefits of non-statistical and statistical methods. This hybrid algorithm is a two-stage technique combining both approaches. The examples presented in this paper show the improvements in performance over traditional STAP algorithms and illustrate the importance of the issues raised.

3.1 Hybrid (D3/JDL) STAP

Performance degradation of STAP algorithms arising due to non-homogeneous data occurs in two forms. In one form the secondary data is not i.i.d., leading to an inaccurate estimate of the covariance matrix. The second form of performance loss is due to discrete point non-homogeneities within the test range ring. For example, a large target within the test range ring but at a different angle and/or Doppler may cause a false alarm. These non-homogeneities enter through the sidelobes of the adapted pattern. Since secondary data do not carry information about these discrete non-homogeneities, a statistical algorithm cannot suppress such interference within the range cell under test. The example presented in Section 2.4 illustrated the impact these point like discretises.

The inability of statistical STAP algorithms to counter non-homogeneities in the primary data motivated our interest in the area of the D^3 algorithm. These algorithms use data from the range cell of interest only, eliminating the sample support problems associated with statistical methods. The main contribution of this paper is the introduction of a two-stage hybrid STAP algorithm combining the benefits of both the non-statistical D^3 algorithm and the statistical JDL algorithm. This hybrid approach uses the D^3 algorithm as a first-stage filter to suppress discrete interference present in the range cell of interest, and serves as an adaptive transform from the space-time domain to the angle-Doppler domain. This is followed by JDL processing in the second stage. This adaptive approach replaces the steering vector based non-adaptive transform used in Section 2.2. The second stage is designed to filter out residual distributed interference [Hale 00].

3.1.1 Two-Stage Hybrid Algorithm

Consider the general framework of any STAP algorithm. The algorithm processes received data to form a complex weight vector for each range bin and angle/Doppler. The weight vector then multiplies the primary data vector to yield a complex number. The process of obtaining a real scalar from this number for threshold comparison is part of the post-processing and not inherent to the algorithm itself. The adaptive process therefore estimates the signal component in the look direction and hence adaptive weights can be viewed in a role similar to the non-adaptive steering vectors used to transform space-time data to the angle-Doppler domain.

The JDL algorithm begins with a transformation of the data from the space-time domain to the angle-Doppler domain. This is followed by statistical adaptive processing within a LPR in the angle-Doppler domain. The hybrid approach uses the D^3 weights, replacing the non-adaptive steering vectors. By choosing the set

of look angles and Dopplers to form a LPR, the D^3 weights perform a function analogous to the non-adaptive transform. As shown in Figure 8, the D^3 algorithm serves as a first stage adaptive transformation from the space-time to the angle-Doppler domain.

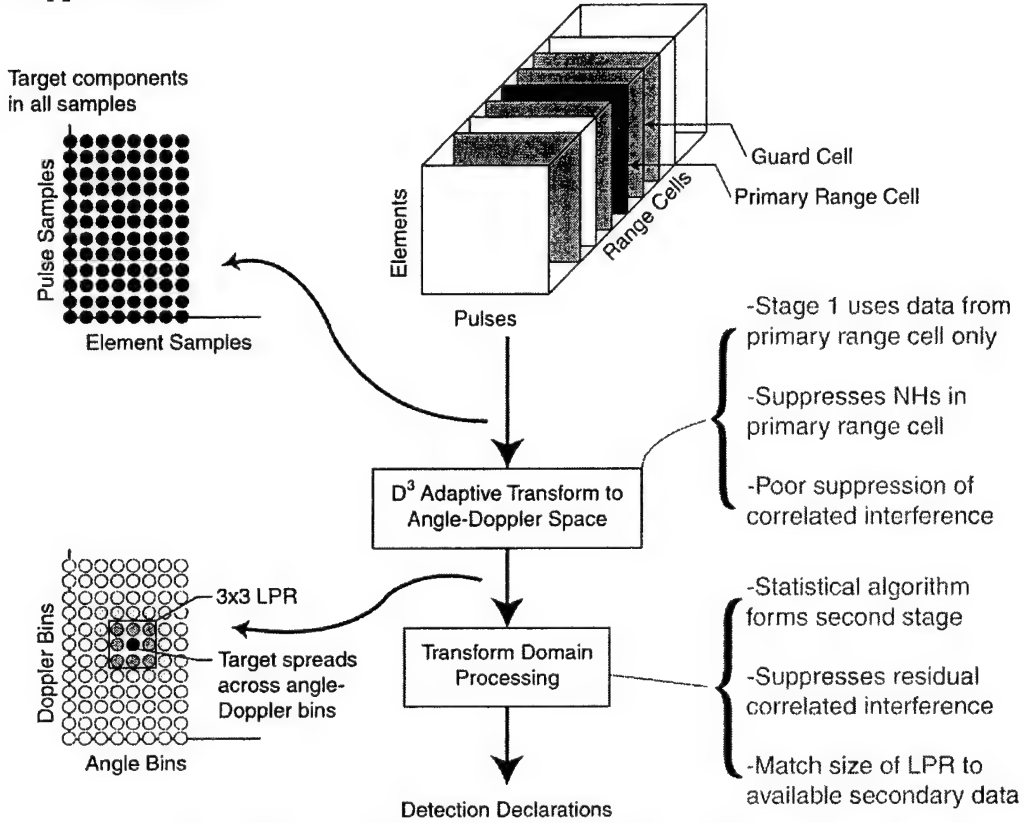


Figure 8: Block diagram of the Two-Stage Hybrid Algorithm.

JDL statistical processing in the angle-Doppler domain forms the second stage of adaptive filtering to reject residual correlated interference. The D^3 algorithm is used repeatedly in η_a look angles and η_d look Doppler frequencies to form a LPR. The space-time data is transformed to the angle-Doppler domain using these adaptive weights. Using the D^3 weights, the transformation in Section 2.1 is now given by a $MN \times 9$ transformation matrix

$$\mathbf{T} = \begin{bmatrix} \mathbf{w}(\phi_{-1}, f_{-1}) & \mathbf{w}(\phi_{-1}, f_0) & \mathbf{w}(\phi_{-1}, f_1) \\ \mathbf{w}(\phi_0, f_{-1}) & \mathbf{w}(\phi_0, f_0) & \mathbf{w}(\phi_0, f_1) \\ \mathbf{w}(\phi_1, f_{-1}) & \mathbf{w}(\phi_1, f_0) & \mathbf{w}(\phi_1, f_1) \end{bmatrix} \quad (13)$$

The same transformation matrix \mathbf{T} is used to transform the primary and the secondary data to the angle-Doppler domain. Furthermore, the steering vector \mathbf{s} is also transformed to the angle-Doppler domain using this transformation. Unlike the JDL algorithm, this transformation matrix changes from test cell to test cell. The hybrid algorithm therefore has a significantly higher computation load than the JDL algorithm, but is applied only to non-homogeneous test cells.

3.1.2 Example 1: Simulated Data

This first example uses the same data as presented in Section 2.4.1 to illustrate the performance of the D^3 method. There it was shown that the D^3 algorithm can suppress a discrete interference source, but does not perform well against distributed interference such as white noise jamming and clutter. This example illustrates the performance of the hybrid algorithm, and uses 3 angle bins and 3 Doppler bins, i.e. 3×3 LPR. The parameter κ is chosen to be $(NM)^{1/2}$.

Figure 9 plots the spatial patterns associated with the three beams used to form an LPR in the angle-Doppler domain. Note that the three beams are separated by 6.5° . All three patterns show a null in the direction of the discrete interferer at angle -51° , and illustrates the benefits of using the D^3 algorithm to transform into the angle-Doppler domain.

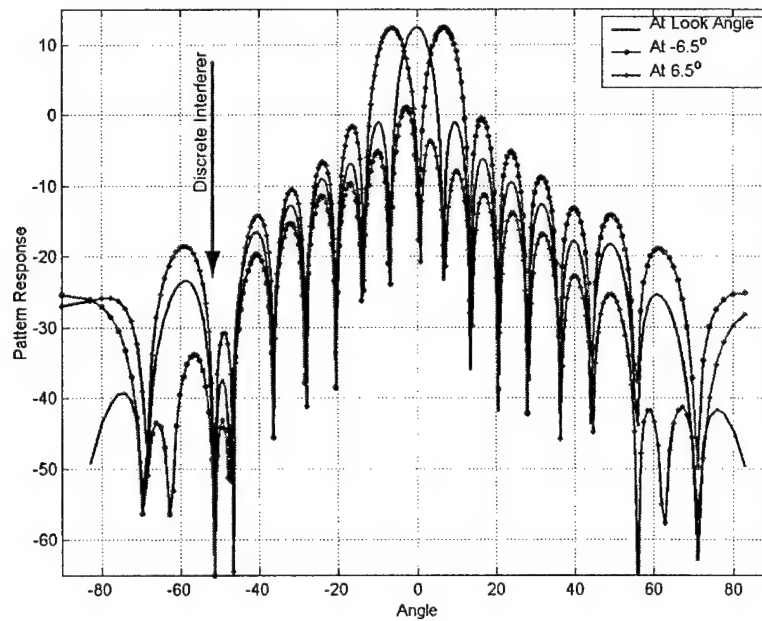


Figure 9: Three D^3 spatial beams used to form an LPR.

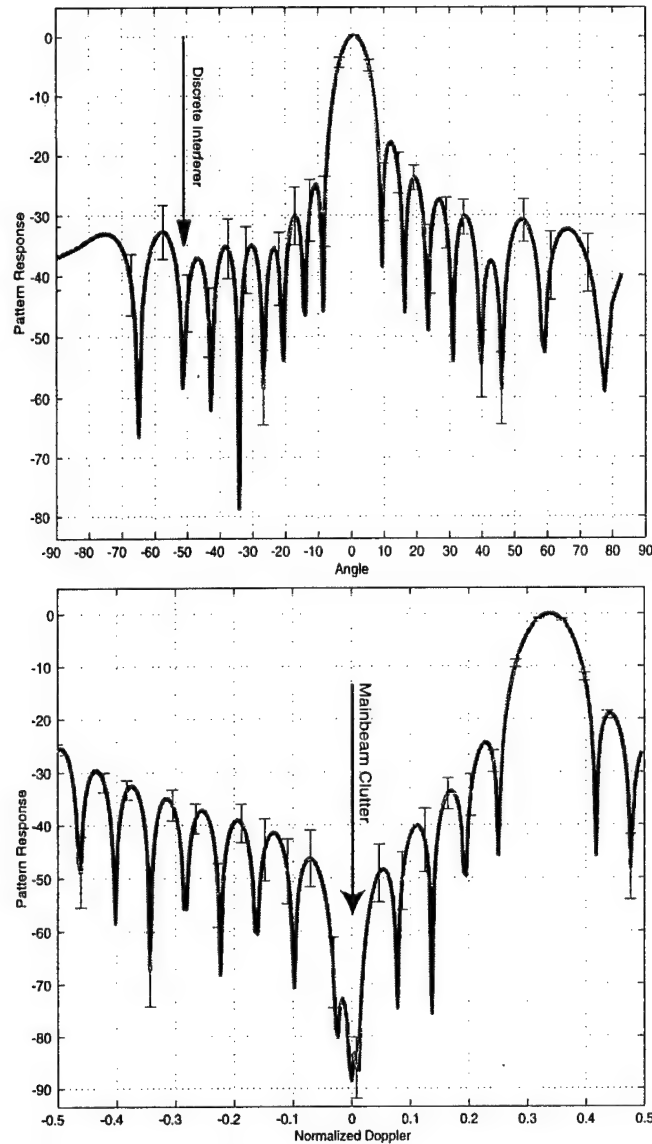


Figure 10: Hybrid Algorithm Patterns at Target Azimuth and Doppler.

Figure 10 plots the antenna beam patterns resulting from application of the hybrid algorithm. This figure shows that the hybrid algorithm combines the advantages of both statistical and non-statistical adaptive processing. The adapted angle pattern shows deep nulls at -21° , 45° , and -51° , the directions of the two jammers and the discrete interferer. Furthermore, the adapted Doppler pattern has a deep null at $\omega=0$ resulting in effective nulling of the main beam clutter. The

hybrid algorithm therefore suppresses correlated interference such as clutter and jamming, as well as a discrete in the primary data.

3.1.3 Applying the Hybrid Algorithm to Measured Data

This section presents analysis of MCARM data using the hybrid algorithm. This example use acquisition 575 on flight 5 to illustrate the suppression of discrete interference in measured data. Before the hybrid algorithm can be applied to MCARM data, array effects must be accounted for. The D^3 method presented in Section 2.4 is for an equispaced, linear array of point sensors. This allowed for the assumption of no mutual coupling between the elements and that, for each pulse, the target signal advances from one element to the next by a constant spatial multiplicative factor z_s . This, in turn, allowed for the crucial assumption of the elimination of the target signal in entries of the interference matrix.

The MCARM antenna is an array of 22 elements arranged in a rectangular 2×11 grid. For a rectangular array these assumptions are invalid. Furthermore, as shown in Section 2.2, a real array is affected by mutual coupling and the spatial steering vector must be measured. Figure 3 presents the measured steering vectors provided with the MCARM database. We compensate for mutual coupling using these measured steering vectors. In the absence of mutual coupling, the spatial steering vector at broadside ($\phi_t = 0$) is given by $\mathbf{a}(\phi_t = 0) = [1 \ 1 \dots 1 \ 1]^T$. Compensation is achieved by an entry-by-entry division of the received voltages at the element level with the measured spatial steering vector entry corresponding to that look direction.

3.1.4 Example 2: MCARM Data Analysis

In this example, a discrete non-homogeneity is introduced into the data by adding a synthetic signal to a single range ring, but not in the main beam. Two cases are considered; no injected target and a weak injected target. The first case illustrates the suppression of a discrete non-homogeneity. In the second case, a weak mainlobe test target is injected at the same range as the non-homogeneity in the sidelobe. This case illustrates the ability of the hybrid algorithm to detect weak targets in the presence of strong discretely. The same data used earlier to illustrate the performance of the JDL algorithm is analyzed. In this case, only 22 of the 128 pulses in the CPI are used, i.e. $N=M=22$. The value of the emphasis parameter is $\kappa = (NM)^{3/2}$. The details of the injected non-homogeneity and weak target are shown in Table 2.

Table 2: Parameters for the injected non-homogeneity and test target.

Parameter	Non-homogeneity	Test Target
Amplitude	0.0241	0.000241
Angle bin	35	65 (broadside)
Doppler bin	-3	-2
Range bin	290	290

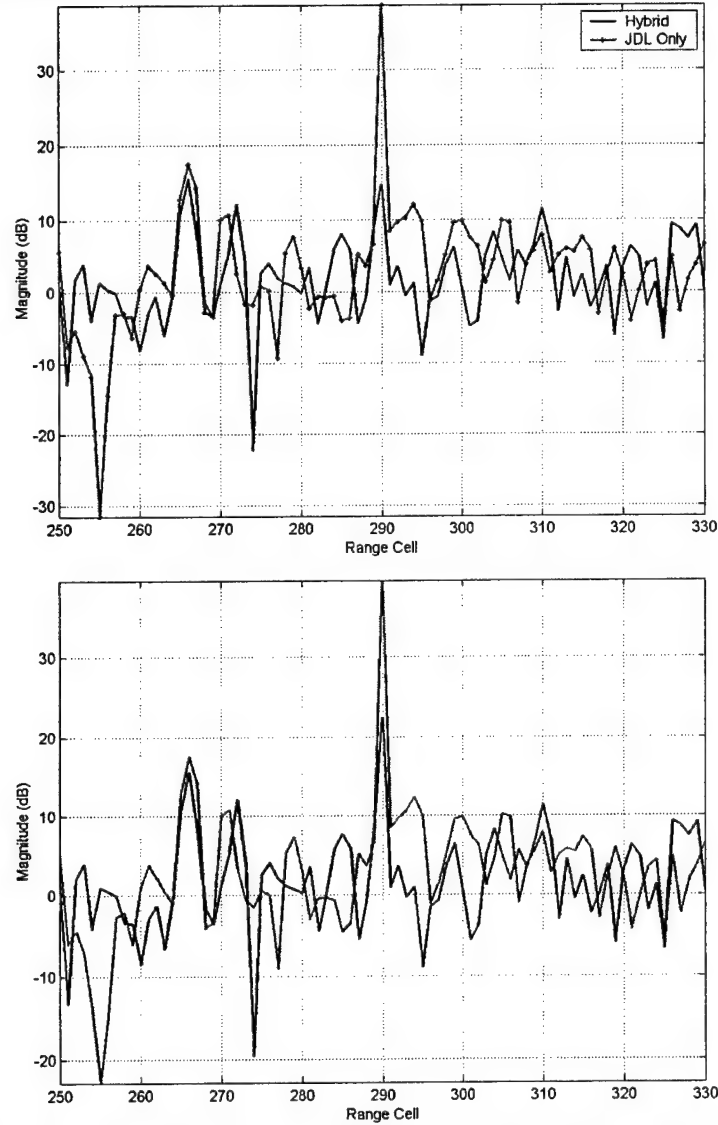


Figure 11: Performance of the Hybrid algorithm in countering non-homogeneities: (a) No target (b), With target.

The hybrid algorithm is applied to data from the range bin under test and surrounding cells. The MSML test statistic is plotted as a function of range. In this example, five Doppler bins and five angle bins form the LPR for both the JDL algorithm and the hybrid algorithm. One hundred secondary data vectors are used to estimate the 25×25 covariance matrix.

For the case with no main beam target, Figure 11a compares the output from the JDL algorithm with the output of the hybrid algorithm. As illustrated, the JDL algorithm detects the presence of a large target in the main beam (angle bin 65). This is because the non-homogeneity (at angle bin 35, Doppler bin -3) is not suppressed by the JDL algorithm, thus leading to a false alarm. However, the hybrid algorithm detects no broadside target. The non-homogeneity is suppressed in the D^3 stage of processing and residual clutter is suppressed by JDL algorithm. A synthetic target injected in the main beam illustrates the sensitivity of the hybrid algorithm. The parameters of the test target are listed in Table 2. Figure 11b compares the output of the two algorithms. The JDL algorithm again shows the presence of a strong target in the look direction. However from Figure 11a, we know that the magnitude of the test statistic is altered by presence of the non-homogeneity. For the hybrid algorithm, the test statistic at the target range bin is only 6.9 dB above the next highest peak, demonstrating that the hybrid algorithm may be used to detect weak targets in the presence of discrete non-homogeneities within a range ring of interest.

4.0 Conclusions and Future Work

This paper presented the hybrid algorithm, developed specifically to process non-homogeneous test data. Statistical algorithms cannot suppress discrete non-homogeneities because the secondary data contains no information regarding such interference. The D^3 method, presented above, can suppress such discrete interference. However, performance of the D^3 algorithm in homogeneous interference is inferior to classical STAP algorithms. The two-stage hybrid algorithm alleviates this drawback by implementing a second stage of statistical processing after using the D^3 algorithm as an adaptive transform to the angle-Doppler domain. This algorithm combines the advantages of both statistical and non-statistical methods. The D^3 method is particularly effective at countering non-homogeneous discrete interference. The JDL algorithm then improves upon the suppression of residual correlated interference.

The current focus of our research is on applications of the hybrid algorithm to non-standard arrays including circular phased arrays and sparse arrays of potentially dissimilar antennas. Our ultimate goal is the generalization of multidimensional adaptive processing resulting in advanced portable algorithms applicable to a wide range of fielded sensor systems.

5.0 Acknowledgement

Dr. Ravi Adve and Capt. Todd Hale are gratefully acknowledged for their contributions to this research.

6.0 References

[Adve 00] R.S. Adve, T.B. Hale and M.C. Wicks, "Joint Domain Localized Adaptive Processing in Homogeneous and Non-homogeneous Environments. Part I: Homogeneous Environments", *IEE Proc. on Radar, Sonar and Navigation*. April 2000.

[Antonik 97] P. Antonik, H. Shuman, P. Li, W. Melvin, M. Wicks, "Knowledge-based Space-Time Adaptive Processing", *Proc. of the 1997 IEEE National Radar Conference*, Syracuse, NY, May 1997.

[Chang 97] H.H. Chang, "Improving Space-Time Adaptive Processing (STAP) Performance in Nonhomogeneous Clutter", Ph.D. thesis, Syracuse University, August 1997.

[Fenner 96] D.K. Fenner and W.F. Hoover Jr., "Test Results of a Space Time Adaptive Processing System for Airborne Early Warning Radar", *Proc. IEEE National Radar Conference*, pp. 88-93, Ann Arbor, MI, May 1996.

[Hale 00] R.S. Adve, T.B. Hale and M.C. Wicks, "Joint Domain Localized Adaptive Processing in Homogeneous and Non-homogeneous Environments. Part II: Non-Homogeneous Environments", *IEE Proc. on Radar, Sonar and Navigation*. April, 2000.

[Reed 74] I.S. Reed, J. Mallet, and L. Brennan, "Rapid convergence rate in adaptive arrays", *IEEE Trans. on AES*, vol. 10, no. 6, pp. 853-963, December 1974.

[Sarkar 89] T.K. Sarkar and N. Sangruji, "An Adaptive Nulling System for a narrow band signal with a Look Direction Constraint Utilizing the Conjugate Gradient method", *IEEE Trans. on AP*, vol. 37, no. 7, pp. 940-944, July 1989.

[Wang 94] H. Wang and L. Cai, "On adaptive spatial-temporal processing for airborne surveillance radar systems", *IEEE Transactions on AES*, vol. 30, No. 3, pp. 660-669, July 1994.

RANKING AND SELECTION FOR TRAINING DATA SELECTION IN MULTI-CHANNEL RADAR

Pinyuen Chen

Michael C. Wicks

Radar Signal Processing Branch

Air Force Research Laboratory

Rome, NY 13441

Abstract: Traditional signal detection algorithms assume homogeneous covariance matrix for all the secondary data. We deal with the nonhomogeneity via a partitioning procedure, which screens out dissimilar secondary data prior to any detection. The partitioning statistic and its distribution will be used to derive $P(CP)$, the probability of a correct partition. The procedure parameters can be found from $P(CP)$ and be used to perform simulation studies and for data analysis. Simulation results and numerical analysis using the US Air Force Multi-Channel Airborne Radar Measurement data collected by Westinghouse (now Northrop Grumman) will be presented to illustrate our theory.

1. Introduction

In signal detection, one is interested in the problem of detection of a given radar signal s which is a complex vector in the presence of noise in transmission. The actual observed data Y may be a pure noise vector n or the signal s plus a noise vector n . It is assumed that the noise follows a complex multivariate normal distribution with mean 0 and covariance matrix Σ . Statistically, the model can be described as $Y = s + n$ where s is a specific signal and n is a noise random vector. The goal is to test the null hypothesis that $Y = n$ versus the alternative hypothesis that $Y = s + n$. [1] Reed, Mallett and Brennan (1974) discussed an adaptive procedure for the above detection problem in which two sets of input data are used, which are called the primary and secondary data. A radar receives primary data y_0 which may or may not contain a signal, and secondary data which are assumed to contain only noise, independent of and statistically identical to the noise components of the primary data. The goal is to test $H_0 : \mu = 0$ versus $H_1 : \mu = s$ where μ is the population mean of y_0 . [2] Kelly

(1986) used the likelihood ratio principle to derive a test statistic for the above hypothesis testing problem.

[3] Chen and Wicks (1999) proposed a selection procedure which compares the covariance matrices of the secondary data with that of the primary data. It is used to identify and eliminate those observations that have different covariance structure from the secondary data. As described in [3] Chen and Wicks (1999), this procedure can be applied prior to the step of estimating the covariance matrix of the secondary data in [1] Kelly (1986).

2. The Selection Procedure

Let $Y_0 \sim CN_p(\mu, \Sigma)$ denote the primary data which is received by a receiver and is to be tested for a specific signal s where s is a known vector. Let $Y_1, Y_2, \dots, Y_n \sim CN_p(0, \Sigma)$ be the secondary data which is to be used to estimate the unknown covariance matrix Σ . The random vector Y_0 is independent of the secondary data. Let S denote n times the sample covariance matrix of the secondary data sample Y_1, Y_2, \dots, Y_n . Our goal is to test

$$(2.1) \quad H_0 : \mu = 0 \quad \text{versus} \quad H_1 : \mu = s.$$

Kelly's likelihood ratio test statistic for (2.1) can be written as

$$(2.2) \quad \eta = \frac{|s^* S^{-1} Y_0|^2}{(s^* S^{-1} s)(1 + Y_0^* S^{-1} Y_0)}.$$

The null hypothesis is rejected for large observed η . It was shown in Kelly (1986) that under H_0 , $\eta \sim \text{Beta}(1, n - p + 1)$, a Beta distribution with parameters 1 and $n - p + 1$.

Following Reed, Mallett, and Brennan (1974)'s structure of radar data, Kelly's test also assumes an i. i. d. sample Y_1, Y_2, \dots, Y_n for the secondary data and an independently distributed primary data Y_0 . Let $\pi_1, \pi_2, \dots, \pi_k$ represent k p -variate complex normal populations $CN_p(\mu_i, \Sigma_i)$, $i = 1, 2, \dots, k$, and let π_0 be a control p -variate complex normal population $CN_p(\mu_0, \Sigma_0)$. Those k populations are the resources of the k cells which may or may not have the same or similar covariance structures as the control population π_0 from which the secondary data are taken.

Here “similarity” is defined in (2.3) and (2.4) and the paragraph after (2.4) later in this section. Thus, from each of the k experimental populations, only one observation is taken, and from the control population, n observations are taken. We assume that $\mu_i = 0, i = 0, 1, 2, \dots, k$ since the k experimental populations are the cells which are assumed to have zero mean. Let $\lambda_{i,1} \geq \lambda_{i,2} \geq \dots \geq \lambda_{i,p} > 0$ denote the ordered eigenvalues of $\Sigma_i \Sigma_0^{-1}$. We define the two disjoint and exhaustive subsets, Ω_G and Ω_B , of the set $\Omega = \{\pi_1, \pi_2, \dots, \pi_k\}$, by using a pair of distance functions d_1 and d_2 defined as follows:

$$(2.3) \quad d_1(\Sigma_i, \Sigma_0) = \lambda_{i,1}; \quad d_2(\Sigma_i, \Sigma_0) = \lambda_{i,p}$$

$$(2.4) \quad \Omega_B = \{\pi_i \mid \delta_2^* \leq d_2(\Sigma_i, \Sigma_0) \text{ or } d_1(\Sigma_i, \Sigma_0) \leq \delta_1^*\}, \Omega_G = \Omega - \Omega_B,$$

where $\delta_1^* < \delta_2^*$ are pre-assigned positive real numbers which are used to define similar and dissimilar populations. A population is considered similar to a control population when the distance measures are close to unity. Our goal is to separate the populations obtained from the guard cells into two disjoint subsets, S_G and S_B . The separation is correct if $S_G \subset \Omega_G$, meaning that all populations included in selected subset S_G have similar covariance structure as the control population. We require a procedure R that will satisfy the probability requirement that $\Pr(\text{the separation is correct} \mid R) = \Pr(\text{CS} \mid R) \geq P^*$, where P^* satisfies $2^{-k} < P^* < 1$.

The procedure R defined in Chen and Wicks (1999) is as follows.

Procedure R : For each population π_i ($i = 1, 2, \dots, k$), we first compute $T_i = (x_i^H S^{-1} x_i) / n$ where x_i 's are the data vectors from experimental cells, x_i^H is the conjugate transpose of x_i , and S is the sample covariance matrix associated with population π_0 . Then we partition the set of populations $\Omega = \{\pi_1, \pi_2, \dots, \pi_k\}$ into two subsets S_G and S_B . The subset S_G consists of those populations π_i with $c \leq T_i \leq d$ where c and d are chosen such that the probability requirement $P(\text{CS}) \geq P^*$ is satisfied and $S_B = \Omega - S_G$.

To implement the procedure with a pre-determined probability requirement P^* , Chen and Wicks (1999) have shown that constants c and d have to satisfy the following integral equation:

$$(2.5) \quad \min_{\Omega} P(\text{CS}) = \min_{0 \leq m \leq k} P(T_i < c, i = 1, \dots, m; T_j > d, j = m+1, \dots, k)$$

$$\begin{aligned}
&\geq \min_{0 \leq m \leq k} \{1 - mP(T_i > c) - (k-m)P(T_i < d)\} \\
&= \min_{0 \leq m \leq k} \left\{1 - m \left(1 - F_{2p, 2(n-p+1)}\left(\frac{(n-p+1)}{p} \frac{c}{\delta_1^*}\right)\right) - \right. \\
&\quad \left. (k-m) F_{2p, 2(n-p+1)}\left(\frac{(n-p+1)}{p} \frac{d}{\delta_2^*}\right)\right\}
\end{aligned}$$

where $F_{2p, 2(n-p+1)}$ is the distribution function of an F distribution with $2p$ and $2(n-p+1)$ degrees of freedom. We also define $T_0 \equiv 0$ and $T_{k+1} \equiv 0$.

3. Simulation Study and An Example

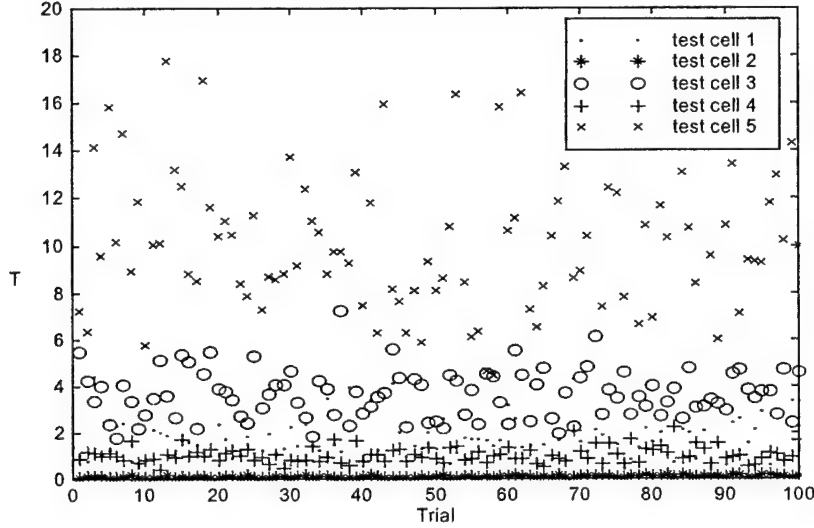
Example: Five test (or guard) cells are to be examined and to be compared with a sample of secondary cells. Each cell π_i is represented by a 20×1 random vector x_i from a multivariate complex normal distribution with mean 0 and covariance matrix Σ_i . The covariance matrix of the secondary cells is denoted by Σ_0 . The five test cells come from normal populations with covariance matrices Σ_i such that

$$\begin{aligned}
\Sigma_1 \Sigma_0^{-1} &= \text{diag}(2.8, 6.7, .06, .05, .08, .07, .06, .05, 1.68, .09, 11.7, 9.6, .05, \\
&\quad .08, .07, .06, .05, .08, .07, .06); \\
\Sigma_2 \Sigma_0^{-1} &= \text{diag}(.1, .1, \dots, .1); \\
\Sigma_3 \Sigma_0^{-1} &= \text{diag}(1.2, 2.5, 3.1, .8, 2.3, 5.4, 3, 2.9, 6.1, 3.3, 5.3, .5, .9, 7.3, 1.7, \\
&\quad 5.5, 2.3, 3.1, 6.4, 5.5); \\
\Sigma_4 \Sigma_0^{-1} &= I; \Sigma_5 \Sigma_0^{-1} = \text{diag}(10, 10, \dots, 10).
\end{aligned}$$

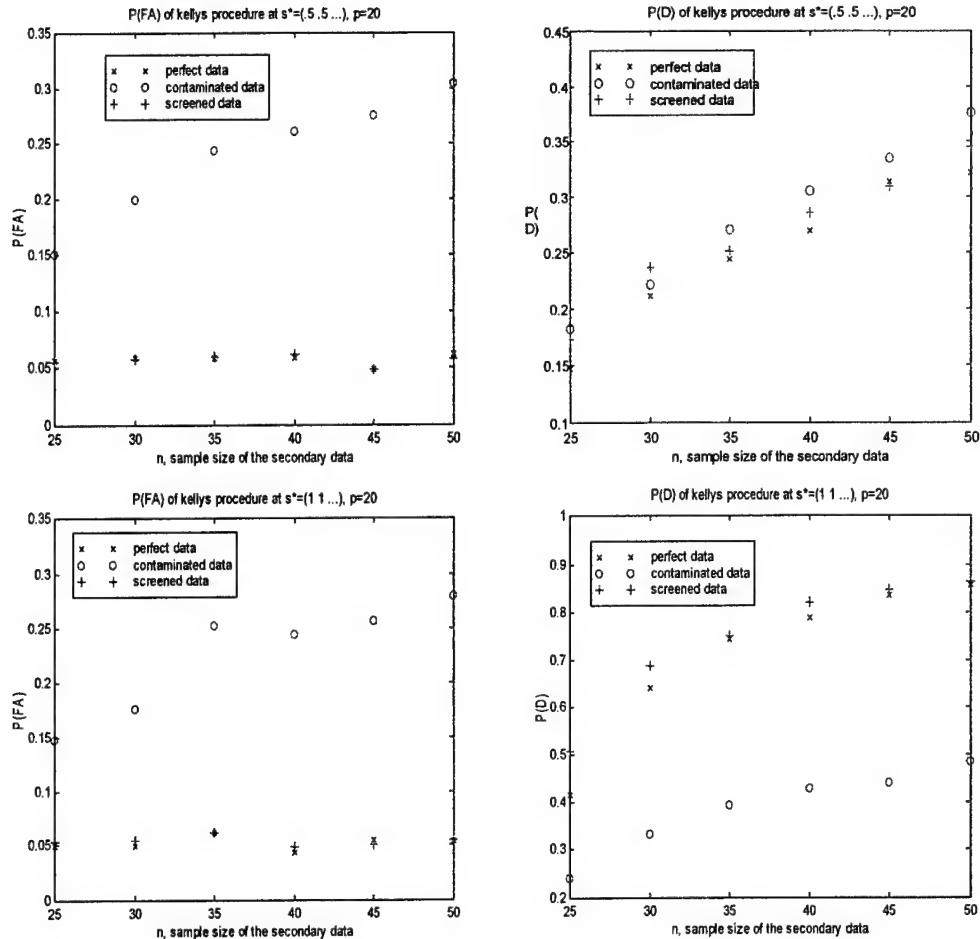
Suppose we want to eliminate the test cell π_i if either the largest eigenvalue of $\Sigma_i \Sigma_0^{-1}$ is smaller than or equal to $\delta_1^* = .1$ or the smallest eigenvalue of $\Sigma_i \Sigma_0^{-1}$ is larger than or equal to $\delta_2^* = 10$. Then by choosing $c = .2$ and $d = 5$, we find from a computing algorithm for (2.5), for the case $k = 5$, $p = 20$, $\delta_1^*/c = 1/2$, and $\delta_2^*/d = 2$, that the required sample size is $n = 39$ for the secondary data to achieve $P^* = .90$. We simulated 100 trials of x_i ($i = 1, \dots, 5$) and S from the multivariate complex normal populations with mean 0 and with respective covariance matrices satisfying the above conditions. Then for each trial, we calculate the test statistic $T_i = x_i^H S^{-1} x_i / n$. The results are plotted in Figure 1 at the end of the paper. From the definition of Procedure R given in Section 2, Cell π_i is retained if $.2 < T_i < 5$. It is clear from the figure that Cell 4 is always retained. Cell

2 and Cell 5 are always eliminated. Cell 1 and Cell 3 are retained most of the times. Notice that Cell 4 is a perfect cell while Cell 1 and Cell 3 are both considered good cells.

Fig 1: 100 trials of T for 5 test cells x and a sample covariance S from $n=39$ secondary cells



In our next simulation illustrations, we show, in Figures 2 to Figure 5, the probability of the false alarm ($P(FA)$) and the probability of the detection ($P(D)$) when Kelly's adaptive detection algorithm is applied to three different data sets. The first data set is the perfect data set where all the observations in the secondary data are simulated from the same multivariate complex normal distribution as the primary data. The second data set is the contaminated data set where the secondary data includes some observations that were obtained from simulation of various multivariate complex normal distributions whose covariance matrices are significantly different from the covariance matrix of the primary data. The third data set is the screened data set which consists of those observations that were originally in the contaminated data set and were retained in the secondary data after our procedure R has been applied. We consider the following cases: n , the sample size of the secondary data, = 25, ..., 50; $p = 20$; and $s = (.5, \dots, .5)^*$ and $(1, \dots, 1)^*$. The level of significance is set at .05 for all the cases considered. In Figures 2-5, the 'o's' are for the contaminated data set. The 'x's' are for the perfect data set, and the '+'s are for the screened data set. It is clear from the illustrations that Kelly's algorithm does not provide a constant false alarm rate (CFAR) for the contaminated data set and it always gives CFAR for the perfect data set and screened data set.



'o': the contaminated data set; 'x': the perfect data set; '+': the screened data set.

4. References

- [1] Reed, I. S., Mallett, J. D., and Brennan, L. E. (1974) Rapid Convergence In Adaptive Arrays, *IEEE Transactions on Aerospace & Electronic Systems*, vol. 10, #6, 853-863.
- [2] Kelly, E. J. (1986). An Adaptive Detection Algorithm *IEEE Transactions on Aerospace & Electronic Systems*, vol. 22, #1, 115-127.
- [3] Chen, P. and Wicks, M. C. (1999) Identifying Non-homogenous Multivariate Normal Observations. Technical Report. Submitted for publication.

Efficient Architectures for Implementing Adaptive Algorithms

David C. Ricks and J. Scott Goldstein
Science Applications International Corporation
4001 Fairfax Drive, Suite 675
Arlington, VA 22203

Abstract

Recently the Multistage Wiener Filter has been introduced as a tool for signal detection, estimation, and classification. It can be used to filter a block of data snapshots to extract the part of the data that matches a steering vector or a replica vector. It is a minimum mean square error filter that can solve for the Minimum Variance Distortionless Response (MVDR). Here we consider the numerical efficiency of the Multistage Wiener Filter on the MVDR problem. This paper introduces a new implementation of the Multistage Wiener Filter that eliminates the need for blocking matrices or projection matrices in the numerical calculations. Compared to the traditional MVDR solution based on the inversion of a covariance matrix, we find the Multistage Wiener Filter now offers significantly greater computational efficiency, as well as other advantages such as hardware scalability.

1. Introduction

This paper considers the computational efficiency of a problem in the estimation of Minimum Mean Square Error (MMSE). In particular, we consider the computational cost of filtering a data set to obtain the Minimum Variance Distortionless Response (MVDR) [1].

Figure 1 motivates the problem schematically. We want to filter a set of column data vectors $\mathbf{x}(k)$ to extract the part of the data that matches a column steering vector \mathbf{s} . The filtering should pass the part of the data that matches \mathbf{s} while it suppresses the part of the data that does not match \mathbf{s} .

This work was sponsored by the Office of Naval Research under contract N00014-00-C-0068.

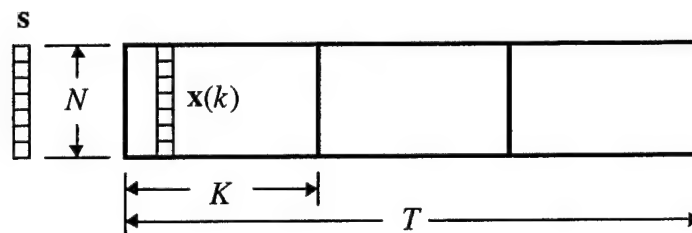


Fig. 1. Schematic diagram of the data to be processed, where $\mathbf{x}(k)$ is a single column data vector with N entries or elements. The total number of data vectors T is broken into blocks of K vectors per block. We want to extract the part of the data that matches a column steering vector \mathbf{s} .

This concept has a broad range of applications. For single-frequency adaptive beamforming, \mathbf{s} can be a model of the spatial pattern a signal can trace over the array (and \mathbf{s} is typically complex). For wireless communications, \mathbf{s} can be the spreading code of an individual user in CDMA (and \mathbf{s} is typically real). For Space-Time Adaptive Processing (STAP), \mathbf{s} can be a pattern in time and space (being transformed to frequency and angle).

The traditional solution involves the calculation of a data covariance matrix, followed by the numerical inversion of that matrix [1]. The data snapshots are column vectors with N entries or elements each, so the covariance matrix is N -by- N . Computationally, the matrix inversion involves a cost of $O(N^3)$ [2].

As an alternative, here we solve the MVDR problem with the Multistage Wiener Filter (MWF) [3]. The MWF is a “subspace” or “reduced rank” technique. As such, it might be compared to the technique of Principal Components (PC) that intends to approximate the solution using the leading eigenvalues and eigenvectors of the covariance matrix. However, the MWF concentrates on characterizing the *most significant* part of the *interference* (instead of trying to characterize the *most energetic* part of *all* the data). We might say the MWF is “interference-centric” (versus “data-centric”).

This paper reconsiders the MWF solution with an eye toward the computational costs. We introduce a modification to the algebra and the architecture that will be shown below in Figure 2. We find that, in some situations, the computational cost may be as low as $O(N)$. Physically, the potential for this efficiency comes from

the “interference-centric” view expressed in a suitable “reduced rank” formulation. Numerically, the potential for this efficiency is realized by accounting for all the subspace projections in the fixed perspective of the original N -dimensional space.

2. Problem Statement

To state the filtering problem mathematically, let $\mathbf{x}(k)$ be a column vector of data with N entries. The data may be complex. The index k means that $\mathbf{x}(k)$ is one snapshot in a block of snapshots, where $1 \leq k \leq K$. Increasing k typically corresponds to increasing time. Let the block of snapshots be the N -by- K matrix

$$\mathbf{X} \equiv [\mathbf{x}(1), \mathbf{x}(2), \dots, \mathbf{x}(k), \dots, \mathbf{x}(K)]. \quad (1)$$

We want to filter the block \mathbf{X} to extract the part of the data that best matches a steering vector or a replica vector \mathbf{s} . The steering vector may be complex (*e.g.*, for single-frequency beamforming) or real (*e.g.*, for a spreading code). For any of these cases, we make the steering vector dimensionless with unit norm

$$\|\mathbf{s}\| = (\mathbf{s}^H \mathbf{s})^{1/2} = 1. \quad (2)$$

To formulate the filtering mathematically, a simple and popular approach is MVDR filtering [1]. This approach multiplies the data snapshots onto a weight vector \mathbf{w} that minimizes a quadratic cost function, subject to the constraint that the weight vector should pass the data that matches a replica vector \mathbf{s} . To state this mathematically, all averages in this paper will be averages over a finite block of snapshots (not ensemble averages)

$$\langle \rangle_K \equiv \frac{1}{K} \sum_{k=1}^K. \quad (3)$$

We write the minimization with the constraint $\mathbf{w}^H \mathbf{s} = 1$ as

$$\min_{\mathbf{w}^H \mathbf{s}=1} \langle |\mathbf{w}^H \mathbf{x}(k)|^2 \rangle_K. \quad (4)$$

Now we will solve the MVDR problem with particular attention given to the computational costs.

3. Traditional Solution

The traditional solution to the MVDR problem formulates the solution in terms of a data correlation or covariance matrix

$$\mathbf{R} = \langle \mathbf{x}(k) \mathbf{x}^H(k) \rangle_K = \mathbf{X} \mathbf{X}^H / K. \quad (5)$$

Using \mathbf{R} , the minimization (4) can be re-written as

$$\min_{\mathbf{w}^H \mathbf{s}=1} (\mathbf{w}^H \mathbf{R} \mathbf{w}). \quad (6)$$

The traditional solution assumes that \mathbf{R} has full rank (so \mathbf{R} has an inverse), and the traditional solution of (4) or (6) is

$$\mathbf{w}_{\text{Traditional}} = \mathbf{R}^{-1} \mathbf{s} / (\mathbf{s}^H \mathbf{R}^{-1} \mathbf{s}). \quad (7)$$

To calculate \mathbf{R} , evaluating (5) for one block would cost $O(N^2 K)$. Calculating the matrices for the total number of snapshots T would cost $O(N^2 T)$. To calculate \mathbf{R}^{-1} , the matrix inversion for one block would cost $O(N^3)$ [2], and for the total number of snapshots T , the inversions would cost $O(N^3 T/K)$. To multiply \mathbf{s} onto \mathbf{R}^{-1} for each block would cost $O(N^2)$, and for the total number of snapshots T , it would cost $O(N^2 T/K)$. These flop counts will be put in perspective later in the paper.

4. Efficient Solution

Now we solve the MVDR problem with the Multistage Wiener Filter (MWF) [3]. Figure 2 shows the same MWF that was published originally [3], except that here we introduce a new arrangement of the algebra and the architecture that will give the same numerical results with significantly greater computational efficiency.

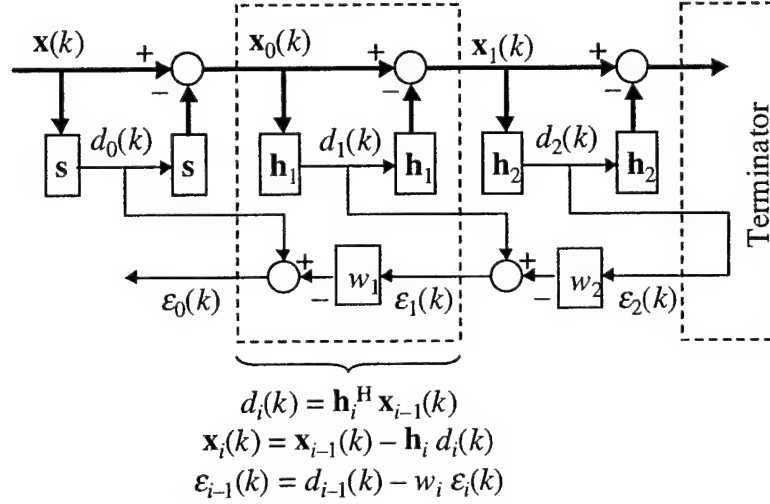


Fig. 2. The Multistage Wiener Filter re-arranged into the new efficient form introduced in this paper. The architecture is modular and scalable. The upper chain analyzes the data (flowing from left to right). The lower chain synthesizes the filter weights and the filter output (flowing from right to left).

The processing begins with some non-adaptive calculations. First, the data vectors are projected onto the steering vector to form an initial estimate of the desired signal

$$d_0(k) = \mathbf{s}^H \mathbf{x}(k). \quad (8)$$

For example, $d_0(k)$ may be the output of a conventional beamformer or a matched filter. Of course, the trouble is that $d_0(k)$ contains interference that

comes into the sidelobes of \mathbf{s} . To prepare for a statistical analysis that will identify and subtract this interference, we isolate the rest of the data by writing

$$\mathbf{x}_0(k) = \mathbf{B} \mathbf{x}(k), \quad (9)$$

where \mathbf{B} is a “blocking matrix” that projects the data onto the nullspace of \mathbf{s} .

The projection operation in (9) is uniquely defined. However, the projection can be accounted for two ways. In the original concept [3], the blocking matrix was rectangular to account for the result being an $N - 1$ dimensional vector (literally). The other possibility is to use the square blocking matrix

$$\mathbf{B} = \mathbf{I} - \mathbf{s}\mathbf{s}^H. \quad (10)$$

The square matrix accounts for the same projection, but the projection is viewed as a subtraction in the fixed perspective of the original N -dimensional space.

The choice between these two blocking matrices is the key to the numerical efficiency realized in paper. By choosing the square blocking matrix in (10), we can re-write (9) as

$$\mathbf{x}_0(k) = [\mathbf{I} - \mathbf{s}\mathbf{s}^H] \mathbf{x}(k) = \mathbf{x}(k) - \mathbf{s}d_0(k). \quad (11)$$

By accounting for the projection with the subtraction shown in (11), the computational cost for a block is $O(NK)$. This gives us a significant savings over the matrix multiplication shown in (9), which would cost $O(N^2K)$.

Given $d_0(k)$ and $\mathbf{x}_0(k)$ as inputs, the processing continues with a recursion of adaptive stages. The index i identifies the adaptive stage number (where $i = 1$ is the first adaptive stage, and so on). To support stage i , we calculate the snapshot-averaged correlation between the two inputs to that stage

$$\mathbf{r}_{i-1} = \langle \mathbf{x}_{i-1}(k) d_{i-1}^*(k) \rangle_K. \quad (12)$$

Stage i will use this correlation in terms of its magnitude and its direction

$$\delta_i = \|\mathbf{r}_{i-1}\| = (\mathbf{r}_{i-1}^H \mathbf{r}_{i-1})^{1/2}, \quad (13)$$

$$\mathbf{h}_i = \mathbf{r}_{i-1} / \|\mathbf{r}_{i-1}\|. \quad (14)$$

To find the projections of the data along this direction and orthogonal to this direction, we recall the numerical efficiency achieved in (11), and we choose to account for the projection as a subtraction

$$d_i(k) = \mathbf{h}_i^H \mathbf{x}_{i-1}(k), \quad (15)$$

$$\mathbf{x}_i(k) = [\mathbf{I} - \mathbf{h}_i \mathbf{h}_i^H] \mathbf{x}_{i-1}(k) = \mathbf{x}_{i-1}(k) - \mathbf{h}_i d_i(k). \quad (16)$$

This recursive analysis may be terminated in different ways. If the block of data \mathbf{X} has full rank, then the projections may continue until all the data is projected onto a set of orthogonal unit vectors $[\mathbf{s}, \mathbf{h}_1, \mathbf{h}_2, \dots, \mathbf{h}_{N-1}]$. This analysis would use $N - 1$ stages (because \mathbf{s} accounted for one direction already). Or, if the block of data \mathbf{X} is not full rank (for example, if we intentionally choose $K < N$), then the rank of the data will gracefully “underflow” in the analysis. In that case, $\mathbf{x}_i(k)$ would contain only zeros for the highest stages. Or, the filtering may be intentionally truncated to some smaller number of stages we will call S (where $1 \leq S \leq N - 1$). Truncation is shown graphically in Figure 2 with the “terminator” that sets $\varepsilon_S(k) = d_S(k)$.

After the analysis is finished, the initialization $\varepsilon_S(k) = d_S(k)$ begins the synthesis along the lower chain of Figure 2 from right to left. The synthesis is recursive. For each adaptive stage i (from $i = S$ to $i = 1$), we calculate

$$\xi_i = \left\langle |\varepsilon_i(k)|^2 \right\rangle_K, \quad (17)$$

$$w_i = \delta_i / \xi_i, \quad (18)$$

$$\varepsilon_{i-1}(k) = d_{i-1}(k) - w_i \varepsilon_i(k). \quad (19)$$

The ultimate result is the scalar output $\varepsilon_0(k)$.

Finally, we offer an observation to help compare this filter to other filters that use weight vectors explicitly. The synthesis of $\varepsilon_0(k)$ can be written as

$$\begin{aligned} \varepsilon_0(k) &= d_0(k) - w_1[d_1(k) - w_2[d_2(k) - w_3[d_3(k) - \cdots]]] \\ &= d_0(k) - w_1 d_1(k) + w_1 w_2 d_2(k) - w_1 w_2 w_3 d_3(k) + \cdots. \end{aligned} \quad (20)$$

Further, when the orthogonal vectors $[\mathbf{s}, \mathbf{h}_1, \mathbf{h}_2, \mathbf{h}_3, \dots]$ all have N entries (as they do in this paper), the dependence on $\mathbf{x}(k)$ can be written directly as

$$\varepsilon_0(k) = [\mathbf{s}^H - w_1 \mathbf{h}_1^H + w_1 w_2 \mathbf{h}_2^H - w_1 w_2 w_3 \mathbf{h}_3^H + \cdots] \mathbf{x}(k). \quad (21)$$

This identifies an equivalent weight vector for the Multistage Wiener Filter

$$\mathbf{w}_{\text{WMF}} \equiv \mathbf{s} - w_1 \mathbf{h}_1 + w_1 w_2 \mathbf{h}_2 - w_1 w_2 w_3 \mathbf{h}_3 + \cdots. \quad (22)$$

We may not implement this weight vector numerically because we have direct access to the filter output $\varepsilon_0(k)$ shown in Figure 2.

5. Numerical Example

To show a numerical example, Figure 3 shows a simple simulation of an underwater acoustics problem. A horizontal line array with $N = 100$ elements is resolving three spatially discrete sources of sound in a background of noise. The discrete sources and the noise are all computed as pseudorandom complex Gaussian variables to represent the contents of a single FFT frequency bin. The data snapshots are spaced once every second. The units in the figure are dB re $1 \mu\text{Pa}^2/\text{Hz}$ to represent the units of a frequency bin in a passive sonar problem (where a frequency spectrum integrates to give a variance in μPa^2). At the element level, the ambient acoustic noise level is 65 dB (re $1 \mu\text{Pa}^2/\text{Hz}$), and the ambient noise is isotropic to simplify this demonstration. The frequency bin being processed is centered on a frequency that is one third of the maximum frequency that the array can process without aliasing in space, and this gives the isotropic ambient noise some correlation between elements [4]. Uncorrelated element noise is also modeled with an effective level of 25 dB (re $1 \mu\text{Pa}^2/\text{Hz}$). The three spatially discrete sources are modeled here as locally plane waves with arrival angles of 0° , 30° , and 60° from endfire respectively. Their RMS amplitudes at the element level are 85, 65, and 75 dB respectively (re $1 \mu\text{Pa}^2/\text{Hz}$). The beamforming is calculated for a range of steering angles $0 \leq \phi \leq 180^\circ$ by increments of $\Delta\phi = 0.25^\circ$. (This very fine resolution is used here so the narrow peaks will register their peak levels properly in the TIFF graphic output.) The results are shown for a single block of $K = 200$ snapshots (covering 200 seconds).

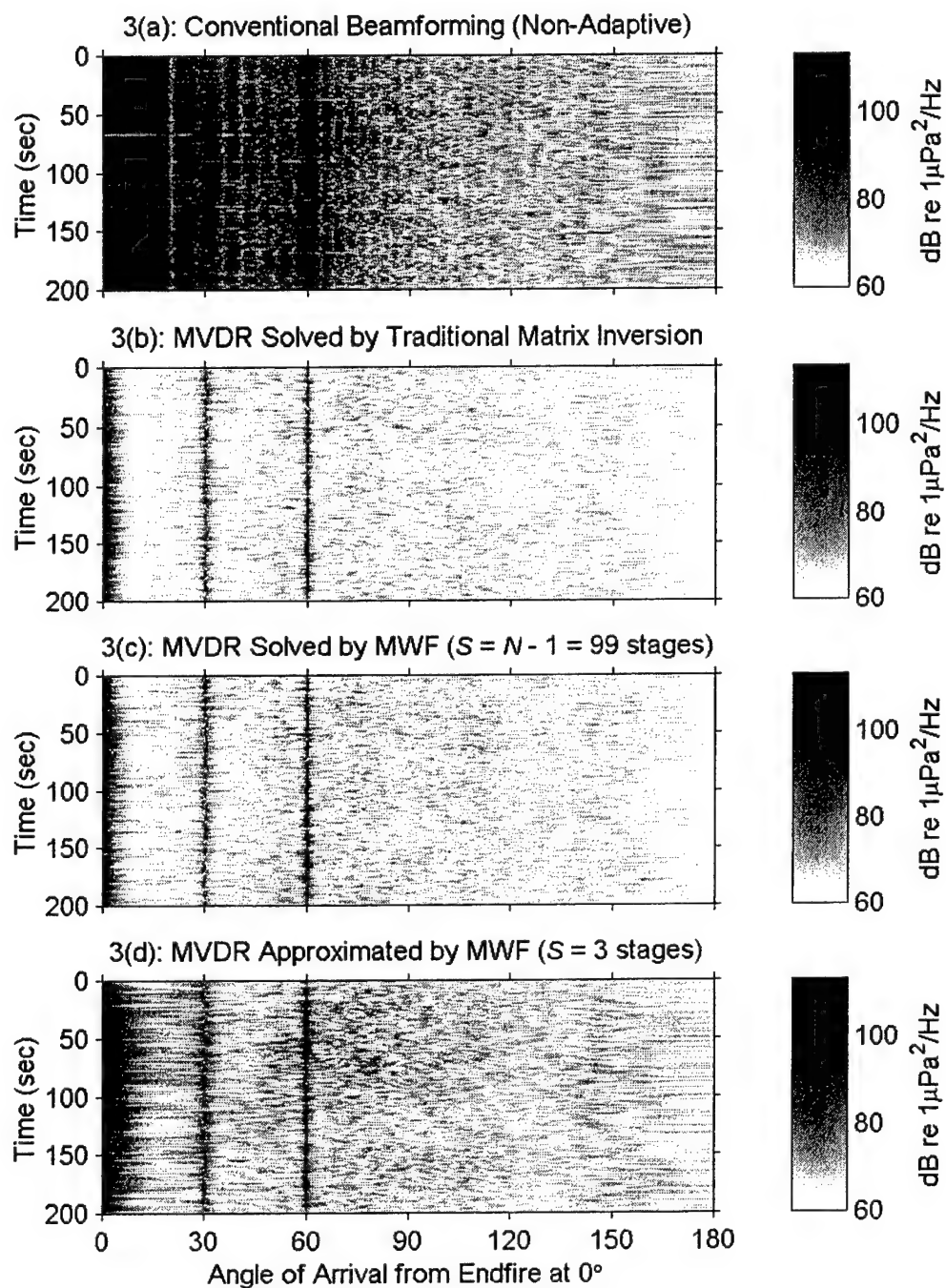


Fig. 3. Example: single-frequency adaptive beamforming.

Figure 3(a) shows the result of conventional beamforming (CBF) as a reference for the amplitudes and the angular resolution. For CBF, the fixed weight vector here is simply the steering vector without tapering ($\mathbf{w}_{\text{CBF}} = \mathbf{s}$). To calculate the real output shown, the complex snapshots $\mathbf{x}(k)$ are multiplied onto the weight vector to give a power-like quantity with units of $\mu\text{Pa}^2/\text{Hz}$

$$P_{\text{CBF}}(\phi, k) = |\mathbf{w}_{\text{CBF}}^H(\phi) \mathbf{x}(k)|^2. \quad (23)$$

The cost for $K = 200$ snapshots is $O(NK)$ for each steering angle. We plot $10 \log_{10}[P_{\text{CBF}} / (1 \mu\text{Pa}^2/\text{Hz})]$ to show units of dB re $1 \mu\text{Pa}^2/\text{Hz}$.

Figure 3(b) shows the traditional adaptive solution computed by the matrix inversion in (7). The matrix \mathbf{R} is computed for the entire block of $K = 200$ snapshots at a cost of $O(N^2K)$, and the inversion is computed at a cost of $O(N^3)$ [2]. For each steering angle, an adaptive weight vector $\mathbf{w}_{\text{Traditional}}$ is computed for the entire block by (7), then the snapshots are multiplied onto the weight vector to calculate a power-like quantity

$$P_{\text{Traditional}}(\phi, k) = |\mathbf{w}_{\text{Traditional}}^H(\phi) \mathbf{x}(k)|^2. \quad (24)$$

Figure 3(c) shows the MWF solution computed with full rank ($S = N - 1$ stages), where the computational cost is $O(N^2K)$ for each steering angle. As the plot shows, the full-rank MWF recovers the traditional solution. We could calculate the power-like output with the weight vector in (22), but instead we calculate it most efficiently from the scalar output $\varepsilon_0(k)$ as

$$P_{\text{MWF}}(\phi, k) = |\varepsilon_0(k)|^2. \quad (25)$$

Figure 3(d) shows the MWF solution computed with reduced rank ($S = 3$ stages), where the computational cost is $O(NKS)$ for each steering angle. This is a remarkable result. The super-resolution of adaptive beamforming is achieved with a computational cost comparable to conventional beamforming.

6. Other Benefits

The architecture shown in Figure 2 has other benefits.

One benefit is that the computational costs of the MWF are insensitive to the choice of K dividing the total number of snapshots T into smaller blocks. In contrast, with the traditional matrix inversion, choosing smaller K would cause the cost to rise because there would be more matrices to invert.

Another benefit is a robust degradation of performance when the data has bad channels or data samples. While still using a given hardware implementation of Figure 2, we can simply pad the bad channels or samples with zeros and reprogram the steering vector \mathbf{s} to have zeros there and have unit norm ($\mathbf{s}^H \mathbf{s} = 1$). The zeros will flow through the hardware without being involved. If this makes the block of data \mathbf{X} rank deficient, the filter will handle the “underflow” of rank gracefully if we simply make sure that the denominators in $w_i = \delta_i / \xi_i$ have small non-zero numerical values to avoid division by zero. This minor fix adds no significant computational expense.

This graceful “underflow” of rank also facilitates the processing of rank-deficient blocks caused by intentionally choosing the number of snapshots K to be less than the number of sensors N . In such cases ($K < N$), the minimization in (4) or (6) is indeterminate (having more unknowns in \mathbf{w} than equations to determine them). This allows \mathbf{w} to have extra degrees of freedom that do not affect the cost function in (4) or (6). In such cases, the MWF finds the *minimum norm* weight vector $\min(\|\mathbf{w}\|)$ that solves the MVDR or “least squares” problem stated in (4) and (6).

7. Conclusions

Remarkably high computational efficiency was achieved by rearranging the Multistage Wiener Filter into the form shown in Figure 2. For example, in the adaptive beamforming problem shown in Figure 3, the super-resolution of adaptive beamforming was achieved at a computational cost only slightly higher than conventional beamforming. The architecture is modular and scalable, which makes it amenable to implementation in dedicated hardware.

We find some lessons learned. One lesson is that reduced rank processing can lead to computational efficiency when the reduced rank processing is the Multistage Wiener Filter. Another lesson is that a subspace projection may be

formulated as a *multiplication* onto a projection matrix, but the efficient numerical realization of a projection should be *implemented* as a *subtraction* in the fixed perspective of the original N -dimensional space. Maintaining the fixed perspective minimizes the computational requirements.

Incidentally, the processing in this paper made no assumptions of stationarity or Gaussianity for the interference being suppressed. The only such assumptions were made for convenience in the generation of the simulated data and the choice of a fixed steering vector \mathbf{s} . All of the equations written in this paper describe the minimization of the quadratic cost function for the blocks of data shown in Figure 1. No assumptions were made about the world outside the data block \mathbf{X} .

Acknowledgments

Thanks go to Dr. John Tague at the Office of Naval Research for technical discussions about reduced rank processing and its applications. Thanks go to Dr. Joe Guerci at Defense Advanced Research Projects Agency for noting that the square blocking matrix works in the MWF. Respect and appreciation go to Prof. Irving Reed at the University of Southern California for his long-standing interest in the significant issue of computational efficiency, and for his original derivation of the expansion shown above in (20).

References

- [1] S. Haykin, *Adaptive Filter Theory*, 3rd edition, Prentice Hall, 1996.
- [2] G. H. Golub and C. F. Van Loan, *Matrix Computations*, 3rd edition, Johns Hopkins University Press, 1996.
- [3] J. S. Goldstein, I. S. Reed, and L. L. Scharf, "A multistage representation of the Wiener filter based on orthogonal projections," *IEEE Transactions on Information Theory*, vol. 44, no. 7, pp. 2943-2959, November 1998.
- [4] R. J. Urick, *Principles of Underwater Sound*, 3rd edition, p. 231, Peninsula Publishing, 1983.

DESIGN CONSIDERATIONS FOR THE REFLECTOR ANTENNA SYSTEM OF THE HIGH ALTITUDE MMIC SOUNDING RADIOMETER (HAMSR)

Vahraz Jamnejad, Abraham L Riley, Ray T Swindlehurst
Jet Propulsion Laboratory
California Institute of Technology
Pasadena, CA 91109
818-354-2674
vahraz.jamnejad@jpl.nasa.gov

***Abstract*—This paper describes some design aspects of the reflector antenna system for the High altitude MMIC sounding radiometer (HAMSR) on a remotely piloted aircraft. The goal of HAMSR project is to design, build, and demonstrate in the field, a miniaturized microwave atmospheric sounder implemented with Monolithic Microwave Integrated Circuit (MMIC) receiver modules and other solid state components. This passive microwave radiometer operating at millimeter wavelengths will make temperature soundings at oxygen emission lines at 53 and 118 GHz, and humidity sounding at water vapor emission line at 183 GHz. In this paper we will outline the design process and the analytic results for the three feed/reflector systems at the above three frequencies.**

1. INTRODUCTION

High altitude MMIC sounding radiometer (HAMSR) on a remotely piloted aircraft makes a radical departure in design from previous microwave sounders resulting in reductions in mass and power by an order of magnitude and reduction in cost by a significant factor from the current state of the art.

The goal of HAMSR project is to design, build, and demonstrate in the field a miniaturized microwave atmospheric sounder implemented with Monolithic Microwave Integrated Circuit (MMIC) receiver modules and other solid state components. This passive microwave radiometer operating at millimeter wavelengths will make temperature soundings at oxygen emission lines at 53 and 118 GHz, and humidity sounding at water vapor emission line at 183 GHz.

Previous humidity and temperature soundings have mainly been done at 22.2 and 54 GHz, which require relatively large and heavy hardware. The instrument is required to have a temperature sounding accuracy of 2 degrees Kelvin and a humidity sounding accuracy of 20%. It will have a vertical resolution of 2 km in the troposphere and a horizontal resolution of 2 km. HAMSR instrument is intended primarily as a tropospheric sounder but is configurable to make other types of measurements.

This project will demonstrate the maturity of the MMIC technology and the mass, cost, power, and cost benefits of a miniaturized MMIC-based sounding system. It will verify the scientific validity and effectiveness of temperature soundings at 118 vs. 54 GHz soundings. In addition, it will demonstrate the operational capabilities of a UAV-based sounder.

The HAMSR instrument is designed to be flown aboard solar powered UAVs being developed under the NASA Environmental Research Aircraft and Sensor Technology (ERAST) program.

One of the main features of HAMSR is an optics module composed of reflector antennas, calibrators, scanners, and diplexers, which can be easily modified to satisfy specific spatial sampling and coverage requirements.

In this paper we will outline the design process and the analysis results for the feed/reflector systems as well as the diplexer or dichroic plate. Fabrication and test results for the various components of the system will be presented in a future paper.

2. OPTICAL PRESCRIPTION

As shown in Figure 1, three offset-fed parabolic reflector systems are designed for operation at 54, 118, and 183 GHz. They are arranged in the following way. The 55 GHz reflector takes direct input radiation from Earth, while the input radiation is directed to the 118 and 183 GHz reflectors via a flat plate reflector and a frequency selective surface (FSS) or dichroic plate. The RF specifications for the antenna systems are summarized as follows.

Frequencies

The HAMSR optics system will operate in three bands centered at 55 (49.4-56.9), 118 (112.5-125.0) and 183 (162.0-194.8) GHz.

Beamwidth

The HPFW beamwidth will be 5.7 degrees \pm 10% at all frequencies.

Polarization

Polarization shall be linear and in the scan plan of the antenna system. At nadir pointing the polarization of all three beams shall be in the same direction.

Cross-Polarization

The ratio of the integrated cross-polarized power within the 14.3 degrees (2.5 x HPFW beamwidth) to the co-polarized power shall be less than 17 dB for all three beams at the nadir pointing position.

Beam Efficiency

The integrated main beam energy, within 14.3 degree from beam center, shall be greater than 95% of the total integrated energy.

The reflector beam patterns must have very low sidelobes (less than 30 dB) to obtain the required high beam efficiency, which mandates highly tapered reflector aperture illumination and stringent surface accuracy and alignment requirements. Corrugated circular feedhorns are used to receive the radiation.

As shown in Figure 1, the 55 GHz reflector and the flat plate mirror rotate around a single axis of revolution in order to provide the nadir coverage in $\pm 55^\circ$ range. In each revolution the reflectors will be exposed to hot and cold targets for the purpose of calibration. A three dimensional overall view of the optical bench and a more close-up view of the reflectors and the hot and cold targets, as generated by the Mechanical Desktop, are shown in Figures 2 and 3.

3. DESIGN PROCEDURE

Full wave mode-matching technique is used to analyze and design the feed horns, while the reflector analysis and design is based on the physical optics theory.

The analysis of the oblique incidence on the dichroic plate is based on method of moments with floquet harmonics expansion in the free space and waveguide modal expansion in the aperture and interface matching.

The analysis of the oblique incidence on the dichroic plate is based on method of moments in conjunction with Floquet harmonics theory. Computer programs used in the analysis are based on the codes developed at JPL for the analysis of the reflector systems, corrugated horns, waveguide junctions, and frequency selective surfaces [1-3]. Also utilized were the modified forms of codes in [4-6]. Additional programs for geometrical layout of the feed horns and reflectors and plotting of the various field quantities were developed in MATLAB language.

4. THEORETICAL ANALYSIS

Feed horns

All three reflectors use circular corrugated horns and include a matching/transition section from circular to rectangular waveguide. Corrugated feed horns were used to equalized the E and H plane field patterns. Approximate length and dimensions of the feed horns including the distance from aperture to the receiver flange, which comprises the horn length and the circular /rectangular transition region, are given in the following table. For brevity, the geometry of the corrugations are not presented in this paper, but will be presented in a future paper.

Patterns of the circular corrugated horns are produced based on the modal expansion in the horn and are presented in the next section.

Table 1. Geometrical parameters of the feed horns

Freq.	Rectangular guide	Circular guide Diameter	Horn aperture	Total length
55 GHz	WR 19 (40-60 GHz) In: 0.188" x 0.094" Out:0.268" x 0.174"	0.22" 5.6 mm	17.3 mm	35.7 mm
118 GHz	WR 8 (90-140 GHz) In: 0.08" x 0.04" Out:0.156" diameter	0.1" 2.6 mm	7.6 mm	15.6 mm
183 GHz	WR 4 (170-260 GHz) In: 0.043" x 0.215" Out:0.156" diameter	0.06" 1.5 mm	5.3 mm	11.4 mm

Reflectors

The reflector patterns are obtained using the calculated near field patterns of the feed horns. Due to the high offset in the 55 and 183 GHz reflector systems, the cross pol is relatively high but still acceptable (< 17 dB). A trade-off was conducted to obtain the best illumination taper and corresponding reflector far field patterns.

An optimized set of parameters and corresponding figures are presented for the 16 dB reflector edge taper which is equalized at the two edges. The feed aperture has been moved toward the reflector from the focal point in order to make the patterns as circularly symmetric as possible. Figures 4(a,b,c), 5(a,b,c), and 6(a,b,c) present the geometry, feed pattern and reflector far field patterns at the 55, 118, and 183 GHz frequencies, respectively.

Dichroic plate

The FSS or dichroic plate is a high pass filter designed to transmit the 183 GHz signal while reflecting the 118 GHz signal, both incident at 22.5 degrees from normal. The geometry of a segment of the plate is shown in Figure 7. The computed reflection and transmission response of the plate is given in Figure 8. This is a design very sensitive to dimensional tolerances, which must be maintained within a fraction of a mil.

5. CONCLUSIONS AND FUTURE PLANS

In this paper we have presented some of the design parameters and theoretical analysis results for the optics of the HAMSR radiometer. All the components of the optics have been fabricated based on the above results and are presently under test.

ACKNOWLEDGMENT

The work described in this paper was conducted by the Jet Propulsion Laboratory, California Institute of Technology, under contract with National Aeronautics and Space Administration.

REFERENCES

- [1] R. E. Hodges, W. A. Imbriale, "Computer Program POMESH for Diffraction Analysis of Reflector Antenna," Internal Report, Jet Propulsion Laboratory, February 1992.
- [2] D. Hoppe, "Scattering Matrix Program for Circular Waveguide Junctions," Internal Report, Jet Propulsion Laboratory, October 1984.
- [3] J. C. Chen, "Analysis of a Thick Dichroic Plate with Rectangular Holes at Arbitrary Angles of Incidence," TDA Progress Report 42-104, Jet Propulsion Laboratory, Pasadena, California, pp. 110-134, February 15, 1991.
- [4] C. C. Chen, "Transmission of Microwave Through Perforated Flat Plates of Finite Thickness," IEEE Trans. Microwave Theory Tech., vol. MTT-21, pp. 1-6, January 1973.
- [5] P.J.B. Clarricoats and A.D. Olver, "Corrugated horns for microwave antennas," London, UK: P. Peregrinus on behalf of the Institution of Electrical Engineers, 1984.
- [6] Leo Diaz, Thomas Milligan, *Antenna Engineering Using Physical Optics*, Boston: Artech House, 1996.

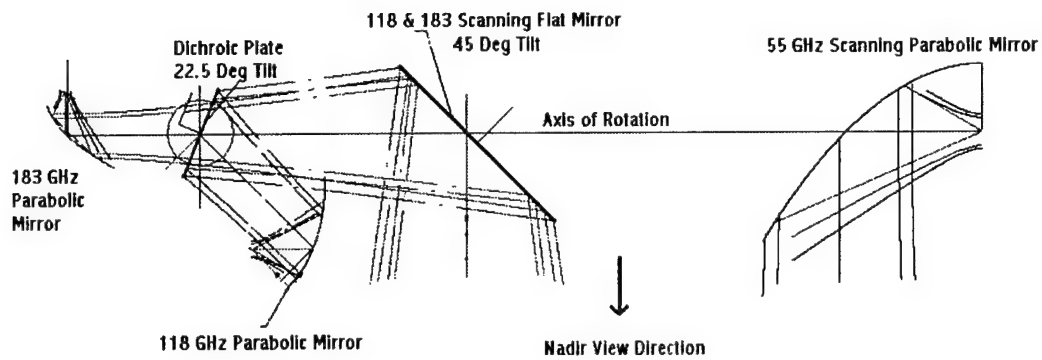


Figure 1. Schematic configuration of the three reflector antenna systems

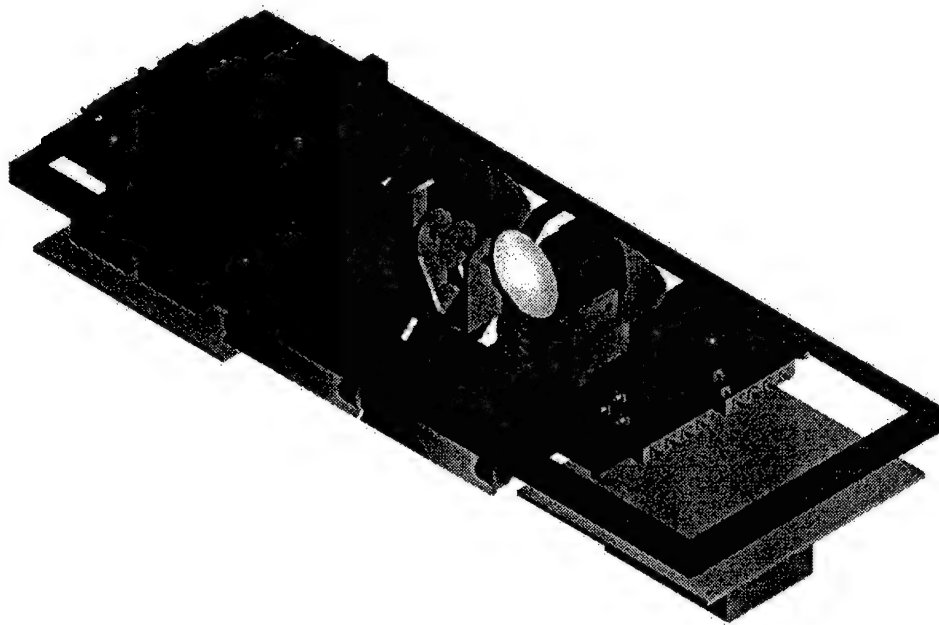


Figure 2. A Mechanical Desktop view of the overall system optics

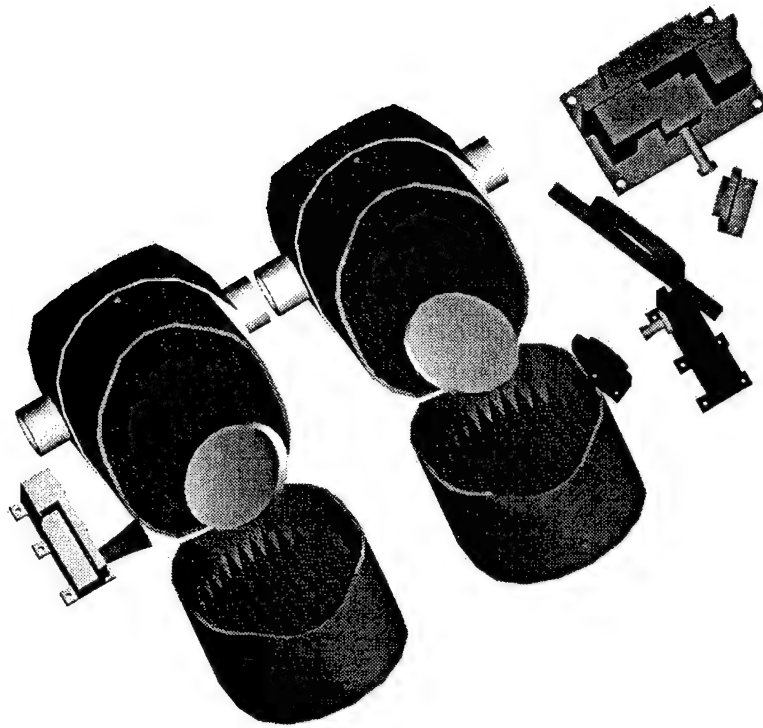


Figure 3. A Mechanical Desktop layout of the reflector antenna components.

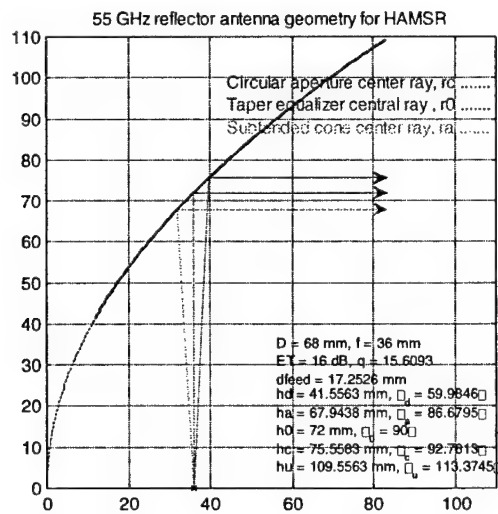


Figure 4(a). Reflector geometry for 55 GHz operation

Corrugated feed patterns, Freq. (GHz): 55, Diam. (mm): 17.3, Half-flare angle (deg): 12, y-pol

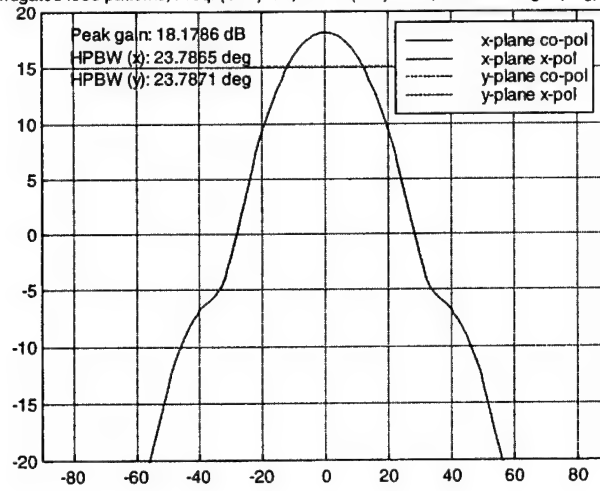


Figure 4(b). 55 GHz Feed pattern

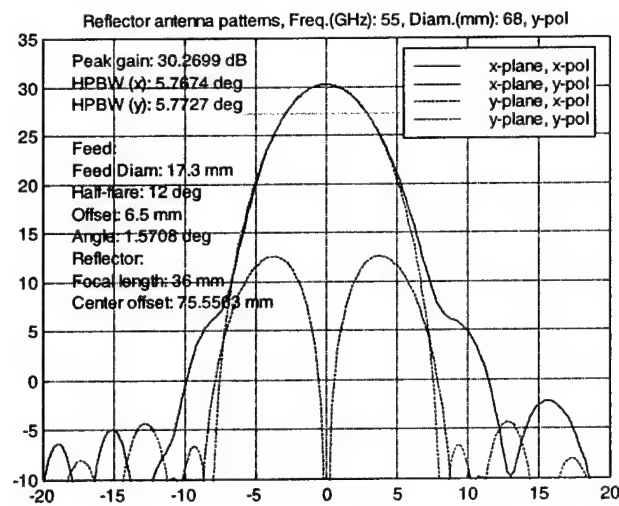


Figure 4(c). 55 GHz Reflector pattern

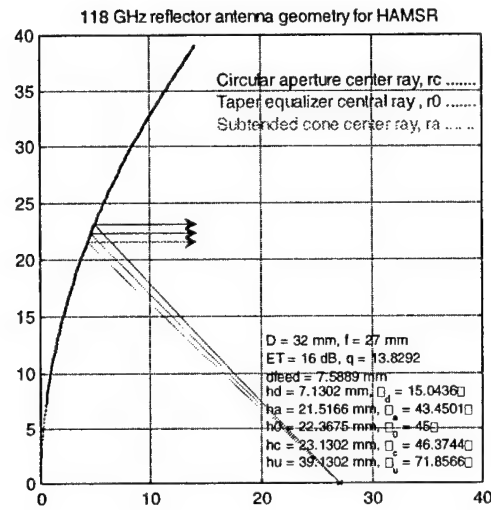


Figure 5(a). Reflector Geometry for 118 GHz operation

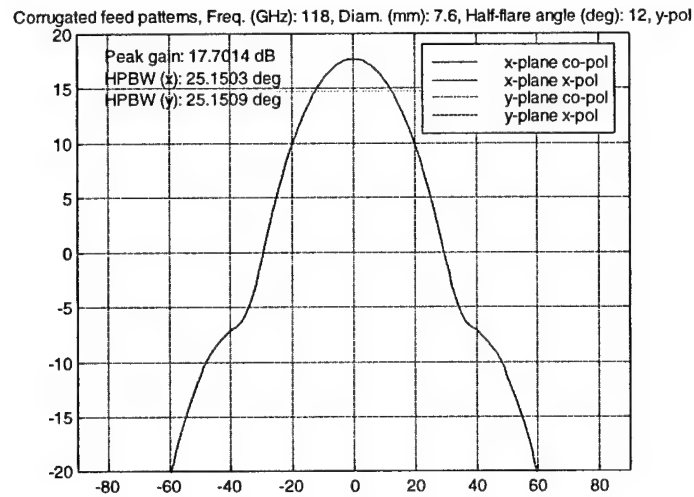


Figure 5(b). 118 GHz Feed pattern

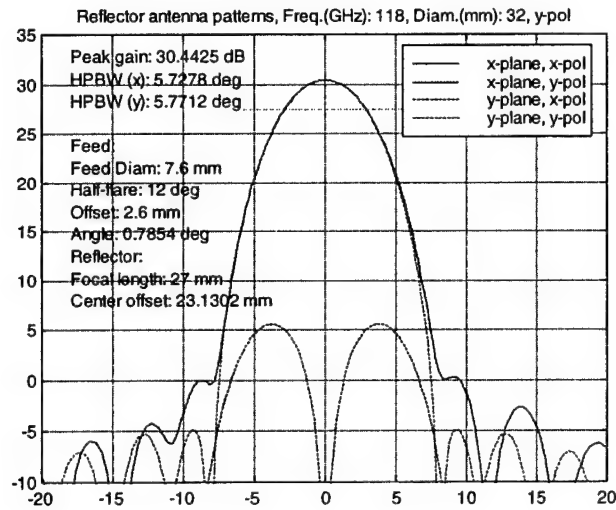


Figure 5(c). 118 GHz Reflector pattern

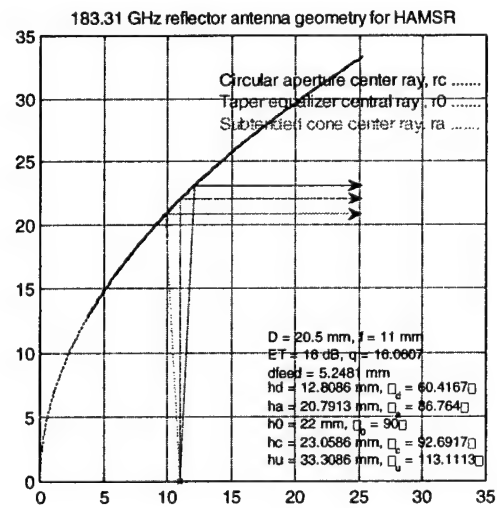


Figure 6(a). Reflector geometry for 183 GHz operation

Corrugated feed patterns, Freq. (GHz): 183.31, Diam. (mm): 5.3, Half-flare angle (deg): 12, y-pol

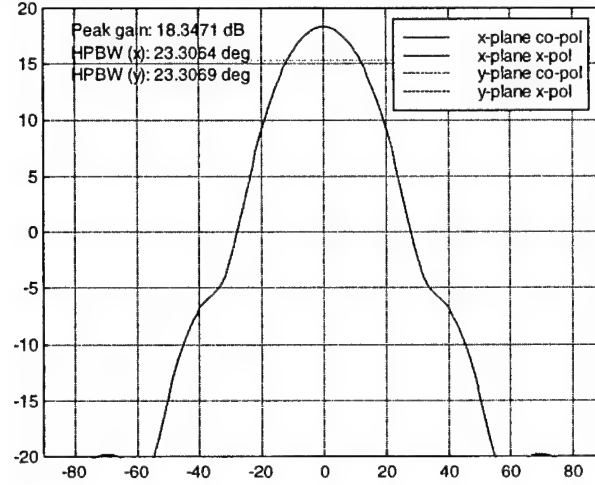


Figure 6(b). 183 GHz Feed pattern

Reflector antenna patterns, Freq.(GHz): 183.31, Diam.(mm): 20.5, y-pol

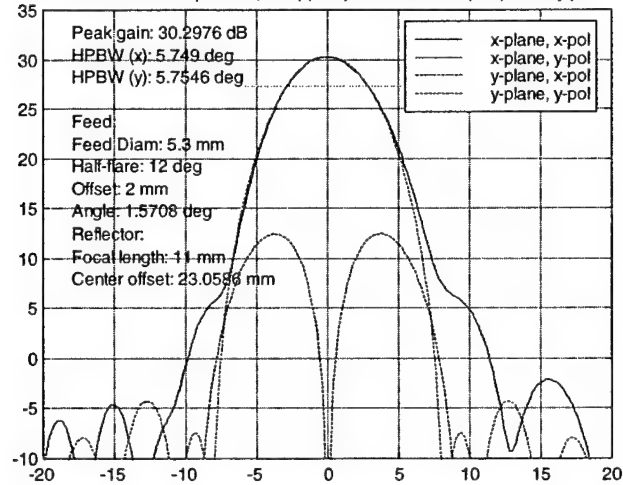


Figure 6(c). 183 GHz Reflector pattern

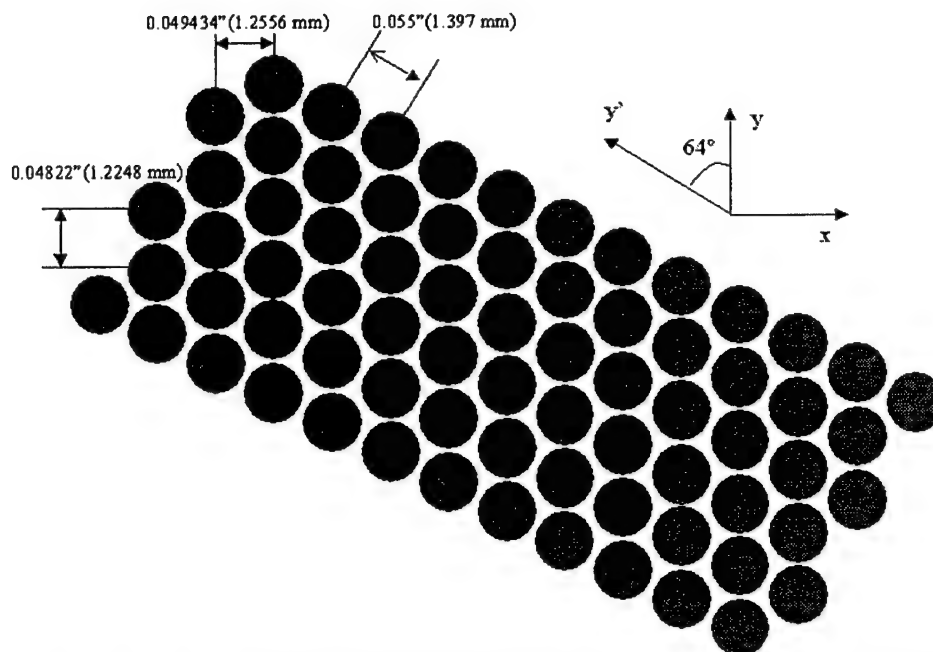


Figure 7. Geometrical configuration of a sample segment of the dichroic

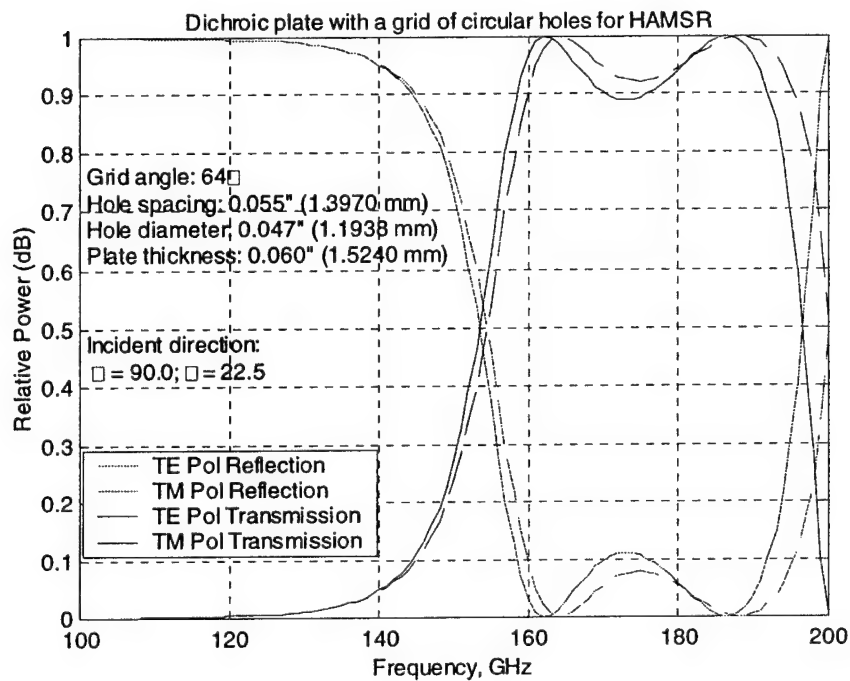


Figure 8. Computed transmission & reflection characteristics of dichroic plate.

Transmitter/Receiver Pulse-Driven Antenna Array with Near-Field Beam-Forming for UWB Subsurface Imaging Radar

A. Boryssenko¹, E. Boryssenko², V. Ivashchuk², V. Prokhorenko²

¹ Antenna Laboratory,
University of Massachusetts,
Amherst, MA, 01003, USA

² Research Company "Diascarb",
P.O. Box No. 148
Kiev, 02222, Ukraine

Abstract: The paper is devoted to design of impulse or equivalent ultra-wide band array antenna for subsurface radar system. Receiving elements of this antenna are arranged in array with small physical aperture and polarimetric features. Two transmitting element support two polarization states for radiating signals. The radar antenna provides down-looking scanning in subsurface medium for small areas covered by array aperture and big areas due to synthetic aperture processing when array moves in 2-D plane along scanning lines. Operation in proximity to a rough dielectric interface affects significantly on radar operation. This and other factors are involved in array antenna design to get enough 3-D spatial scanning with the maximum resolution and range for the available bandwidth. Results of such array analysis, numerical simulation and experiments are presented and discussed.

1. Introduction

Subsurface radar or ground-penetrating radar (GPR) technique is widely applied as a powerful technology of remote sensing and microwave imaging in many fields of science and engineering [6,7]. Among different schemes of building of GPR systems there are two dominant ones. The first schema is impulse or equivalent ultra-wide band (UWB) radar that operates in time-domain (TD). The second one involves stepped frequency or synthetic-pulse GPR and operates in frequency-domain (FD). The both radar have some mutually excepting benefits and drawbacks as well as different design approaches to radar antennas [6]. Relative simplicity and inexpensive way of TD-GPR implementation are practically preferable for some applications. Due to this reason the UWB array antenna for TD schema of GPR is a subject of the presented study.

Principal engineering aspects of subsurface radar design involve mostly signal processing and antennas besides other topics [6]. Signal processing

opportunities evolves with progress in computational software/hardware and digital signal processing. At the same time antennas designers are still situated in the rigid frame of physical limitations. The last are caused due to inherent and inaccessible features of impulse antennas loaded by the subsurface interface. Such features include ringing, impedance mismatching and so on. They cause degradation of radar performances and GPR antennas are more critical system component than in air-operated radar [3]. Another sufficient peculiarities of GPR antenna design are originated from necessity to employ UWB signals for good range resolution and operation in the near-field range of radar antenna [7].

There are generally two viable approaches for subsurface radar design. The first way, a designer has to reduce antenna internal reflections and other unwanted phenomena as much as possible, thereby simplifying signal-processing problem for radar. The second way that realized here is to live with a certain amount of antenna internal reflections and take those out in signal processing [6]. Therefore some optimal combination of efforts in antenna design and signal processing technique should be done for each specific system. In our early attempts [3] we explored behavior of single impulse transmitting (Tx) and receiving (Rx) antennas in free space and near the air-ground interface. The impulse array antenna with Rx polarimetric features and two cross-polar Tx channels is a final goal of array design project described in this work.

The presented array antenna is a principal component of UWB subsurface down-looking radar for non-destructive testing of concrete structural elements. Such GPR should be installed on a robotic platform with remote control for operation on the radioactive polluted territories near the Chernobyl destroyed nuclear reactor, Ukraine, in the frame of the big project that is in progress now. This radar should be employed for detection in thick concrete environment the metallic inclusions and non-uniform internal regions. Other missions involve offset 3-D image formation in bistatic 2-D geometry with small base as well as using synthetic aperture radar (SAR) technique for big survey areas.

The reminder of this paper is organized in the following order. Section 2 gives a glance on key aspects of antenna design for GPR. Some numerical results with approximated TD simulation technique are reviewed in Section 3. Design of UWB antennas with Rx array including single antenna elements, monostatic antenna pair, 2-element Rx array antenna and end-point array antenna project are discussed in Section 4. In Section 5 basic algorithms for array data processing with TD near-range beam-forming for physical aperture, synthetic aperture and polarimetric techniques are considered. Some experimental results are shown in Section 6. Final conclusions and reference list are at the end of this paper.

2. Basic Principles of Impulse Antenna Design

Let consider principal aspects of antenna design affected on radar performances. Firstly, antenna position with respect to sounding medium must be specified. There are three possible geometrical arrangements such as stand-on, stand-over and stand-off, Figure 1. Stand-on antenna operation for GPR system is chosen and considered here because in this case down-looking GPR provides maximum available coverage of sounding media. This feature is evident from the angular spectrum compression shown schematically in Figure 1. This effect takes place when low dielectric half-space is sounding from higher air-filled medium due to evident background physics of the Snell's Law [7]. In this case refraction at the surface tends to compress the angular extent of the wave number space (k -space) spectrum into a nearly plane wave.

At the same time in down-looking case the close coupling antennas to the ground produces effects that are not of concern for stand-off applications. These effects of stochastic nature include rough surface disturbance and impedance mismatch between antennas and Rx/Tx front-ends. The last can cause up to -20 dB degradation of GPR performance factor [3]. In this case among other problems GPR needs in a wide dynamic range receiver. However energy transfer through subsurface interface is most effective for stand-on operation when radar antennas are laid on the border between two media, i.e. the upper air-filled and the lower subsurface interior. Also impact of electromagnetic interference (EMI) signals on radar performances with stand-on antennas is minimum. The final argument for choice a stand-on antenna schema for GPR is based on the requirements to radar to operate in some space-limited conditions with low-height ceiling etc.

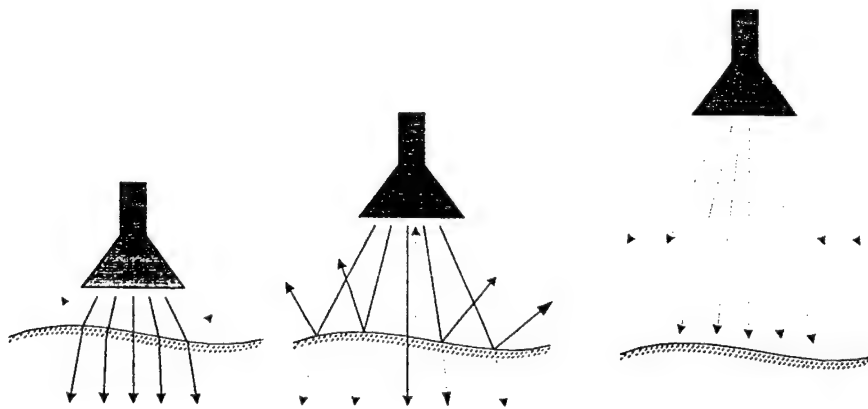


Figure 1. Basic arrangement of radar antenna position with respect to sounding media: stand-on, stand-over and stand-off or quasi-plane wave operation.

The most fundamental choice in GPR design is a center frequency and a bandwidth of the radar. Low frequencies provide deeper penetration; the higher frequencies give better range resolution. The system designer should successfully resolve this common tradeoff. There are many factors governing the choice of central frequency related to targets to be detected and electrical properties of environment where radar to be employed like attenuation in some kind of soils etc. [4]. Furthermore even for high-resolution subsurface radar a low-frequency part of spectrum is important too. If high-frequency spectrum provides target shape and its consistence in detail, the low-frequency one enables target detection [4]. Evidently here is a practical limitation of low-frequency performance of GPR antenna determined by its maximum dimension. Note that the near-range field of pulse antenna contains dominant low-frequency spectrum.

Generally range resolution of the radar is governed by the used bandwidth. We will show later that the designed array antenna covers 0.2-0.9 GHz band at -20 dB reference level, which is an optimal one for detection of deep and shallow targets in concrete. The key antenna candidates to be employed in the designed array are shown schematically in Figure 2 including dipole, bow-tie, V-shape, TEM-horn, exponential horn and tapered slot antennas. The choice among those antennas to be used in radar is based on the following main criteria:

- 1) accessible bandwidth due to definite geometry;
- 2) pattern features including directivity and cross-polar level;
- 3) efficiency of antenna coupling to sounding environment;
- 4) loading performances to be terminated to Tx/Rx front-end devices;
- 5) implementation feasibility including printed circuit technology;
- 6) effectiveness of distributive resistive loading to prevent long ringing signals;
- 7) simplicity of introducing of antenna shielding for interference immunity.

Actually large number of unknowns from environmental conditions to radar parameters exists in the GPR array antenna design. Application of simulated data gives parametric estimations useful for array design. Some numerical simulations of such kind based on computing of approximated models will be demonstrated in the next section. Due to complexity of overall design of UWB array antenna with pulse excitation we introduce here some heuristic consideration. Thus qualitative comparison of antenna types, Figure 2, with respect to formulated above criterion is presented in Table 1. It is mostly based on our own experience as well as known literature data [3,6,7]. As followed from Table 1 the bow-tie antenna is more preferable for Rx mode while TEM or exponential horn is the best choice for powerful Tx devices where low input impedance is needed. For low-power Tx antenna bow-tie configuration is also suitable. For some Rx cases TEM horn and tapered slot antenna can be interesting.

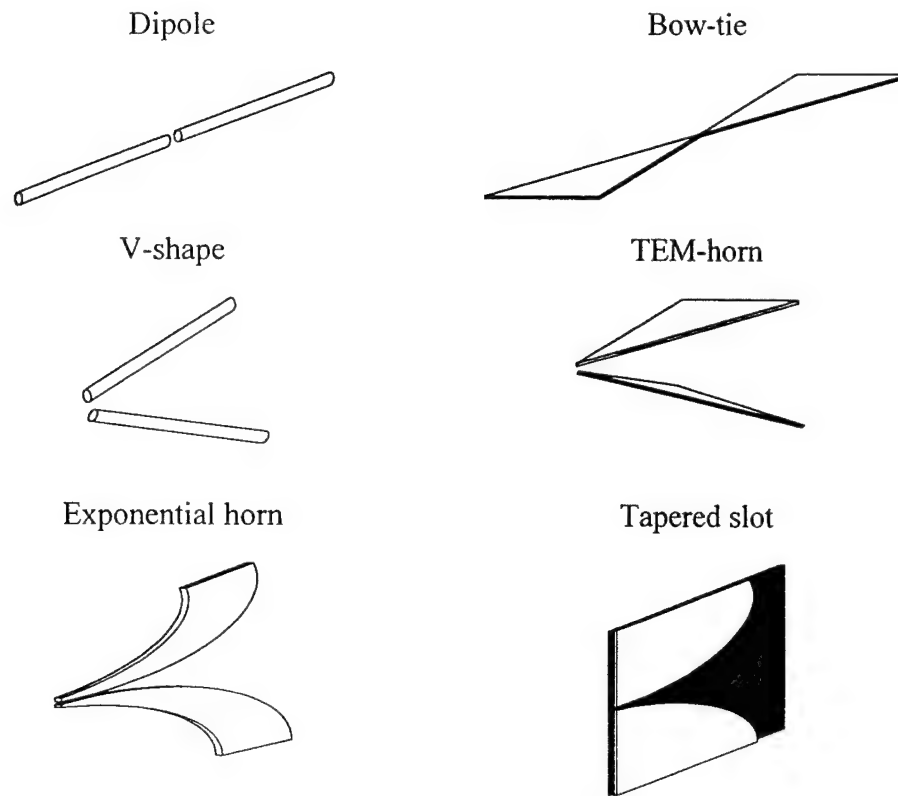


Figure 2. Basic antenna configurations to be chosen for array implementation.

Table 1. Comparison of antenna types for application in UWB GPR.

	Dipole	bow-tie	V-shape	TEM horn	Exponential horn	Tapered slot
Relative Bandwidth	Low	Middle	low	wide	wide	very wide
Pattern Directivity	low	Low	middle	high	high	high
Cross-polar Level	middle	high	middle	Middle	low	middle
Coupling Factor	low	very high	low	low	low	low
Input Impedance	high	high middle	high	low	low middle	middle high
Production Complexity	high	low	high	middle	high	low
Resistive Loading	difficult	difficult	difficult	difficult	difficult	difficult
Shielding Possibility	easy	easy	difficult	difficult	difficult	difficult

3. Antenna Analysis in Time Domain

For antenna analysis TD waveform transformations and equivalent FD spectrum presentation are considered. Both approaches are mathematically equivalent to be connecting through the Fourier transform. However due to UWB signal nature and transient antenna operation the TD mathematical modeling is more relevant and numerically effective. Also experimental TD technique gives broadband information for test environment that is more simple than using the FD measurement in an anechoic chamber for much frequency points [3]. Finally we will consider array beam forming algorithm, which has the best implementation in TD [12] rather than common FD techniques with k-spectrum presentation [5].

Note that the most of known studies present transient antennas operated in far-field range while practically sufficient operation range of subsurface radar is related to the near-field range. There are some principal effects to be carefully treated for antenna and especially for array antenna due to specific features of energy distribution in space and time [13] that are different from those presented in literature for far-field range operation. In many studies presented in literature rather than considering the signal waveform and its transformations, analysis and design are concentrated around the expected spectrum of the return signal after its propagation to the target, reflection, and propagation back to the radar antenna. However quality of imaging technique in GPR can be easily estimated by using TD waveforms, i.e. by specification how long in time its late-time history of radar response or/and how predictable is waveform transformation. Thus TD presentation is very useful and informative besides traditional FD data.

Ordinary for the transient electromagnetic problems, including antennas, numerical approaches like FD or TD method of moments or FDTD are applied. Besides Carl Baum [2] developed analytical approaches with the Laplace transform for some asymptotic cases. Generally widely used numeric studies have principal drawback followed from sufficient programming and computing efforts. Finally the physical meaning of the most numerical solutions is not enough evident and tedious verification is required. Therefore we developed simple mathematical models, which enable numerical simulations with universal mathematical software like Maple, Mathcad, Matlab etc. The result of such simulations will illustrate the major points of our study. The necessity of such consideration follows from the fact that TD technique in UWB antenna theory did not receive yet features of engineering discipline.

To give a glance on the principal choices made in array design we illustrate some fundamental waveform and spectrum transformations for signal in UWB

antennas of GPR. Skipping numerous details of mathematical modeling and numerical simulation, which require special consideration, let present the fundamental results on signal transformations in pulse driven Tx and Rx antennas like those in Figures 3 and 4 respectively. Bow-tie antennas are under treatment here. They are center-excited in double passing mode [3] when they are matched in the driven point only. Note that for Tx and Rx antennas the specific driven pulses are applied. These antennas are laid on air-dielectric ($\epsilon = 5$) interface and their properties are studied in the intermediate range where the effect of the near-field is clear visible and discussed later.

One can observe in Figures 3 and 4 typical waveforms of driven signals in pulse antennas and other waveform variations versus direction of radiation/reception. Basically the effect of the near field resulted in broader spectrum in its low-frequency part. If the distance to observation point decreases the spectrum is broader spread to lower frequencies and DC component appears. The changing in TD waveforms and frequency spectrum transformations is also clear visible when reflector is employed in both Tx and Rx antennas. Basically the reflector shifts slightly spectrum to higher frequencies. Also signal in antenna with reflector has slightly more duration and amplitude gain up to 6 dB. As followed from Figures 3 and 4 such antennas demonstrate dominant broadside radiation where amplitude of signal has maximum value and registered waveform has specific shape to be useful for its discrimination. At the same time the antenna pattern is wide spread and special signal processing techniques can improve it.

Let consider finally a classical wireless channel to present basic peculiarities of transient excitation. For far-field range system formed by pair of center-fed, pulse-driven, linear dipole elements (one terminated to transmitter and other to receiver) Zialkowski [13] introduced the equivalent network presentation where main feature is a specific number of time derivatives applied to input waveform.

So far we concentrated on the near-field range effects in antenna we present transient radio channel model with three same dipole antennas operating in transmitting, scattering and receiving modes without any limitations concerning near or far range, antenna type and its excitation. Such generalized system is shown in Figure 4 and can be simulated with mentioned above models. Its own transformation operators $A_{1,2,3}$ characterize each antenna in Figure 4. For example, Figure 5 demonstrates results of Mathcad simulation with respect to the notations in Figure 4. In this case we have three center-fed dipole antennas with double passing excitation and the effect of near-field range is observable in these data.

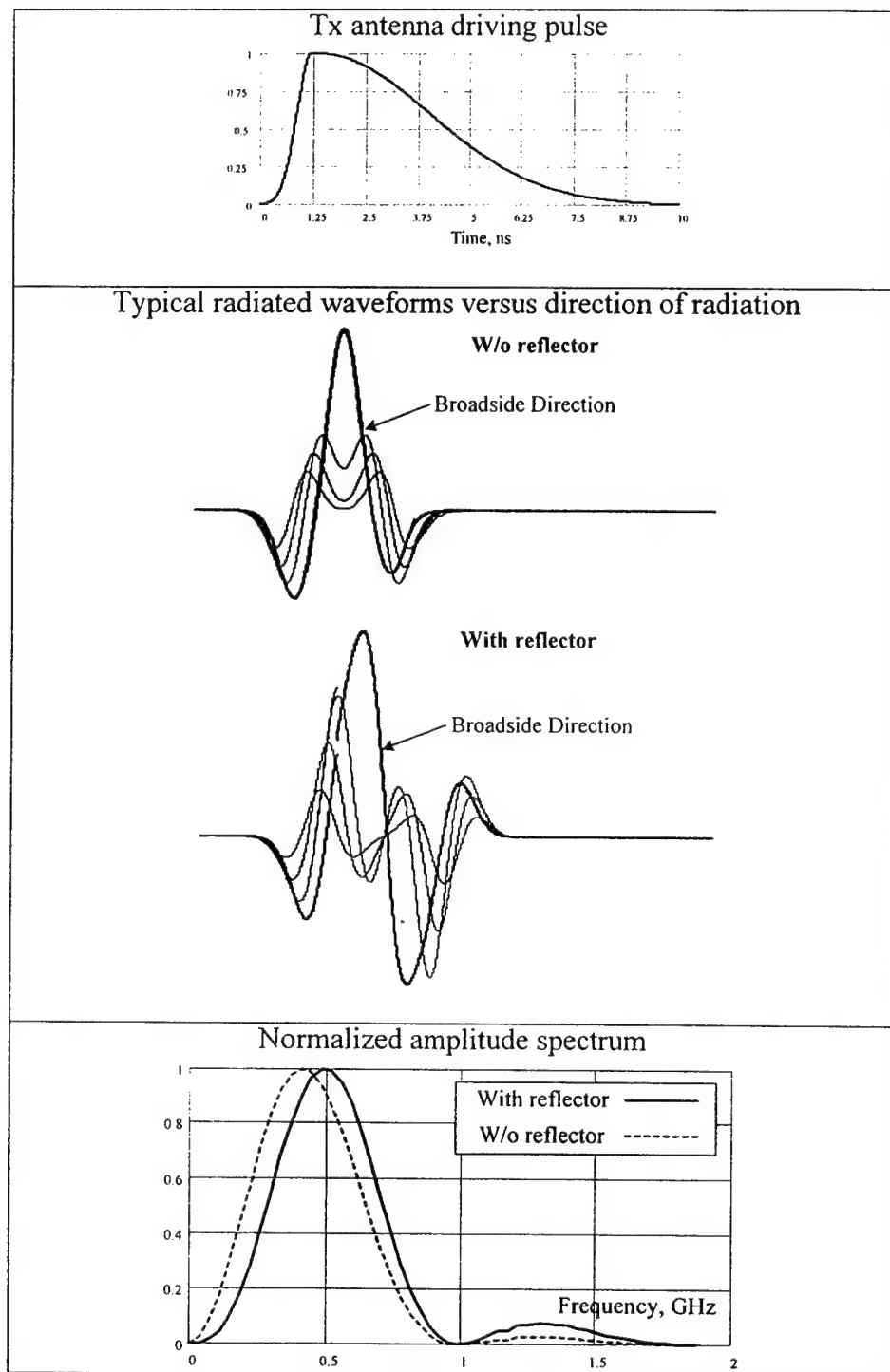


Figure 3. Waveform and spectrum transformations in Tx bow-tie antenna.

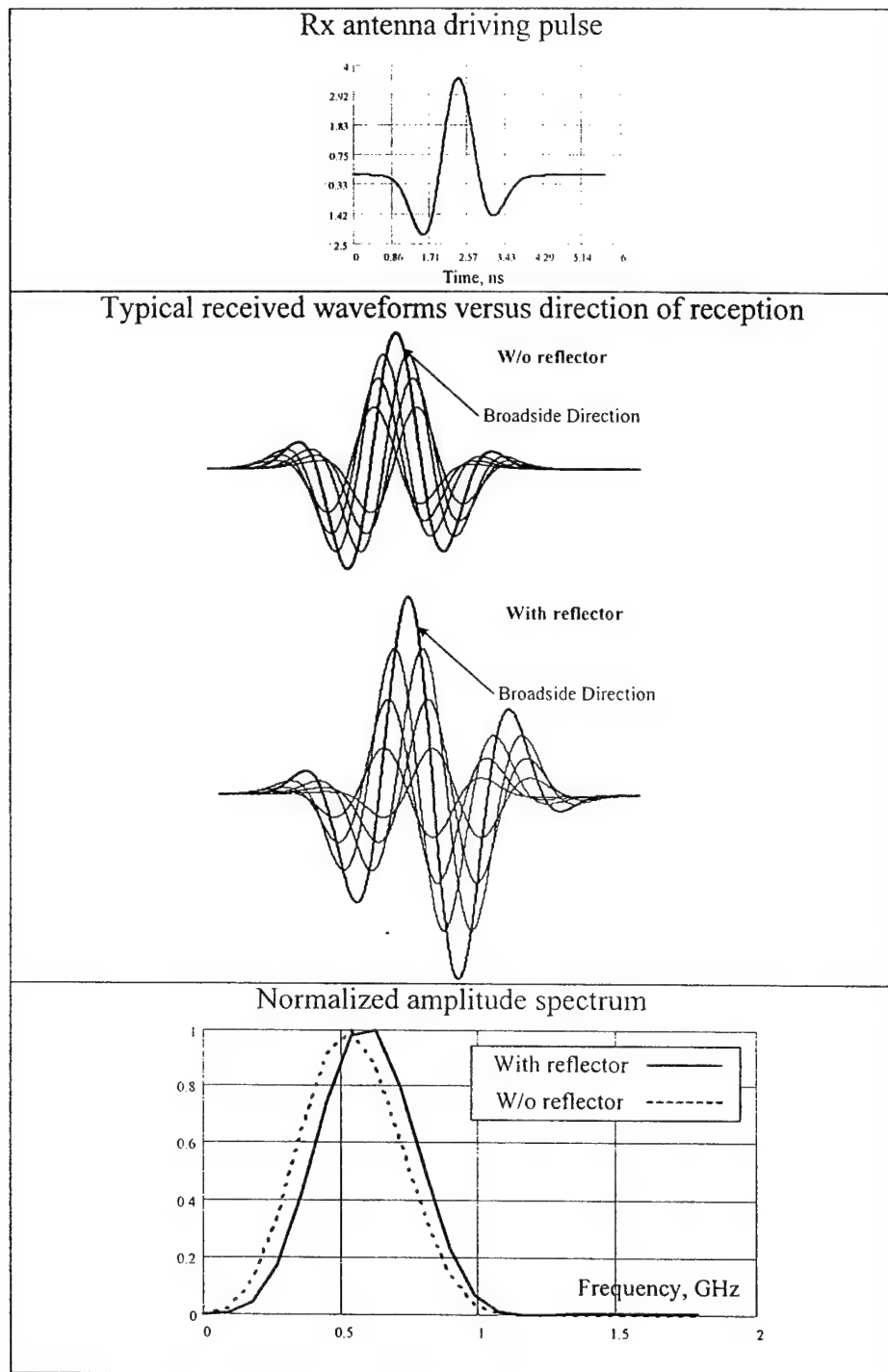


Figure 4. Waveform and spectrum transformations in Rx bow-tie antenna.

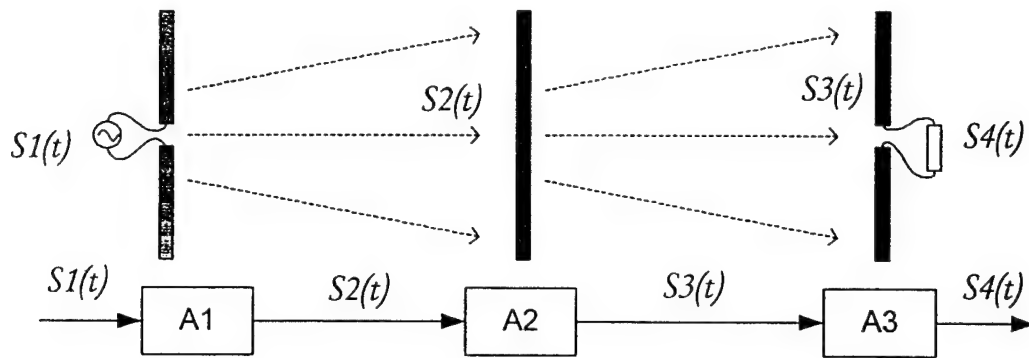


Figure 5. Network presentation of signal transformation passed consequently between transmitting – scattering – receiving center-fed dipole antennas.

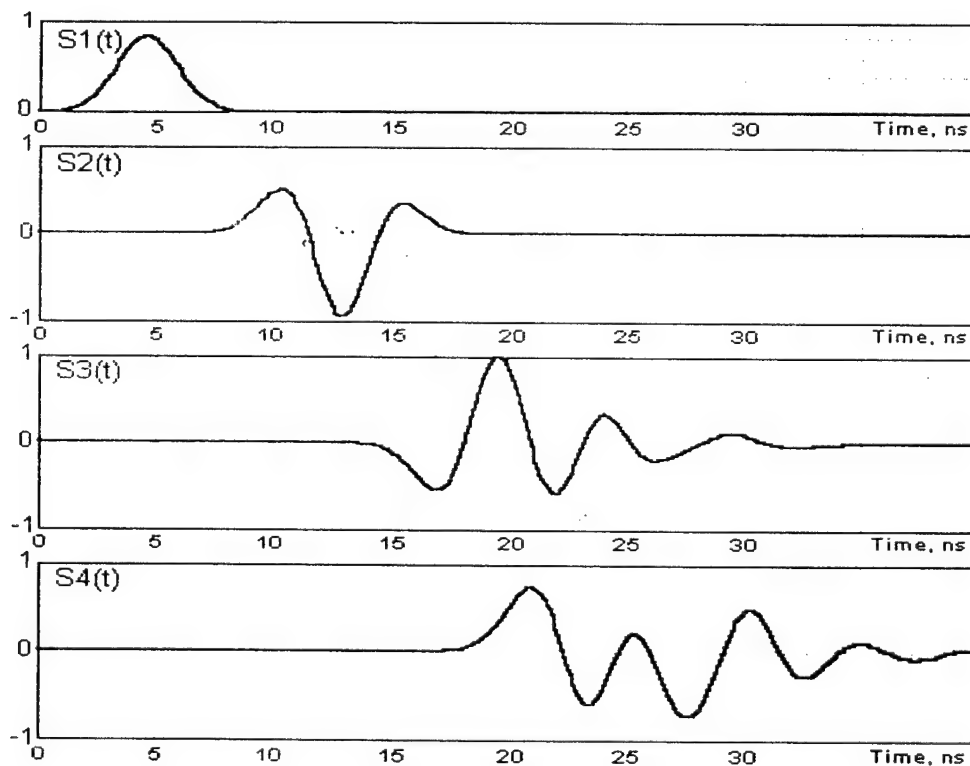


Figure 6. Mathcad simulated waveform transformation with the near-field effects for the system in Figure 5.

4. Antenna Array Design

4.1 Single antenna element design

Waveform and bandwidth having been chosen, the GPR designer must implement an antenna commensurate with bandwidth. As stated above the antenna design becomes particularly critical for radar operation near the surface of the sounding media. In this case some preventing measures are needed to minimize antenna mismatching and ringing effects. Pure antenna matching can cause multiple reflections between the antenna and the surface (or within radar itself), and such "ringing" can hide target returns. Other problems caused by the proximity of Earth's surface are distortion of the antenna pattern and near-field effects. Both make it more difficult to predict what the GPR should see and hence make more difficult the interpretation of results.

One of the ways to minimize ringing effect in antenna is implementation of its resistive loading. However we use antenna without resistive loading rather antenna with double passing excitation [3]. The reasons are low energy efficiency and technical difficulty to put in practice resistive loading for big size antennas. It is easy to show that energy efficiency of such antenna with complete suppression of wave reflected from opened antenna end will be at least -20 dB lower than in antenna with double passing of exciting pulse. Also we do not use here impedance matching technique studied before [3] due to its complexity. Of course for such design preference we have additional lobes in signal and its stretching in time but we follow here our general design strategy to make simple antenna design and improve quality of radar imaging as more as possible by signal processing.

Another problem to be treated in design of single antenna element is minimization EMI effects and false alarm rate due to scattering in upper half-space. One of the approaches is based on introducing adsorbing materials which fill some volume above antenna to adsorb electromagnetic energy in above half-space. But this method being complex for its realization does not give practically valuable results as followed from our experience and some published data. Moreover if difference between electrical properties of sounding media and adsorbent material increases the radar performances can degrade and be worse than in antenna without adsorbent material. The more preferable way is using antenna with simple reflector. Whole antenna is placed in metallic box with one open face as an aperture. Additionally about 3dB rise of antenna directive gain is reached. Note some changing in spectrum take place also as followed from results of simulation in Section 3.

Special attention should be paid to optimization of Tx/Rx units with respect to waveforms in them or equivalent effective spectrum. All discussed above topics and chosen design preferences have initially been verified with simple antenna design including monostatic antenna pair, and two Rx and one Tx channel array antenna. The last one is described at the next section.

The monostatic antenna pair, Figure 7, includes a pair of the same bow-tie antennas mounted on the base plane and directly terminated to the Tx/Rx front-end units. Being put on the air-ground interface these antennas have broadside radiation features. Really their pattern is disturbed due to interface influence. Such antenna layout has been studied before [3].

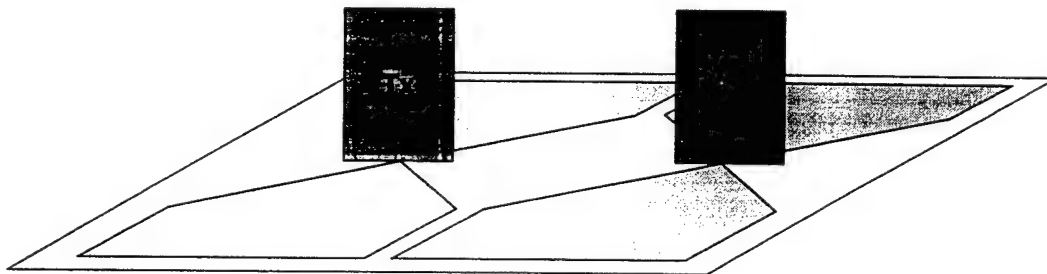


Figure 7. Design of monostatic antenna pair with terminated to Tx/Rx front-ends bow-tie antenna elements.

Transmitter electronics is based on bipolar transistor switchers with following leading edge sharpening by step-recovery diode (SRD). The Tx module is built with two identical step voltage stages either terminated with Tx antenna's arms. The main trouble of the scheme is necessity of mutual delay reduction between two outputs step voltage. Transmitter electronics provides pulse excitation similarly to that in Figure 3 above with 0.5 - 1 ns rise time and 30-60 Volts peak voltage. Pulse repetition rate is 100 kHz.

Receiver consists of wideband low-noise input RF amplifier, sampling circuit and buffer amplifier. Total input bandwidth is up to 10 GHz. Spectral transformation rate or equivalent time-sampling is approximately 10^6 .

Synchronizer unit executes control functions and interface board provides communication with the main PC unit. Block diagram of the GPR with single Tx/Rx antenna pair is shown in Figure 8.

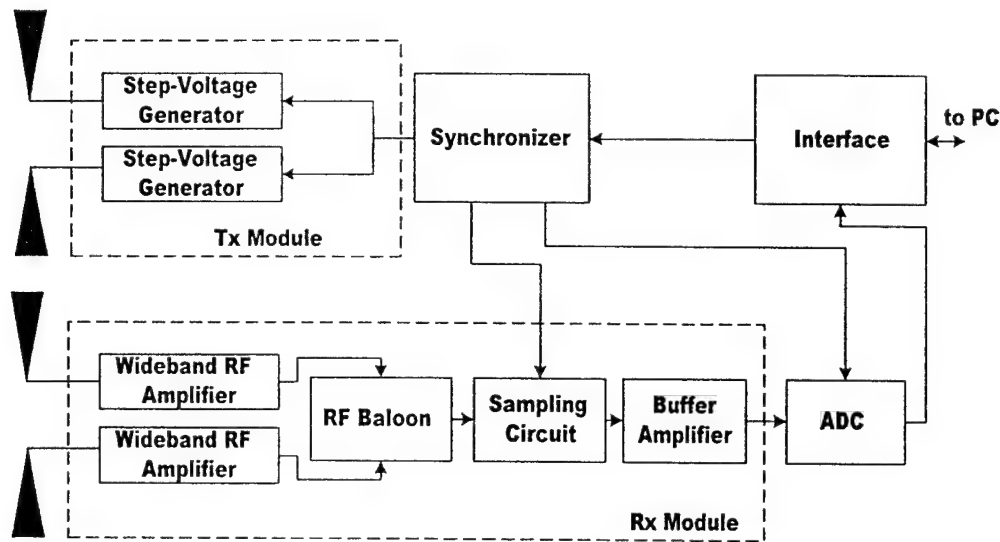


Figure 8. Block diagram of the GPR with single Tx/Rx antenna pair.

4.2. Two Rx and one Tx module antenna array

The next step of our research and design efforts is to build multi-element impulse array antenna. It includes two-Rx and one-Tx element array. Draft picture of this array antenna and accompanied electronics mutual arrangement is shown in Figure 9.

This array is assembled in a single box that forms simultaneously a shielding package and reflector for whole array antenna. Its inner space is filled by closed-cell foam plastic. This solution provides simple mechanical support and reciprocal disposition of antennas, shields and electronics. In order to improve directivity properties like V-dipole antennas are used instead of bow-tie antennas.

This design is realized with the same Rx and Tx modules, as described above. The main goal of the construction was simultaneous data acquisition from several Rx antennas for the principal algorithm examination. Note that considered data collection strategy assumes replacement of wide-band controlled time-delay units to computer processing of acquired data. Thereby it eliminates any problems connected with necessity to compensate mutual delay between different antenna elements. A block diagram of the GPR with described antenna array design is shown in Figure 10.

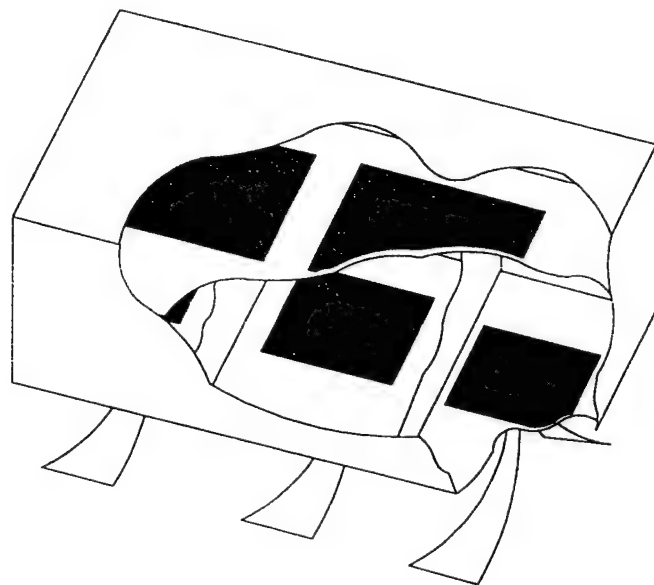
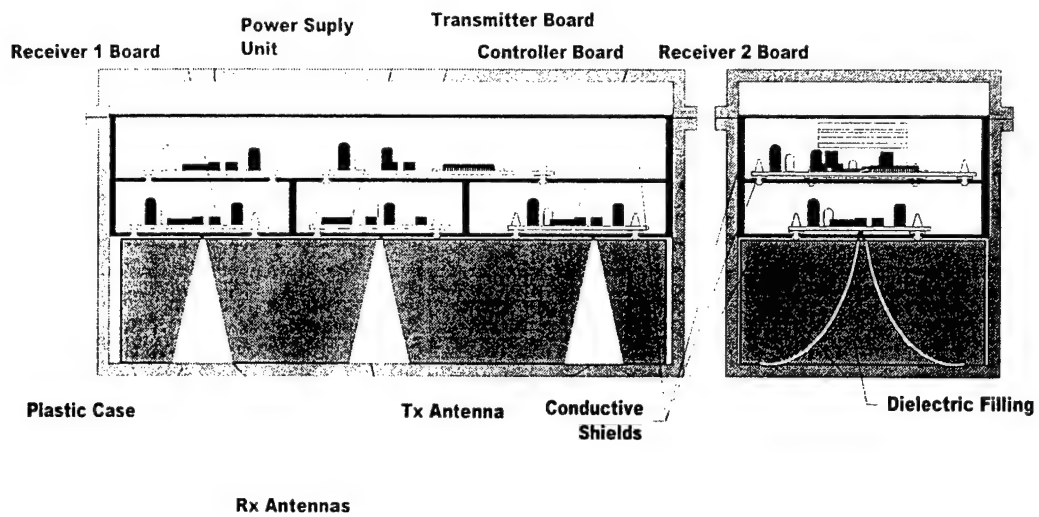


Figure 9. Design of antenna array with one Tx and two Rx modules.

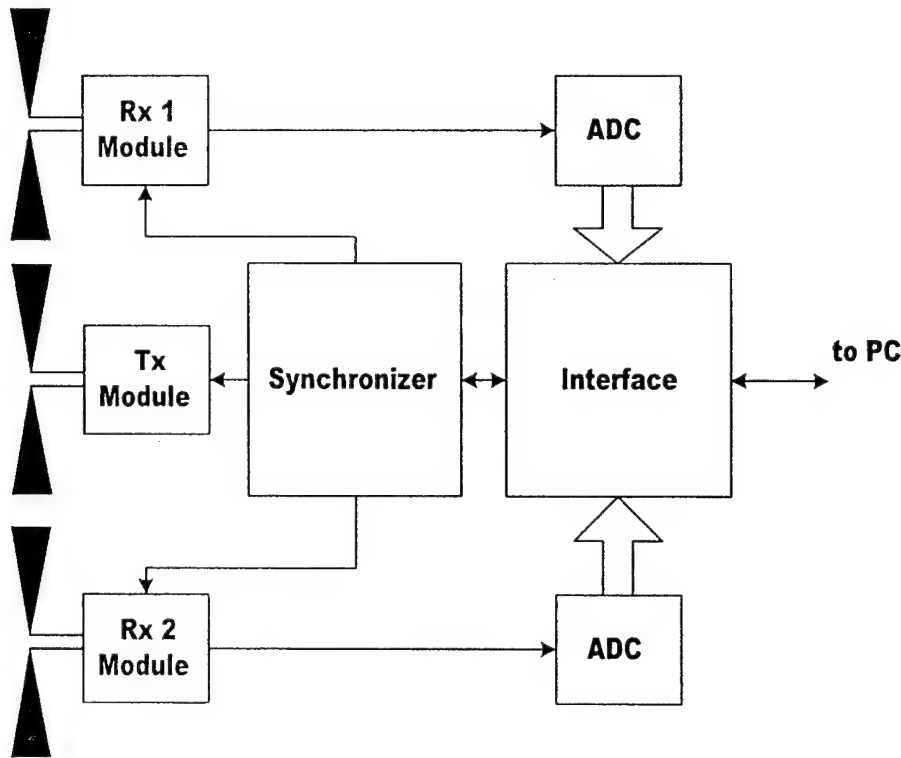


Figure 10. Block diagram of the GPR with Tx/2Rx antenna array.

4.3 Basic endpoint array configuration

Two versions of the basic design of array with two cross-polarized transmit antennas and 8 receive ones (4 and 4 per each E- and H-polarized direction in cross-down range) are shown in Figure 11. The first version, Figure 11 a, includes low-power Tx units connected to bow-tie antennas. Each Tx/Rx unit in array is presented as a separate module. Generally this design version allows array antenna with flexible reconfiguration opportunities by using new frame with separated Tx and Rx modules. The second version, Figure 11 b, has a rigid functional structure with low configurability. In this version a cross-polar antenna pair for each Rx and Tx elements are used. Bow-tie Rx antenna cross-polar pair is shown in Figure 12 a and exponential horn Tx antenna pair in Figure 12 b, accordingly.

The transmitter and receiver electronics modules are directly terminated to the antenna array elements. Receiving electronics is the same as the previous described one.

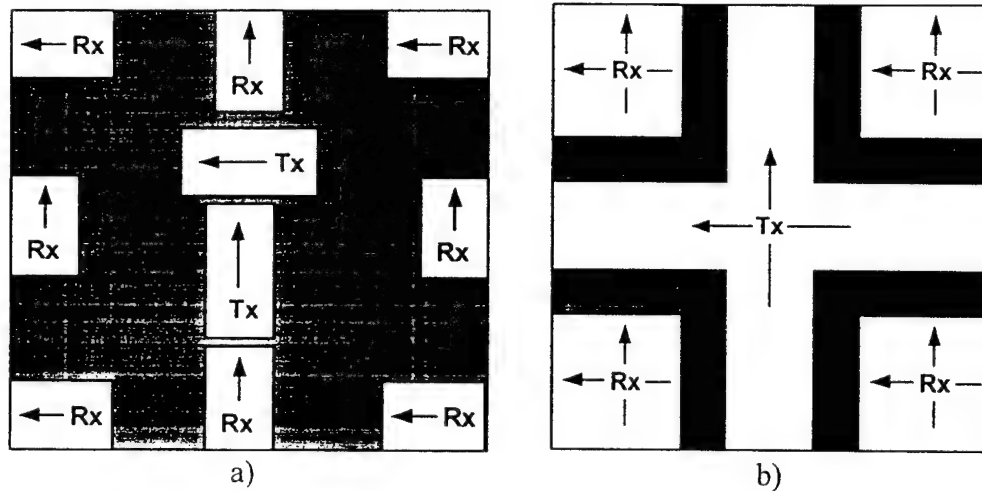


Figure 11. Array configurations: (a) separate Tx/Rx modules, (b) cross-polar one.

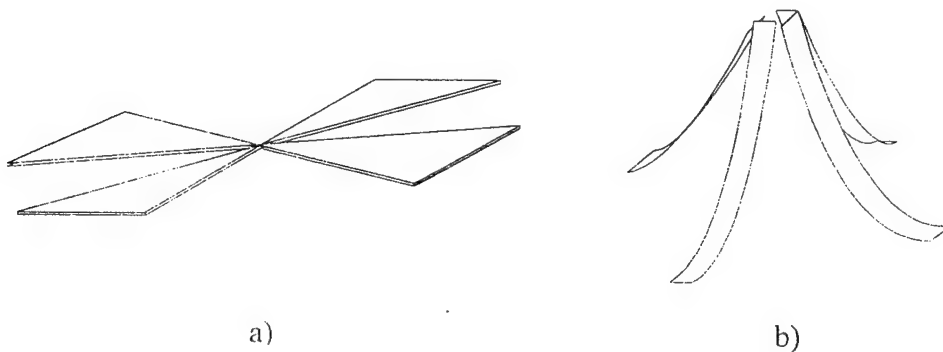


Figure 12. Antenna cross-polar elements: (a) bow-tie, (b) exponential horn.

At the same time it was utilized a new transmitter unit. In order to improve the GPR performance factor of high power nanosecond generator has been designed [9]. It forms impulse 1.5-2 ns rise time and peak voltage up to 550 V on 50-Ohm loading. Maximum pulse repetition rate reached up to 25 kHz. Power consumption was less than 6 W (500V @ 20 kHz conditions). Transmitter design combines power MOS-FET technology with drift step-recovery diode (DSRD) sharpener abilities. Note that the DSRD is the most suitable active element for solid-state up to 1 MW and more nanosecond impulse generation. Thanks to simple design, high output power, efficiency and stability, relatively durability and high repetition rate, based on DSRD Tx modules can be applied in various UWB radar design [1.8].

The array covers 0.2-0.9 GHz at -20 dB level as can be predicted from simulation results in Figures 3 and 4. As discussed above the whole array antenna has upper shielding for improving system interference immunity and low false alarm rate. The array antenna width is 1 m on each side. This array antenna employs ground contact or nearly ground antenna positioning with elevation 0.05-0.2 m above ground to compensate some surface roughens on the searching areas. For the sake of enhancing array's performances achieved with physical aperture its size can be bigger than 1.0x1.0 m.

Such chosen size of the antenna is dictated by requirement to the designed GPR to be able to operate in some rooms to investigate their underground environment. Typically these rooms have entrances of 75x150-cm size. From the other hand implementation of SAR technique allows to have bigger equivalent aperture. Technically this solution is less expensive and simple than implementation of specialized UWB array antenna with big physical aperture. Finally SAR approach enables variety of scenarios of data collection including variable cross-range resolution. The price paid for these advantages are a relatively slow data-collection rate [6] that is not principal topic for slow moving robotic platform where the designed GPR with array antenna will be housed.

In the case of the designed radar there is necessity to employ array antenna with definite physical aperture because the SAR technique can not be effectively applied anywhere. The most important sites of the searching territory near the destroyed Nuclear Power Plant Unit in Chernobyl are located on so-called Cascade Walls. Strong edge effect there as shown in Figures 13 does not give possibility to employ SAR technique there. Efficiency of resulted SAR procedure computed by estimation of available length of scan lines is shown in Figure 14. Thus application of some physical aperture in antenna is too necessary.

4.4 Array control and data collection subsystem

Block scheme in Figure 15 consists of two Tx and eight Rx modules, synchronizer, data acquisition and interface units. All Rx modules sample and digitize input signals simultaneously. Mutual delays are removed during primary digital processing or later. Synchronizer is a "heart" of the system. It forms control signals for all modules and allows to realize any scanning algorithm under main computer control. Using digitally controlled sweep-generator and Rx time-varying gain-control (TVGC) amplifiers allows executing flexible GPR control.

- 1) 1-, 2-, 3-D filter procedures in original, spectrum or combined (F-K) spaces;
- 2) velocity analysis for common midpoint gathers and velocity migration [10];
- 3) array signal processing for physical aperture for in-situ image focusing;
- 4) synthetic aperture processing technique;
- 5) full polarimetric data processing.

Inherently beam pattern of subsurface radar antennas is widely spread and to improve its physical aperture and SAR techniques are applied that are subject of items 3-4. In order to overcome of such existing GPR technique limitations as in a hand-held radar, we will combine physical aperture technique with SAR opportunities.

5.1 Antenna beam forming with physical aperture

One should distinguish two kind of antenna beam forming methods implemented in the presented array antenna project. The first technique is 'in-situ' image focusing method in TD while second one is implemented by SAR processing. Note that antenna features effect strongly on such both beam-forming techniques. The basic idea of implemented algorithm of array beam-forming in TD is schematically shown in Figure 16. This beam forming technique is introduced by adjusting time delay magnitudes in Rx channels of array. In this way an array beam is focused on a definite space point (really spot) inside volume covered by array antenna [10,12]. There is a set of limiting factor on the size of array focusing spot due to decorrelation of signals in different Rx channels forced by the difference in antennas features and practical inhomogeneity of real sounding media. There are some finite errors in estimation of velocity propagation, which quantity is used inherently in beam forming algorithm.

Actually array structure in Figure 16 implements post-processing array technique for radar imaging with improved signal-to-noise ratio [12]. Some inter-channel correlation processing can be algorithmically introduced with threshold estimation of resulted signal correlation products in fixed element of scanning volume. Generally it gives effective suppression of interference signals with out of interesting arriving.

The Rx antenna elements in Figure 16 are spaced at the distance of about 90-cm. The higher frequency in spectrum is about 800-900 MHz that corresponds to wavelength about 35 cm in free space and at least two times more in sounding media with typical $\epsilon \geq 4$. For such elements spacing the grating lobe can be observed at the scan angle 22° in free space and 52° in sounding media. The scan angle is measured from the antenna broadside direction, which is normal to the

array aperture plane. But this effect of grating lobes is not principal for down-looking radar systems with maximum scan angle equals to $10-15^\circ$, i.e. array antenna looks through space covered by its aperture. Practically smallest insufficient elements of radar images can be distorted.

Moreover for the central frequency of used spectrum the grating lobe appears at 52° in air and absent in subsurface media. Note that same differences in E- and H-planes scanning will take place but these effects are high-order ones. Also here is some blindness effects in the H-plan due to specific features of pattern of pulse antenna in this plan. This effect is revealed in radar images as some artifact distorted radar signature of target. It must be subject of detailed next studies including the some specificity of pulse array antennas loaded by subsurface interface

Computational requirements for implementing antenna beam forming algorithm are low due to its realization as a post-processing algorithm. It processes the signals registered by each single Rx channel element and stored in computer memory. This algorithm has been successfully tested with two-Rx-one-Tx pulse array antenna in Figures 9 and 10 will be under experimental examination soon in the complete 8-Rx and 2-Tx array antenna.

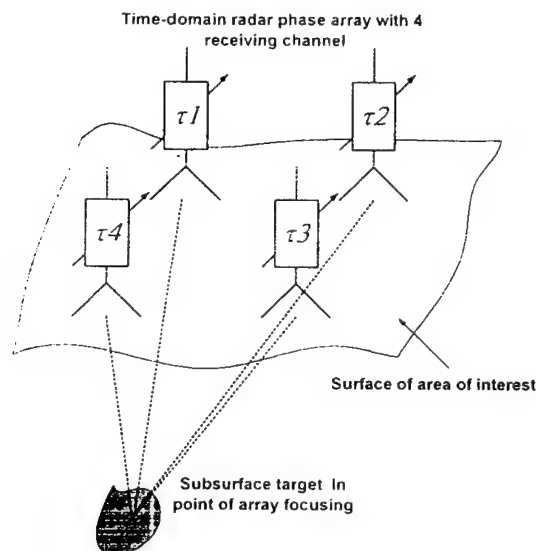


Figure 16. Schematic presentation of array antenna TD beam-forming algorithm with focusing in the cross-track and down-track directions.

5.2. Synthetic aperture processing

Generally SAR processing is well-established method to transform the data collected along a scan trajectory of electrically small real aperture to data collected with big virtual aperture. Fourier transform is mostly used for such mathematical operation to transfer from wave-number space (k_x, k_y, k_z) to Cartesian coordinate space [12]. The broader supports in k -space, i.e. longer scan trajectories, the finer impulse response in transform space. Practically it requires enough long scan line for 2-D imaging and enough scanning areas for 3-D radar imaging. This SAR technique is widely applied in GPR with single monostatic antenna pair like that in Figure 7.

Practically the strong influence of antenna properties takes place on the reconstructed SAR images including some defocusing phenomena to focus simultaneously early and late time response [12]. These affects require special detailed consideration and are outside frame of the paper. Also as illustrated in Figures 13-14 the SAR technique has sometimes very limited opportunities when GPR system must be applied on the sites limited by their areas.

5.3. Polarimetric processing with array antenna

To collect all available information about target the complete polarimetric technique is employed when two orthogonal polarizations are consequently transmitted and simultaneously received. Employing coherent radar, the polarization scattering matrix (PSM) is processed to provide target shape information [11]. Real problem should be carefully treated is a level of polarization isolation of antennas, especially in the near-field range. Our own results as well as the data in literature indicate about problematic of this issue for real GPR system especially for shallow target. At the same time this technique is promising for deeper target. Also using of cross-polarized antennas tends to discriminate against the surface clutter return. We do not have at this time enough experimental data on this issue that should be done soon.

Generally the radar polarimetric technique enables potentially target characterization by fixing the difference in the phase/amplitude/waveform of signals registered for different polarization states of transmitting $Tx1...2$ and receiving $Rx1...8$ antennas (Figure 15). The scattering matrix for each receiving element presents measured scattered signals of both polarization $E_{R1,2}^S$ versus those incident transmitted signals $E_{T1,2}^I$.

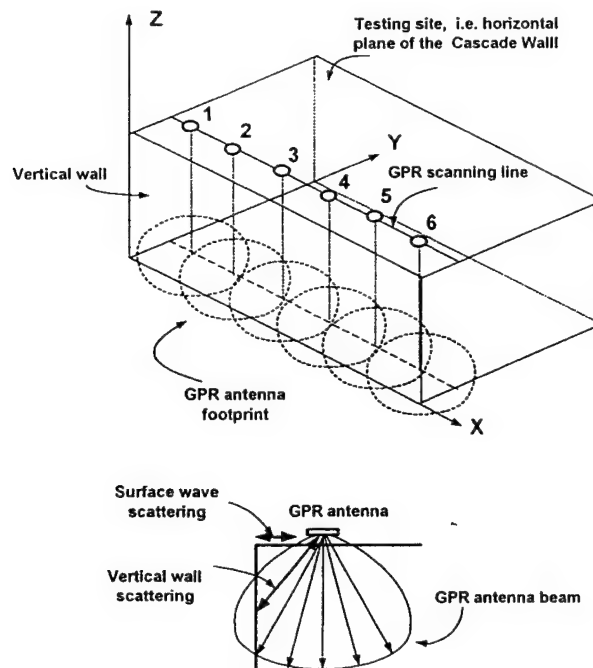


Figure 13. Schematic presentation of the GPR measurement on the Cascade Wall.

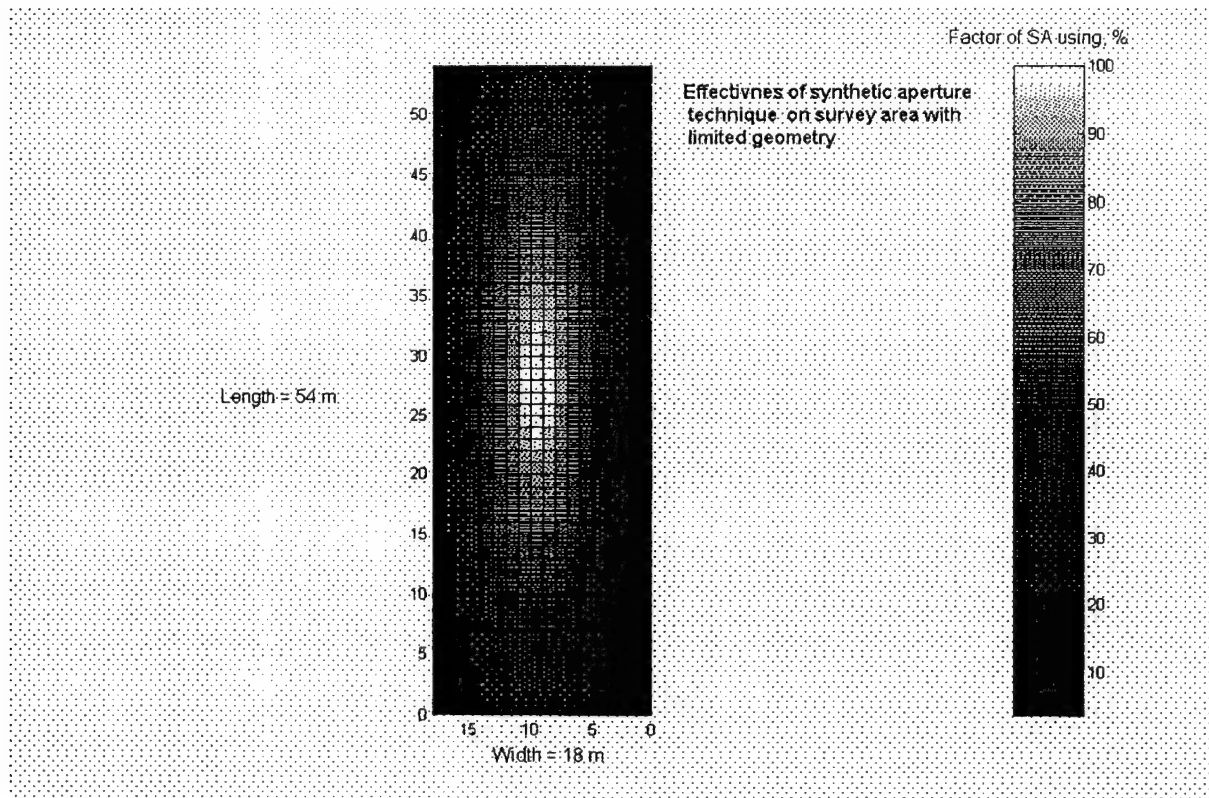


Figure 14. Effectiveness of SAR technique due to geometrical factor.

$$\begin{bmatrix} E_{R1}^S \\ E_{R2}^S \end{bmatrix} = \begin{bmatrix} S_{11} & S_{21} \\ S_{21} & S_{22} \end{bmatrix} \cdot \begin{bmatrix} E_{T1}^I \\ E_{T2}^I \end{bmatrix}$$

Separated radar Rx antennas simultaneously operate in the both polarization states resulting in four measurements of the co-polar (S_{11} , S_{22}) signals and cross-polar (S_{12} , S_{21}) ones.

Let note that consequent scanning in two opposite linear polarization does not make possible target classifications by its polarimetric features. In this case at least only the S_{11} and S_{22} members of the scattering matrix can be estimated. It is not enough for a proper target characterization that is important issue for highly cluttered media around the Chernobyl destroyed reactor where the designed radar should be employed.

6. Some Results of Experimental Investigations

Some experimental studies have been conducted with 2-Rx-1-Tx antenna for GPR design as a prototype of complete 8-Rx-2-Tx array antenna that is in progress now. The presented experiments are not directly associated with the Chernobyl radar project but give useful information for our endpoint design. Firstly additional opportunities of GPR system based on array antenna with respect to ordinary GPR with monostatic antenna pair to detect and discriminate the target with specific shape have been explored.

Figure 17 presents simulated and SAR measured data for square metal plate as a buried target. On the left in Figure 17 a is a 2-D geometry for simplest subsurface scattering problem to help communicate to next figures. Note that simulated image at the right of Figure 17 a does not present geometrical shape of target rather than its signature with specific edge effect expressed in hyperbolic leading and edge tails [7]. Since radar visualization of internal regions is inherently more qualitative than quantitative, one must concentrate on the signature of target than its exact geometrical shape that can not be reconstructed in details. In the context of our array antenna project we will consider here the effects of antennas on radar signatures.

In Figure 17 b one can observe the presence of two shallow targets like that in Figure 17 a. In contrast to simulated data the image of real medium is different. Here is a direct coupling signal between Tx and Rx antennas [3] as well as ringing effects at the right side of picture. A ringing effect inside sounding media is produced by internal interface in it with strong scattering and can be

7. Conclusions and Summary

It is expected that sufficient two-dimensional spatial scanning in down-looking GPR system, where physical aperture with SAR and polarimetric processing are combined, provides maximum 3-D resolution that can be achieved by the given bandwidth. The last factor is limited due to rigid background physics of electromagnetic propagation inside matter and antenna features to radiate and receive broadband or UWB signal with $< 100\%$ relative bandwidth.

Besides limitations in antennas UWB properties there are many problems in design Tx/Rx electronics with fine time accuracy and resolution or equivalent high sampling frequency as a jitter problem. Practically it is difficult to maintain operation over 5-10 GHz operation frequency. In this case FD techniques with UWB signal synthesis seems more promising.

Finally the practical distribution in array antenna design efforts tends towards to dominant role should be played by signal processing technique. As we found the potential in antenna design are sufficiently limited. Employment of antenna array adds some flexibility in GPR system design by introducing the advanced processing/imaging opportunities.

Additionally scanned antenna/array allows additional capabilities to produce synthetic aperture imaging. Doing so, however, requires careful attention to knowledge of antenna position and correction of propagation effects within soil. The last factor limits the performances of real GPR system. Note that array antenna with some spacing between its element enables potentially some calibration procedures to estimate velocity of signal propagation inside media. It is interesting opportunity to be subject of next research efforts.

Fundamentally signal processing and imaging/display options in subsurface radar are strongly driven by signal waveform choice and its implementation taking into consideration inherent signal transformation in antennas like simulated data shown in Figure 3-6. Thus relevant choice of antenna types, array configuration are important issue of overall GPR system design.

Presented results have been obtained into the frame of some subsurface radar projects for archeology and landmine detection. Now the array antenna for the advanced GPR system to be applied near the Chernobyl nuclear power plant is in focus of research and design efforts. Most of components of radar system have been designed and tested including prototype of antenna array.

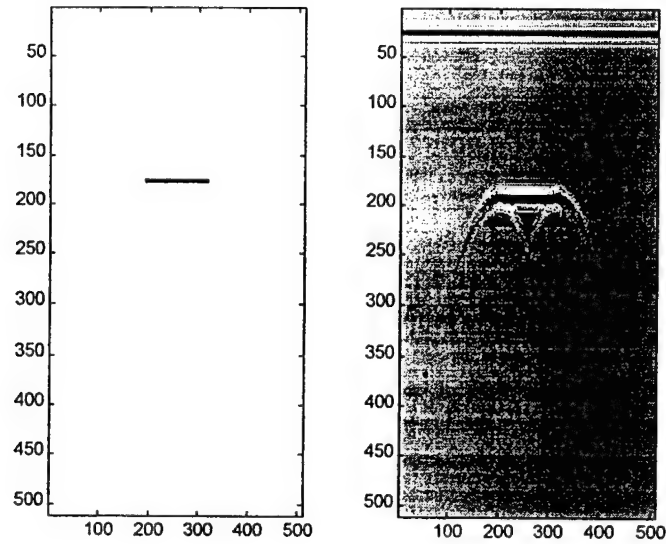
partially removed from image by some processing technique. This effect is often very unwanted for GPR because such clutter obscure valuable information, can overload internal circuits of receiver and decrease radar dynamical range. There are no receipts in antenna design other than application full-polarimetric and other enhanced signal processing techniques that can be effective for some cases.

The application of TD beam-forming technique is illustrated in Figure 18 for 2-D scan implemented with 2-Rx-1-Tx radar array antenna. The final image in this Figure is a result of post processing technique applied to focus image covered by array aperture. Radar antenna was moved along the straight scan line and the focused image is computed in broadside direction as cross-correlation of delayed signals in the Rx channels. Some threshold level was being adjusted to improve focusing and cut signal tails. We observe here absence of hyperbolic curves but image has finite level of focusing due to multi-lobe structure of signals. At the same time some artifacts are present but major reflections are strongly stressed, which correspond to internal objects should be detected. One can conclude that this technique is not perfect enough. However we expect that for such case like the Cascade Wall in Figure 13 it can be useful.

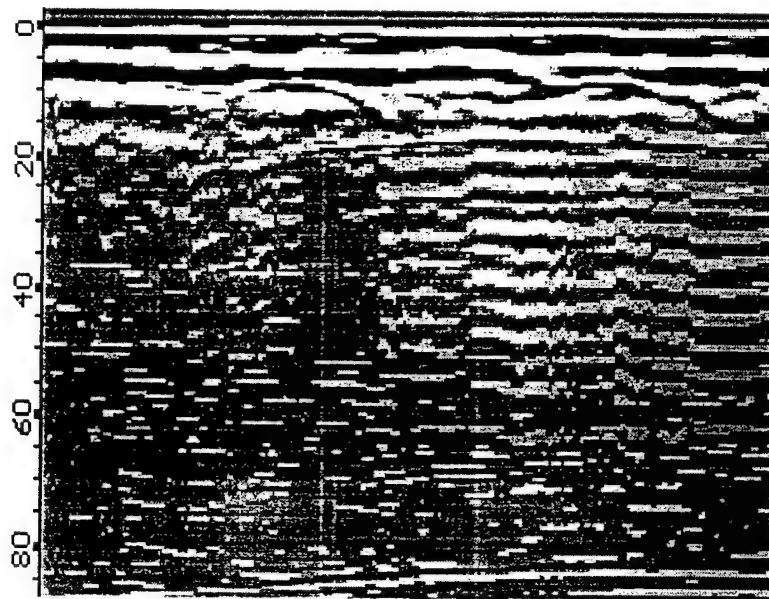
Results of radar imaging of specific subsurface target received with simple 2-Rx and 1-Tx array are shown in Figure 19. At the right one can see horizontal slice of cylindrical shallow subsurface target and the left picture presents its vertical slice. This target is like a antitank landmine at the depth of 30 cm and has the 35-cm diameter and the 15-cm height. Horizontal slice has been obtained as a set of linear scan over searching area.

The presented images do not give of course exact geometrical shape of target being defocused and with artifacts. At the same time to get best quality of radar images is very problematic. From the point of view of strong physical limitations it is impossible to obtain better imaging because wavelengths in the used signal spectrum are comparable with geometrical features of target and phased information is partially lost. Disturbance effect of medium on antenna and some uncertainty of signal velocity force the last factor too.

However the results in Figure 19 demonstrate evidently that using of "non-ideal" antennas in radar with some "ringing" etc. and coherent processing enables obtaining valuable visualization of subsurface media with GPR. Generally signal-processing component as sufficient part of design efforts is very important here and this issue is finally discussed in conclusion section.



a)



b)

Figure 17. (a) simulated and (b) experimental radar image of subsurface with specific shaped target.

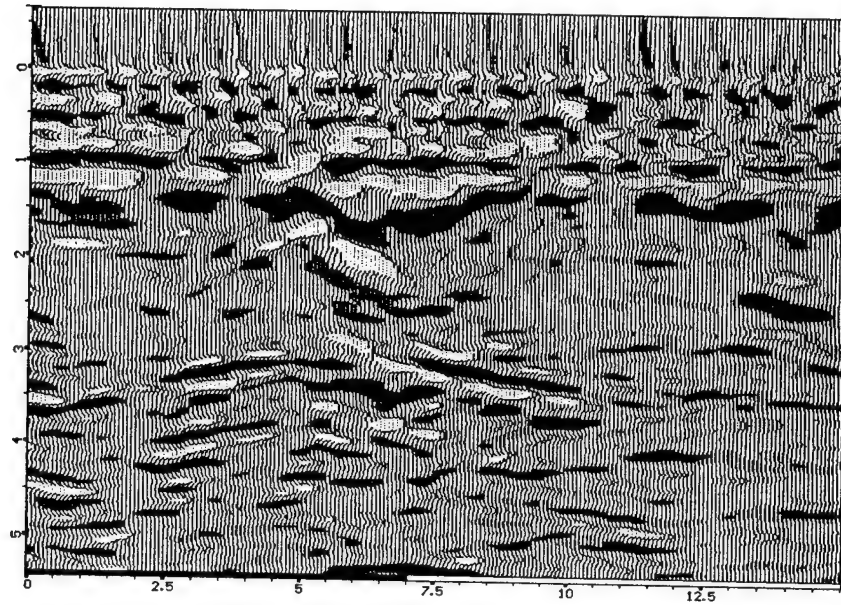


Figure 18. Radar 2-D vertical scan imaging of subsurface region obtained with 2-Rx array antenna and application of TD beam forming data processing.

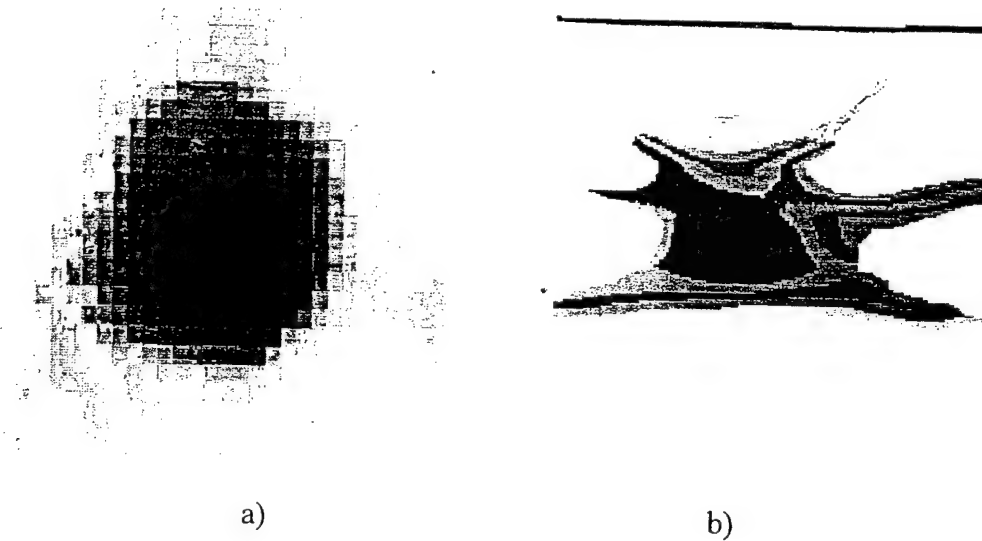


Figure 19. Vertical and horizontal slices for GPR imaging of cylindrical shallow target.

References

- [1] Agee F. J., Baum C. E., *et al*, "Ultra-wideband transmitter research", *IEEE Trans. Plasma Science*, 1998, 3, pp. 860.
- [2] Baum C., "Some characteristics of electric and magnetic dipole antennas for radiating transient pulses", *Sensor and Simulation Notes*, No. 125, 1971.
- [3] Boryssenko A., Tarasuk V. "Ultra-wide band impulse antennas for subsurface radar applications", *Proceedings of Antenna Application Symposium*, 1999, pp. 478-504.
- [4] Brock B. C., Patitz W.E., "Factors governing of operation frequency for subsurface-imaging synthetic-aperture radar", *Proceedings of SPIE Conference*, SPIE Vol. 2217, 1994, pp. 176-187.
- [5] Claude S. *et al*, "K-space imaging algorithms applied to UWB SAR", *Proceedings of IEEE APS*, 1994, pp. 491-495.
- [6] Daniels D.J., "System design of radar for mine detection", *Proceedings of SPIE Conference*, SPIE Vol. 3752, 1999, pp. 390-401.
- [7] Finkelstein M. I., Mendelson V. L., Kutejev V.A., *Radar for layered soils*, Moscow, Soviet Radio, 1977.
- [8] Kardo-Sysoev A. F., Zazulin S. V., *et al*, "High repetition frequency power nanosecond pulse generation", *Proceedings of the 11th IEEE Int. Pulse Power Conf.*, 1997, pp. 420.
- [9] Prokhorenko V., Boryssenko A., "High power subnanosecond generator for UWB radar", *Submitted to EUROEM 2000: Euro Electromagnetics*, 2000.
- [10] Rapport C. M., Reidy D. M., "Focused array radar for real time imaging and detection", *Proceedings of SPIE Conference*, Vol. SPIE 2747, pp. 202-213.
- [11] Stiles J. M., Parra-Bocaranda P., Apte A., "Detection of object symmetry using bistatic and polarimetric GPR observations", *Proceedings of SPIE*, Vol. SPIE 3710, 1999, pp. 992-1002.
- [12] Tuo J.S., Buchenauer C.J., Schoenberg J.S.H., "Beamforming in time-domain arrays", *Proceedings of APS*, 1999, pp. 2014-2017.
- [13] Ziolkowski R.W., "Properties of electromagnetic beams generated by ultra-wide bandwidth pulse-driven arrays", *IEEE Trans. on Antenna and Propagation*, Vol. 40, No. 8, August 1992, pp. 888-905.

Antenna Time-Domain Effects on Waveforms and Advanced Signal Processing

Daniel A. Leatherwood, David D. Aalfs, Larry E. Corey, Rickey B. Cotton, and
Barry S. Mitchell
Georgia Tech Research Institute
Atlanta, GA 30332-0852

Abstract: Time-domain characteristics of phased arrays can vary considerably from that of a reflector antenna. These time-domain characteristics will affect both the transmitted and received waveforms and can therefore affect both advanced signal processing techniques and countermeasures techniques. This paper presents findings from a fundamental investigation of the time-domain effects of phased array antennas on the transmitted waveforms in both the main beam and sidelobe regions and the resulting effects on sidelobe cancellers.

1. Introduction

This paper describes initial findings from a research program to investigate the main beam and sidelobe impulse responses of large phased array antennas and reflector antennas typically used for radar applications. Particular emphasis is given to the way that the impulse response changes from the main beam to the sidelobe region of the antenna. Antennas are designed to radiate a plane wave with a given polarization and frequency in a specified main beam direction. However, the time-domain impulse response will vary according to the actual implementation of the antenna design. Reflectors are designed to collimate a radiated beam by creating equal path delays and tend to have few parts. This produces a relatively simple and short time-domain impulse response. A phased array, on the other hand, generally collimates the beam by adjusting phases instead of path delays. In addition, there are more parts, which introduce multiple reflections. This gives the phased array a more complicated and longer impulse response than a reflector. These time-domain effects affect transmit and received waveforms and therefore advanced signal processing algorithms such as adaptive digital beamforming (ADBF) and space-time adaptive processing (STAP). The Georgia Tech Research Institute (GTRI) has instituted an internal research program to investigate the time-domain phenomenology of phased array antennas and develop computer simulation tools and measurement capability for characterizing these phenomena [1,2]. Section 2 provides a brief discussion of the time-domain phenomena and the variation of the effects with antenna

architecture. An overview of the method GTRI is using to investigate these phenomena is given in Section 3. An analysis of the resulting waveforms is presented in Section 4, and an analysis of the time-domain effects on sidelobe cancellers is presented in Section 5.

2. Architecture Effects on Time-Domain Phenomena

A variety of architectures exist for directing radiated RF energy in a specified direction. Two broad classes of architectures are reflector and phased array antennas. A simple parabolic reflector antenna collimates energy from a feed located at the focal point of the parabola by providing equidistant path delays from the feed to a plane perpendicular to the antenna boresight, as shown in Figure 1. In the direction of the main beam, this produces a very narrow impulse response, which implies that the transmitted waveform in the main beam direction will be very similar to the waveform input to the antenna terminals. Deviations from a true impulse result from multiple reflections and dispersion within the feed, multiple reflections between the feed and reflector, diffraction off the reflector edge, and scattering off the feed and feed struts. Furthermore, distances from the feed to different areas of the reflector are different, which implies that the region where currents are set up on the reflector surface grow over a short period of time [3,4]. In addition, the gain increases with frequency. In the sidelobe regions, the impulse is broadened by dispersion that results from differences in path lengths from the feed to the reflector and then to a plane perpendicular to the sidelobe direction. Some sidelobes may also be affected by spillover from the feed.

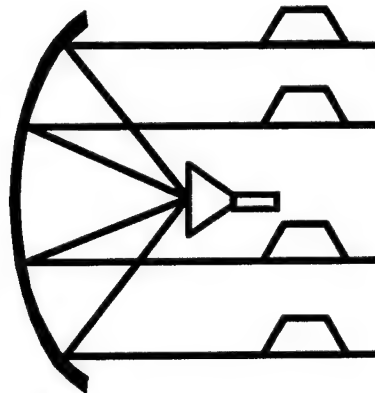


Figure 1. Parabolic reflector antenna

Most phased array antennas collimate a beam by using phase shifters to adjust the phase of the waveform radiated from each element in the array. In general, this

implies that the path delay from the antenna terminals to the plane perpendicular to the main beam direction is different for every element. Some radars use time-delay units (TDUs) at the subarray level to decrease the dispersion in the main beam. However, phase shifters are still used at the element level, so some dispersion still exists. In addition, when the beam is scanned away from broadside, the TDUs actually increase the dispersion in the far-off sidelobes. Other sources of time-domain effects in phased arrays are multiple reflections between the different components in the phased array and dispersion within the feed waveguides and phase shifters. Some architectures, such as a space-fed array, will have direct radiation from spillover that will affect sidelobes. If polarized screens and polarizing grids are used, polarization misalignments will produce polarization transients at the beginning of the pulse. A time-varying effect will result if the pulse is transmitted before the phase shifters have settled into a steady state.

Several phased array architectures are used for radar applications. Some are space-fed lens arrays, constrained-fed arrays, reflect arrays, and subarrayed arrays. Each of these architectures has a distinct time signature. A series-fed constrained feed phased array, as shown in Figure 2, will have large differences in the delay time to each of the element radiators. On the other hand, a parallel-fed constrained feed phased array, as shown in Figure 3, will have the same delay time to each element. This provides a very wide bandwidth when the beam is steered to boresight, but unless TDUs are used, the bandwidth will decrease significantly as the beam scans. Figure 4 shows a space-fed phased array. Again, there are differences in the time delay to each element, although these differences are typically smaller than for a series-fed constrained feed phased array with the same aperture size.

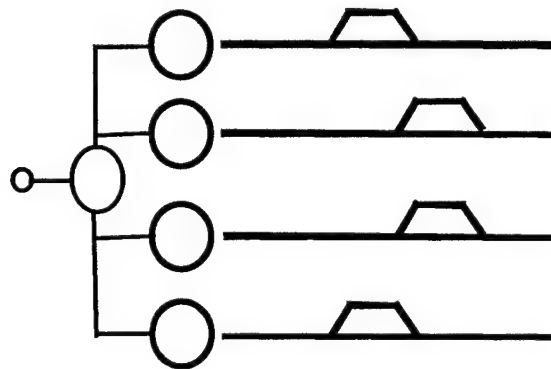


Figure 2. Series-fed constrained feed phased array

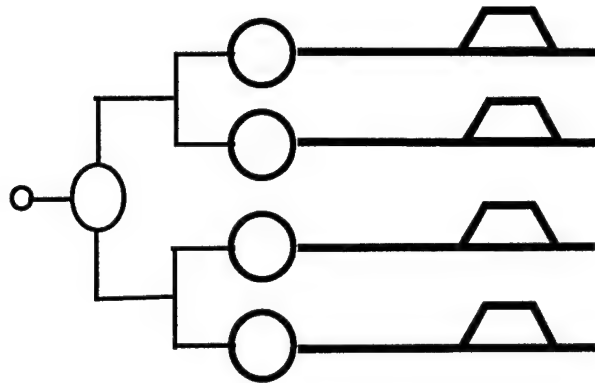


Figure 3. Parallel-fed constrained feed phased array with TDUs

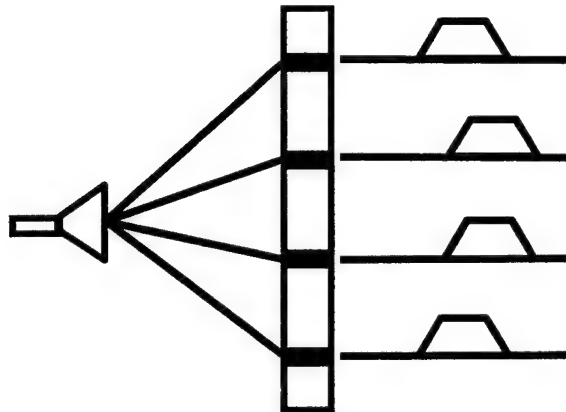


Figure 4. Space-fed phased array

3. Approach

The first step in studying the time-domain phenomena is to catalog all of the sources of time-domain effects and then determine which of these effects are significant. Using this analysis, computer simulation models have been developed to investigate these effects. For the initial modeling effort, it is assumed that the antennas are linear and time-invariant, which allows the use of the Fourier transform convolution theorem so that calculations can be performed in both the frequency and time domains. The transmitted waveform is the convolution of the input waveform with the antenna impulse response.

Measurements are performed to validate the modeling. GTRI has upgraded its near-field measurement range so that measurements can be multiplexed at a number of frequencies. The near-field measurement at each frequency is

transformed to the far-field domain, which gives a wide-band frequency response over a large range of observation angles. Transformation of these frequency responses to the time-domain produces synthesized impulse responses for the antenna as a function of observation angle. In addition, the far-field range has been upgraded to perform swept-frequency measurements. This allows synthesized time-domain impulse measurements of backlobes and measurements of antennas mounted on vehicles, measurements that are not suitable for the near-field range.

4. Waveforms

The output waveform of a linear time-invariant antenna, $y(t)$, is the convolution of the input waveform, $p(t)$, with the impulse response of the antenna, $h(t)$, i.e.,

$$y(t) = p(t) * h(t) \quad (1)$$

The impulse response is the inverse Fourier transform of the frequency response. Thus, the output waveform for an arbitrary input waveform can be computed if the frequency response of the antenna is known and converted to an impulse response.

Synthesized time-domain measurements have been made of a simple four-foot parabolic reflector antenna, a large limited field-of-view (LFOV) target engagement radar (TER) antenna, and a demonstration space-fed array. The TER is a series-fed constrained feed phased array with ferrite phase shifters. The antenna comprises 24 rows and 24 columns of element radiators with the elements spaced 3 wavelengths apart. The elements are divided into 4 quadrants that are parallel-fed, where each quadrant has a horizontal constrained waveguide that series-feeds 12 vertical constrained waveguides that each series-feeds the 12 elements on that column. The space-fed array consists of approximately 650 elements on a triangular grid with the elements spaced approximately 0.66 wavelengths horizontally and 0.38 wavelengths vertically.

Figure 5 shows the frequency domain response in the main beam of both the four-foot reflector and the TER with the beam steered to broadside over the frequency range of 12.4 to 18 GHz. The phase shifters of the TER are set to collimate the beam at approximately 14.5 GHz. It is seen that the reflector is a wideband antenna with the gain increasing with frequency. The ripples in the response are likely due to diffraction and scattering off the feed and feed struts. The TER has a much narrower instantaneous bandwidth. This is a result of the different path delays, which cause the main beam to quickly decollimate away from the collimation frequency. Actually, as we move away from the collimation frequency, the main beam splits into four beams that scan diagonally away from

boresight as the frequency increases. As the frequency increases further, these four beams move towards the center again and the beam recollimates, which explains the peak seen in the graph at 18 GHz. The space-fed array, which is collimated at 8.4 GHz, has a wideband frequency response, as shown in Figure 6, because of its small size. The multiple reflections within components and between components of the antenna have a much stronger influence on the response, whereas, for the TER the response is controlled predominantly by the array geometry.

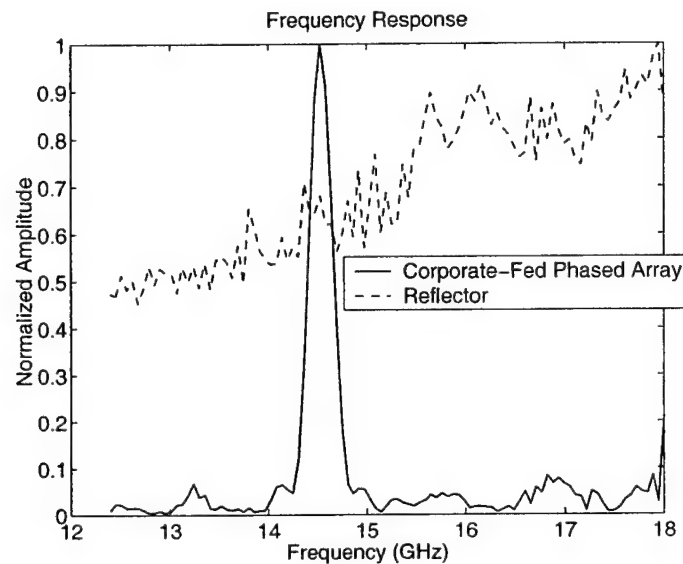


Figure 5. Frequency response of reflector and series-fed phased array

Fourier transforming the frequency response provides the impulse response of the antenna. Figure 7 shows the magnitude of the complex envelope for the main beam of the reflector and the TER. It is seen that the reflector has a very narrow impulse response. This results from the nearly identical delay times for all the radiation paths. The different path delay times for the TER produces a broadened impulse response lasting about 6 or 7 ns, which corresponds to the difference in delay times from the center elements to the outer elements of the array. Figure 8 shows the magnitude of the co-polarized and cross-polarized complex envelopes of the impulse response for the space-fed array in the main beam. Observe that the co-polarized and cross-polarized responses can have very different shapes.

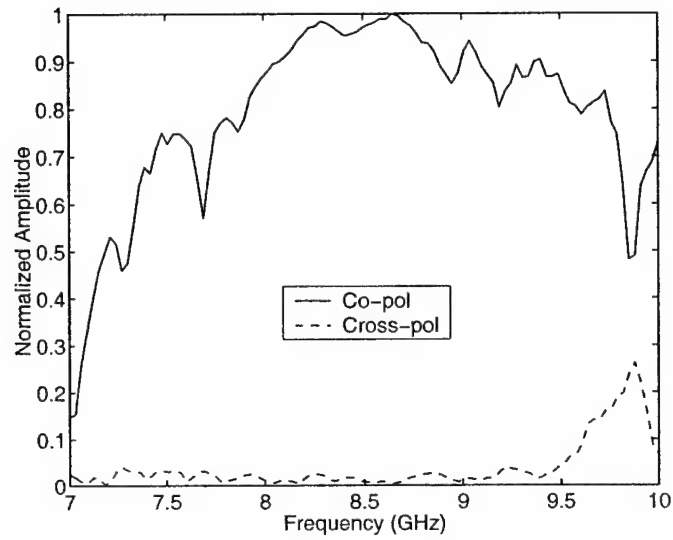


Figure 6. Frequency response of space-fed array

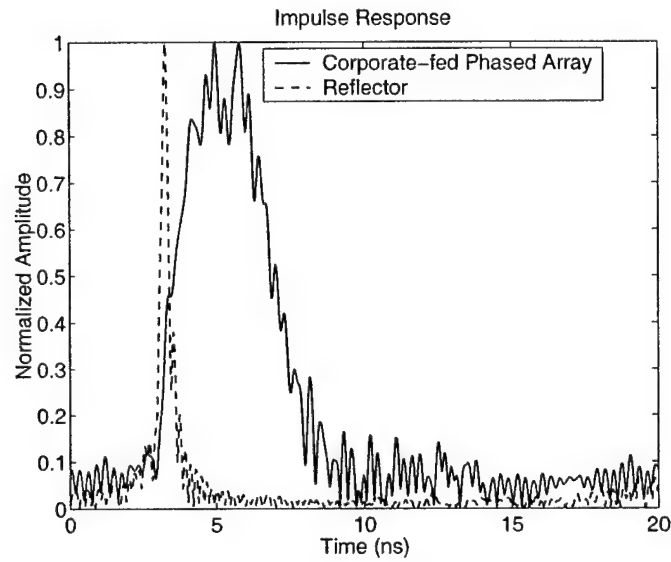


Figure 7. Main beam impulse response of reflector and TER array

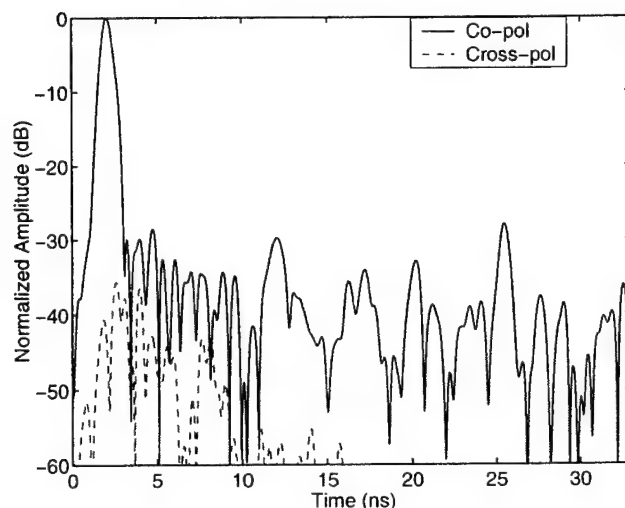


Figure 8. Main beam impulse response of space-fed array

The impulse function of an antenna changes with the angle to the field point. Figure 9 shows the measured impulse response of the TER in the sidelobe region for several different field point angles. The main beam is steered to broadside, and the impulse responses at $(Az, El) = (0.5^\circ, 0.5^\circ)$, $(1.5^\circ, 1.5^\circ)$, $(2.5^\circ, 2.5^\circ)$, and $(3.5^\circ, 3.5^\circ)$ are plotted. The shapes of the impulse responses are significantly different and produce different transmitted waveforms, as shown later. The impulse response can produce interesting transmitted waveforms in the sidelobe regions. Even in a null of the antenna pattern, a continuous (CW) pulse will have a transient spike at the beginning and end of the pulse. A linear frequency modulated (LFM) pulse is even more interesting because the angular location of the null will scan with frequency.

As described earlier, the output waveform can be determined by convolving the input waveform with the antenna impulse response. Figure 10 shows the envelope magnitude of the transmitted waveform for the reflector antenna using a step CW pulse at approximately 14.5 GHz in the main beam. Figure 11 shows the main beam transmitted waveform at the collimation frequency for the TER using both a 1 GHz and a 5.6 GHz bandwidth in the measurement of the frequency response. Note that the rise time of the pulse is much slower than for the reflector antenna. Figure 12 shows the transmitted waveform for the TER at the sidelobe angles listed above. Observe that at one angle the peak of the transient response is much larger than the steady-state response. Figure 13 shows the transmitted waveform for the space-fed antenna in the main beam, located at $(Az, El) = (-5^\circ, 0^\circ)$ and several sidelobes, located at $(Az, El) = (-6^\circ, 0^\circ)$, $(-8^\circ, 0^\circ)$, and $(-10^\circ, 0^\circ)$.

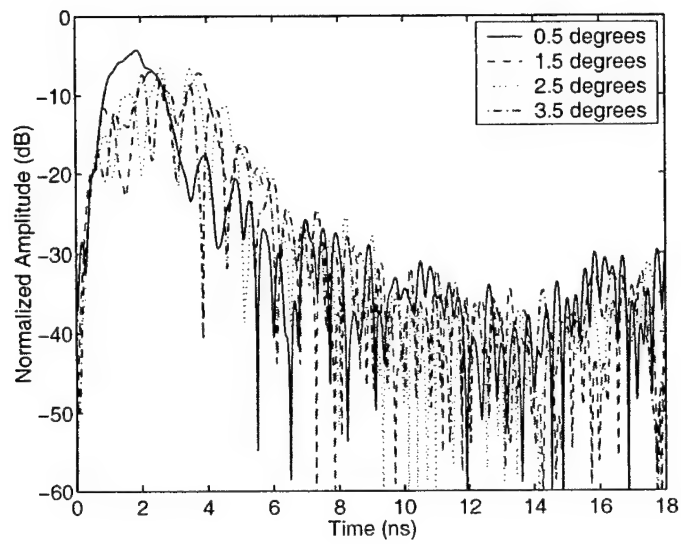


Figure 9. Sidelobe impulse response of TER array

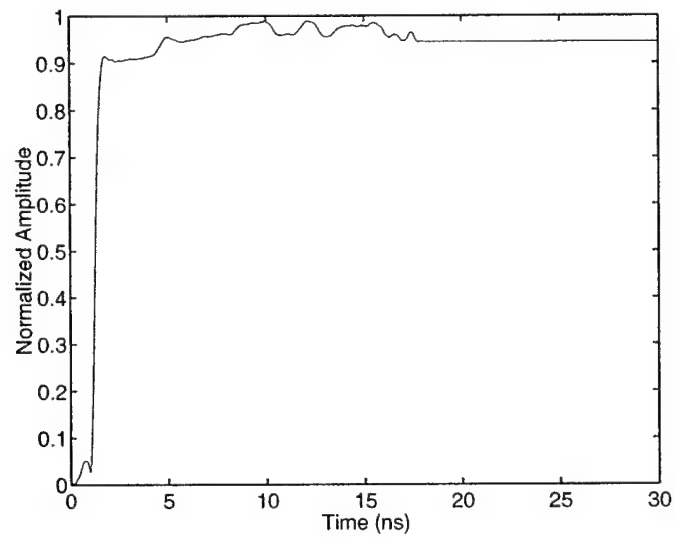


Figure 10. Transmitted waveform in main beam of reflector antenna

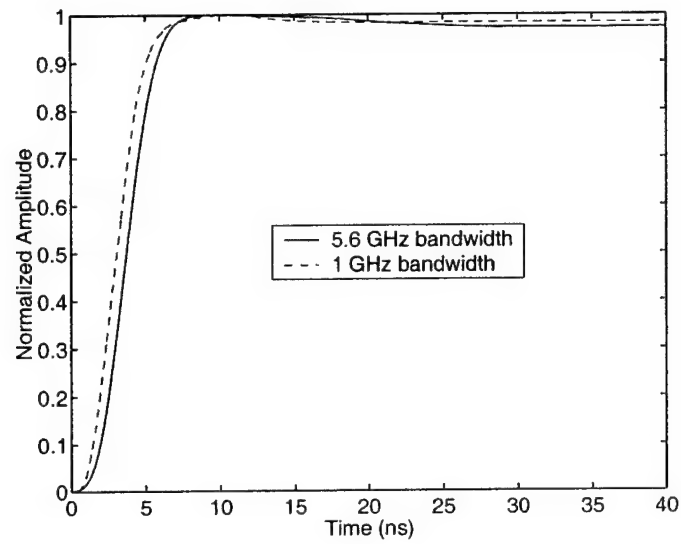


Figure 11. Transmitted waveform in main beam of TER array

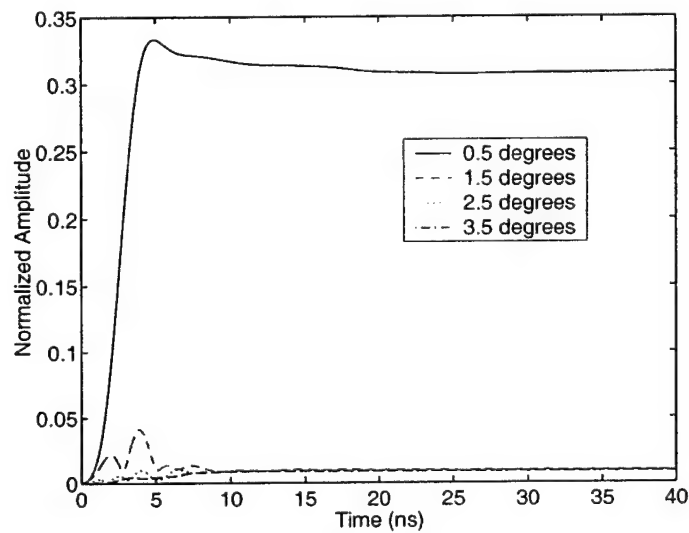


Figure 12. Transmitted waveform in sidelobes of TER array

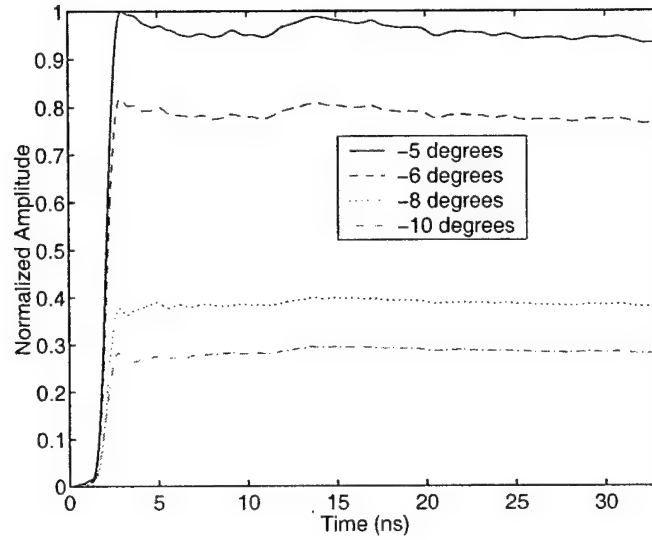


Figure 13. Transmitted waveforms in main beam and sidelobe of space-fed array

As mentioned earlier, the impulse response for the co-polarized signal and the cross-polarized signal can have significantly different shapes, which implies that the polarization content of the transmitted waveform can change as a function of time. Figure 14 shows the voltage fraction of the transmitted waveform that is co-polarized in the main beam and several sidelobes (listed above) for the TER antenna. The main beam polarization remains fairly constant, but modest changes occur at the beginning of the pulse for the sidelobes. Figure 15 shows similar data for the space-fed array for the main beam and the sidelobes listed above. For these cases, the polarization remains fairly constant. Figure 16 shows the co-polarized voltage fraction for the space-fed array at the sidelobes located at $(Az, El) = (-20^\circ, 0^\circ)$, $(-30^\circ, 0^\circ)$, and $(-40^\circ, 0^\circ)$, which are much farther from the main beam. For $(Az, El) = (-20^\circ, 0^\circ)$, the voltage fraction changes considerably at the beginning of the pulse.

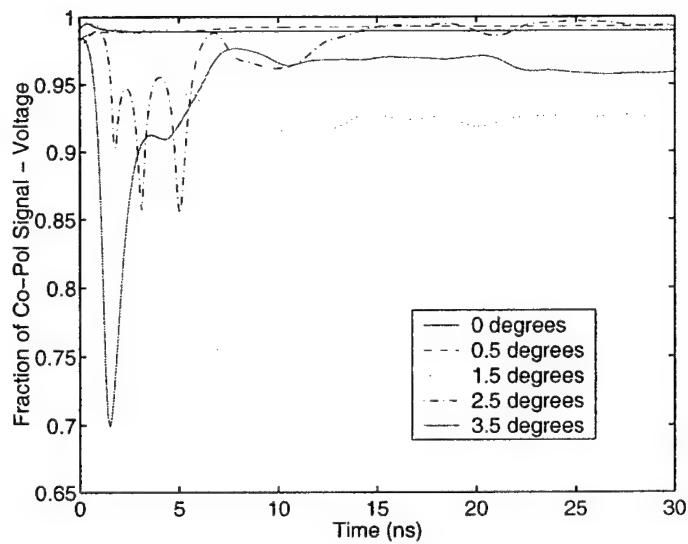


Figure 14. Fraction of co-polarized voltage in output waveforms from TER array

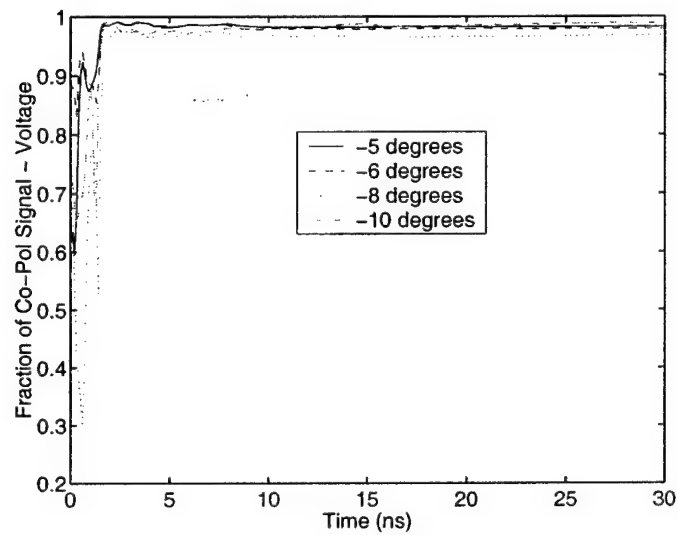


Figure 15. Fraction of co-polarized voltage in output waveforms from spaced array in and near main beam

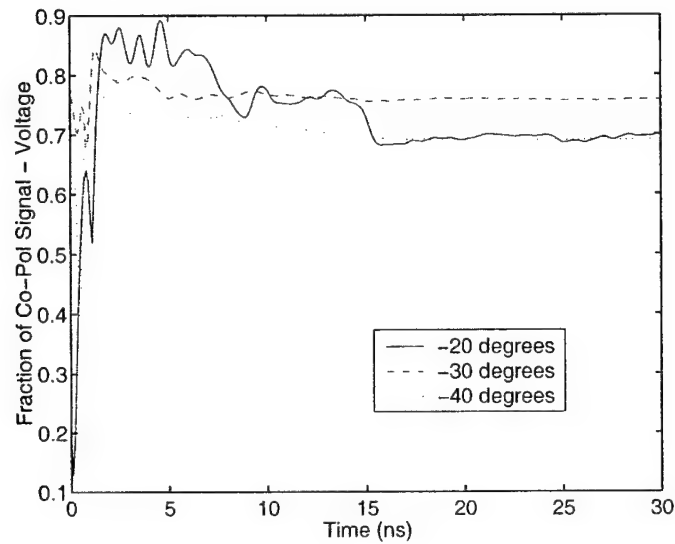


Figure 16. Fraction of co-polarized voltage in output waveforms from space-fed array in far sidelobes

5. Sidelobe Canceller

The sidelobe canceller (SLC) is a form of adaptive beamformer that uses a weighted combination of one or more auxiliary antennas to cancel jammers in the sidelobes of the main antenna pattern. Figure 17 shows a schematic diagram of the sidelobe canceller.

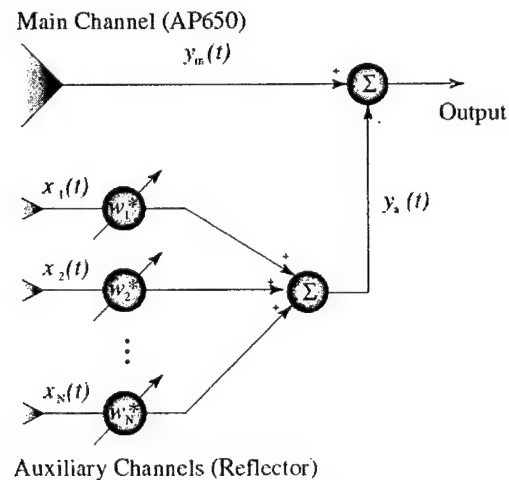


Figure 17. Sidelobe Canceller

The values of the weights that are applied to the auxiliary channels are determined by

$$\mathbf{w}_{\text{aux}} = \mathbf{R}_{\text{aux}}^{-1} \mathbf{r}_{\text{ma}}, \quad (2)$$

where

$$\begin{aligned} \mathbf{R}_{\text{aux}} &= E[\mathbf{x}_{\text{aux}} \mathbf{x}_{\text{aux}}^H], \\ \mathbf{r}_{\text{ma}} &= E[\mathbf{x}_{\text{aux}} y_m^*], \end{aligned} \quad (3)$$

and

$$\mathbf{x}_{\text{aux}} = \begin{bmatrix} x_1 \\ x_2 \\ \vdots \\ x_N \end{bmatrix}, \quad (4)$$

and the other variables are shown in Figure 17.

To support wider bandwidths, transversal filters can be used in each auxiliary channel to adaptively control the frequency response as well as the spatial response of the antenna, as shown in Figure 18. Each weight in the transversal filter for a particular channel will be referred to as a tap.

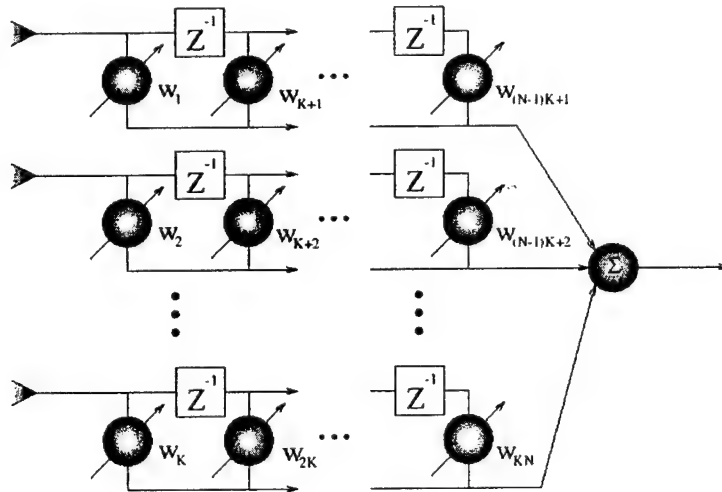


Figure 18. Transversal filter

In order to evaluate the impact of the antenna frequency response on a conventional sidelobe canceller, an example case was run using the space-fed array as the main channel and the reflector model as an auxiliary. The aperture radius of the parabolic reflector was set to 3.14 cm to produce a broad pattern suitable for use as an SLC auxiliary. In the examples that follow, a 40 dB jam-to-noise ratio (JNR) jammer was located at (Az, El) = (30°, 0°), and the space-fed array main beam was steered to (Az, El) = (-5°, 0°). Figure 19 shows an azimuth cut of the antenna patterns of the space-fed array and the reflector at the center frequency of 8.4 GHz. Consider a narrowband jammer with energy concentrated at the center frequency, then an SLC with a single auxiliary will produce an antenna pattern frequency response shown in Figure 20. In the plot, the solid curve is the response of the space-fed array without SLC, the dotted curve is the response of the weighted auxiliary, and the dashed-dotted curve is the composite SLC response. Note that in the SLC response, a null is produced at the frequency of the jammer. A performance metric that will be used here to measure the amount of jammer cancellation by the SLC is the cancellation ratio, CR, which is defined as the ratio of the jammer power at the output of the space-fed array with SLC to the jammer power at the output of the space-fed array without SLC, i.e.,

$$CR = \frac{P_j \text{ (with SLC)}}{P_j \text{ (without SLC)}}$$

For the case shown in Figure 20, the cancellation ration was -32.8 dB.

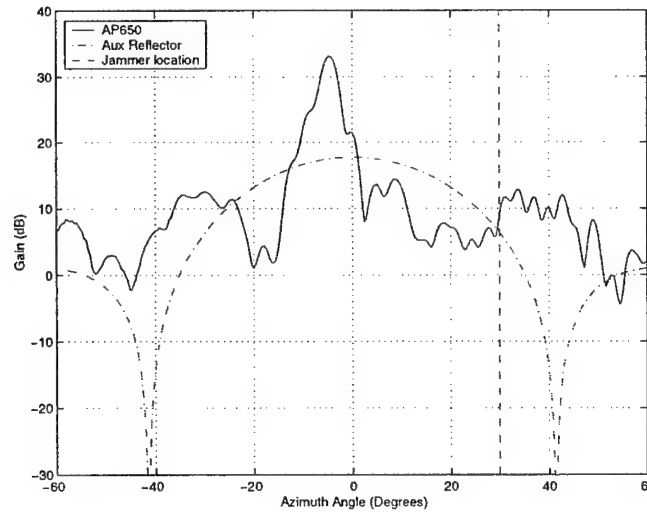


Figure 19. Space-fed antenna and reflector antenna patterns

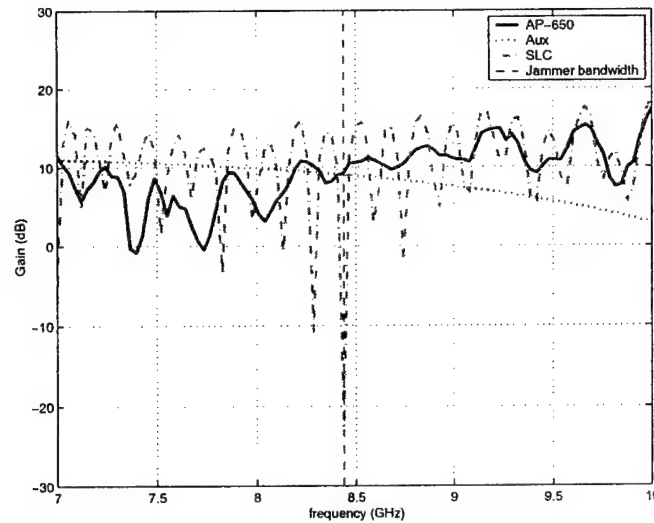


Figure 20. Antenna pattern frequency response in jammer direction (one tap, one auxiliary)

To evaluate the impact of the antenna frequency response on the SLC, the jammer bandwidth was increased to 0.06 GHz. Figure 21 shows that for a single auxiliary with a single tap weight, the SLC is only able to achieve a shallow null over the jammer bandwidth, and the cancellation ratio was only -1.4 dB. Figure 22 shows the SLC performance when the number of auxiliaries is increased to three with two tap weights per auxiliary channel. In this case, a deeper null is maintained across the jammer bandwidth for a cancellation ratio of -12.8 dB. Note that the gain of the SLC response outside the jammer bandwidth has increased, which will result in greater thermal noise power; however, this increase in thermal noise is more than offset by the reduction in jammer power.

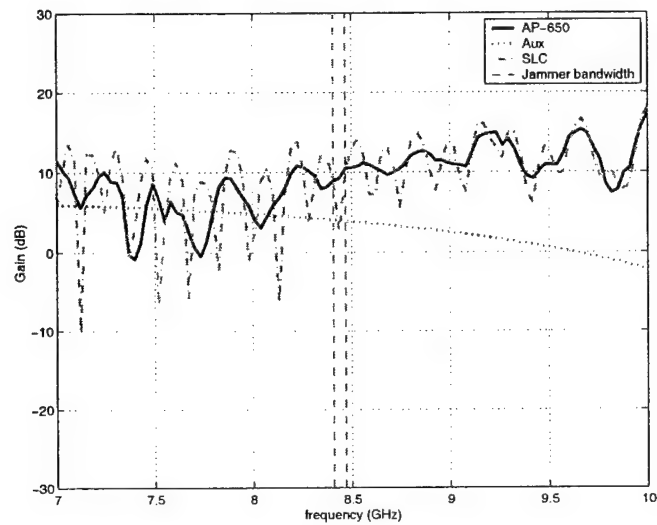


Figure 21. Antenna pattern frequency response in jammer direction (one tap, one auxiliary)

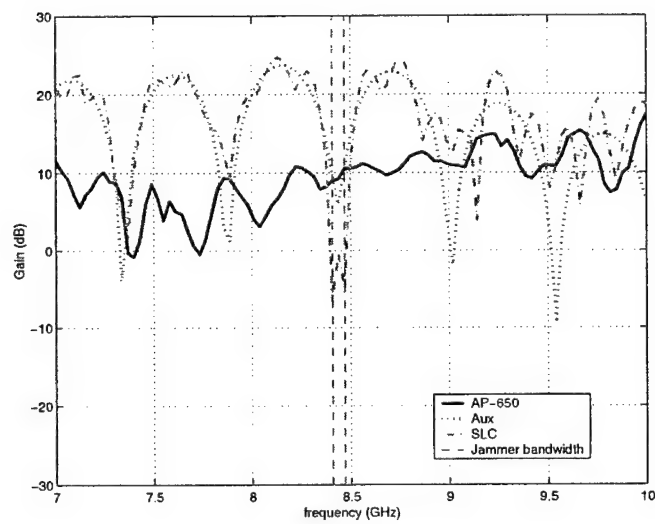


Figure 22. Antenna pattern frequency response in jammer direction (two taps, three auxiliaries)

Figure 23 shows the CR performance of the SLC as a function of the number of taps and parameterized by the number of auxiliary channels for the narrowband jammer case. Cancellation performance improves dramatically with an increasing numbers of taps or similarly with an increasing numbers of auxiliaries. For a single jammer, adding auxiliaries is similar to adding taps where the amount of delay is given by the propagation delay from one auxiliary to the next. In effect, the extra spatial degrees of freedom due to the additional auxiliaries are being utilized as temporal degrees of freedom to help control the frequency response at the jammer location. If additional jammers were introduced at other angles of arrival, then these auxiliaries would be called upon to generate spatial nulls at the angles corresponding to those jammers.

The cancellation performance for the medium band case (0.06 GHz jammer bandwidth) is shown in Figure 24. The SLC has more difficulty canceling the jammer over the wider bandwidth. Adding one auxiliary produced a significant improvement in performance, but adding more auxiliaries beyond that produced little additional improvement. In fact, for more than two taps per channel, the two Aux SLC provided slightly better performance than the three Aux SLC.

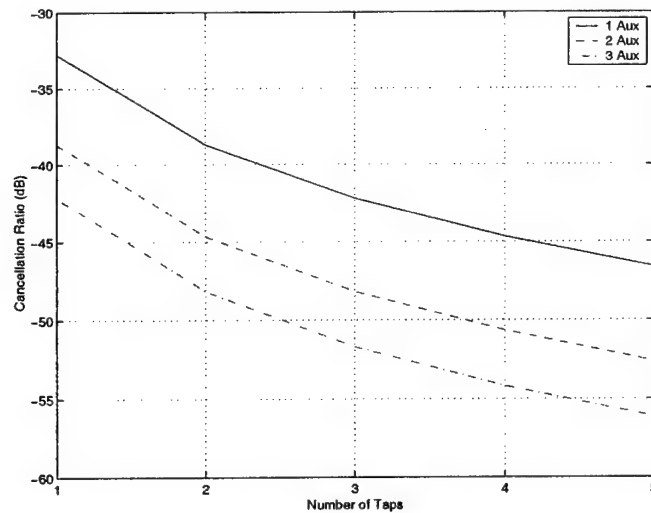


Figure 23. Cancellation ratio versus number of taps for narrowband jammer

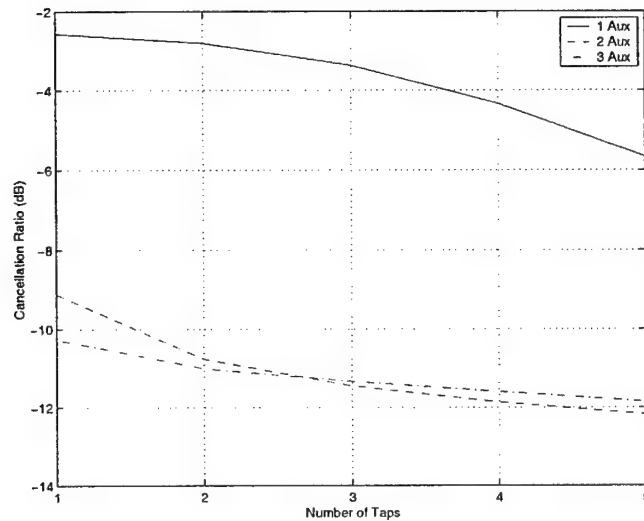


Figure 24. Cancellation ratio versus number of taps for medium band jammer

From this analysis, it is apparent that the antenna frequency response has a significant impact on the performance of an SLC. Knowledge of the antenna frequency response will be crucial in predicting the performance of an SLC in radar systems. These preliminary results show how the cancellation performance depends on the number of auxiliary channels and the number of taps in each channel. In this study, the effects of the receiver have been neglected; therefore, future work might include an evaluation of the aggregate effects of the antenna and receiver frequency responses. In addition, the effects of the cross-polarization on cancellation have been ignored because the idealized reflector model generated a negligible cross-polarization response. If measured data were collected on some auxiliary-type antennas, then a full polarization analysis could be performed.

6. Conclusions

All antenna architectures are designed to produce a radiated wave in a given direction, but the differences in the implementation can produce significant differences in the time-domain response of the antenna. These responses will vary with the beam-scanning angle of the antenna and with observation angle. Reflector antennas have relatively simple impulse responses that will not induce noticeable changes to transmitted or received waveforms. However, as indicated above, phased array antennas can have complex and extended impulse responses

that have the potential to modify the transmitted or received waveforms in significant ways.

7. References

- [1] D. A. Leatherwood, et al., "Time-Domain Properties of Phased Array Antennas," IEEE International Conference on Phased Array Antennas and Technology, May 20-26, 2000, Dana Point, California.
- [2] D. A. Leatherwood, et al., "Comparison of Time-Domain Responses of Reflector and Phased Array Antennas," *IEEE Antennas and Propagation Society International Symposium*, July 16-20, 2000, Salt Lake City, Utah.
- [3] R. C. Hansen, "Short-pulse excitation of reflector antennas," *IEE Proceedings-H*, vol. 139, No. 1, February 1992.
- [4] R. C. Hansen and E. Kramer, "Correction to 'Short pulse excitation of reflector antennas'," *IEE Proceedings-H*, vol. 139, No. 1, February 1992.

Wideband Digital Subarray Beamforming Using True Time Delay Steering at the Element Level

Mark G. Parent, James J. Alter, Ray Pickles, J.B.L. Rao, Jeffrey O. Coleman
and Dan P. Scholnik
Naval Research Laboratory
4555 Overlook Avenue, SW
Washington, DC 20375

ABSTRACT

The ability to implement digital beamforming at each element of a phased array antenna system depends mainly on the architecture used to obtain and process the data from the array. For large phased array antennas, the amount of processing required is overwhelming and is currently unfeasible even with today's computing capabilities. The use of phase shifters at the element level and digital beamforming at the subarray level reduces the amount of digital receivers required but places a limit on the useable bandwidth of the array due to frequency squinting effects. This paper will describe a wideband beamforming concept that combines analog True Time Delay (TTD) steering at the element level and digital TTD beamforming following each of 16 subarrays. The antenna array is designed to operate over a 1 – 4 GHz bandwidth, with each subarray consisting of 36 flared notch radiating elements on a rectangular grid with inter-element spacing of 1.8 inches. Each subarray incorporates six, 6-bit TTD networks using Surface Mount (SM) GaAs switches, 5-bit SM digital attenuators and 6-way Wilkinson power dividers. The digital beamformer is designed using Field Programmable Gate Array (FPGA) technology and is capable of operating over a 400 MHz instantaneous bandwidth with an A/D sampling rate of 1 GHz. The design and various concepts of this phased array system will be discussed as well as some preliminary performance measurements from the antenna system.

1.0 INTRODUCTION

The ability for a phased array to operate over a wide instantaneous bandwidth requires both the elements and the beamformer to have characteristics that maintain their beam integrity over the required bandwidth. In the case of the antenna element, VSWR characteristics and pattern shape (no multimode) are optimized over the operating bandwidth, while the beamformer used behind the elements typically incorporate some method of true-time delay to reduce the effects of beam squint. A standard method to minimize the required time-delay circuitry requires separating the array into discrete subarrays, where each subarray is dimensioned according to the bandwidth of the system [1]. Even though the subarray utilizes phase shifters (no time delay) in its beamformer, the subarray is dimensioned such that the beam squint due to the subarray is less than a quarter of the 3 dB beamwidth [2]. The subarrays are then coupled using a series of true time delay switched cable networks or, more recently, utilize modern optical techniques to provide for the correct time delay between each subarray [3]. In either case, the effect of phase shifters at the element level can cause large sidelobes for wideband signals in addition to some degree of beam squint. To eliminate these effects, analog true-time delay has been implemented at the element level in each subarray while digital true-time delay has been implemented at the subarray level. The purpose of this paper is to discuss the use of analog true time delay steering at the element level while implementing wideband Digital Beamforming Techniques at the subarray level. Therefore, the paper is broken up into two distinct parts; the first 7 sections discuss the analog components of the array while the last 3 sections discuss the digital aspects of the array.

2.0 ARRAY DESIGN OVERVIEW

The array being developed consists of 576 active receive elements which are configured as sixteen, 36 element subarrays. The array is designed to operate over a 1 – 4 GHz bandwidth and have an instantaneous bandwidth of 400 MHz. Each subarray consists of 36 wideband, horizontal polarized elements that are placed on a 6 x 6 rectangular lattice with 1.8 inch interelement spacing. The 1.8-inch interelement spacing allows for 60 degree (azimuth or elevation plane) scanning at the highest frequency (4 GHz) without introducing any grating lobes. The 36-element layout (including TTDs and power dividers) is shown in Figure 1. The front view of the array, showing its general shape, is shown in Figure 2. The array is constructed from individual boards that contain 6 wideband elements, 36 TTD circuits, 6 RF amps, 6 digital attenuators, a 6-way power divider and the associated

digital switching logic. Figure 3 displays both the entire array and the RF receivers. Each of the subarrays is connected to an RF receiver through a series of phase-matched cables as seen in Figure 3.

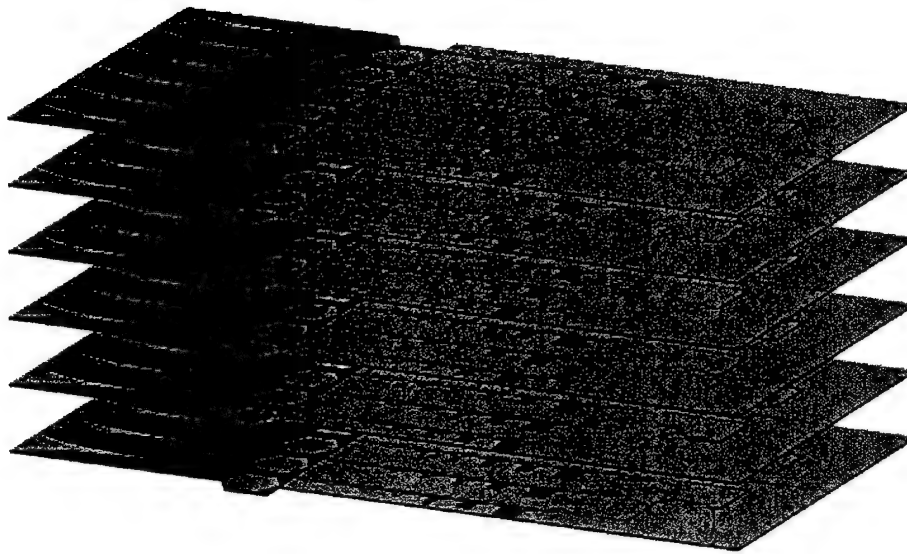


Figure 1. 36-element subarray

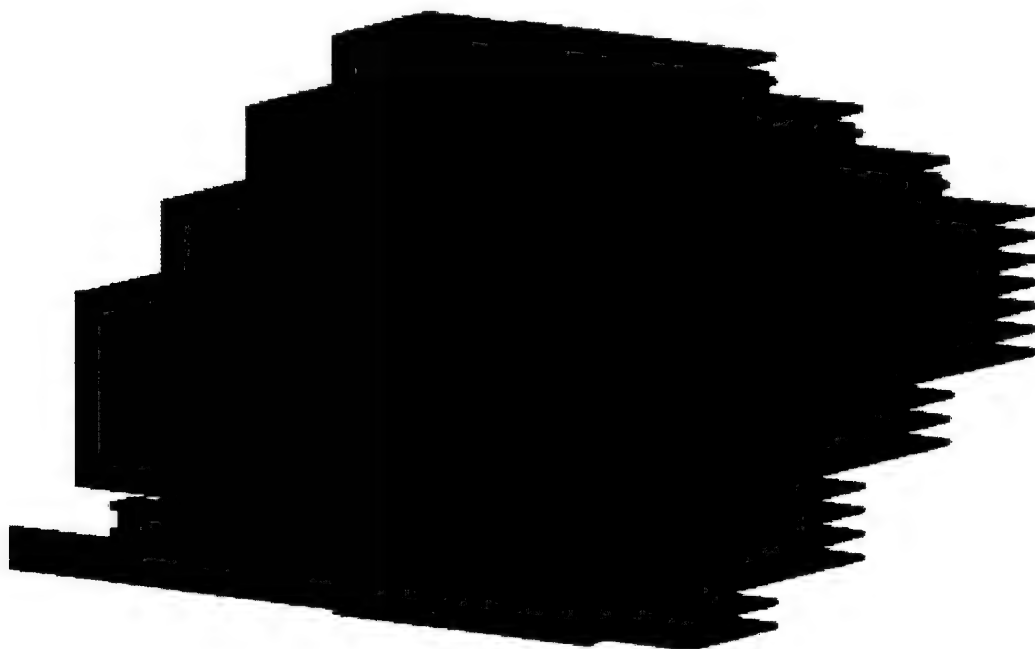


Figure 2. 576-element array outline

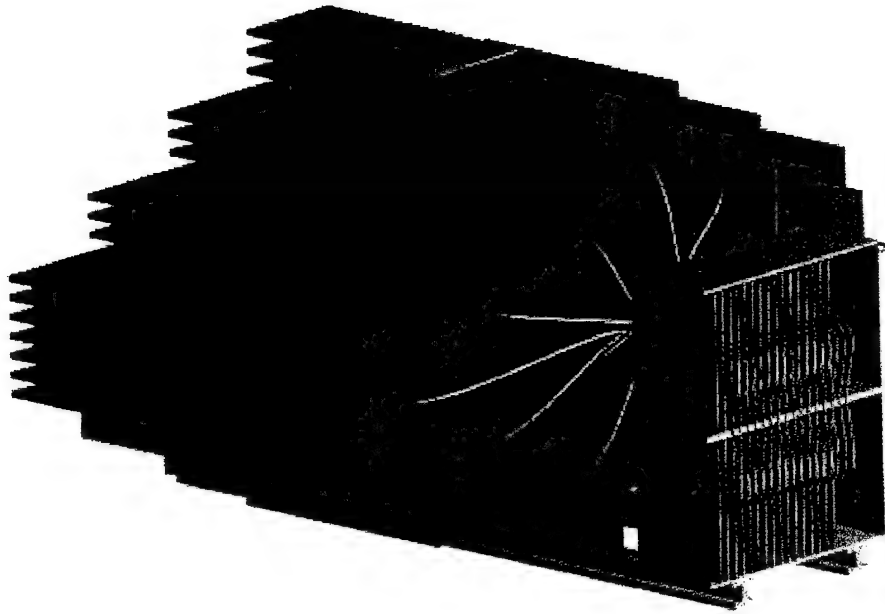


Figure 3. 576 element 1- 4 GHz phased array antenna
with digital receivers displayed

3.0 SUBARRAY - TTD DESIGN

Because of the cost and complexity of placing an A/D device behind each of the 576 elements, 16 subarrays with 36 elements each are used. Behind each element is a 6-bit switched line TTD, a 5-bit digital attenuator for amplitude control and a broadband MMIC amplifier. Figure 4 shows a drawing of a typical delay line used on the board. Figure 5 shows a prototype delay line with its delay paths highlighted for clarity. Each delay bit has associated with it two SPDT surface-mount GaAs switches. The switches are

configured to have either a through path or a specified delayed path. For the subarray size chosen, the total delay required, to allow for scanning in both planes (60 degrees azimuth, 60 degrees elevation), requires slightly less than 1 nsec of delay. Each subarray card utilizes coplanar waveguide techniques to facilitate the mounting of the electronics components required on each card. Each card consists of a mutli-layer circuit board comprised of a single layer of Taconic RF35 material and a single layer of FR4 material. All RF components

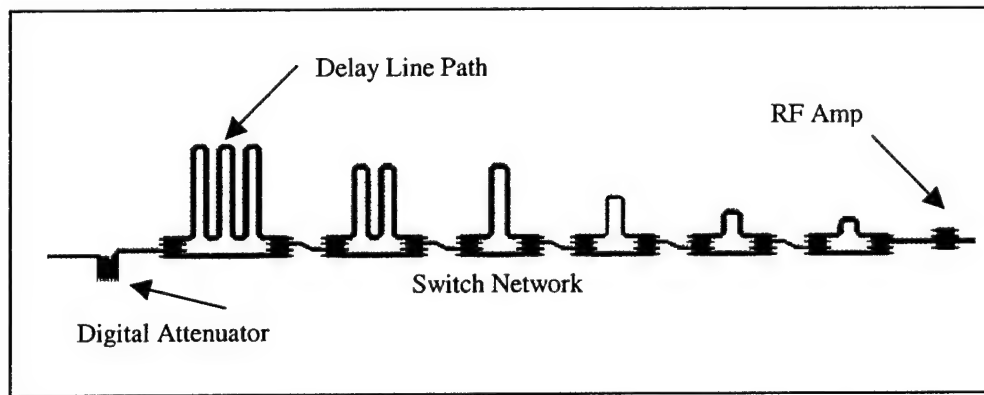


Figure 4. TTD circuitry

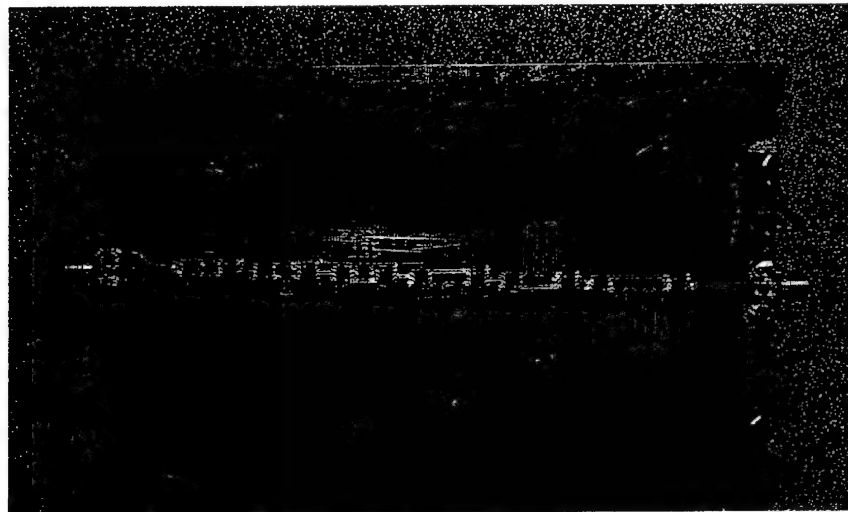


Figure 5. Prototype delay line

and circuitry are made on the Taconic board while all DC and switching signals are routed through the FR4 board. Figure 6 shows the DC connections to the TTD circuit. The switch that is currently used in the TTD circuit is an ITT C02AB (discontinued) distributed by GASTEK (now MACOM).

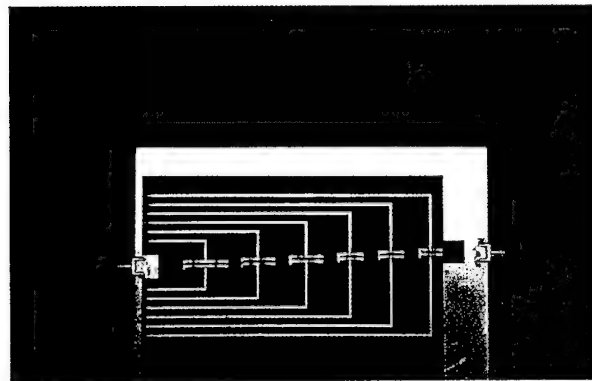


Figure 6. Prototype board showing DC connections to switching network

A 6-bit prototype TTD circuit was designed using Touchstone™ and was constructed using AUTOCAD™ and Camtastic™ software. Computed and measured values of the delay for various bit states are given in Table 1. The measured delays are calculated from the slope of the phase data shown in Figure 7. All measured delays were slightly longer than what was designed for, possibly due to the inclusion of microstrip bends instead of coplanar waveguide bends. This was due to the limitation of the Touchstone™ software. A second prototype is being designed using ANSOFT™ HFSS to model the coplanar waveguide bends more accurately.

Table 1. Measured and calculated delay for the TTD circuit

Bit State	Calculated Delay (psec)	Measured Delay (psec)
1	15	23.9
2	30	39.7
3	60	68.8
4	120	169
5	240	288
6	480	511

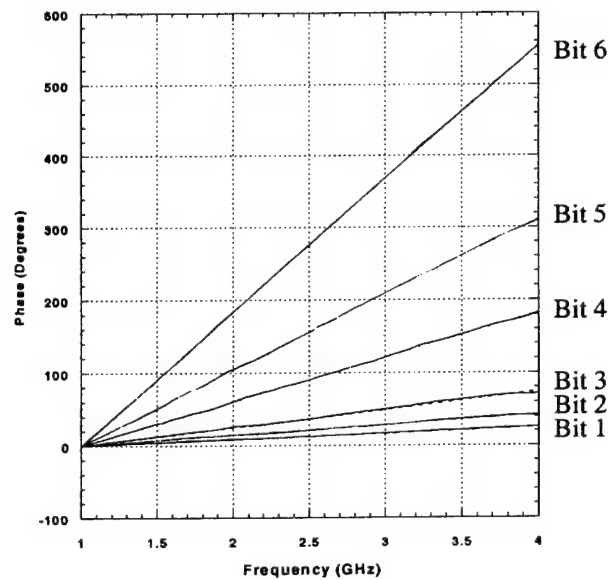


Figure 7. Phase delay plot

To provide amplitude control for aperture weighting and calibration, a broadband GaAs digital attenuator is incorporated at each element. This attenuator is a Hittite model HMC306MS10 with 5 bits and 1 dB LSB. Typical characteristics (less insertion loss) are shown in Figure 8 for various bit states. An improved version of this attenuator (HMC306MS10), which has less insertion loss and a 0.5 dB LSB is available in September 2000 and will be incorporated into the final array.

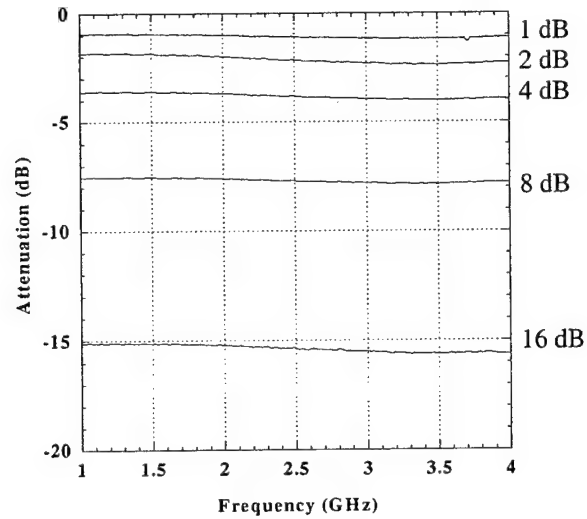


Figure 8. Attenuator amplitude vs. frequency

4.0 ELEMENT DESIGN

The element design is based on a rectangular spacing of 1.8 inches in both planes and utilizes a flared notch construction that incorporates a double Y balun to transform from a coaxial input to a slot radiator. The 6-element array is shown in Figure 9 and the details of the balun are shown in Figure 10.

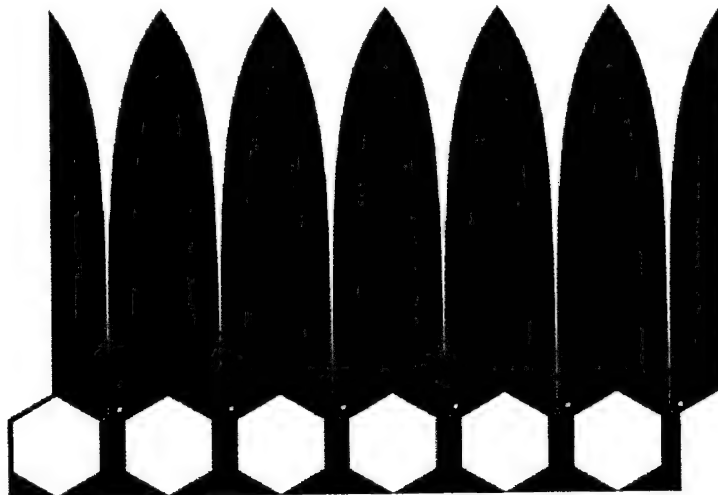


Figure 9. 6 wideband flared notched elements

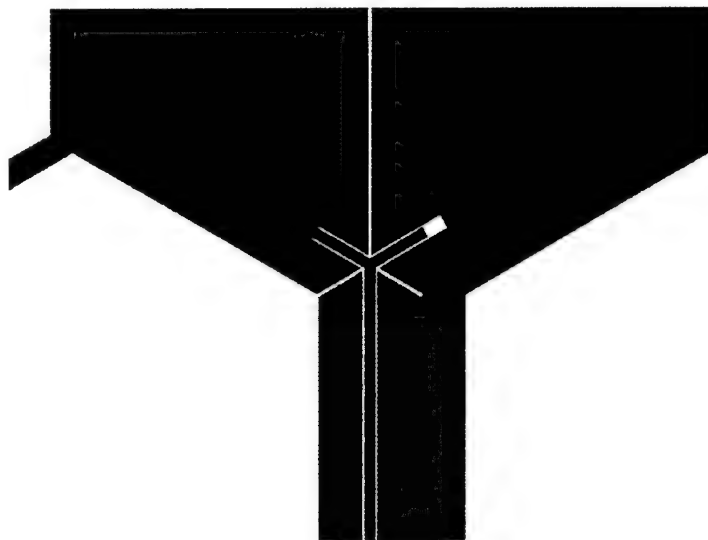


Figure 10. Closeup view of the double Y balun

The design of the double Y balun was developed using Ansoft™ HFSS software; their respective VSWR and transmission plots are shown in Figures 11 and 12. To model the performance of the double Y balun, two baluns were modeled back to back as shown in Figure 13. The transmission data presented in Figure 12 represents the transmission through two baluns. Therefore, the actual loss of a single balun is half of what is shown in Figure 12.

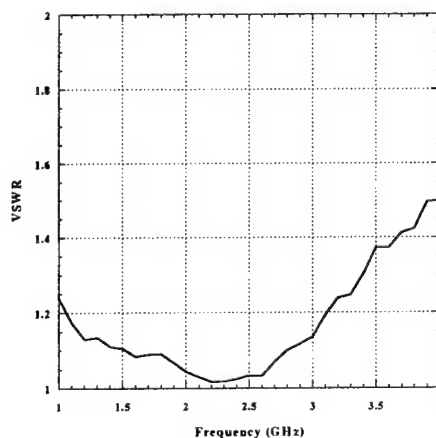


Figure 11. Calculated input VSWR of a double Y balun

Since the design of the wideband element requires 6 elements to be fed actively to incorporate the mutual coupling effects, active VSWR measurements are not possible at this time. The only 6-way power divider available at these frequencies is a Wilkinson power divider, which gives good results even when the output of the divider is terminated in open/short circuit. To estimate the VSWR of the balun transition, a network analyzer is used in the time-domain mode to display the effective VSWR. Figure 14 shows the time-domain plot over the 1-4 GHz frequency range. Using gating techniques available on the network analyzer, the VSWR vs frequency is plotted in Figure 15. The first reflection shown in Figure 14 is due to the balun and has a return loss of -20 dB. This corresponds to a VSWR of 1.2:1 (averaged over the 1-4 GHz frequency range) and matches the average calculations presented in Figure 11. The second response is that of the element transition to free space. The return loss of -10 dB represents an averaged VSWR of 2.0:1, which is typical for this type of antenna element.

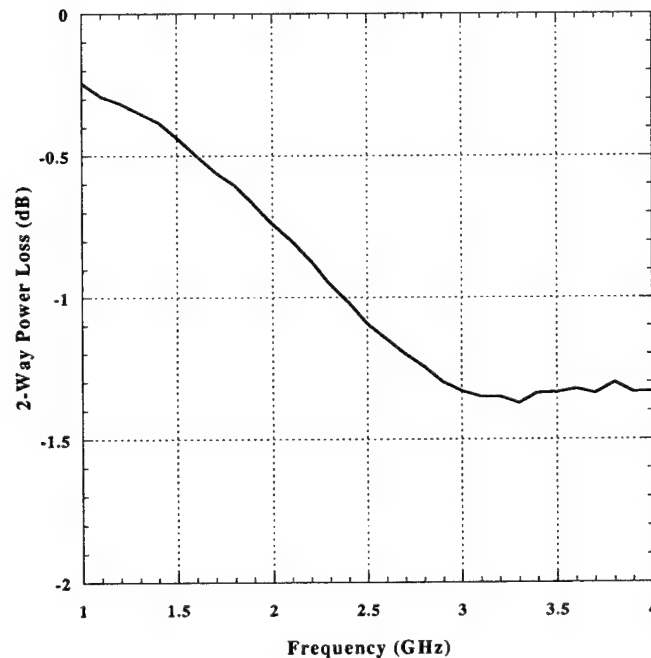


Figure 12. Calculated transmission loss for back-back double Y baluns

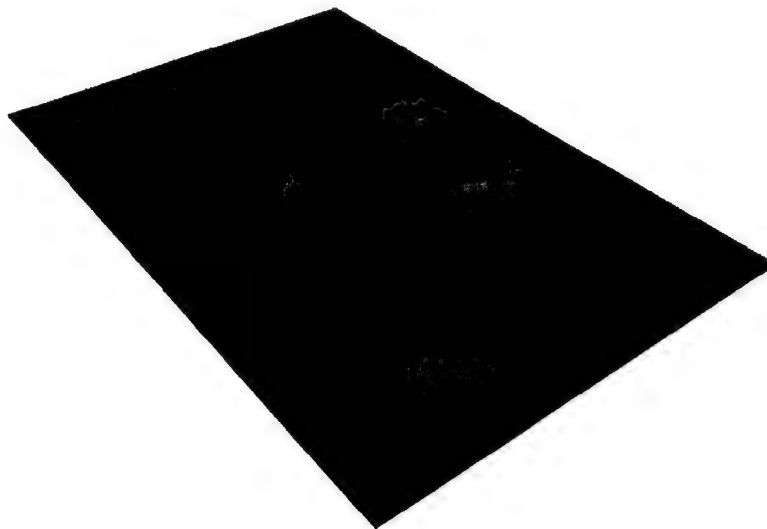


Figure 13. Back to back double Y balun configuration

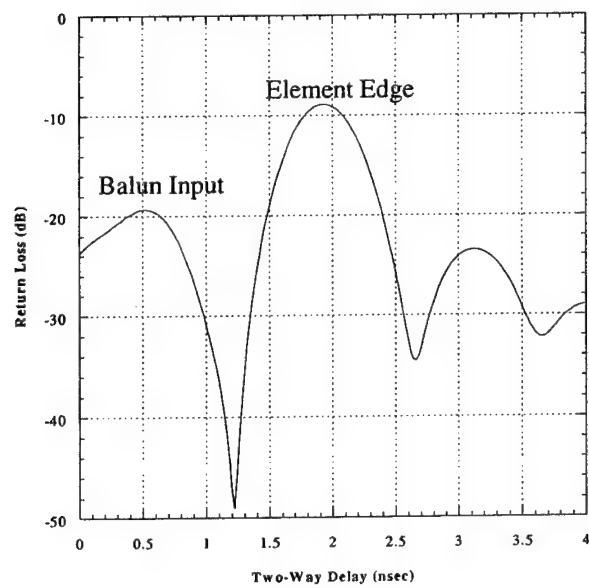


Figure 14. Time response of antenna / balun

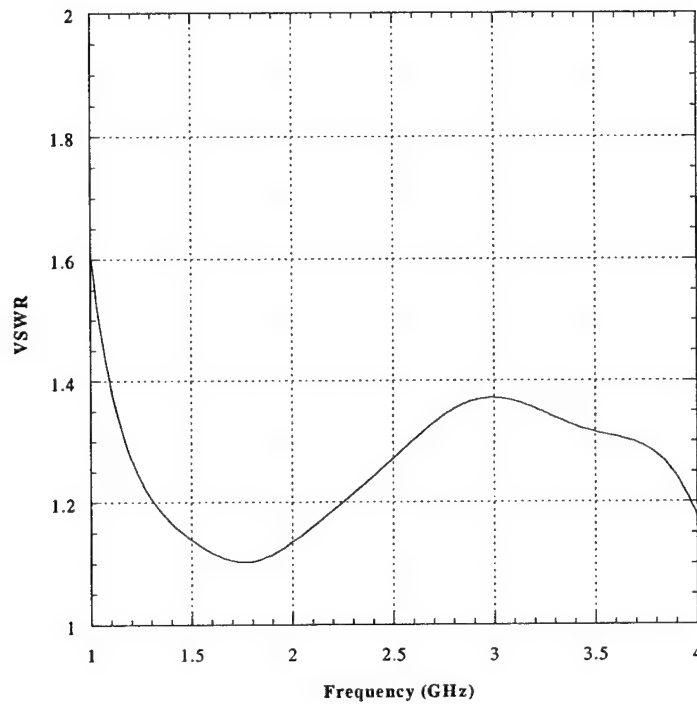


Figure 15. VSWR of balun input

5.0 6-WAY POWER DIVIDER DESIGN

The 6-way power divider in Figure 16 was designed using the Touchstone™ software package. Since our current version of Touchstone™ doesn't model co-planar waveguide bends, microstrip bends were utilized instead. The power divider is based on a Wilkinson design that utilizes

resistors in each line to isolate each channel output. In this design 200-ohm and 100-ohm resistors were used. The power divider is constructed to provide equal amplitude and delay across each of the six output ports. Figures 17 and 18 show the relative amplitude and phase plots for the measured response of the divider. Figure 19 shows the prototype divider with a 6-element array attached.

Measurements show that the outer two ports are unbalanced in amplitude by 0.5 dB and differ in electrical line length by approximately 0.3 inches. A new design, using ANSOFT[™] HFSS to model the co-planar waveguide bends, is currently being developed.

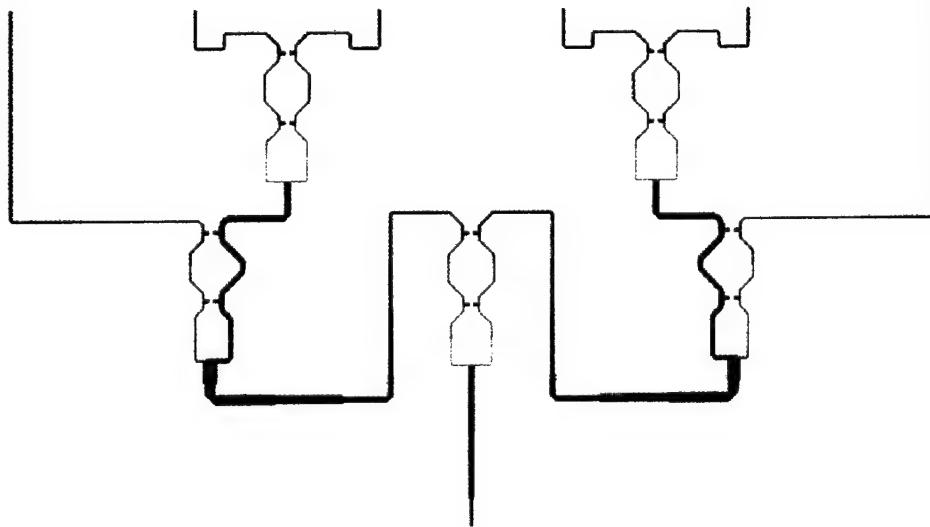


Figure 16. 6-way Wilkinson power divider

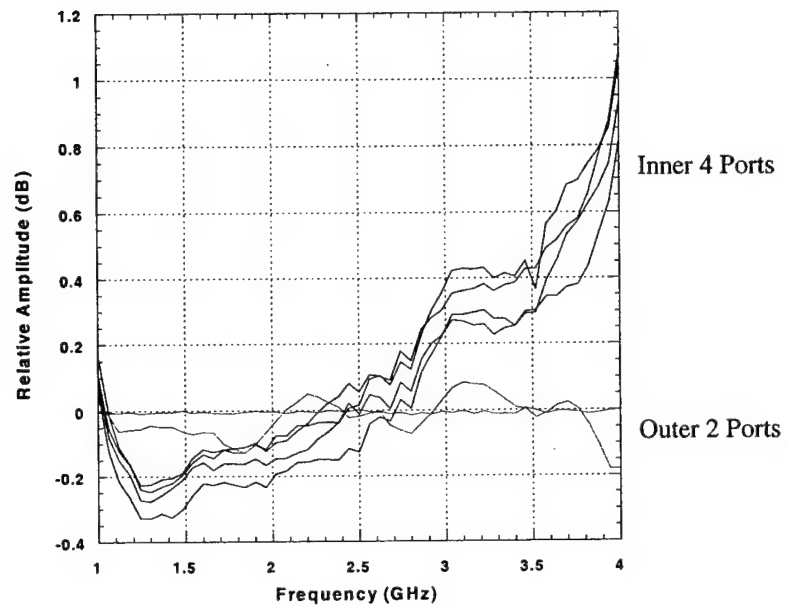


Figure 17. Relative amplitude vs frequency for the 6-way power divider

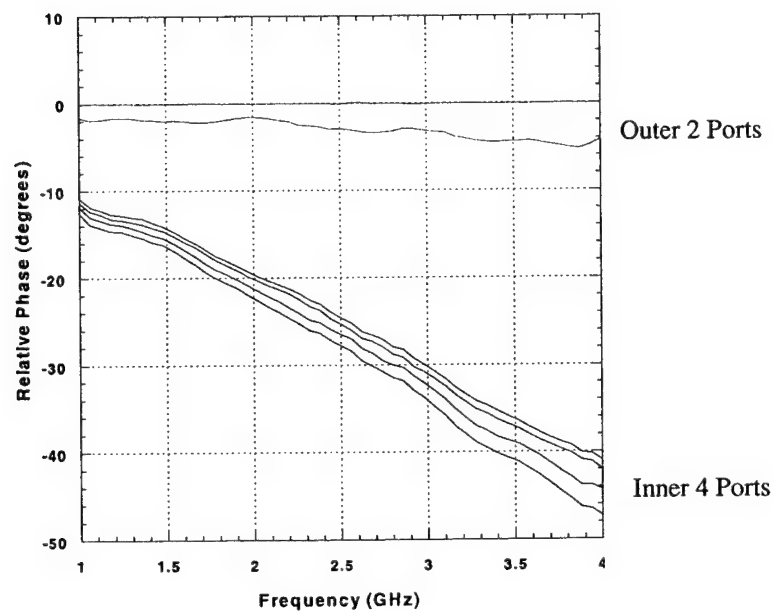


Figure 18. Relative phase vs frequency for the 6-way power divider

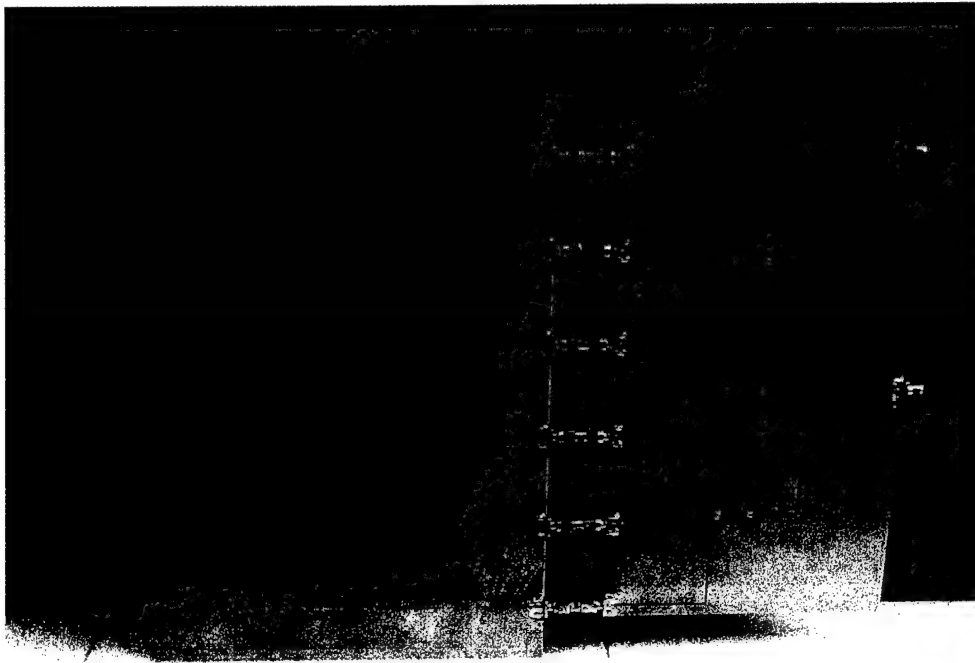


Figure 19. 6-way power divider with 6-element array attached

6.0 MEASURED PATTERNS

A series of pattern measurements were made on the 6-element array and are shown in Figures 20 – 22. The array was configured with the power divider, as shown in Figure 19, and measurements of the H-plane and E-plane patterns were taken. Also shown is the cross polarization patterns taken in the E-plane (Figure 22). The measurements were taken in the NRL Compact Range Facility over a 2 – 4 GHz range. Both the E-plane and H-plane plots show representative patterns for this type of antenna element. The cross polarization patterns show levels between 20 and 25 dB at broadside.

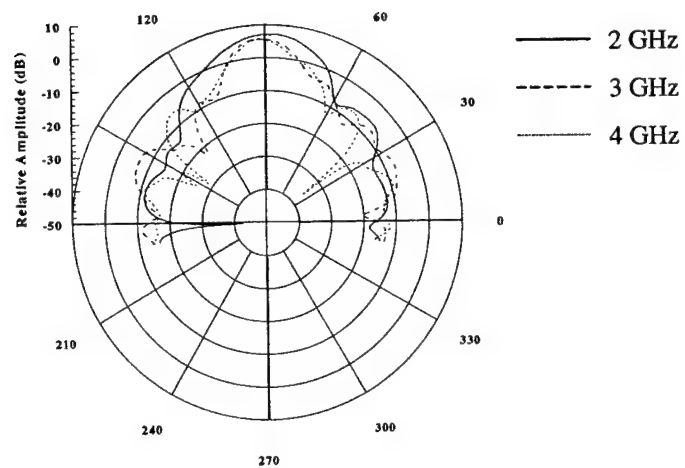


Figure 20. Co-polarization E-plane plots for 2,3 and 4 GHz

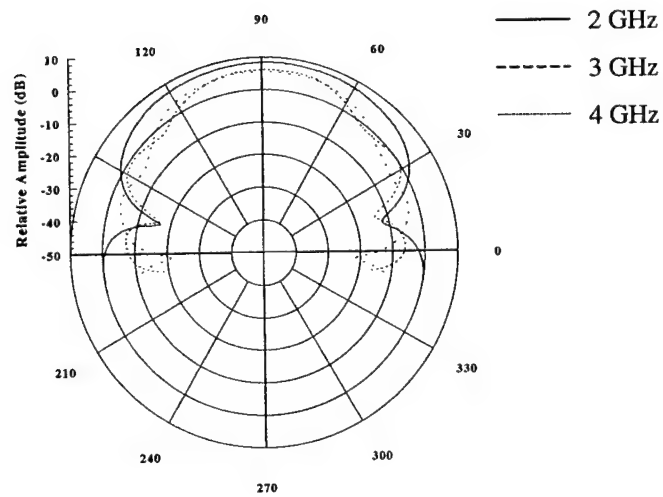


Figure 21. Co-polarization H-plane plots for 2,3 and 4 GHz

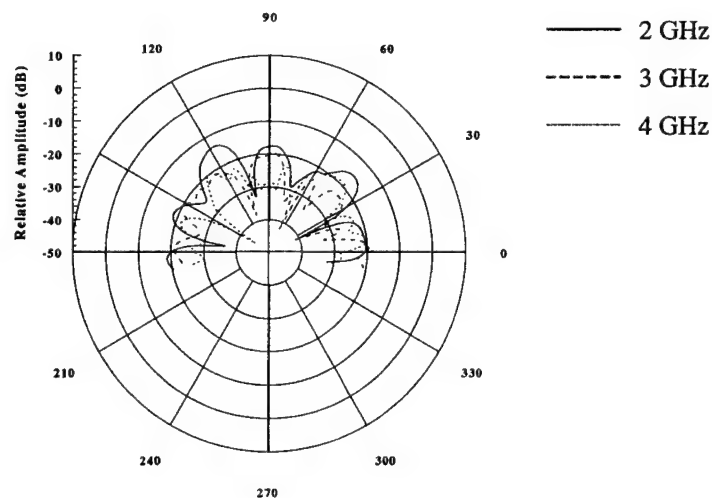


Figure 22. Cross-polarization E-plane plots for 2,3 and 4 GHz

7.0 RF RECEIVER DESIGN

The double-conversion receiver design is shown in Figure 23. The RF input is first upconverted to 8.7 GHz by LO 1 and then downconverted by LO 2 to produce a signal centered at 750 MHz IF with a 400 MHz bandwidth. This signal is then routed to an analog-to-digital (A/D) receiver in the digital processor. Figure 24 shows the prototype RF receiver.

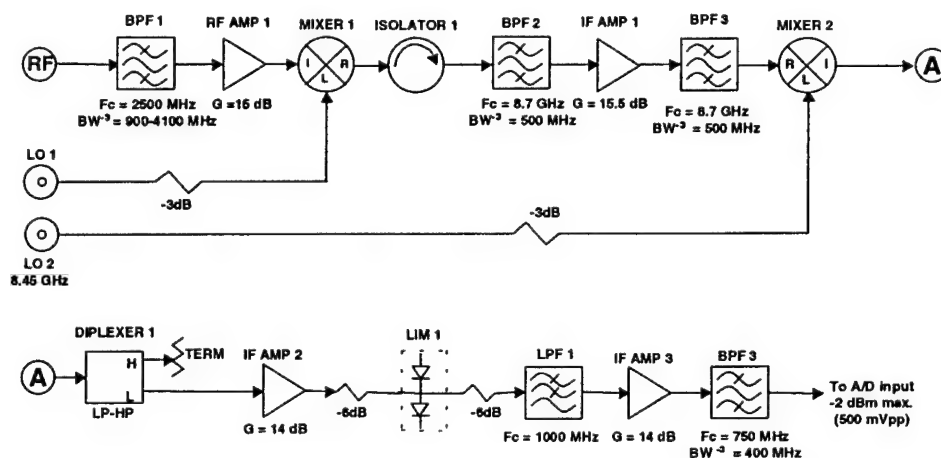


Figure 23. Double conversion receiver design

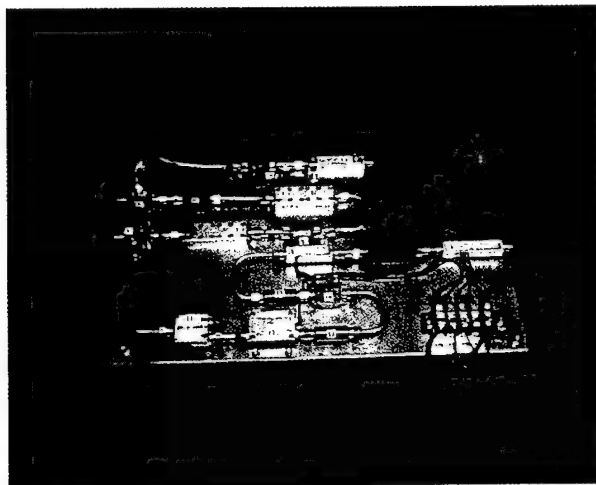


Figure 24. Prototype receiver layout

8.0 DSP FILTERING AND DEMODULATION STRATEGY

Figure 25 contains a series of frequency-domain plots that show the stages through which the signal is transformed as it passes through the DSP portion of the system, which is depicted in Figure 26. The analog IF is first sampled at a 1 GHz rate. Equalization filtering and time-delay filtering, both of which can be designed with second-order cone-programming techniques [4], follow immediately and are shown in the figure as a single "real digital filtering" operation for simplicity. Equalization compensates for receiver-to-receiver variations in the analog receiver components through which the signal passed before sampling. The frequency response of the time-delay filtering approximates a linear phase in the +550 MHz to +950 MHz band and is designed so that the effect on the signal is, for practical purposes, equivalent to a pre-sampling delay.

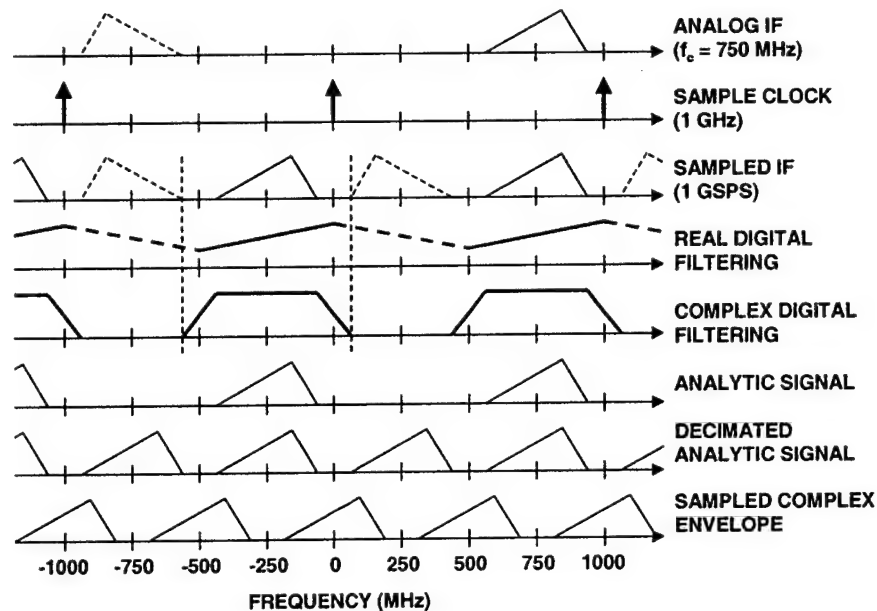


Figure 25. I/Q demodulation strategy

Different impulse responses can be loaded into the filter to effect the different delays needed in each channel for beamsteering. To realize multiple beams, this and all succeeding DSP operations must be duplicated for each desired beam. It should be noted here that this technique would not form totally independent beams. Since beamsteered subarrays are used, the digital beamformer is restricted to forming squinted beams in the same general direction that the subarray beams are pointing. To produce independent beams, either the subarrays need to form more than one beam, or the receivers and A/Ds need to be placed behind every element, abandoning subarrays altogether. This is the extent of the processing that must be done for each receiver output. The beamforming sum then combines the digitally processed receiver outputs into a single digital IF signal.

Note that I/Q demodulation of the signal does not occur until after the beam is formed. This simplifies the processing by only requiring this function to be performed once per beam, as opposed to performing it sixteen times (once for every receiver output). I/Q demodulation of the beamformed digital IF signal produces complex-envelope samples of the form $I+jQ$ through a number of steps [5]. The first step is filtering with a complex impulse response, corresponding here to a frequency response (see "complex digital

filtering" in Figure 25) that is not symmetric about the origin, in order to remove the IF signal's spectral-image component, shown in the figure with dashed lines. This image-suppression filtering produces a signal, here loosely termed "analytic" for its one-sided spectrum (within an origin-centered spectral period), that can be decimated to a 500 MHz rate and then is shifted in frequency by 250 MHz to produce the desired output samples. If desired, some band shaping can be included in the image-suppression filter [6], perhaps to compensate for the average distortion expected from the analog receiver components.

9.0 DIGITAL HARDWARE IMPLEMENTATION

The signal processing described above assumes that the digital hardware can support a 1 GHz sample rate. Since commercially available components cannot support this rate, the processing will be performed using polyphase techniques. Figure 26 shows a block diagram of the digital hardware being developed.

The 8-bit, 1 GHz output of the A/D converter will first pass through a DEMUX process, which demultiplexes the data stream by a factor of 8, producing 64 bits (representing eight consecutive 1 GHz data samples) at 125 MHz. This data then passes through several field-programmable gate arrays (FPGAs), which implement the polyphase digital filters required for equalization and time delay and the running sum for the beamformed output, as described in the previous section. After the beam is formed, another FPGA

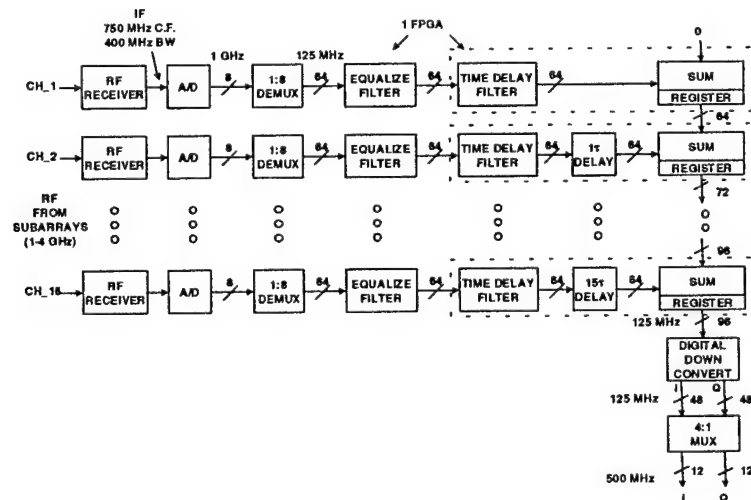


Figure 26. Digital processing for one beam

implements the filters required for I/Q demodulation. As can be seen in Figure 27, multiple beams can be formed by duplicating the hardware after the equalization filters. In each channel, the output of the equalization filter is sent to two time-delay and beam-combining circuits to form two beams. It is currently planned to use million-gate Xilinx Virtex FPGAs to implement the processor. These should be able to support 125 MHz clock rates.

Figure 28 shows how a 16-tap FIR filter could be realized in polyphase form. On each 125 MHz clock edge, 64 bits (corresponding to eight 1 GHz A/D samples in parallel) will be clocked into a three-stage shift register, providing delayed 8-bit data samples D_0, \dots, D_{23} . Before the next clock edge, the sixteen filter coefficients (C_0, \dots, C_{15}) are multiplied by sixteen contiguous data samples and summed to form a filter output. Eight such filters need to be computed simultaneously, where the data samples input to each filter are offset by one 1 GHz clock period (that is OUT0 is produced by data samples D_0, \dots, D_{15} , OUT1 is produced by samples D_1, \dots, D_{16} , etc.).

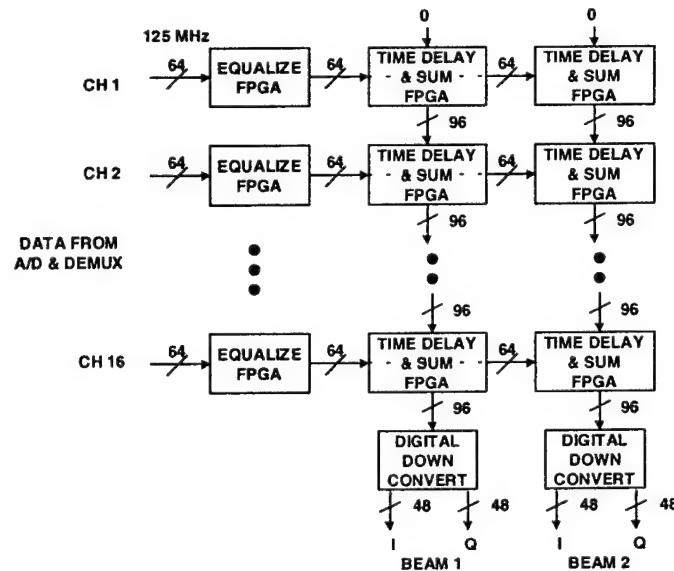


Figure 27. Digital processing for two beams

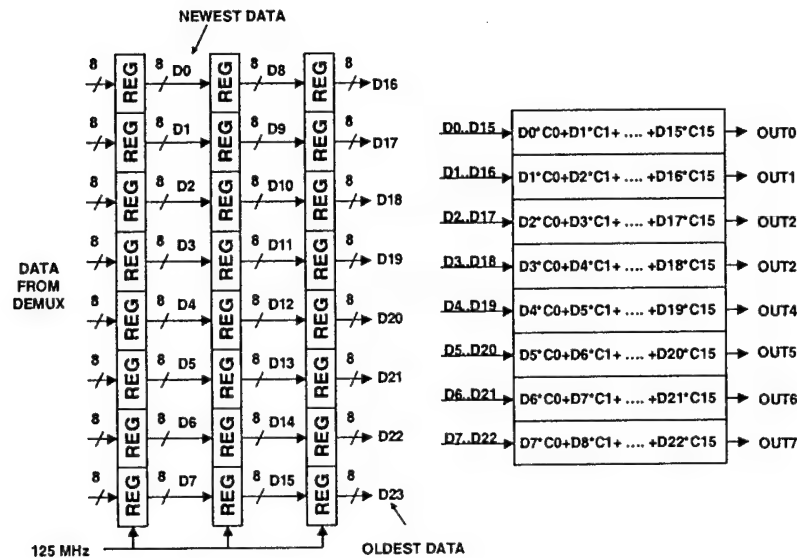


Figure 28. Polyphase implementation of a 16-tap FIR filter

10.0 ARRAY – PATTERN OPTIMIZATION

The flexibility of the hardware will support several types of experiments in the use of optimized array patterns. The primary design goal of the system is to support the first of these.

Wideband steering of a narrowband pattern design - A narrowband boresight pattern at the lower band edge will first be designed as the usual linear combination of element outputs, leading to a wideband pattern in which the beamwidth narrows with increasing frequency. This wideband pattern can be realized with the analog attenuators and steered with true time-delay using a combination of switched analog delay lines on individual elements and digital time-delay filters in each subarray receiver.

Shaped off-axis narrowband beams - A narrowband beam can be designed for a particular pointing angle and with main-beam shape and sidelobe characteristics traded off as desired (subject to geometrical constraints). For

example, at some sidelobe cost, a circular main-beam shape is possible far off boresight, and stopband attenuation can be made greater in more-important directions, perhaps corresponding to known interference sources. Such beams are not useful over a wide band as they will squint with frequency, nor are they really suitable for steering. The idea is simply to load a particular pre-designed custom beam for each desired look direction. Analog attenuation and phase shifts are adequate for realization of such beams.

Wideband beams jointly shaped in space and frequency - If the subarrays are given a common, fixed subarray pattern, that pattern can be considered the "element pattern" of what is in effect a sixteen-element array with custom-loadable digital filters (the "time-delay" filters) on each element. Then array patterns can be formed by combining element outputs processed through individual custom frequency responses rather than simply with attenuation and phase shift. A pattern so formed need not scale only with frequency. Instead it can be designed to a desired behavior (within reasonable limits) as a function of frequency and direction-of-arrival variables.

It is well known that array functions for simple narrowband linear arrays behave mathematically like FIR-filter frequency responses. Indeed, the techniques for optimization of FIR filters [4,7] apply directly to such array patterns and can be generalized to multi-dimensional and wideband arrays. Early experiments have shown that with the right strategies [8], narrowband patterns for arrays of a few hundred elements can be optimized in a quarter to half an hour on ordinary office computers equipped with perhaps slightly extraordinary amounts of memory. Optimization of FIR frequency responses for the elements of a wideband array is more involved. A companion paper explores some of the issues [9].

11.0 SUMMARY

The Radar Division at the Naval Research Laboratory is developing a wideband receive array which incorporates 6-bit analog true time-delay beamsteering at the element level and digital true time-delay at the subarray level. The system will support a 400 MHz instantaneous bandwidth over a 1 – 4 GHz operating frequency. Commercially available components are being utilized in both the RF and digital portions of the receive array. This includes: switches, attenuators and RF amplifiers and the FPGAs to process the 1 GHz A/D data. The final system will be used as a testbed to demonstrate optimal beamforming techniques, which are currently under development. This work is being performed under ONR base funding at NRL.

REFERENCES:

- [1] R.J. Mailloux, *Phased Array Antenna Handbook*, pp. 511-521, Boston-London, Artech House, 1994.
- [2] M.I. Skolnik, *Radar Handbook*, chapter 11, p. 44, New York: McGraw-Hill, 1970.
- [3] P.J. Matthews and R.D. Esman, "Cascading prism dispersion [phased array antenna]", IEEE Potentials, Volume: 18 Issue: 5, Dec. 1999-Jan. 2000, pp. 13 – 15.
- [4] J. O. Coleman and D. P. Scholnik, "Design of Nonlinear-Phase FIR Filters with Second-Order Cone Programming," Proc. 1999 Midwest Symp. on Circuits and Systems, Las Cruces, NM, August 1999.
- [5] D. P. Scholnik and J. O. Coleman, "Simple, Exact Models of Sample-Interleaving Demodulators/Modulators for Quadrature Bandpass Sampling/Reconstruction," Proc. Conf. on Information Sciences and Systems, Baltimore MD, March 1997.
- [6] D. P. Scholnik and J. O. Coleman, "Integrated I-Q Demodulation, Matched Filtering, and Symbol-Rate Sampling using Minimum-Rate IF Sampling," Proc. of the 1997 Symposium on Wireless Personal Communication, Blacksburg VA, June 1997.
- [7] J. O. Coleman, "Systematic Mapping of Quadratic Constraints on Embedded FIR Filters to Linear Matrix Inequalities," Proc. 1998 Conf. on Information Sciences and Systems, Princeton University, March 1998.
- [8] J. O. Coleman and R. J. Vanderbei, "Random-Process Formulation of Computationally Efficient Performance Measures for Wideband Arrays in the Far Field," Proc. 1999 Midwest Symp. on Circuits and Systems, Las Cruces, NM, August 1999.
- [9] D. P. Scholnik and J. O. Coleman, "Optimal Design of Wideband Array Patterns," IEEE International Radar Conference", pp. 172 – 177, Washington, DC, May 2000.

MUTUAL COUPLING BETWEEN ELECTRICALLY SMALL GENETIC ANTENNAS

Edward E. Altshuler
Air Force Research Laboratory
Sensors Directorate
80 Scott Drive
Hanscom AFB, MA 01731-2909

Tel: 781 377 4662, Fax: 781 377 1074, e-mail: edward.altshuler@hanscom.af.mil

Terry O'Donnell
ARCON Corporation
260 Bear Hill Rd
Waltham MA 02451

Tel: 781 377 1720, Fax: 781 377 5040, email: teresa.odonnell@hanscom.af.mil

Abstract

It has been shown that it is possible to design an electrically small resonant antenna using a genetic algorithm (GA). In this paper the mutual coupling between small genetic antennas is investigated and compared with that of resonant monopoles. The mutual coupling is weaker for the genetic antennas.

1. Introduction

One of the most challenging problems in antenna design is that of the electrically small antenna [1-9]. Wheeler[1] defines a small antenna as one whose maximum dimension is less than the "radianlength" which is $1/2\pi$ wavelength. The associated volume is often defined as a "radiancube with a radianlength equal to the side of the cube, or a radiansphere with the radianlength equal to the radius of the sphere. Chu [2] defined the electrical size of the antenna in terms of a sphere of radius a/λ , within which the antenna is enclosed. This definition is convenient for the analysis of antennas when the fields are represented by spherical wave functions. For this investigation we define the size of the antenna as that enclosed within a cube of height, h/λ over an infinite ground plane. Thus the total volume within which the equivalent antenna in free space is confined is $2 (h/\lambda)^3$. This

definition is chosen because the computations are done with the Numerical Electromagnetics Code (NEC) [10], which uses Cartesian coordinates.

The parameter which characterizes the bandwidth of a small resonant antenna is the quality factor, Q , which is defined as the ratio of the resonant frequency of the antenna to the frequency difference at which the radiated power decreases to $\frac{1}{2}$ that at resonance. The lower the Q , the more broadband the antenna. The main problem in small antenna design is that as the size of the antenna is decreased its radiation resistance approaches zero and its reactance approaches plus or minus infinity depending on whether it behaves as an inductance (loop) or as a capacitance (monopole) off resonance. Most small antennas are inefficient and non-resonant and thus require matching networks. The GA produces an antenna configuration for which the capacitive and inductive coupling between the wire segments cancel, thus achieving resonance. The far-field pattern is predominantly that of a vertical electric dipole and a horizontal magnetic dipole.

In this investigation the mutual coupling of a pair of antennas is computed and measured. The computations are done for the antenna over an infinite ground plane; the measurements are conducted over a square ground plane that is 4 ft x 4 ft (1.22 m x 1.22 m) or about 1.6λ on a side. Reflections off the edge of the ground plane affect the impedance and its finite size prevents the radiation pattern from having a maximum along the horizon. However, this limitation should not have a significant affect on the mutual coupling. The mutual coupling between a pair of resonant monopoles is also measured for comparison.

2. Approach

We use a genetic algorithm (GA)[11,12] in conjunction with the NEC to search for resonant wire configurations that best utilize the volume within which the antenna is confined. The objective of this optimization is to minimize the Voltage Standing Wave Ratio (VSWR) and corresponding Q of an electrically small resonant antenna. In order to obtain a resonant antenna, the total length of the wire should be at least $\lambda/4$. Thus, as the size of the cube within which the antenna is enclosed is decreased, more wire segments have to be used. Intuitively, the antenna should consist of wires that are orthogonal where possible and which do not contain parallel wires that are too close together. The GA optimization was done at about 400 MHz. We obtained a set of small genetic antennas that had from two to ten segments connected in series and were enclosed within a cube of approximately $.1\lambda$ down to $.03\lambda$ on a side. The computed configurations have been built and tested. The corresponding Q s and VSWRs increased from about 16 and 2.0 to about 350 and 90 respectively. The radiation patterns for these

antennas were elliptically polarized and had near hemispherical coverage. The impedance and VSWR were measured with a Hewlett-Packard Model 8510 Network Analyzer.

For this investigation we chose a pair of 7-segment genetic antennas as is shown in Fig. 1. The computed parameters for this antenna are as follows. The resonant frequency is about 403 MHz; its input impedance is 2.7 ohms and VSWR is 18.5. It has a Q of 102. Its physical size is contained within a cube of 3.3 cm on a side, thus it has an electrical size of about $.045\lambda$. Two antennas were then fabricated. Because of the complexity of the shape, it was very difficult to obtain exact replicas of the model. These antennas had a resonant frequency at 383 MHz, an input impedance of 2.5 ohms, a VSWR of 20 and a Q of 110. The actual size of the fabricated antenna had a maximum dimension of 3.15 cm, thus its electrical size was $.040\lambda$.

The mutual coupling is determined from the scattering matrix, where S_{11} and S_{22} are the reflection coefficients for the signals from a 50-ohm line into the antennas and S_{12} and S_{21} are the transmission coefficients between antennas. The mutual coupling is the magnitude of the signal that is coupled from one antenna to the other, with both antennas matched. For the computations the scattering parameters cannot be determined directly; they must be obtained from the impedance matrix. The impedance parameters are computed using the symmetric-antisymmetric method [13]. The scattering parameters can be measured directly using the HP8510 Network Analyzer. If the antennas were matched to the transmission line then the coupling would be S_{12} . However, for both computations and measurements we have to take the mismatch into account.

Defining the coupling as

$$C_1 = \frac{|S_{12}|^2}{1 - |S_{11}|^2} \quad (1)$$

takes the mismatch of the transmitting antenna into account.

The mismatch of the receiving antenna can be approximately taken into account by dividing again by $1 - |S_{11}|^2$ to give

$$C_2 = \frac{|S_{12}|^2}{(1 - |S_{11}|^2)^2} \quad (2)$$

which becomes more accurate with increased spacing between the antennas.

3. Results

The mutual coupling between genetic antennas was computed with NEC2 and measured as a function of element spacing, which was varied from about $.125$ to $.40\lambda$. The results are summarized in Fig. 2. We show the computed and measured mutual coupling for unmatched antennas. Although the agreement is only fair, the decrease in coupling as a function of separation is excellent. The approximate coupling, which is corrected for the mismatches, is also shown for both the computations and measurements. For comparison, the mutual coupling between a pair of resonant monopoles is included. Since the resonant monopoles are reasonably well matched, a mismatch correction is unnecessary. Note that the coupling between genetic antennas is generally weaker for separations greater than 0.1λ . For closer spacing, the mutual coupling for matched genetic antennas cannot be accurately determined.

Acknowledgements

The authors wish to thank Dr. Arthur Yaghjian for helpful discussions and Dr. Arje Nachman at AFOSR for his support.

References

- [1] H. A. Wheeler, "Fundamental limitations of small antennas," Proc. IRE, vol. 49, pp. 1479-1484, Dec. 1947.
- [2] L. J. Chu, "Physical limitations on omni-directional antennas," J. Appl. Phys., vol. 19, pp. 1163-1175, Dec. 1948.
- [3] R. F. Harrington, "Effect of antenna size on gain, bandwidth and efficiency," J. Res. Nat. Bur. Stand., vol. 64D, pp. 1-12, Jan.-Feb. 1960.
- [4] R. L. Fante, "Quality factor of general ideal antennas," IEEE Trans. Antennas Propagat., vol. AP-17, pp. 151-155, Mar. 1969.
- [5] H. A. Wheeler, "Small Antennas," IEEE Trans. Antennas Propagat., vol. AP-23, pp. 462-469, Jul. 1975.
- [6] G. S. Smith, "Efficiency of electrically small antennas combined with matching networks," IEEE Trans. Antennas Propagat., vol. AP-25, pp. 369-373, May 1977.
- [7] R. C. Hansen, "Fundamental limitations in antennas," Proc. IEEE, vol. 69, pp. 170-182, Feb. 1981.
- [8] A.D. Wunsch and S-P Hu, "A closed-form expression for the driving - point impedance of a small inverted L antenna," IEEE Trans. Antennas Propagat., vol. 44, pp. 236-242, Feb. 1996.

- [9] J. S. McLean, "A re-examination of the fundamental limits on the radiation Q of electrically small antennas," IEEE Trans. Antennas Propagat., vol. 44, pp. 672-675, May 1996
- [10] G. J. Burke and A. J. Poggio, "Numerical Electromagnetics Code (NEC)- method of moments," Rep. UCID18834, Lawrence Livermore Lab., CA, Jan. 1981.
- [11] Y. Rahmat-Samii and E. Michielssen, *Electromagnetic Optimization by Genetic Algorithms*, John Wiley & Sons, New York, 1999.
- [12] E. E. Altshuler and D. S. Linden, "Process for the Design of Antennas using Genetic Algorithms," U. S. Patent 5,719,794, Feb. 17, 1998.
- [13] E.E Altshuler, "The Measurement of Self and Mutual Impedances," IRE Trans. Antennas Propagat., vol. 8, pp. 526-527, Sept 1960.

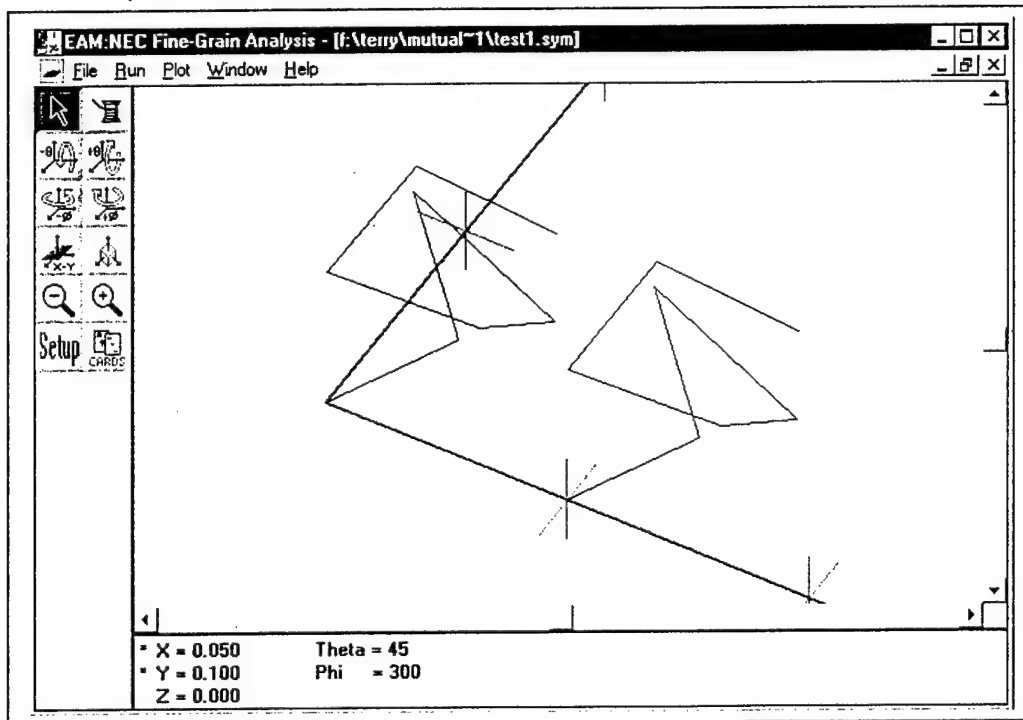


Figure 1 Pair of seven-wire genetic antennas

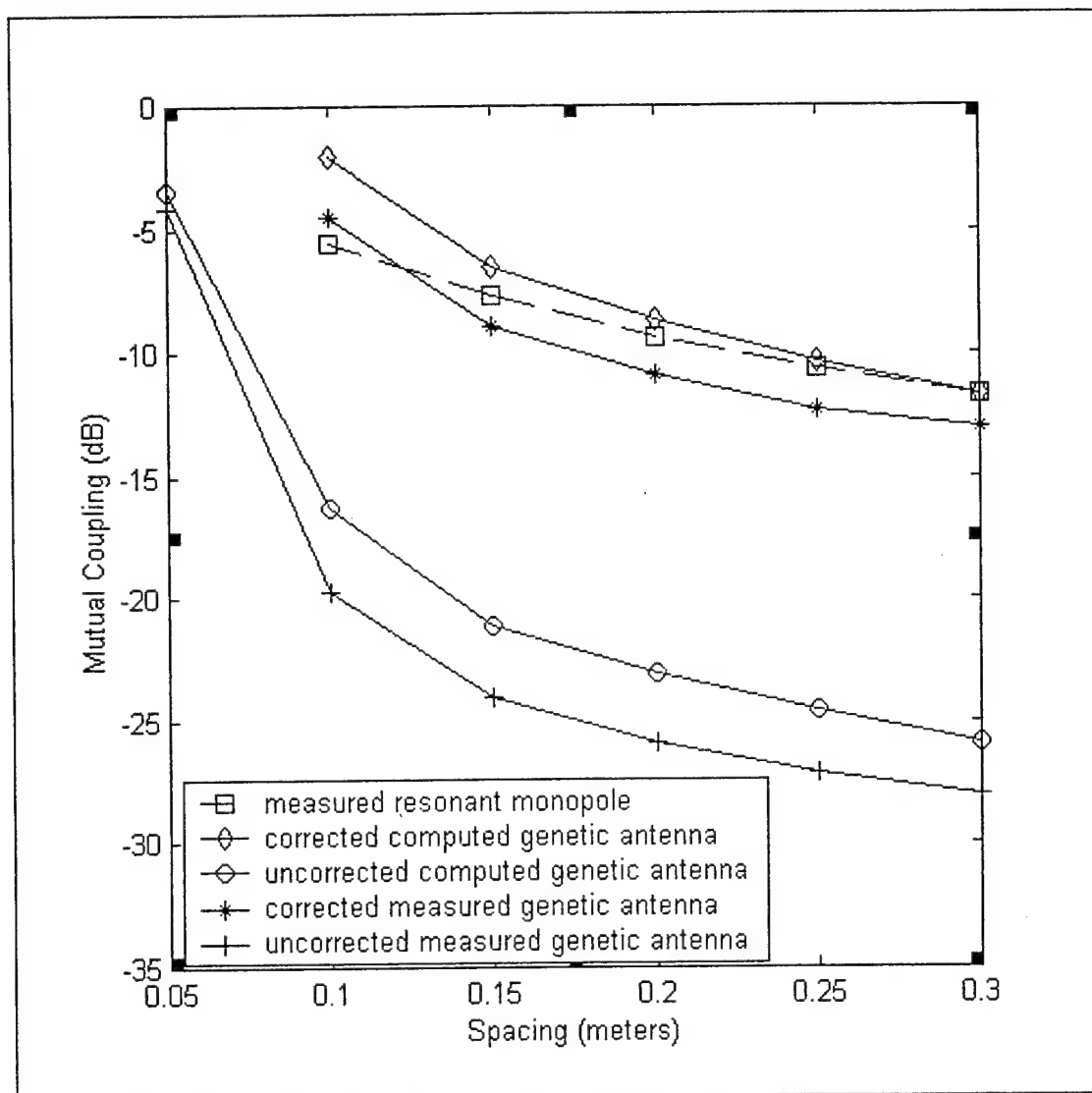


Figure 2 Computed and measured mutual coupling

THE CELLULAR SCANNING CONCEPT AND ITS APPLICATIONS

Dr. Probir K. Bondyopadhyay
MAHANAD COMMUNICATIONS INC.
14418 Oak Chase Drive
Houston, Texas 77062
E Mail : p.bondy@worldnet.att.net

**Leave the beaten track occasionally and dive into the woods,
You will be certain to find something that you have never seen before.**

--- Alexander Graham Bell

ABSTRACT

The cellular scanning concept for satellite communications in the context of the invention of the Geodesic Sphere Phased Array Antenna system[1] is described. The phased array architecture consists of a multiplicity of planar triangular subarrays arranged in the geodesic sphere configuration. Two specific practical architectures - one, based on the regular icosahedron, a Platonic solid and the other based on the truncated icosahedron - an Archimedean solid are considered. The communication space of the entire sky is subdivided into smaller cellular regions corresponding to the geodesic sphere arrangement. An appropriate section of contiguous subarrays is energized to form a beam to scan the corresponding cellular space. Two representative practical phased array antennas for low earth orbit satellite tracking and communications are considered and preliminary design parameters are outlined and discussed.

1. INTRODUCTION

There exists an important need for low cost efficient and affordable phased array antenna for tracking and communications with satellites in Low Earth Orbit (LEO), Medium Earth Orbits(MEO) and Geosynchronous(GEO) orbits from mobile or fixed platforms on earth. At minimum, the phased array should be able to track and communicate from a fixed platform(the home of an ordinary citizen of

the world) with a moving satellite and be able to switch from horizon to horizon momentarily (inertialess) from the setting satellite to the rising satellite without interruptions in communications.

2. THE INVENTION

This paper describes the invention[1-2] and applications of a *new* phased array architecture -- the Geodesic Sphere Phased Array Antenna system that has several advantages in terms of construction, operation, performance and maintenance. The array consists of equilateral or substantially equilateral triangular subarray panels organized in a geodesic sphere configuration based on the icosahedron, a Platonic solid, or a truncated icosahedron, an Archimedean solid. A schematic of the geodesic sphere phased array antenna architecture based on the icosahedron is shown in Figure 1. The geodesic sphere structure could be derived from other regular (Platonic) solids or semi-regular (Archimedean) solids[1].

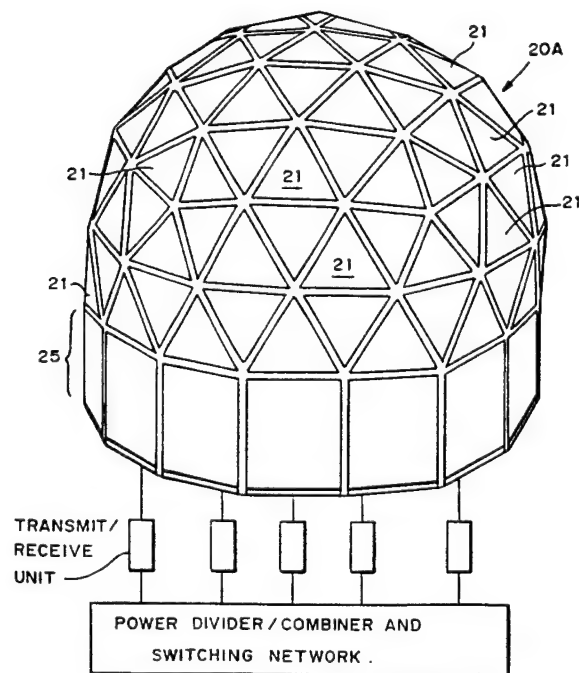


Figure 1 A schematic of a Geodesic Sphere Phased Array Antenna architecture

3. THE INVENTION IN HISTORICAL PERSPECTIVE

This year 2000 marks the 100 hundredth anniversary of the invention and application of Array Antennas. It was approximately in the later half of 1900 that Marconi decided to use special arrays of the grounded monopole Marconi antenna to radiate sufficient wireless power to signal across the Atlantic ocean. Sir John Ambrose Fleming, the inventor of the vacuum diode, who as the technical advisor to Marconi designed the first transatlantic wireless transmitter at Poldhu, Cornwall, England provides a rare first hand inside view of the design effort for this first array antenna[3].

Over fifty years later, after the radar was invented deployed and successfully used for defense purposes during the second world war, practical needs developed for electronically scannable phased array antennas for searching and tracking aerial vehicles and objects in the entire sky with high power and narrow beams in the microwave frequency range. Driven by this defense need, a considerable amount of effort has been spent in the research, development and deployment of phased array antennas capable of electronically scanning the entire sky or a major portion of it. In 1965 Knittel published a paper[4] describing the division of hemispherical communication space into multiple parts and providing for planar phased arrays on the faces of a pyramid or a frustum of a pyramid, each face covering one such divided space. Knittel's work was revisited some thirty years later by Wu[5] to consider optimum choice of the number of planar phased arrays based on several array performance criteria. Chethik[6] in a recent patent, described a cluster of three planar phased arrays on the faces of a pyramid, and placed with an appropriate angular tilt to provide satellite communications at 20GHz frequency band.

Side by side, attention has also been focused on spherical phased arrays since the 1960s[7 -14]. Field analysis has been carried out using electromagnetic fields expressed in the spherical coordinate frame and essential array performance characteristics have been determined through research efforts spread over quarter of a century. In all of the studies, antenna elements have been arranged on a full

regular curved sphere. One such research work of analysis involved circular aperture elements arranged in concentric rings(latitudes) around the spherical axis [15].

Robert C. Hansen in his recent book[16] published in 1998 has devoted a single page on spherical arrays and provided the summary statement :

"A Spherical array behaves much like a cylindrical array scanned only in azimuth, but the lattice and depolarization problems are unique to the sphere."

which is too simplified to be accurate in the context of a large phased array operation. Robert J. Mailloux in his recent book[17] on Phased Array Antennas published in 1994 has devoted two pages on the subject of spherical phased arrays reviewing some prior work done by others. The above referenced descriptions of prior works conclusively demonstrate that the Geodesic Sphere Phased Array Antenna structure was not dreamt of by anyone else before in the past ninety nine years of the 20th century !

4. ELEMENT ARRANGEMENTS IN THE GEODESIC SPHERE PHASED ARRAY ANTENNA

In the array, each triangular subarray panel constitute a module with antenna elements arranged in a triangular grid.

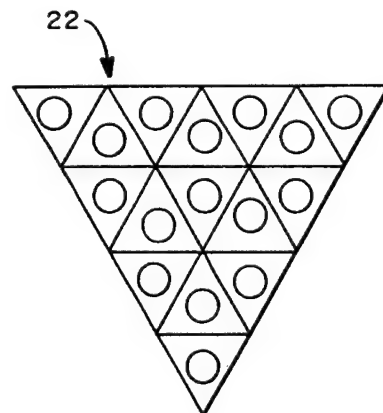


Figure 2 A preferred arrangement of elements in a triangular subarray of Geodesic Sphere Phased Array Antenna

5. THE CELLULAR SCANNING CONCEPT

It is known for the past thirty years that element spacings in a spherical array could be substantially increased beyond half wavelength before grating lobe type deteriorating conditions arise. This fact could be skillfully exploited to design the geodesic sphere phased array. Further it may also be less costly to group together four elements as a single cluster for simplified subarray feeding purposes. Still further, it may be advantageous to employ an entire subarray as the switchable unit in the construction of the energized portion of the array. Under these conditions, it is practicable to divide the entire communication space into smaller cellular regions and electronically scan each such cellular space by means of subarray switching and element or subarray level phase shifters.

6. APPLICATIONS OF THE GEODESIC SPHERE PHASED ARRAY ANTENNA

The immediate application of the geodesic sphere phased array antenna is in tracking and communication with Low Earth Orbit (LEO) and other nonstationary Orbit satellites requiring electronic scanning. There are commercial applications as well as military applications for this phased array with the novel architecture.

7. PERFORMANCE ANALYSIS OF THE GEODESIC SPHERE PHASED ARRAY

In order to carry out performance analysis of the geodesic sphere phased array it is necessary to perform accurate electromagnetic field analysis of the underlying array structure. This could best be accomplished in the spherical coordinate frame[15].

The radiated electromagnetic field is represented in terms of spherical waveguide modes and the element excitations are resolved in two orthogonal directions in the global longitudinal and latitudinal unit vector directions at the element position. Spherical transmission line relations are used to account for the geodesic geometry in the field calculations. Various symmetries inherent in the array play a crucial role in determining the symmetry and side lobe levels of the

radiated field. Extensive numerical analysis is necessary to characterize the performance of the array.

8. ADVANTAGES OF THE GEODESIC SPHERE PHASED ARRAY ANTENNA

The immediate advantage of the geodesic sphere phased array antenna architecture is its modular construction with planar surfaces. No curved surface or line are involved and this aspect of the structure simplifies construction and maintenance.

In the past forty years considerable amount of civil engineering, mechanical engineering and architectural research efforts have been expended to design and construct geodesic sphere structures. This body of knowledge is already available to design the phased array structure proposed here.

9. PRELIMINARY DESIGN CONSIDERATIONS AND TRADE-OFFS.

In order to be commercially successful, the phased array antenna system for tracking and communication with satellites must be affordable. Every aspect of the phased array design and implementation that leads to lower construction and maintenance costs have to be explored. Simplified design with the minimum cost is the design goal. In mass applications involving home based satellite communication systems, the requirement will essentially involve tracking and communication with satellites in a known orbit and smooth handover from a setting satellite to the rising satellite. This means that for mass scale home based applications the phased array antenna is involved in tracking and communicating with only one satellite only except when horizon to horizon inertialess satellite transfer is necessary (from the setting satellite to the rising satellite).

From the cost point of view as well as for simplified operations it may be feasible and desirable to create a design such that a subarray participates in forming a single beam only even during the above-mentioned transfer. Such a design may lead to a substantial reductions in the number of Transmit/Receive units required for the array for a required communication link budget.

10. REFERENCES

- [1] P. K. Bondyopadhyay, "Geodesic Sphere Phased Array Antenna for multi-satellite Communications", U.S. Patent Application No. 60/121,874, Filed, 26th February 1999.
- [2] P. K. Bondyopadhyay, "Geodesic Sphere Phased Array Antenna System", U.S. Patent Application No. 09/513,014, Filed, 25th February 2000.
- [3] J. Ambrose Fleming, Personal Notebook, Manuscript No. MS. Add 122/20, Fleming Collection, Rare Manuscripts Division, University College London, 1900-1902.
- [4] G. H. Knittel, "Choosing the Number of Faces of a Phased Array Antenna for Hemispherical Scan Coverage", IEEE Trans. Antennas and Prop., Vol. AP-13, Nov. 1965, pp. 878-882.
- [5] T. K. Wu, "Phased Array Antenna for Tracking and Communication with LEO Satellites", Symposium Digest, 1996 IEEE Symposium on Phased Array Technology, Boston, MA, October 1996.
- [6] F. Chethik, " Triangular pyramid phased array antenna", U.S. Patent. No. 5,543,811, filed Feb. 7, 1995, issued August 6, 1996.
- [7] D. L. Sengupta, T. M. Smith and R. W. Larson, "Radiation Characteristics of a Spherical Array of Circularly Polarized Elements", IEEE Trans. Antennas and Prop., Vol. AP-16, Jan. 1968, pp. 2-7.
- [8] A. K. Chan and R.A. Siegelmann, " experimental Investigation on Spherical Arrays", IEEE Trans. Antennas and Prop., Vol. AP-17, May 1969, pp. 348-349.
- [9] H. E. Schrank, " Basic Theoretical Aspects of Spherical Phased Arrays", in Phased Array Antennas, [A. A. Oliner and G.H. Knittel Editors], ARTECH HOUSE INC. Dedham, Mass. 1972, pp. 323-327.

- [10] J. Juntunen, " Radiation Properties of Spherical Arrays", Proceedings of the Fourth European Microwave Conference, Montreux, Switzerland, pp. 283-287, Sept. 10-13, 1974.
- [11] J. J. Stangel and P. A. Valentino, "Phased Array Fed Lens Antenna", U.S. Patent No. 3,755,815, August 28, 1973.
- [12] L. Schwartzman and J. Stangel, "The Dome Antenna", Microwave Journal, Vol. 18, pp. 31-34, Oct. 1975.
- [13] L. Schwartzman and P. M. Liebman, "A Report on the Sperry Dome Radar", Microwave Journal, Vol. 22, No. 3, pp. 65-69, March 1979.
- [14] P. A. Valentino and J. J. Stangel, "Multi-beam, multi-lens microwave antenna providing hemispherical coverage", U.S. Patent No. 4,458,249, applied February 22, 1982, granted July 3, 1984.
- [15] P.K. Bondyopadhyay, "Analysis of rotationally symmetric arrays of apertures on conducting spherical surfaces", IEEE Transactions on Antennas and Propagation, Vol. AP-40, pp. 857-866, August 1992.
- [16] R. C. Hansen, "PHASED ARRAY ANTENNAS, John Wiley & Sons, New York, 1998, Chapter 11, page 445.
- [17] R. J. Mailloux, "PHASED ARRAY ANTENNA HANDBOOK", ARTECH HOUSE INC., Norwood, MA, 1994, Chapter 4, pp. 233-235.

DETERMINATION OF ARRAY FEEDING COEFFICIENTS USING LIMITED ANGLE FARFIELD MEASUREMENTS

**Mr. Harvey E. Tobin
Air Force Research Laboratory
Hanscom AFB, MA 01731**

**Dr. Peter R. Franchi
Arcon Corporation
Waltham, MA 02451**

1. ABSTRACT:

It is often desirable to determine the aperture coefficients on an antenna array. The determination may be accomplished using amplitude and phase data from a measured far field antenna pattern. This method can be used even if the far field pattern is measured over a reduced angular range. This technique can give an accurate element calibration if the angular range is not too limited, and if the measurement errors are small. In this paper we examine these limitations both theoretically and with computer simulations.

2. INTRODUCTION

In a previous paper [1] we showed that by (a) using quadratic phase on the array being tested, and (b), moving the test probe on a special arc, which we termed the focal arc, we could reduce the far field measurement distance by nearly an order of magnitude. One of the deficiencies of this technique was that the far field pattern was only accurate over $\pm 55^\circ$. Beyond this range, higher order phase errors and $1/R$ amplitude errors start to dominate. Because it is possible and desirable to calibrate the antenna, i.e. determine the array element coefficients, from far field phase and amplitude measurements taken over a full angular range of $\pm 90^\circ$, there is the general question of how well the same element coefficients can be determined with only a limited angular range of measurements and, more narrowly, under what conditions could the focal arc technique give accurate array element coefficients. In this paper the relationship between array size, measurement error, and the far field measurement angular range is related to the error in determining array element coefficients.

It is easy to show that with no measurement error the array element coefficients can be determined exactly for any range of scan angles no matter how small. However, with the introduction of any measurement error whatsoever, measurement over too small an angular far field range will lead to high errors in the array coefficients. Even if the full far field angular range is used, the far field measurement accuracy will determine how well the array coefficients can be found. What we attempt to establish in this paper is at what limited range of angles can an array be measured before the accuracy in finding the array

coefficients from the far field data becomes unacceptable. This angular range is tied to the number of elements in the array, the element spacing, and the measurement error in the far field.

Some limitations of this paper should be mentioned. Only linear arrays are addressed here, and we assume that we can separate array element errors from far field measurement errors. We also use aperture errors to approximate realistic perturbations of perfect element coefficients. These perturbed coefficients are what we wish to infer from the far field error measurements. We assume that large far field measurement errors would give incorrect array coefficients, but that small far field error would have very little effect. We assume finally that the errors across the aperture and in the far field, are real and symmetric. This choice has been made only for convenience.

3. THEORETICAL BACKGROUND

This section discusses the inverse transform and matrix correction that are used to determine the aperture coefficients of the array from its far field pattern. We consider two cases: 1) without far field measurement error, and 2) with far field measurement error.

3.1. CASE 1:

The far field pattern of a linear array is

$$E_m = \sum_{n=1}^N A_n e^{jkdxmn\Delta\theta}, \quad (1)$$

where

$k = 2\pi/\lambda$.

N is the number of elements.

dx is the spacing between the elements.

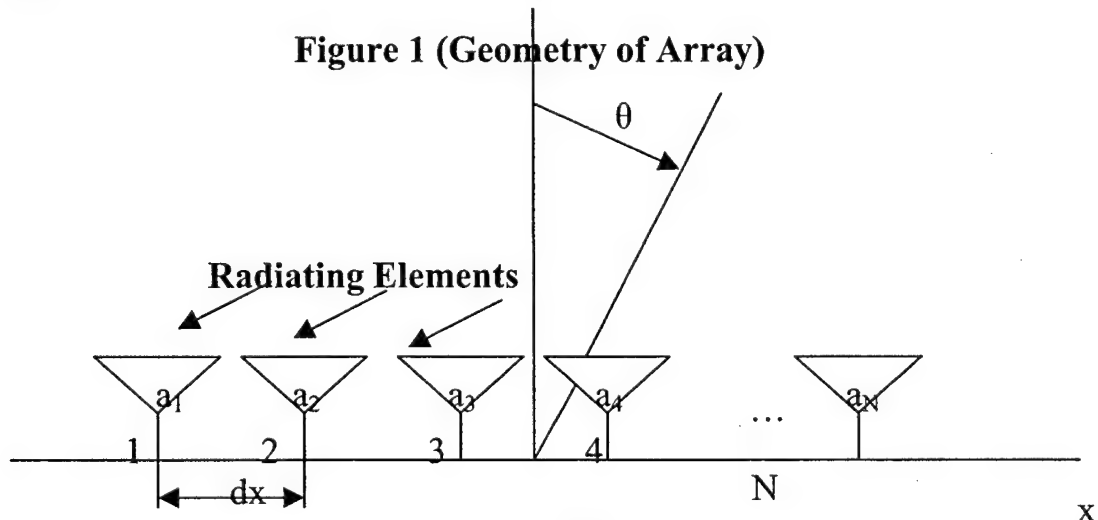
m is the corresponding point in the far field.

n is the corresponding point on the aperture.

$\Delta\theta$ is the sampling rate used to determine the far field pattern over a specified angular range.

A_n is the actual weight, including amplitude and phase errors, of the n th element in the array.

Figure (1) illustrates the geometry of the array.



The inverse transform of the far field is represented by

$$A_l' = \sum_{m=1}^M E_m e^{-jkdxlm\Delta\theta}, \quad (2)$$

where,

A_l' is the new aperture coefficient after transforming field points

E_m is the far field value.

M is the number of far field points, which corresponds to number of elements.

The new aperture coefficients are

$$\begin{aligned} A_l' &= \sum_{m=1}^M \sum_{n=1}^N A_n e^{jkdxm\Delta\theta(n-l)} \\ &= \sum_{n=1}^N A_n \sum_{m=1}^M e^{jkdxm\Delta\theta(n-l)}. \end{aligned} \quad (3)$$

Expanding (3), we obtain

$$\begin{aligned} A_l' &= \sum_{n=1}^N A_n \frac{\sin(\frac{M}{2} kdx\Delta\theta(n-l))}{M \sin(\frac{kdx}{2} \Delta\theta(n-l))} \frac{e^{-jkdx(M/2)\Delta\theta(n-l)}}{e^{-jk(dx/2)\Delta\theta(n-l)}} \\ &= \sum_{n=1}^N A_n \frac{\sin(\frac{M}{2} kdx\Delta\theta(n-l))}{M \sin(k(d/2)\Delta\theta(n-l))}. \end{aligned} \quad (4)$$

To obtain the new set of coefficients, A_n , a correction matrix is applied to the A_l' 's:

$$A_l' = B_{nl} A_n \quad (5)$$

$$A_n = B_{nl}^{-1} A_l'. \quad (6)$$

When the non-diagonal terms of B_{nl} are not zero but small (which is the region of concern for us) B_{nl} is an identity matrix plus a matrix B_{nl}' , which has entries that are all small, the off-diagonal entries being non-zero. Since the B_{nl}' represent small error terms, we can invert the matrix using Neumann's method

$$\begin{aligned} B_{nl} &= I + B_{nl}' \\ B_{nl}^{-1} &= [I + B_{nl}']^{-1} \\ &= I - B_{nl}' + B_{nl}'^2 - B_{nl}'^3 + \dots \text{(Neumann series)} \end{aligned}$$

$$\cong I - B'_{nl}, \quad (7)$$

where

$$B'_{nl} = \frac{\sin[k(M/2)dx\Delta\theta(n-l)]}{M \sin[k(dx/2)\Delta\theta(n-l)]}. \quad (8)$$

If we define the angle-related quantity ε by

$$(k(M/2)dx\Delta\theta) = (\pi - \varepsilon) \quad (9)$$

and if the maximum test angle is θ_T , then

$$(M/2)\Delta\theta \cong \sin\theta_T. \quad (10)$$

The element spacing, dx , is typically determined by the maximum scan angle, θ_n , of the array:

$$dx \cong \frac{\lambda}{1 + \sin\theta_n}. \quad (11)$$

Therefore,

$$(k(M/2)dx\Delta\theta) \cong \frac{2\pi}{\lambda} \frac{\sin\theta_T \lambda}{1 + \sin\theta_n} \quad (12)$$

$$\cong 2\pi \frac{(\sin\theta_T)}{1 + \sin\theta_n}, \quad (13)$$

so,

$$\frac{2\pi(\sin\theta_T)}{1 + \sin\theta_n} = (\pi - \varepsilon). \quad (14)$$

solving for ε ,

$$\varepsilon \cong \pi \left(1 - \frac{2\sin\theta_T}{1 + \sin\theta_n}\right). \quad (15)$$

using (8) and (15),

$$\sin(\pi - \varepsilon)(n-l) = \sin\pi(n-l)\cos\varepsilon(n-l) - \cos\pi(n-l)\sin\varepsilon(n-l) \quad (16)$$

$$\begin{aligned} &= -\cos\pi(n-l)\sin\varepsilon(n-l) \\ &= (-1)(-1)^{(n-l)}\sin\varepsilon(n-l), \end{aligned} \quad (17)$$

thus

$$B'_{nl} = \frac{\sin \varepsilon(n-l)(-1)^{(n-l)}}{M \sin(\frac{kdx}{2}) \Delta \theta(n-l)}$$

$$\cong \frac{(-1)^{(n-l)}(-1)(1 - \frac{2 \sin \theta_r}{1 + \sin \theta_n})}{(\frac{2 \sin \theta_r}{1 + \sin \theta_n})}. \quad (18)$$

We can rewrite (8) as

$$B'_{nl} = (-1)^{(n-l)} C, \quad (19)$$

so that

$$C = \frac{(-1)(1 - \frac{2 \sin \theta_r}{1 + \sin \theta_n})}{(\frac{2 \sin \theta_r}{1 + \sin \theta_n})}. \quad (20)$$

3.2. CASE 2:

Let δ_l be the far field measurement error, both thermal and systematic, and let e_n be the individual element error caused by the far field errors δ_l . Then

$$A'_l = A_l + \delta_l, \quad (21)$$

where A_l and A'_l are as previously defined. Also

$$B_{nl}^{-1} A'_l = B_{nl}^{-1} (A_l + \delta_l), \quad (22)$$

and

$$e_n^2 = |A_n - B_{nl}^{-1} A'_l|^2$$

$$= |B_{nl}^{-1} \delta_l|^2. \quad (23)$$

Thus

$$e_n^2 = |(I - B'_{nl}) \delta_l|^2,$$

where B'_{nl} are the non-diagonal terms of the matrix, as previously noted. Then

$$e_n^2 = |I \delta_l - B'_{nl} \delta_l|^2$$

$$= I^2 \delta_l^2 - I B'_{nl} \delta_l^2 + |B'_{nl}|^2 \delta_l^2.$$

Since $|B'_{nl}| \cong 0$,

$$e_n^2 \cong |B'_{nl}|^2 \delta_l^2. \quad (24)$$

For a fully scanned far field pattern, the non-diagonal terms are all zero, and

$$e^2 = |\delta_l|^2$$

Using (18),

$$e_n^2 \cong M \delta_l^2 + M^2 \left(\frac{1 - \frac{2 \sin \theta_T}{1 + \sin \theta_n}}{\frac{2 \sin \theta_T}{1 + \sin \theta_n}} \right)^2 \delta_l^2 \quad (25)$$

or

$$e^2 = \frac{e_n^2}{M}, \quad (26)$$

and

$$e^2 = \delta_l^2 + M \left[\frac{1 - \frac{2 \sin \theta_T}{1 + \sin \theta_n}}{\frac{2 \sin \theta_T}{1 + \sin \theta_n}} \right]^2 \delta_l^2, \quad (27)$$

recalling that M is the number of elements in the array.

If far field patterns are measured over a large angular range,

$$M^2 \left(\frac{1 - \frac{2 \sin \theta_T}{1 + \sin \theta_n}}{\frac{2 \sin \theta_T}{1 + \sin \theta_n}} \right)^2 \delta_l^2 \ll M \delta_l^2 \quad (28)$$

and

$$e^2 \cong \delta_l^2, \quad (29)$$

which shows that the array coefficients are well determined.

However, if patterns are measured over a small angular range,

$$M \left[\frac{1 - \frac{2 \sin \theta_T}{1 + \sin \theta_n}}{\frac{2 \sin \theta_T}{1 + \sin \theta_n}} \right]^2 \delta_l^2 \gg \delta_i^2, \quad (30)$$

showing that the array coefficients are poorly defined.

In conclusion, the condition for an angular range of measurements to be useful is

$$M \left[\frac{1 - \frac{2 \sin \theta_T}{1 + \sin \theta_n}}{\frac{2 \sin \theta_T}{1 + \sin \theta_n}} \right]^2 \delta_l^2 \cong \delta_i^2, \quad (31)$$

in which case

$$\frac{1 - \frac{2 \sin \theta_T}{1 + \sin \theta_n}}{\frac{2 \sin \theta_T}{1 + \sin \theta_n}} = \frac{1}{\sqrt{M}}, \quad (32)$$

and

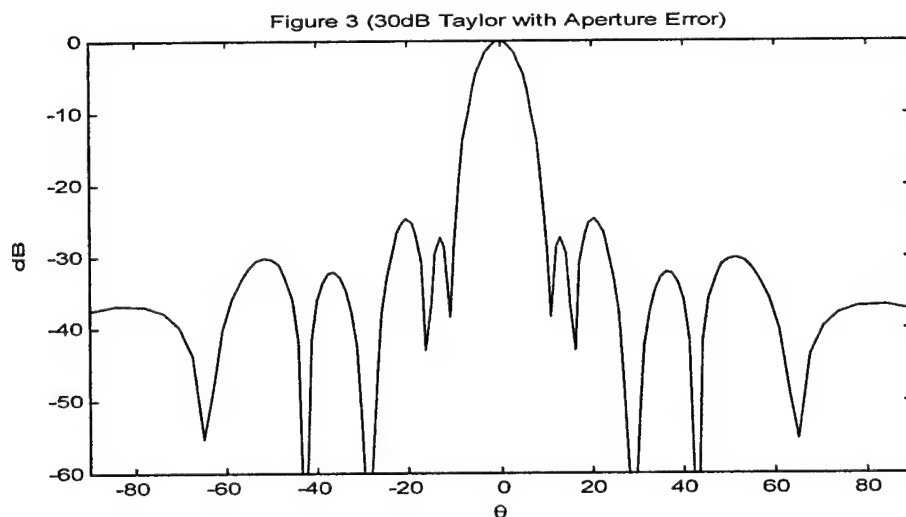
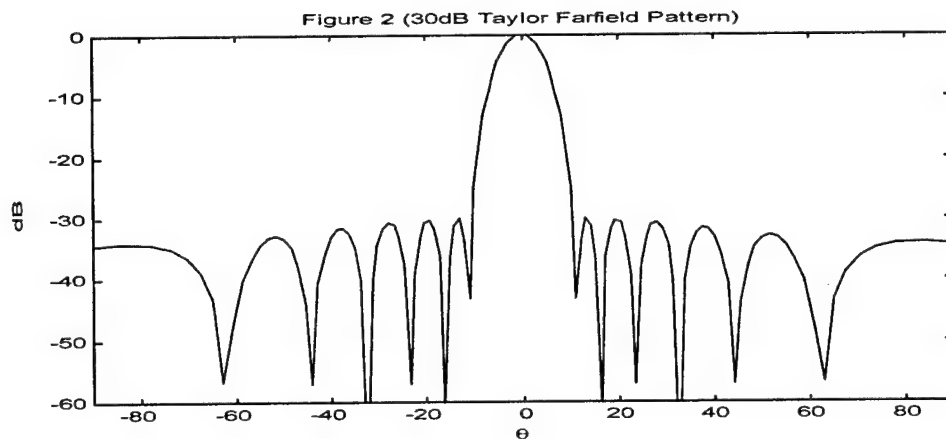
$$\sin \theta_T = \left(\frac{1 + \sin \theta_n}{2} \right) \left(\frac{1}{1 + \frac{1}{\sqrt{M}}} \right). \quad (33)$$

Thus, the required angular range over which measurements should be taken is a function of the element spacing, dx , and the number of elements in the array, M .

4. SIMULATION

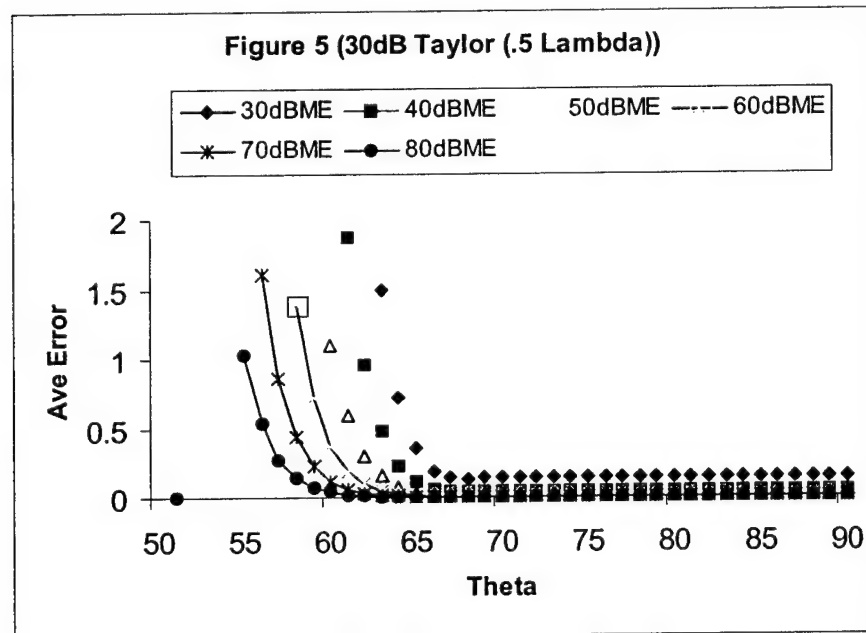
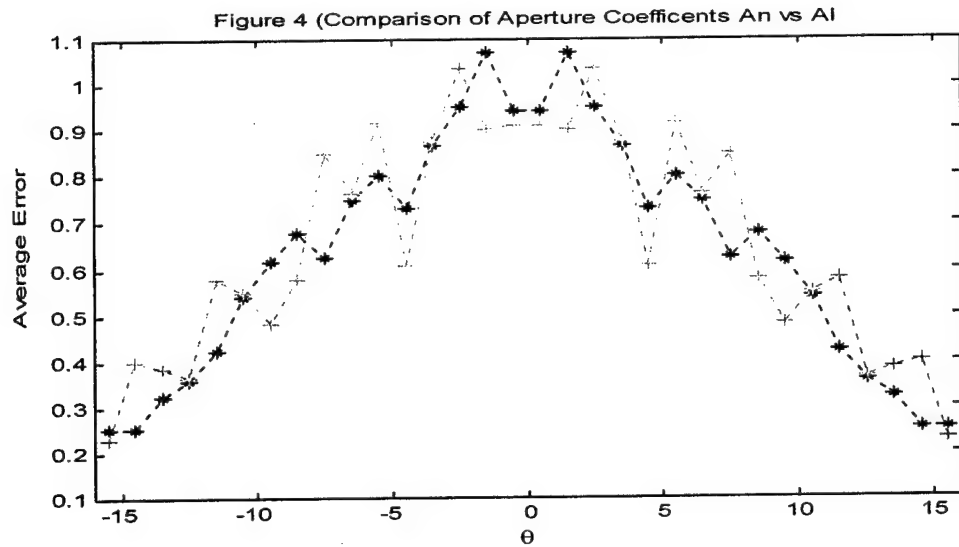
A computer simulation was run using MATLAB with a baseline case of a 30dB Taylor array of 32 elements spaced $\lambda/2$ apart with some aperture errors. As was mentioned earlier the aperture distribution was assumed to be real and symmetrical for simplicity. The measurement errors added to the far field patterns were also real and symmetric to assure that the resulting aperture distribution would also be real. Figure 2 shows the resulting pattern for a 32 element $\lambda/2$ spaced array with 30dB Taylor excitation. Real, symmetric aperture errors were added, giving a far field pattern shown in Figure 3. This random error represents manufacturing error, cable path length errors, etc. These 32 aperture coefficients (actually 16 because of symmetry) are what we wish to determine

from far field data that has been corrupted by measurement error and that has been measured in the far field over a limited range of angles.



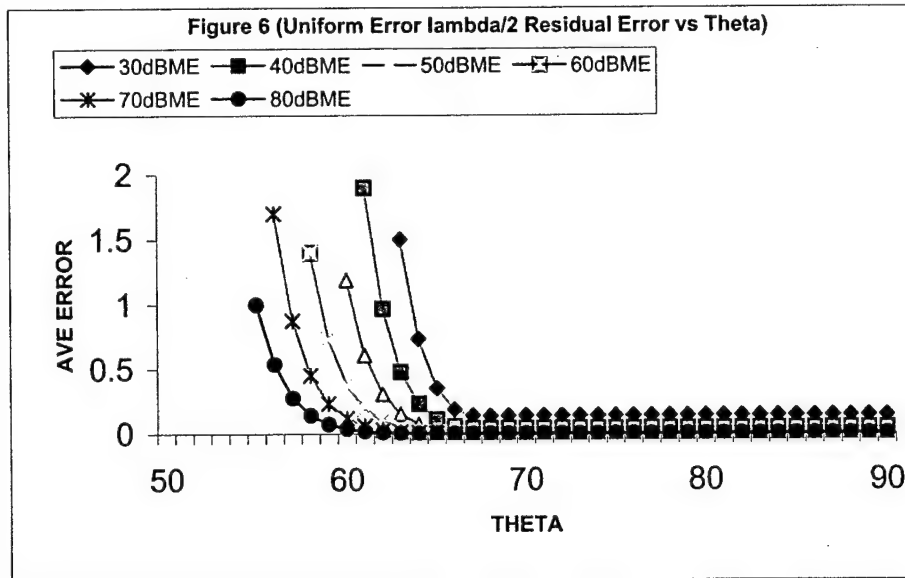
The simulation procedure is to add random error to the 30dB Taylor far field pattern, then take data at angles that are evenly spaced at 32 points over different angular ranges. The first angular range is a full $\pm 90^\circ$. Subsequent angular ranges are reduced in one degree steps. The correction matrix is then applied to these 32 data points, yielding approximate array coefficients that are compared with the actual array coefficients (Figure 4). We then compute the root mean square error between the original array coefficients and those derived from the far field data. The amount of far field measurement error is then decreased and the process is repeated. The results are shown in Figure 5. For a relatively poor measurement facility, i.e. signal-to-noise ratio (30dB), the pattern can be measured over about $\pm 66^\circ$ and still yield acceptably accurate coefficients. An excellent facility, signal-to-noise (80dB) would allow data to be measured over approximately $\pm 57^\circ$, yielding acceptable coefficients. With no measurement error at all, the array coefficients

could be determined from 32 points measured over $\pm 1^\circ$. For a measurement angular range of $\pm 50^\circ$ for the 80dB case the coefficient error is large but for measurements over $\pm 60^\circ$ or greater the coefficient error is insensitive to angular range.

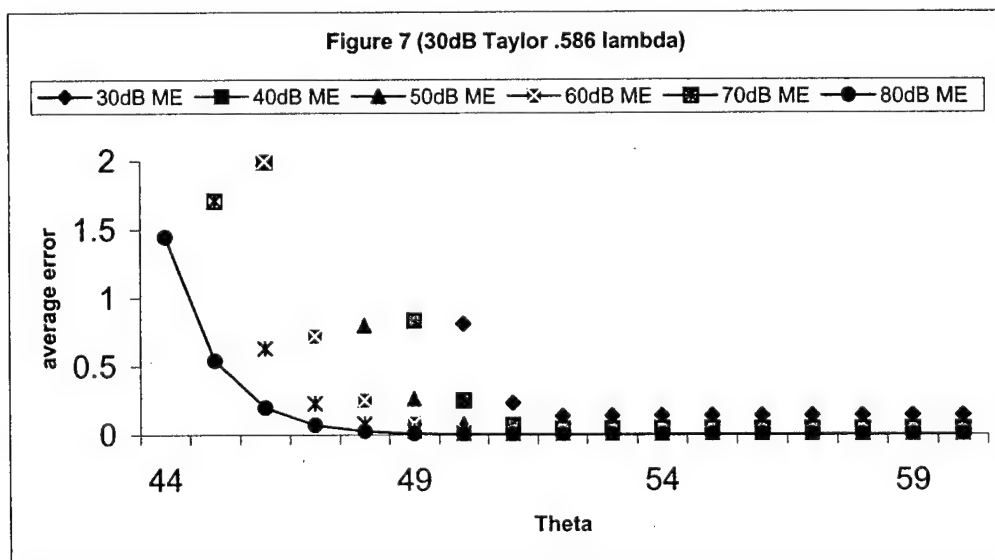


We now examine the effect of changing the aperture weighting. One might expect that a pattern that has high sidelobes outside the angular measurement range would give poor results. The simulations do not confirm this. The errors are independent of sidelobes outside the measurement range. Figure 6 shows the average error for a uniform array.

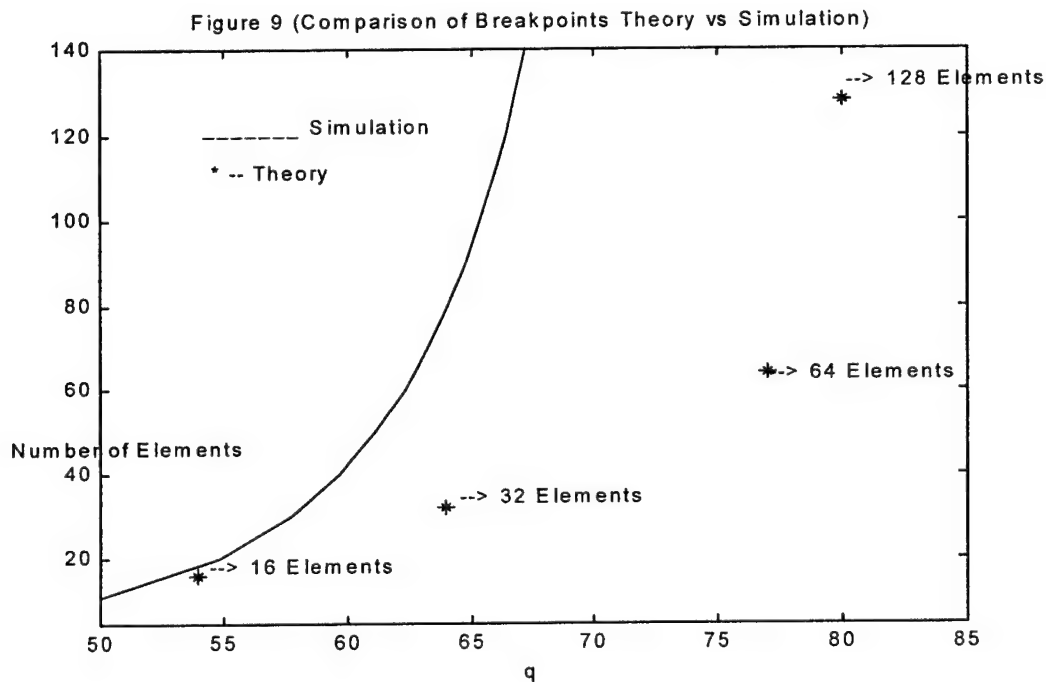
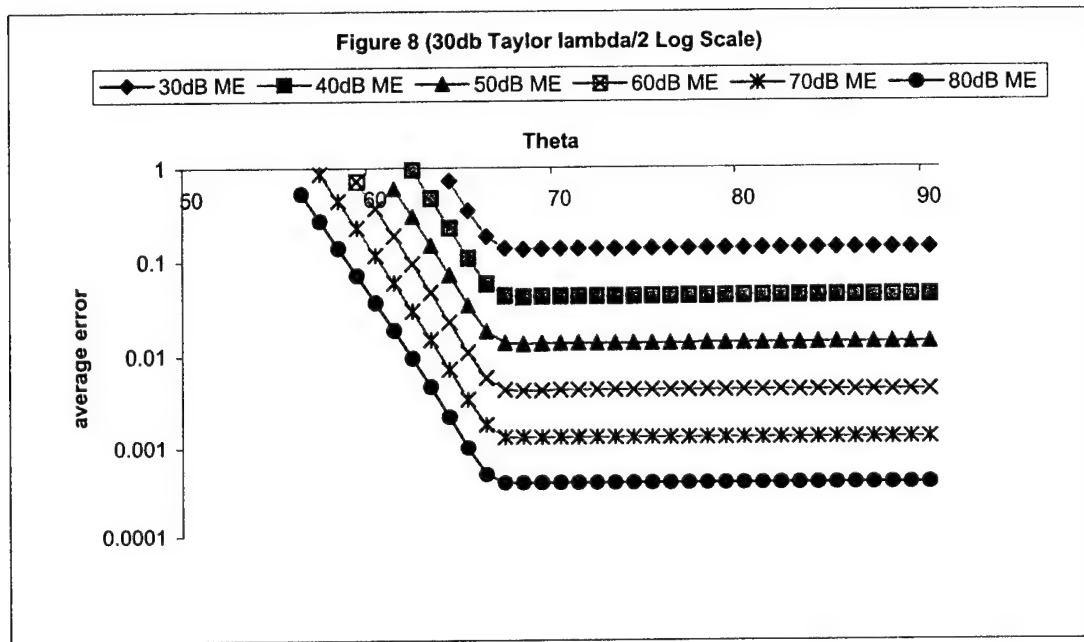
Comparing Figure 5 with Figure 6 shows that the baseline array is identical to the uniform array.



The effect of element spacing is now considered with a more practical case, namely a phased array that scans over $\pm 45^\circ$ and has an element spacing of 0.586λ . As expected from the theory, the change in spacing from $\lambda/2$ shifts the breakpoint in the error curves toward an even smaller angular range (compare Figure 7 with Figure 5). A full measurement range for $\lambda/2$ would be $\pm 90^\circ$. The corresponding range for 0.586λ is $\pm 60^\circ$. Similarly, the angular range at which the break on the error curve occur can be expected to also be reduced. Thus element spacing is a factor in how much the measurement range can be reduced, but array taper is not.



Finally the semi-log plot of Figure 8 establishes that the coefficient error curves have break angles that are independent of the measurement errors. This is also consistent with the theoretical analysis in Section 3. Figure 9 compares the computed breakpoints with four theoretically expected breakpoints.



5. CONCLUSION

We have shown that it is possible to determine array coefficients accurately by measuring the far field pattern over an angular range less than $\pm 90^\circ$. This size of the angular range required depends on the number of elements in the array, the measurement error, and the element spacing. The effect is independent of the array illumination.

6. REFERENCES

- [1] P.R. Franchi, H.E. Tobin, "Arc Range Test Facility", 1992 AMTA Conference, Boulder, CO.
- [2] T.B. Hansen, A.D. Yaghjian, "Plane Wave Theory of Time-Domain Fields", pp. 127, New York: IEEE Press Series.
- [3] M. Nieto-Vesperinas, "Scattering and Diffraction in Physical Optics", New York: John Wiley, 1991.
- [4] C. Muller, "Foundations of the Mathematical Theory of Electromagnetic Waves", New York: Springer-Verlag, 1969.

SPACECRAFT COMMUNICATIONS SYSTEM VERIFICATION USING ON-AXIS NEAR FIELD MEASUREMENT TECHNIQUES

Mr. Thomas Keating, NASA/Goddard Space Flight Center,
Retired

Mr. Mark Baugh, NASA/Goddard Space Flight Center, HST
Carrier Development Integration and Test Manager

Mr. R. B. Gosselin, NASA/Goddard Space Flight Center,
Microwave Engineer, Code 555

Ms. María C. Lecha, NASA/Goddard Space Flight Center,
Microwave Engineer, Code 555

Determination of the readiness of a spacecraft for launch is a critical requirement. The final assembly of all subsystems must be verified. Testing of a communications system can mostly be done using closed-circuits (cabling to/from test ports), but the final connections to the antenna require radiation tests. The Tropical Rainfall Measuring Mission (TRMM) Project used a readily available “near-field on-axis” equation to predict the values to be used for comparison with those obtained in a test program. Tests were performed in a “clean room” environment at both Goddard Space Flight Center (GSFC) and in Japan at the Tanegashima Space Center (TnSC) launch facilities. Most of the measured values agreed with the predicted values to within 0.5 dB. This demonstrates that sometimes you can use relatively simple techniques to make antenna performance measurements when use of the “far field ranges, anechoic chambers, or precision near-field ranges are neither available nor practical. Test data and photographs are provided.

1.0 Spacecraft Description.

The TRMM spacecraft is shown in figures 1 and 2. The dimensions are a height (or length) of approximately 5 meters (16.5 ft) and a cross section of approximately 3.5 meters (11.5 ft). Dry mass is approximately 2,632 kilograms

(5,790 pounds). Critical to mission success was contamination control, especially for the instruments shown in Figure 1. Figure 2 shows the location of the Hi-Gain Communications Antenna. The size and mass of the spacecraft as well as the need for contamination control posed serious limitations to the implementation of a test program to verify the successful mating of the "Forward" (receiving) link and "Return" (transmitting) link of the Communication circuitry to the "Hi-Gain" antenna.

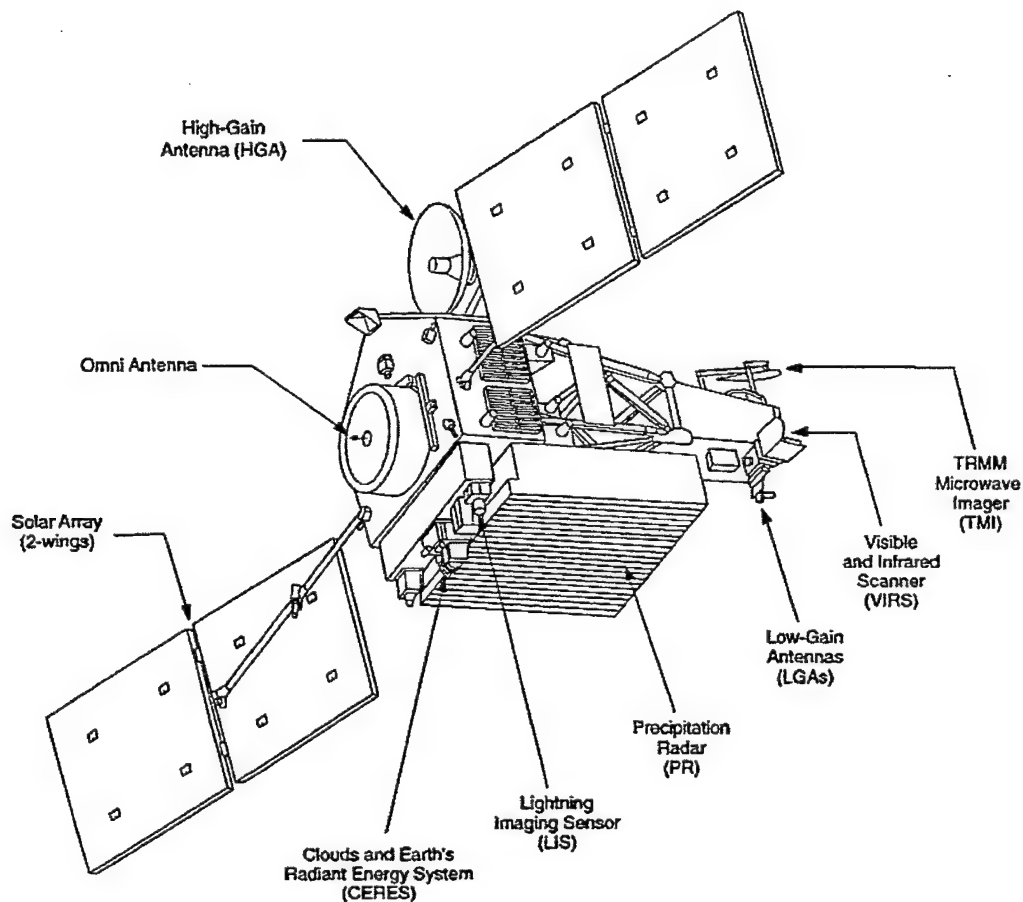


Figure 1: TRMM Drawing of the Spacecraft

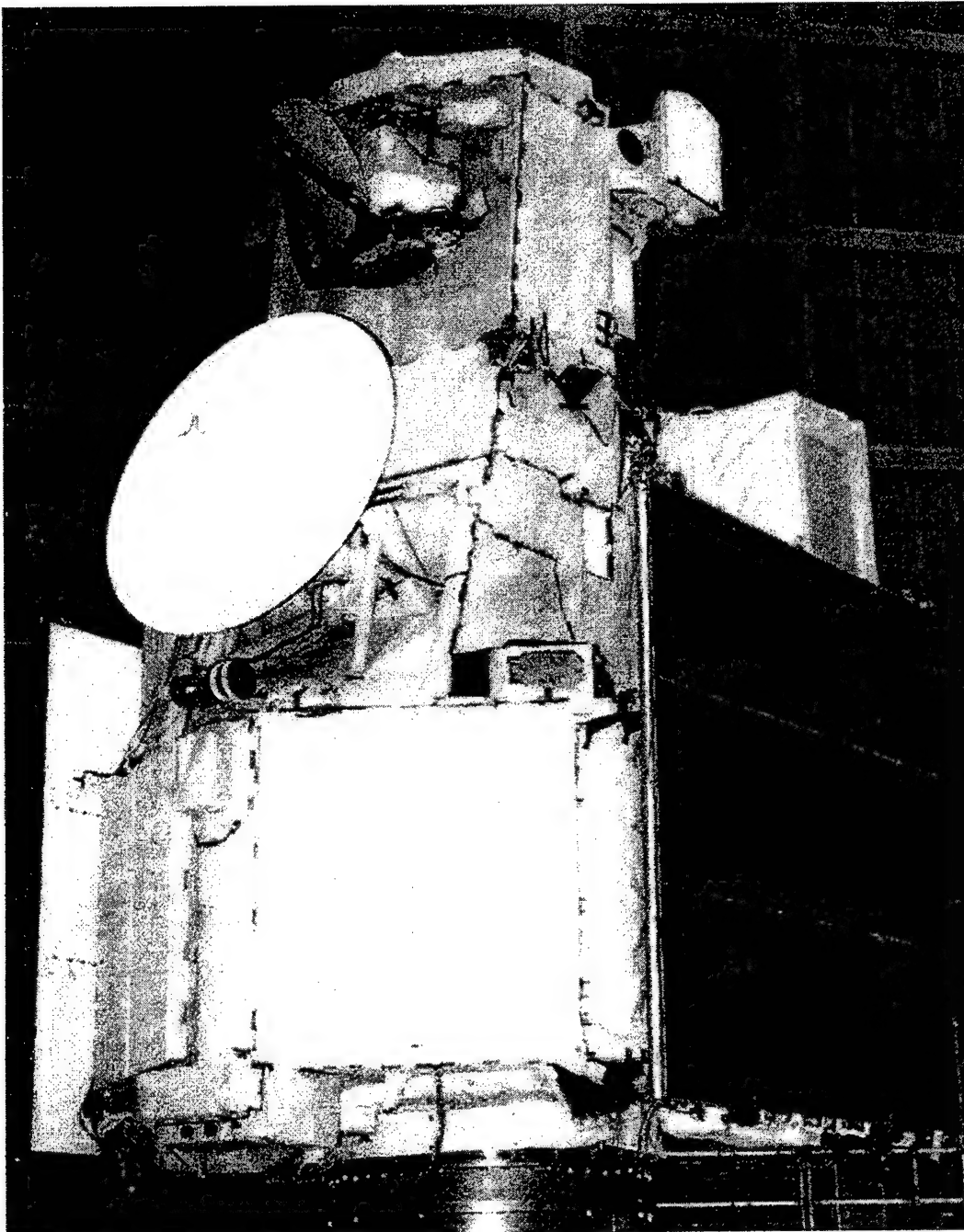


Figure 2: Photograph of the TRMM Spacecraft; the 52-Inch diameter Hi-Gain Antenna is seen in the in the upper left of the photograph.

2.0 Communications Antenna Radio Frequency (RF) links.

There are four RF links to the geostationary Tracking and Data Relay Satellite (TDRS); Namely:

Left Circular Polarization (LCP) Forward (FWD) or receiving,
Left Circular Polarization (LCP) Return (RTN) or transmitting,
Right Circular Polarization (RCP) Forward (FWD) or receiving, and
Right Circular Polarization (RCP) Return (RTN) or transmitting.

FWD (receiving) frequency = 2076.94 MHz
RTN (transmitting) frequency = 2255.5 MHz

3.0 Testing Implementation.

After much consideration of the need for actively verifying (as opposed to assuming a successful mechanical mating) by receiving and transmitting, several approaches were considered. Only two, namely; a “far-field” measurement or a “near-field “ could be considered. Priority was given to the need to perform the verification at both GSFC and TnSC. The GSFC tests were needed to perform “pre-ship” tests and the TnSC were needed to demonstrate successful reassemble (the antenna was removed for shipping to Japan) and launch readiness. Far-field testing would require that the spacecraft be exposed to severe contamination conditions. Large doors would have to be opened to ordinary ambient conditions severely compromising the “clean room” environment. Thus, it was decided to perform the tests using the “on-axis near field power-density” equation shown on page 38 of Microwave Scanning Antennas, Volume I, Academic Press Inc. 1964. Figure 3 depicts the on-axis power density of a tapered circular aperture.

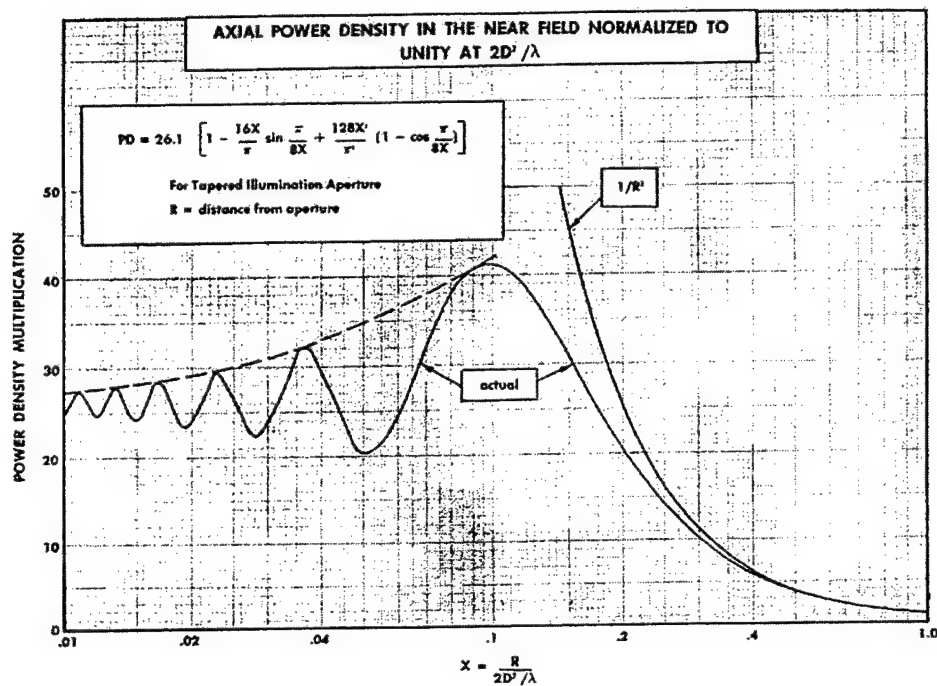


Figure 3: On-axis near field power density - tapered circular aperture

The author had used this information for estimating radiation hazard conditions. It was reasoned that if the testing program could:

- (a) Accurately determine the distances from the spacecraft antenna aperture to a "probe antenna",
- (b) Accurately boresight the two antennas, and
- (c) Could accurately determine both the transmission and reception power levels, then testing within the confines of the "clean rooms" could be relied upon. Initially, it was initially estimated that measurements within 2 dB of predicted values would be acceptable for "verification".

4.0 Testing Program.

Figures 4 and 5 are two views of the test configuration. Figure 6 is a block diagram of the essential RF components of the test. All the cables were measured, the two "probe antennas" were calibrated, and power measurement meters and receiver "AGC" were accurately determined.

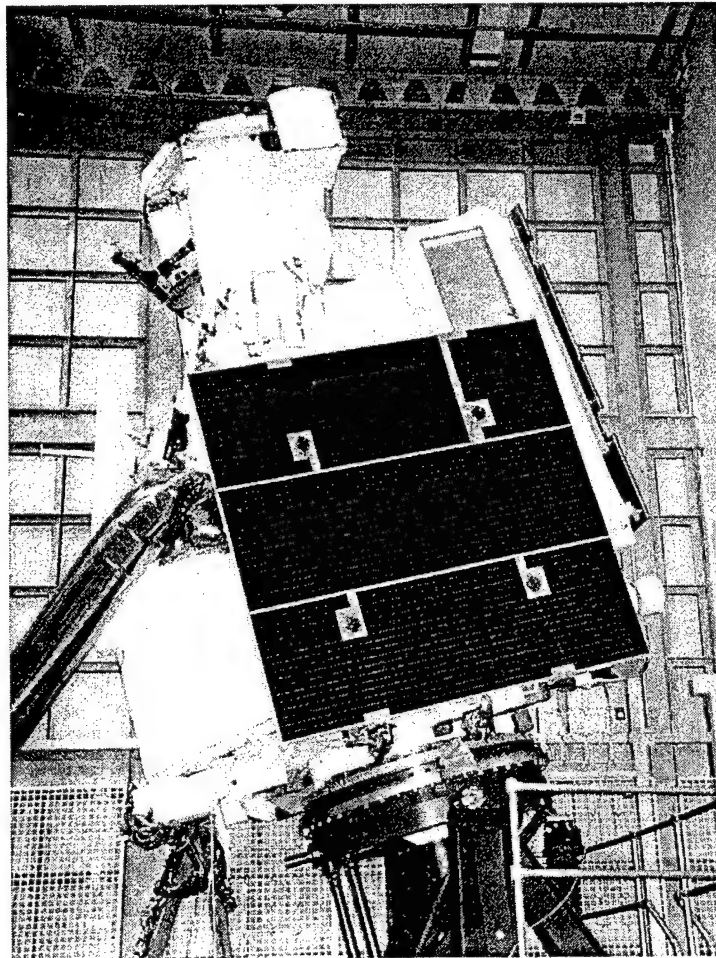


Figure 4: TRMM Spacecraft in "Clean-Room positioned for near field test of Communications Antenna

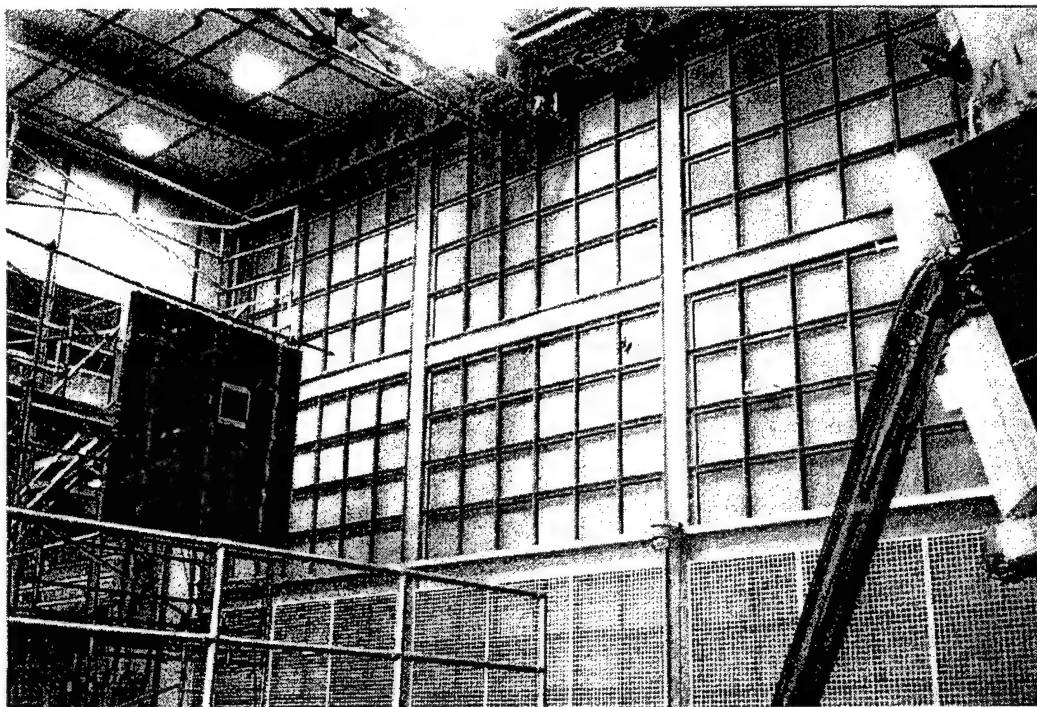


Figure 5: GSFC Range in the Environmental "Clean-Room". LCP Probe Antenna is shown on the RF absorber panel.

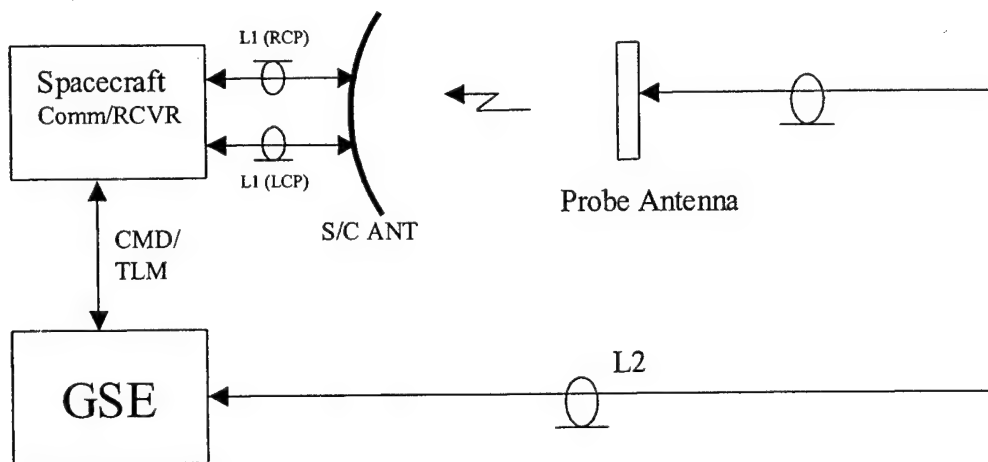


Fig. 6A Forward (Receive) link test set-up

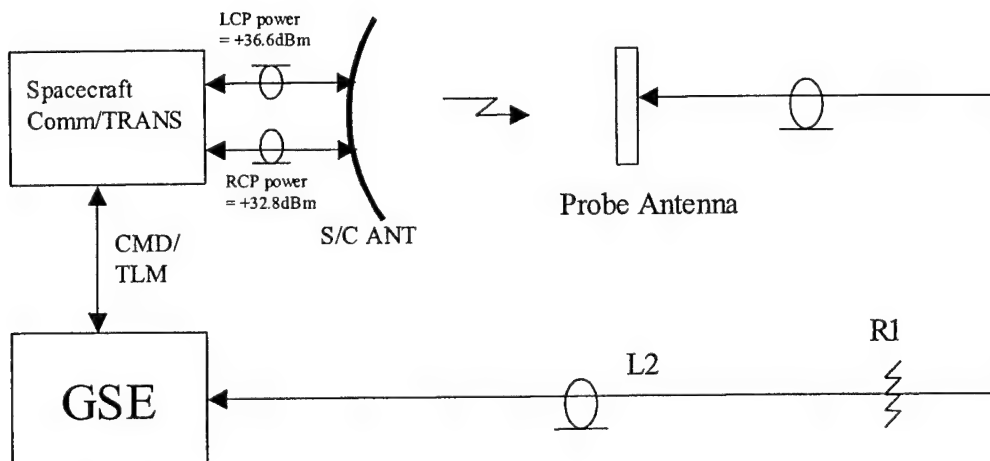


Fig. 6B Return (Transmit) link test set-up
(R1=30dB)

Figure 6: Showing the Forward and Receive Implementation Block Diagram

The parameters used for all computations are shown in Table 1.

Table 1: Constants for Link Calculations

TABLE FOR CONSTANT FACTOR					
		GSFC FWD LCP	GSFC RTN LCP	TnSC FWD LCP	TnSC RTN LCP
LINE L-1	dB	-17.3	0	-17.3	0
LINE L-2	dB	-14.6	-15.7	-22.7	-72.01
GAIN S/C Ant	dB	23.2	27.6	23.2	27.6
GAIN Probe Ant	dB	16.8	16.8	16.8	16.8
FAR FIELD SPACE LOSS	dB	-66.5	-67.9	-66.5	-67.9
FIXED REF "NET"	dB	-58.4	-39.2	-66.5	-95.51
		GSFC: FWD RCP	GSFC RTN RCP	TnSC: FWD RCP	TnSC: RTN RCP
LINE L-1	dB	-18.7	0	-18.7	0
LINE L-2	dB	-14.8	-15.7	-22.1	-51.41
GAIN S/C Ant	dB	23.1	27.4	23.1	27.4
GAIN Probe Ant	dB	6	6.2	6	6.2
FAR FIELD SPACE LOSS	dB	-66.5	-67.9	-66.5	-67.9
FIXED REF "NET"	dB	-70.9	-50	-78.2	-85.71

NOTES:

Forward Link: Line L-1 is from S/C Antenna ports to the S/C receiver

Return Link: Line L-1 is "zero loss" because the transmitter power is referred to the Antenna ports

Line "L-2" is to the Probe Antenna to the GSE; (TnSc L-2 includes 30 dB attenuator)

A total of five range distances were measured at GSFC and four were measured at TnSC. Table 2 compiles the Near-Field factor, which in this table, as well as the test data tables 3 and 4, is defined as the "Hansen Factor (H_f)" in dB.

Table 2
Test Ranges and Hansen Factor (H_f)

Range No.	Range (feet)	Polarization	Link	H_f (dB)
1	32.9	LCP and RCP	FWD	7.5
2	28.9	LCP and RCP	FWD	8.52
3	24.9	LCP and RCP	FWD	9.7
4	21.0	LCP and RCP	FWD	11.0
5	17.0	LCP and RCP	FWD	12.6
1	32.9	LCP and RCP	RTN	8.1
2	28.9	LCP and RCP	RTN	9.2
3	24.9	LCP and RCP	RTN	10.4
4	21.0	LCP and RCP	RTN	11.7
5	17.0	LCP and RCP	RTN	13.2

A complete set of computations for all ranges and links (frequencies) is provided in Appendix A.

6.0 GSFC Test Results.

Table 3 "Near-Field Gain Tests at Goddard Space Flight Center" shows the measured power (Pm) vs the power expected (Pe) for all five range settings. The differences were converted into numeric values and averaged. The numerical average was converted to dB to provide an "Average Deviation in dB".

Table 3: Near-Field Gain Tests at Goddard Space Flight Center

NEAR FIELD GAIN TESTS at GODDARD SPACE FLIGHT CENTER											
RANGE Number	RANGE feet	POL	LINK	FIXED REF dB	Hf db	Pwr Inj dBm	Pwr Exp dBm	Pwr Meas dBm	Pm - Pe dB	Value Numeric	
1	32.9	LCP	FWD	-58.4	7.5	-30.1	-81	-80.72	0.28	1.067	
2	28.9	LCP	FWD	-58.4	8.52	-32.1	-81.98	-81.98	0	1.000	
3	24.9	LCP	FWD	-58.4	9.7	-33.1	-81.8	-81.35	0.45	1.109	
4	21	LCP	FWD	-58.4	11	-35.1	-82.5	-81.98	0.52	1.127	
5	17	LCP	FWD	-58.4	12.6	-37.1	-82.9	-82.93	-0.03	0.993	
AVG DEVIATION (dB)									0.25	1.06	
1	32.9	RCP	FWD	-70.9	7.5	-12.1	-75.5	-74.48	1.02	1.265	
2	28.9	RCP	FWD	-70.9	8.52	-13.1	-75.48	-75.13	0.35	1.084	
3	24.9	RCP	FWD	-70.9	9.7	-14.1	-75.3	-75.13	0.17	1.040	
4	21	RCP	FWD	-70.9	11	-16.1	-76	-75.45	0.55	1.135	
5	17	RCP	FWD	-70.9	12.6	-18.1	-76.4	-75.78	0.62	1.153	
AVG DEVIATION (dB)									0.55	1.14	
1	32.9	LCP	RTN	-39.2	8.1	36.6	5.5	5.45	-0.05	0.989	
2	28.9	LCP	RTN	-39.2	9.2	36.6	6.6	6.61	0.01	1.002	
3	24.9	LCP	RTN	-39.2	10.4	36.6	7.8	7.59	-0.21	0.953	
4	21	LCP	RTN	-39.2	11.7	36.6	9.1	8.95	-0.15	0.966	
5	17	LCP	RTN	-39.2	13.2	36.6	10.8	10.02	-0.58	0.875	
AVG DEVIATION (dB)									-0.19	0.96	
1	32.9	RCP	RTN	-50	8.1	32.8	-9.1	-8.12	0.98	1.253	
2	28.9	RCP	RTN	-50	9.2	32.8	-8	-7.44	0.56	1.138	
3	24.9	RCP	RTN	-50	10.4	32.8	-6.8	-6.31	0.49	1.119	
4	21	RCP	RTN	-50	11.7	32.8	-5.5	-5.12	0.38	1.091	
5	17	RCP	RTN	-50	13.2	32.8	-4	-3.77	0.23	1.054	
AVG DEVIATION (dB)									0.54	1.131	

7.0 TnSC Test Results.

Table 4 "Near-Field Gain Test at Tanegashima Space flight (TnSC)" shows accuracy was not as good as GSFC. The cause is the different mechanisms available for positioning of the RF absorber structure containing the probe antennas. At GSFC the RF absorber structure was mounted on a rigid scaffold (Figures 4 and 5). The determination of the range, horizontal, and vertical positions of the Probe antenna was obtained under reasonably controlled conditions. By contrast, at TnSC, the RF absorber structure was suspended from a crane and ropes were attached to the two bottom corners to steady the structure. This led to a lesser controlled condition for positioning and pointing of the Probe antenna.

NEAR FIELD GAIN TESTS at TANEGASHIMA SPACE FLIGHT CENTER											
RANGE Number	RANGE feet	POL	LINK	FIXED REF dB	Hf db	Pwr Inj dBm	Pwr Exp dBm	Pwr Meas dBm	Pm - Pa dB	Value Numeric	
1	32.9	LCP	FWD	-68.5	7.5		NO TEST				
2	28.9	LCP	FWD	-68.5	8.52	-22	-79.98	-81.03	-1.05	0.785	
3	24.9	LCP	FWD	-68.5	9.7	-23.2	-80	-80.72	-0.72	0.847	
4	21	LCP	FWD	-68.5	11	-24.6	-80.1	-81.35	-1.25	0.750	
5	17	LCP	FWD	-68.5	12.6	-26.1	-80	-80.72	-0.72	0.847	
							AVG DEVIATION (dB)		-0.93	0.807	
1	32.9	RCP	FWD	-78.2	7.5		NO TEST				
2	28.9	RCP	FWD	-78.2	8.52	-10.3	-79.98	-79.45	0.53	1.130	
3	24.9	RCP	FWD	-78.2	9.7	-11.51	-80.01	-79.77	0.24	1.057	
4	21	RCP	FWD	-78.2	11	-12.9	-80.1	-80.1	0	1.000	
5	17	RCP	FWD	-78.2	12.6	-14.4	-80	-80.1	-0.1	0.977	
							AVG DEVIATION (dB)		0.17	1.041	
1	32.9	LCP	RTN	-95.51	8.1		NO TEST				
2	28.9	LCP	RTN	-95.51	9.2	36.6	-49.71	-51.1	-1.39	0.726	
3	24.9	LCP	RTN	-95.51	10.4	36.6	-48.51	-50.2	-1.69	0.678	
4	21	LCP	RTN	-95.51	11.7	36.6	-47.21	-49	-1.79	0.662	
5	17	LCP	RTN	-95.51	13.2	36.6	-45.71	-47.6	-1.89	0.647	
							AVG DEVIATION (dB)		-1.69	0.678	
1	32.9	RCP	RTN	-85.71	8.1		NO TEST				
2	28.9	RCP	RTN	-85.71	9.2	32.8	-43.71	-42.7	1.01	1.262	
3	24.9	RCP	RTN	-85.71	10.4	32.8	-42.51	-41.7	0.81	1.205	
4	21	RCP	RTN	-85.71	11.7	32.8	-41.21	-40.5	0.71	1.178	
5	17	RCP	RTN	-85.71	13.2	32.8	-39.71	-38.7	1.01	1.262	
							AVG DEVIATION (dB)		0.89	1.227	

Table 4: Near-Field Gain Test at Tanegashima Space flight (TnSC)

8.0 Conclusions.

Given limitations in the availability of antenna test facilities or other factors hindering the implementation of more common measurement procedures, the use of the On-axis Near-Field Power Density equation can provide a means to:

- (a) Obtain a quick check of antenna gain, and/or
- (b) Verify operational readiness of a completely assembled communications system.

If care is taken to control the test conditions factors of: (a) the RF transmitted and received powers, and (b) the geometric values of distance and boresight, then an accuracy of ± 0.5 dB is obtainable.

APPENDIX A:

Spacecraft Communications System Verification using On-Axis Near-Field Measurement Techniques

$$F_{\text{fwd}} = 2076.5 \text{ MHz}; \quad F_{\text{rtn}} = 2255.5 \text{ MHz}$$

$$\lambda_{\text{fwd}} = 5.68 \text{ inches}; \quad \lambda_{\text{ret}} = 5.23 \text{ inches}$$

$$\text{Antenna Diameter} = 52 \text{ inches} = D_a$$

$$\text{Far Field for FWD} = FF_{\text{fwd}}; \quad \text{Far Field for RTN} = FF_{\text{rtn}}$$

$$\text{LCP Probe Antenna Gain} = 16.8 \text{ dB (FWD and (RTN))}$$

$$\text{RCP Probe Antenna Gain} = 6.0 \text{ dB (FWD) and } 6.2 \text{ dB (RTN)}$$

$$D_a := \frac{52}{12} \quad \lambda_{\text{fwd}} := \frac{5.68}{12} \quad \lambda_{\text{rtn}} := \frac{5.23}{12}$$

$$D_a = 4.333 \text{ feet} \quad \lambda_{\text{fwd}} = 0.473 \text{ feet} \quad \lambda_{\text{rtn}} = 0.436 \text{ feet}$$

$$FF_{\text{fwd}} := \frac{2 \cdot D_a^2}{\lambda_{\text{fwd}}} \quad FF_{\text{fwd}} = 79.343 \text{ feet}$$

$$FF_{\text{rtn}} := \frac{2 \cdot D_a^2}{\lambda_{\text{rtn}}} \quad FF_{\text{rtn}} = 86.17 \text{ feet}$$

$$\text{Space Loss for Far Field} = L_{\text{ffwd}} \text{ and } L_{\text{ffrtn}}$$

$$L_{\text{ffwd}} := \left[\frac{\lambda_{\text{fwd}}}{4 \cdot \pi \cdot FF_{\text{fwd}}} \right]^2 \quad L_{\text{ffwd}} = 2.254 \cdot 10^{-7} \quad L_{\text{ffwdDB}} := 10 \cdot \log L_{\text{ffwd}}$$

$$L_{\text{ffwdDB}} = -66.471 \text{ dB}$$

$$L_{\text{ffrtn}} := \left[\frac{\lambda_{\text{rtn}}}{4 \cdot \pi \cdot FF_{\text{rtn}}} \right]^2 \quad L_{\text{ffrtn}} = 1.62 \cdot 10^{-7} \quad L_{\text{ffrtnDB}} := 10 \cdot \log L_{\text{ffrtn}}$$

$$L_{\text{ffrtnDB}} = -67.905 \text{ dB}$$

i := 1, 2, 5 i = counter

Rfwd_i :=

Rfwd is the set of test ranges, Rfwd = Rrtn

32.86
28.9
24.93
20.97
16.99

$$Xfwd_i := \frac{Rfwd_i}{FF_{fwd}}$$

Xfwd_i = Xfwd_i is the ratio for the Hansen Factor H_f

1.414
1.364
1.314
1.264
1.214

PDfwd_i is the Hansen formula shown on Page 140 of the 1964 Microwave Engineers Handbook with a counter to compute for all appropriate range values.

$$PDfwd_i := 26.1 \cdot \left[1 - 16 \cdot \frac{Xfwd_i}{x} \cdot \sin \frac{x}{8 \cdot Xfwd_i} + \left[128 \cdot \frac{Xfwd_i^2}{x} \cdot 1 - \cos \frac{x}{8 \cdot Xfwd_i} \right] \right] \quad (1)$$

PDfwd_i =

5.58
7.109
9.342
12.733
18.173

PDfwdDB_i := 10 log PDfwd_i

PDfwdDB_i =

7.466
8.518
9.704
11.049
12.594

$$Rrtn_i := Rfwd_i$$

$$Rrtn_i =$$

2.86
28.9
4.93
0.97
6.99

$$FF_{rtn} := \frac{2 \cdot D_a^2}{\lambda_{rtn}}$$

$$Xrtn_i := \frac{Rrtn_i}{FF_{rtn}}$$

$$Xrtn_i =$$

1.381
1.335
1.289
1.243
1.197

PDrt*n_i* is the Hansen formula shown on Page 140 of the 1964 Microwave Engineers Handbook with a counter to compute for all appropriate range values.

$$PDrt_{n_i} := 26.1 \cdot \left[1 - 16 \cdot \frac{Xrtn_i}{x} \cdot \sin \frac{x}{8 \cdot Xrtn_i} + \left[128 \cdot \frac{Xrtn_i^2}{x} \cdot 1 - \cos \frac{x}{8 \cdot Xrtn_i} \right] \right] \quad (2)$$

$$PDrt_{n_i} =$$

6.522
8.287
10.848
14.687
20.714

$$PDrt_{n_i}DB_i := 10 \cdot \log PDrt_{n_i}$$

$$PDrt_{n_i}DB_i =$$

8.144
9.184
10.353
11.669
13.163

SAC-C SATELLITE ANTENNA GAINS

Valentín Trainotti, Senior Member IEEE, Norberto Dalmas Di Giovanni,
Juan S. Skora, Diego A. Schweitzer.

CITEFA.

Buenos Aires, Argentina

ABSTRACT.

Argentine Scientific Satellite (SAC-C) antennas have been developed in order to fulfill the satellite-ground link requirements for a polar orbit. Wide beamwidth antennas were designed and tested so steering systems are avoided. For the "S" and "X" bands, this task was achieved with modified Kilgus circular polarized antennas. In the "UHF" band, a low profile rectangular patch antenna was developed to fulfill the link requirements. For the "L" band, circular polarized rectangular patch, conical helix and conical helix with reflector antennas were provided by JPL NASA. These "L" band antennas will be used for the different experiments into this frequency band. All these antennas were measured individually but when installed on the satellite mockup their characteristics are modified in some cases substantially.

Antenna radiation patterns and gains were measured installing them on a full-scale satellite mockup. Measurements were performed using an outdoor antenna range to fulfill the far field requirements. Results obtained in each band are provided.

1. INTRODUCTION

Argentine Scientific Satellite (SAC-C) antennas have been developed in order to fulfill the satellite-ground link requirements for a polar orbit. Wide beamwidth antennas were designed and tested so steering systems are avoided.

All antennas installed in the main platform are located among several different scientific experiments metallic structures. These close metallic structures and the metallic satellite structure could affect the antenna radiation characteristics. For this reason, gain measurements must be made with the antennas installed in the

satellite mockup, in order to know the metallic structure effects compared to the gain values obtained for the antennas alone.

Bands, frequencies and functions are shown in the following table:

BAND	Frequency [MHz]	Operation
UHF	401.55	Right Whales Tracking and data adquisition
S	2076	Telemetry and command reception (TT&C)
S	2244	Telemetry and command transmission (TT&C)
S	2255	Low resolution data transmission
X	8386	High resolution data transmission

The characteristics that should be obtained in the designed antennas are:

PARAMETER	UHF	S BAND	X BAND
3 dB Beamwidth	$\pm 60^\circ$	$\pm 60^\circ$	$\pm 60^\circ$
Gain	0 dBic	0 dBi	0 dBi
Polarization	Right hand circular	Right hand circular	Right hand circular
Axial ratio	Less than 10 dB	Less than 10 dB	Less than 10 dB
VSWR	Less than 2	Less than 2	Less than 2

2. "UHF", "S" AND "X" BAND ANTENNAS

2.1 PATCH ANTENNA (395–405 MHz).

This antenna has been designed to work on board the SAC-C satellite. This radiating system is used to link low-resolution data equipment and carrying out the experiment to localize the Southern Hemisphere Right Whales. For both tasks a pattern of practically uniform radiation in the hemisphere toward the earth is required. This task is obtained locating a patch antenna in the main platform of the SAC-C satellite. The main SAC-C platform will look toward the earth as soon as the satellite is stabilized into its orbit. This antenna was chosen due to its low mechanical profile. Low profile permits a minimum shade on the observation cameras and sensors on board of the satellite.

The preliminary designs as well as prototypes have produced optimum results [1]. Several designs of patch type antennas using fiberglass polyester resin and type G10 as dielectric material have been made. This dielectric material fulfills the

space application qualification. Models were also designed with different metallic plane dimensions [2].

Figure 1 shows the patch antenna prototype with G10 as dielectric material.

2.2 “S” BAND MODIFIED KILGUS HELIX ANTENNAS (2 – 2.3 GHz).

This antenna has been designed in order to fulfil the requirements as radiating system on board of the SAC-C satellite. It will work linking the ground station and the satellite for telemetry, control and data. For this reason a practically uniform hemispherically radiation toward the earth is necessary. For these tasks, two similar antennas are used. At the same time a two equal antenna system is used to command the satellite during the early flight phase where the relative satellite position in space is unknown.

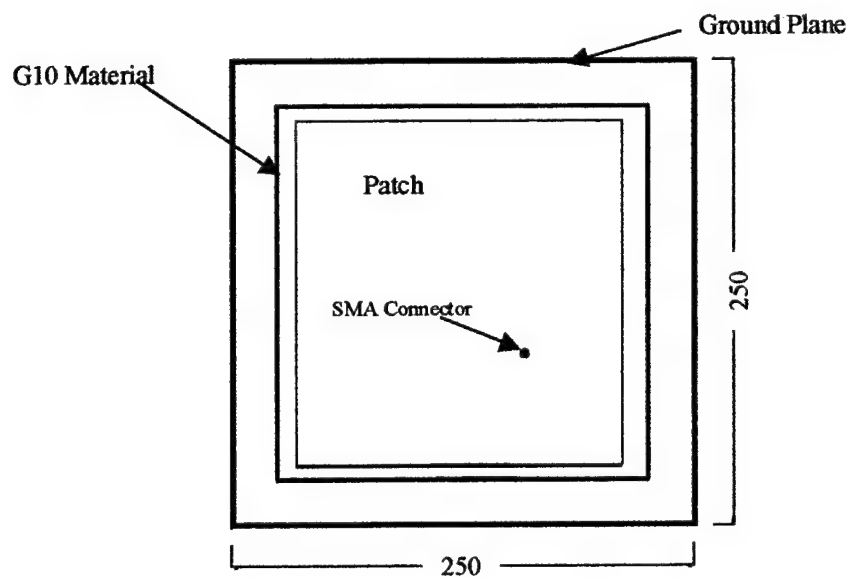
One of the antennas is installed on the looking toward the Earth platform once the satellite is stabilized into the orbit, and the other is installed into the rear platform in order to cover practically all the spherical surface around it. In this manner any command order from the earth station can reach the satellite no matter what is the satellite position in space [1].

During the development of the Kilgus modified helix, a surface corresponding to 180 degrees beamwidth with circular polarized radiation has been covered. Radiation patterns are really optimum nevertheless the optimum axial ratio does not fulfil the same frequencies. For this reason a research was done in order to obtain the same optimum characteristics of both radiation pattern and axial ratio as well gain and input impedance [3].

Figure 2 shows the model 4 prototype of modified Kilgus helix antenna used during measurements.

2.3 “X” BAND MODIFIED KILGUS HELIX ANTENNA (8-8.4GHz).

This antenna has been designed to work onboard of SAC-C satellite. It will work linking the ground station and the satellite for high resolution images data. For this reason, a practically uniform hemispherical radiation toward the earth is necessary. To fulfil this task, two similar antennas are used. These antennas are installed on the platform oriented toward the earth once the satellite is stabilized into the orbit [1].



Dimensions in mm

Figure 1, Patch Antenna prototype with G10 as dielectric material

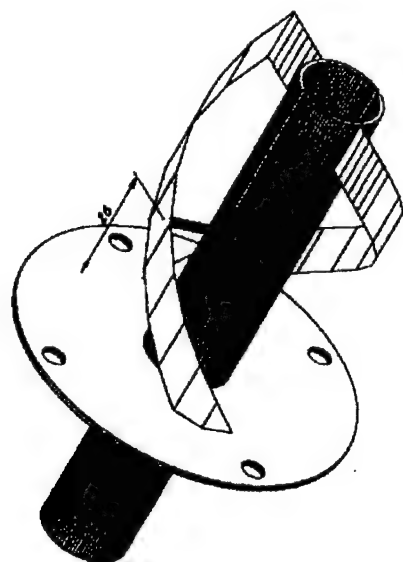


Figure 2, Model 4 "S" Band Modified Kilgus Antenna Prototype

During the development of the Kilgus modified helix, an illuminated surface has been covered. This surface is included within a circular polarized radiation beamwidth close to 180 degrees. Radiation patterns are really optimum nevertheless the optimum axial ratio does not fulfil the same frequencies. For this reason a research was started in order to obtain the same optimum characteristics of both radiation pattern and axial ratio as well gain and input impedance [4].

Figure 3 shows the model 2 prototype of the modified Kilgus helix antenna.

3. ANTENNA GAIN MEASUREMENTS

3.1 ANECHOIC CHAMBER MEASUREMENTS

All antennas were measured previously, as an isolated antenna element to evaluate their gain properties. To perform these tasks, antenna gains were measured in the anechoic chamber using the "Three Antenna Method" [1].

The anechoic chamber gain measurement had been done in the antenna polar axis or perpendicular to the main satellite platform.

3.2 MOCKUP GAIN MEASUREMENTS.

Antennas were installed on the satellite real scale mockup. Their locations are on a metallic structure supported by a metallic tube (except for the "GPS" rectangular patch antenna). This tube is attached to the main satellite platform that will look toward the earth when the satellite is stabilized in its orbit. In the case of the "GPS" circular patch antenna, the metallic tube is attached to the propulsion platform.

In figure 4, an outline of the main (a) and the propulsion (b) platforms of the satellite are shown and the location of all the antennas can be seen.

Gain measurements have been carried out in the far field. Keeping in mind the far field distance criterium or $R = 2 \cdot D^2 / \lambda$. The minimum measurement distance (R) depends on what frequency band the measurement is done. In this case the maximum satellite dimensions take into account the simulated solar panels.

For the "UHF" band, it corresponds at a distance $R=20$ meters. For this reason, the reference antenna was installed at a distance of 25m in order to assure the far field criterium.

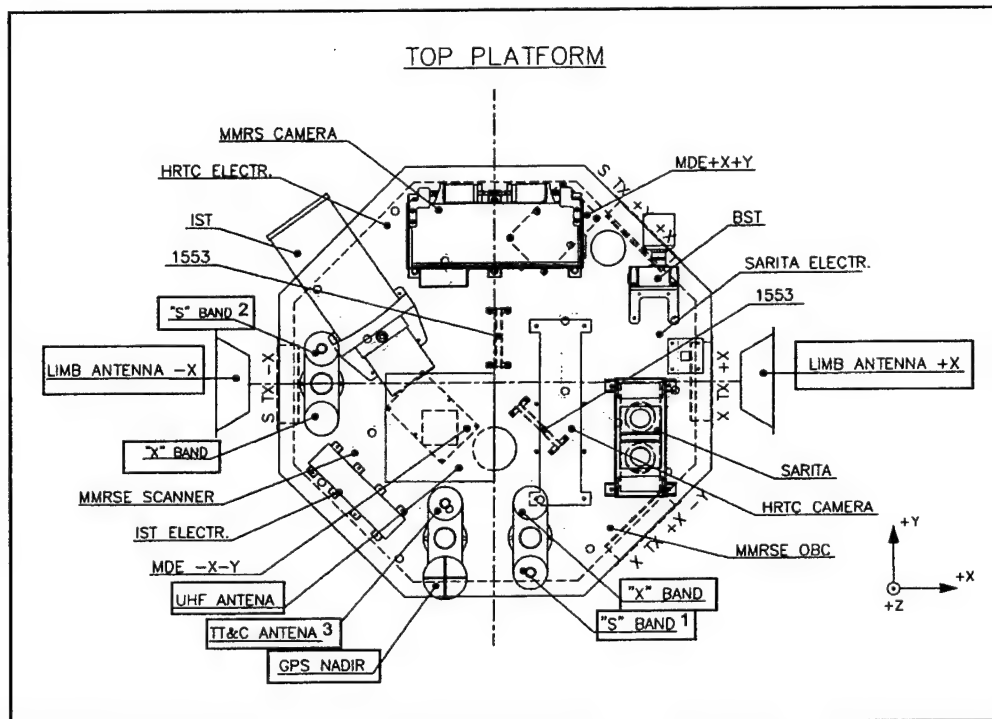
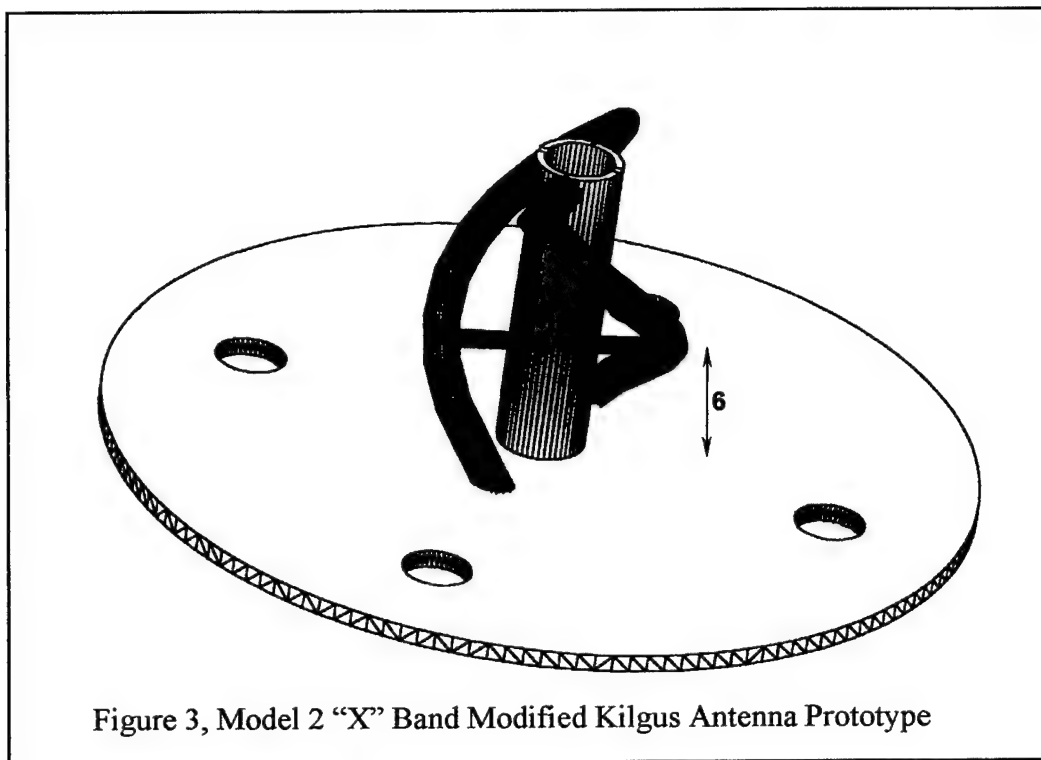


Figure 4 a, Antenna Location in Satellite Main Platform

The measuring distance must be larger than 110 meters for the "S" band, so that, the reference antenna was installed at the distance of 180 meters.

For the "X" band measurements, the minimum distance must be larger than 300 meters, but in this case the reference antenna was installed at the distance of 180m, and it corresponds to $1.1 \cdot D^2/\lambda$. Though the far field criterium was not fulfilled, it was 10% more than D^2/λ . This distance value will not produce substantial errors in gain measurements, but it would produce small variations in the radiation pattern measurements when the secondary lobe levels were computed and high gain antennas are involved.

Several reference antennas were used according to the measurement band. In the case of, "S" and "X" band frequencies, this reference antenna is a parabolic reflector type, while a cylindrical helix was used as a reference antenna for the "UHF" band.

In all frequency bands, the reference antenna is a circular polarization antenna helical type, and its beamwidth is enough to illuminate uniformly the satellite mockup. This avoids in part the signal level produced by the terrestrial reflection. This value is considered to be around 20 dB below the direct ray-illuminating signal according to the transmitting antenna pattern.

In figure 5, an outline of the antenna test range used in the "UHF" band gain measurements is shown. Figure 6 shows a sketch of the antenna range used in "S" and "X" bands gain measurements.

To carry out the gain measurement a spectrum analyzer HP8563E is used. It allows to measure the level of the operation frequency received power. It's important filtering the influence of any spurious signal. These spurious signals are visualized in the screen of the instrument and measurements are not carried out if the interfering signals are at least 30 dB below the useful signal.

Wide band power measurements have been discarded because interference signal level from any part of the spectrum, is extremely high and comparable with the useful signal level, not permitting accurate measurements.

Gain Antenna determination installed in the mockup is very important because this information is paramount for the link budget calculation between the satellite and the earth station. This measurement must be made in the satellite axis as well as in the angular positions of $\pm 30^\circ$ and $\pm 60^\circ$ to assure the link in each position.

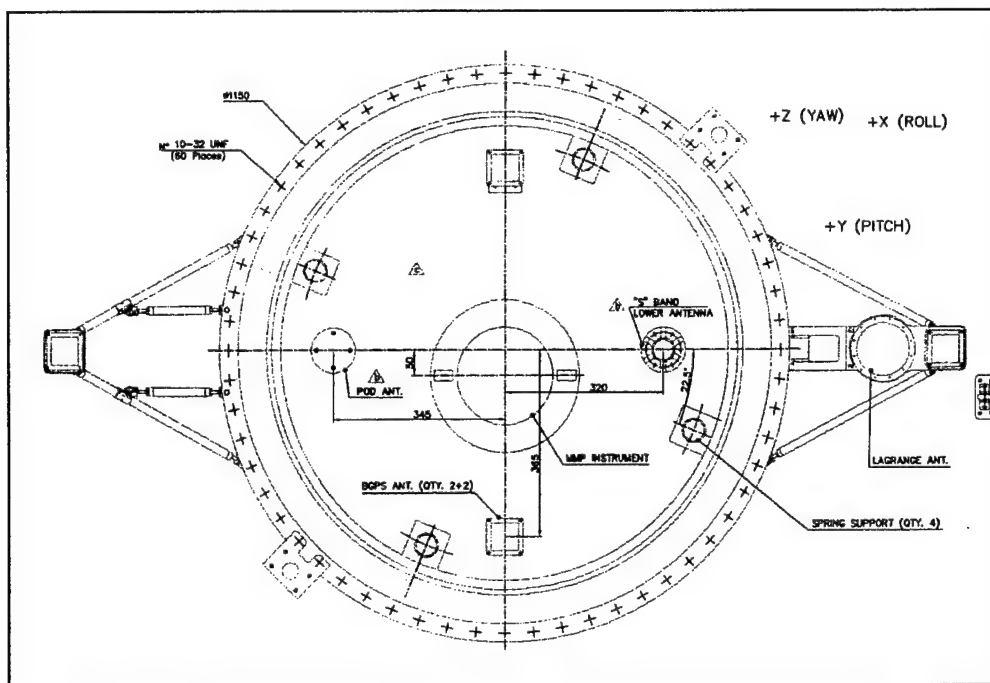


Figure 4 b, Propulsion Platform Antennas Location

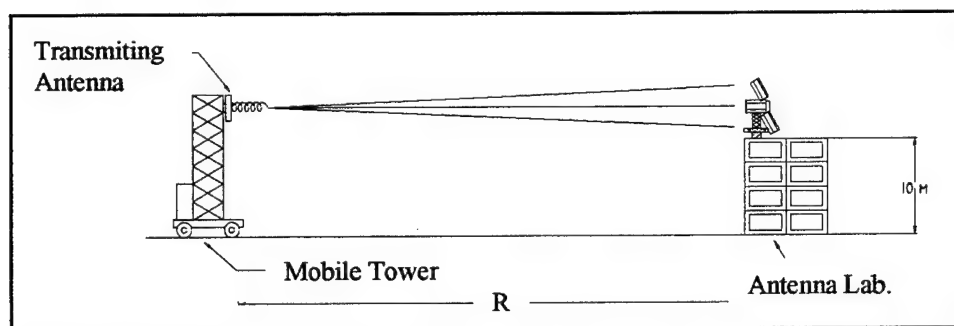


Figure 5, Antenna Test Range used in "UHF" and GPS Bands

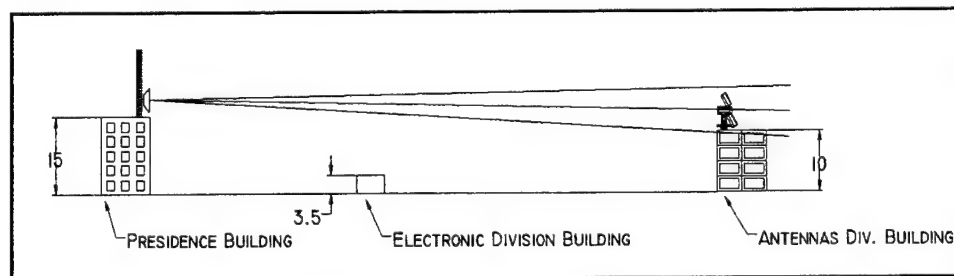


Figure 6, Antenna Test Range used in "S" and "X" Bands

Due to the difficulty of using the three antennas method at these distances, the measurement is made by comparison with an antenna previously calibrated in the anechoic chamber.

The comparison antenna is a cylindrical helix whose gain is approximately of 6 dBic for the "UHF" band, 13 dBic for the "S" band and 12 dBic for the "X" band.

Gain measurement results for the UHF antenna can be seen in figure 7. Results obtained for S1 antenna can be seen in figure 8 for all the antenna positions, i.e. for 0° , $\pm 30^\circ$ and $\pm 60^\circ$. The same measurements for the S2 antenna can be seen in figure 9.

For the antennas S3-S4 installed on the main and rear platform five positions measurements on each frequency were made. First, pointing the main platform toward the reference and later, repeating the same measurements, pointing the rear platform to the reference. Results can be seen in figure 10.

Gain measurement results for "X" Band antenna can be seen in figure 11 (X1) and figure 12 (X2), for all the antenna positions, i.e. for 0° , $\pm 30^\circ$ and $\pm 60^\circ$.

4. "GPS" BAND ANTENNAS (1400 – 1700 MHz)

4.1 SYSTEM DESCRIPTION

These antennas are part of two experiments on board of the Argentine Scientific Applications satellite SAC-C. Four antennas are components of GOLPE experiment (Gps OccuLtation and Passive reflection Experience) among them, two are reflector type conical helix, one is a conical helix located in the principal platform and the last one is a circular patch located in the rear platform. (GPS is the standard Global Positioning System). Additional four rectangular patch antennas are used in the GPS Tensor system of INES experiment (Italian Navigation Experiment for SAC-C).

The GOLPE instrumentation consists of one TurboRogue III GPS receiver, provided by NASA JPL, attached to four independent high gain antennas respectively pointed in the zenith, nadir, fore and aft velocity directions. Three of these antennas are right circular polarized and the Nadir antenna is left circular polarized.

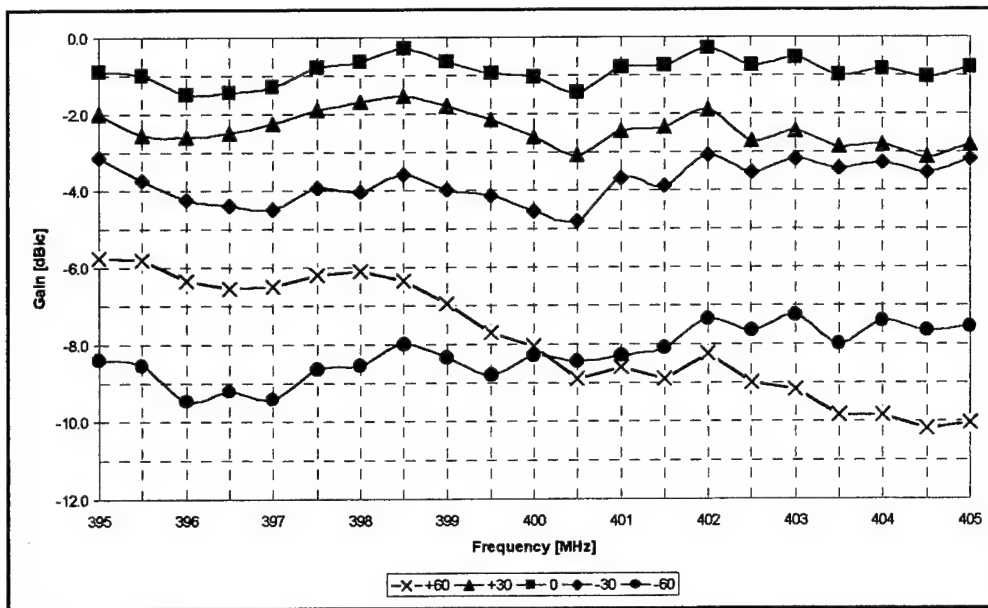


Figure 7, "UHF" patch antenna gain, placed on the SAC-C satellite mockup. A mean between the measurements of two mockup positions was made.

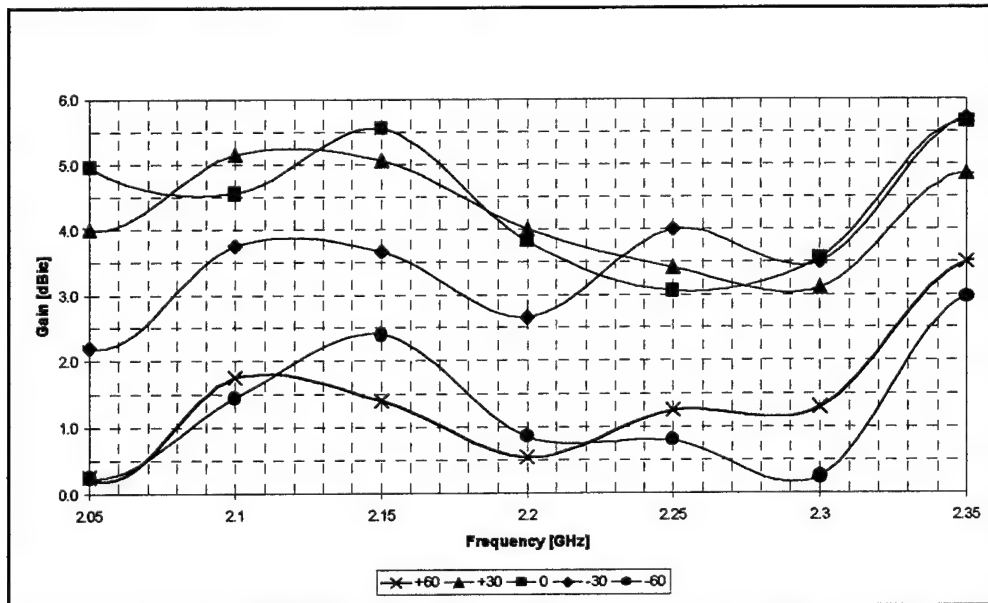


Figure 8, S1 "S" band antenna gain, placed on the SAC-C satellite mockup. A mean between the measurements of two mockup positions was made.

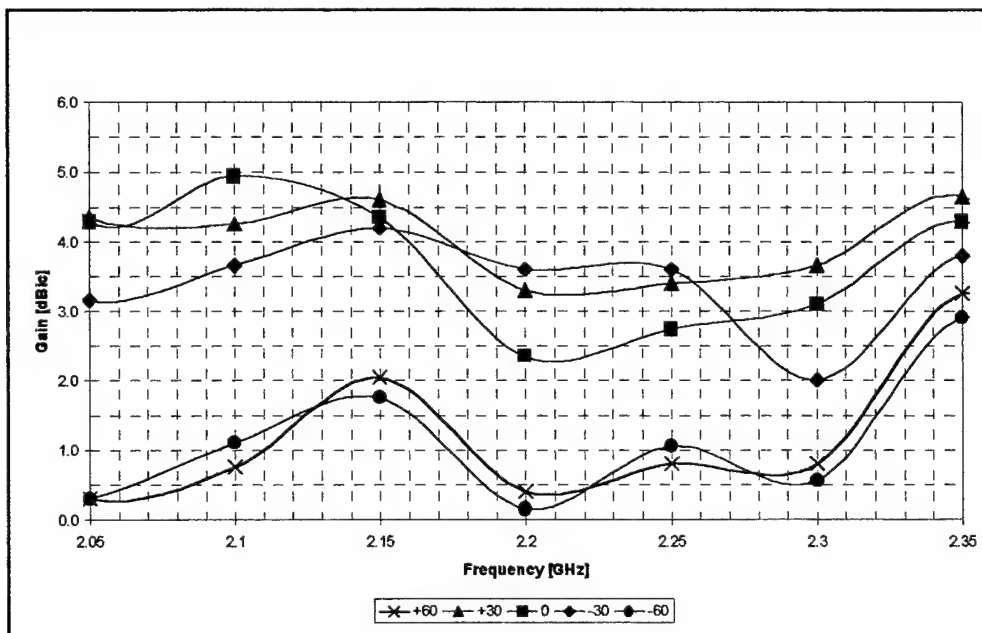


Figure 9, S2 "S" band antenna gain, placed on the SAC-C satellite mockup. A mean between the measurements of two mockup positions was made.

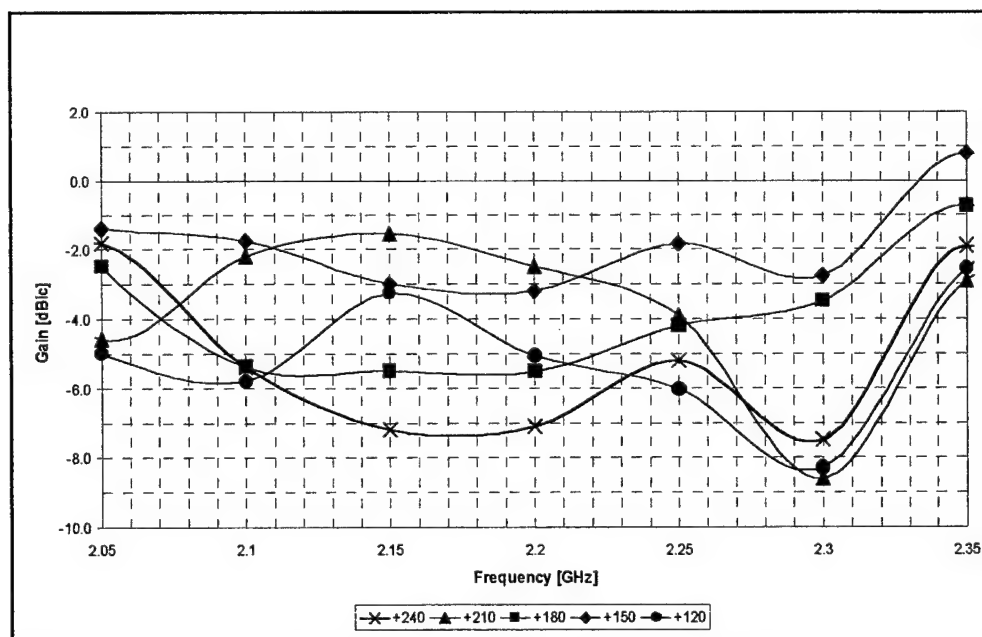


Figure 10, S3-S4 "S" band antenna gain, placed on the SAC-C satellite mockup. A mean between the measurements of two mockup positions was made.

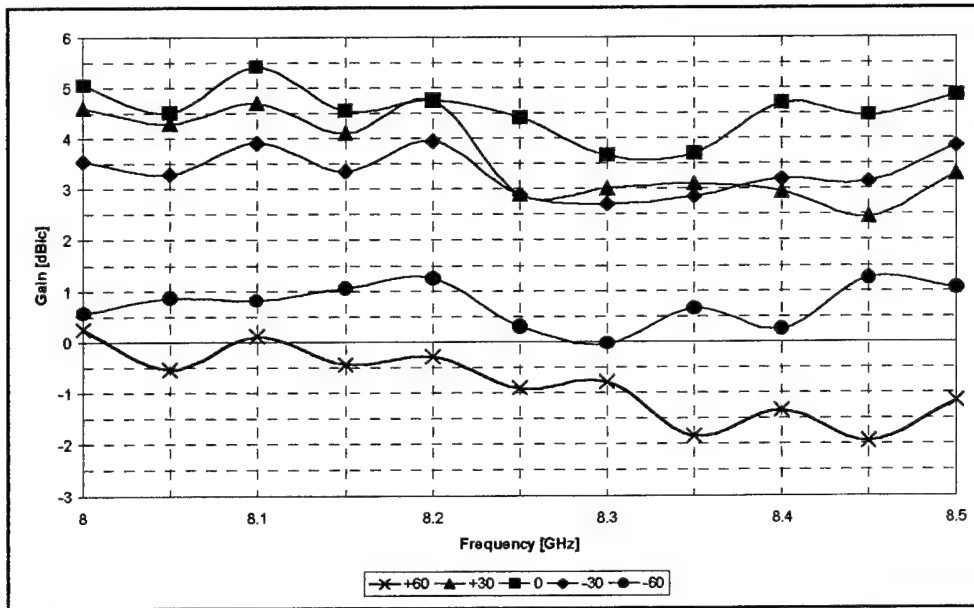


Figure 11, X1 "X" band antenna gain, placed on the SAC-C satellite mockup. A mean between the measurements of two mockup positions was made.

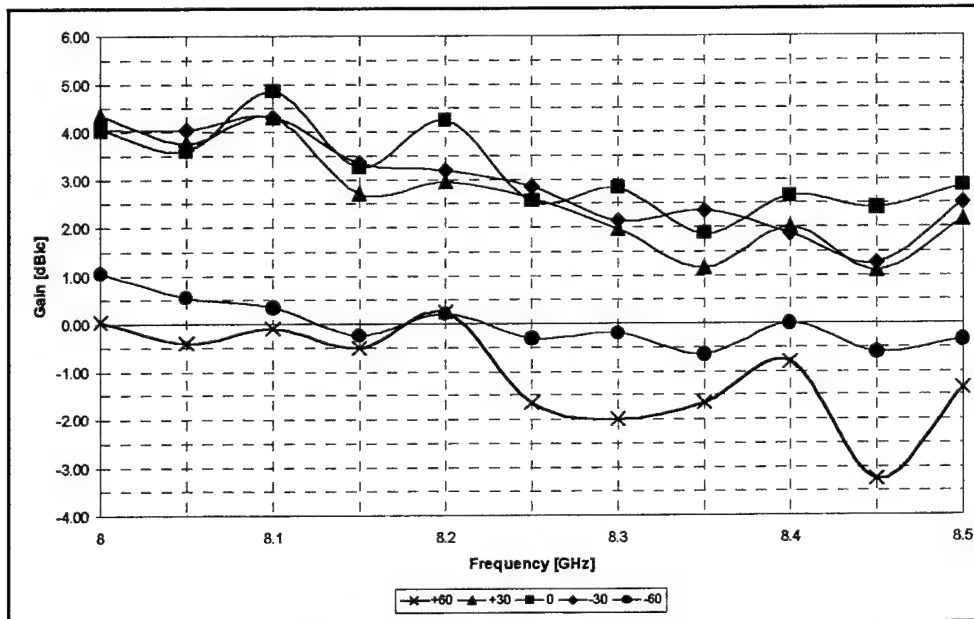


Figure 12, X2 "X" band antenna gain, placed on the SAC-C satellite mockup. A mean between the measurements of two mockup positions was made.

The objective of this instrument is to record all the direct, refracted and Earth reflected **GPS** signals as received by the low earth orbiting SAC-C satellite.

The high gain fore and aft antennas (conical helix with reflector) will receive setting and rising satellites occulted by the Earth's limb permitting the use of **GPS** occultation techniques to determine atmospheric temperature and water vapor at a rate of nearly 500 per day uniformly distributed over the globe. The nadir pointing antenna (conical helix) will be used to determine the utility of **GPS** signals reflected from the Earth's surface to characterize the elevation and roughness of the Earth's surface for applications such as the determination of oceanic circulation and surface winds.

The scientific objective of this experiment is the determination of ionospheric and atmospheric structure and the study of **GPS** signals reflected from the Earth's surface.

The left circular polarized conical helix antenna is installed on a metallic support attached directly on the main platform of SAC-C satellite and it looks toward the earth. The two conical helixes with reflector antennas are located at two lateral faces of the satellite body (Limb antennas). The remaining circular patch antenna is installed over a metallic support and placed in the propulsion platform of the satellite.

The **INES** experiment is composed of two separate systems: the **GPS** Tensor receiver and the Lagrange **GNSS** receiver (Global Navigation Satellite Systems)

These two receivers have completely different objectives. The **INES** instruments are developed by LABEN under funding by the Italian Space Agency (ASI).

The **GPS** Tensor is used by the SAC-C satellite, as a primary **AOCS** (Attitude Orbit Control Subsystem) sensor providing navigation and attitude solutions.

The **GPS** TensorTM receiver is a space-qualified **GPS** attitude and orbit determination system that provides 13 output states of navigation and attitude information. It is composed of two major subassemblies: the receiver/processor unit (RPU) with a RS-422 interface and four rectangular patch antennas and preamplifiers.

All the antennas involved in the **GPS** experiments are provided by NASA, JPL and LABEN. The performance tests of those **GPS** antennas were performed in the CITEFA Antenna and Propagation Laboratory.

At the same time construction, adjustment and testing of several models of conical helices similar to those installed on board of the SAC-C satellite, were made at the CITEFA's Antennas and Propagation Lab, in order to get antennas for pattern and gain measurements [5].

Antennas involved on the different experiments should have a voltage standing wave ratio less than 2 ($VSWR < 2$) and they must be of right hand circular polarization (except for the left hand polarized NADIR antenna) within the operation band. To fulfill this last requirement any antenna must have an axial ratio less than 6 dB.

Figures 13 to 16 show the sketches of these antennas and their main characteristics are:

-CIRCULAR PATCH ANTENNA.

This antenna is supplied by Sensor Systems Inc., Chatsworth, California, United States. Antenna part number S67-1575-14 and serial number 1952 was tested at the CITEFA's Antennas and Propagation Lab.

-NADIR CONICAL HELIX ANTENNA.

This is a left-hand circular polarized conical helix antenna. This antenna is made up by a two turns conical helix. This helix is made up by wire straight pieces, which are placed around a dielectric pyramidal structure and mounted over a metallic ground plane.

-LIMB CONICAL HELIX ANTENNA.

This is a conical helix antenna of right hand circular polarization with an additional metallic reflector. Antenna is made up by two-turn helix formed by straight conductive pieces, which was placed around a dielectric pyramidal structure and mounted over a metallic ground plane.

-RECTANGULAR PATCH ANTENNA.

These antennas were supplied by Trimble Navigation. Antennas with part number 16185-00 and serial numbers 0080243465, 0080243458 and 0080245463 were tested at the CITEFA's Antennas and Propagation Lab.

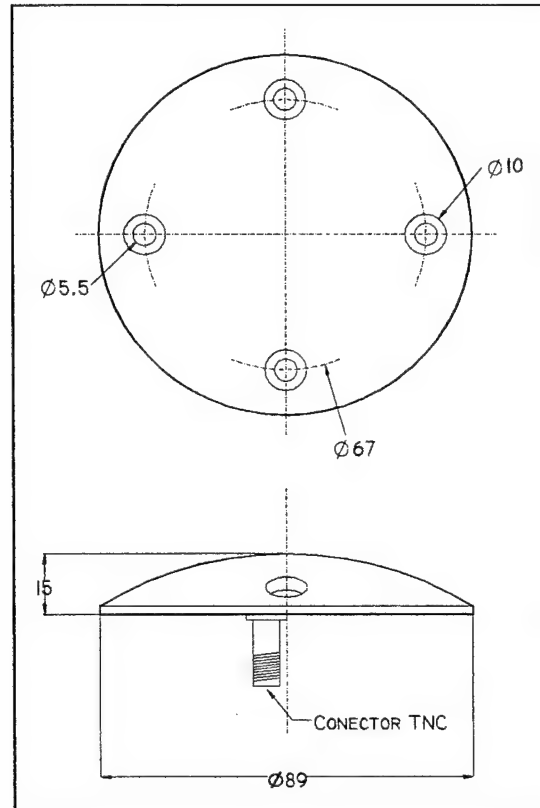


Figure 13, Circular Patch Antenna Outline

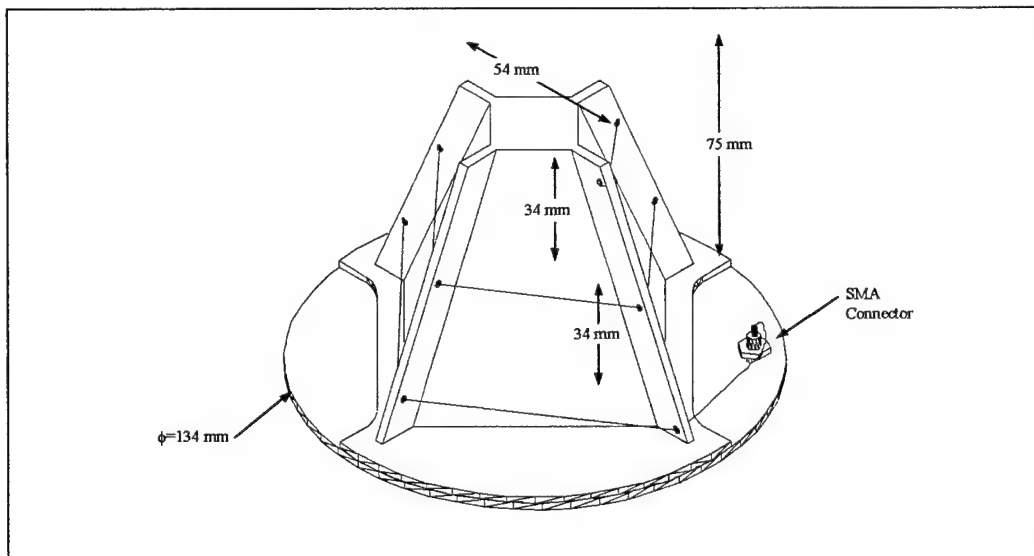


Figure 14, Nadir Conical Helix Antenna Outline

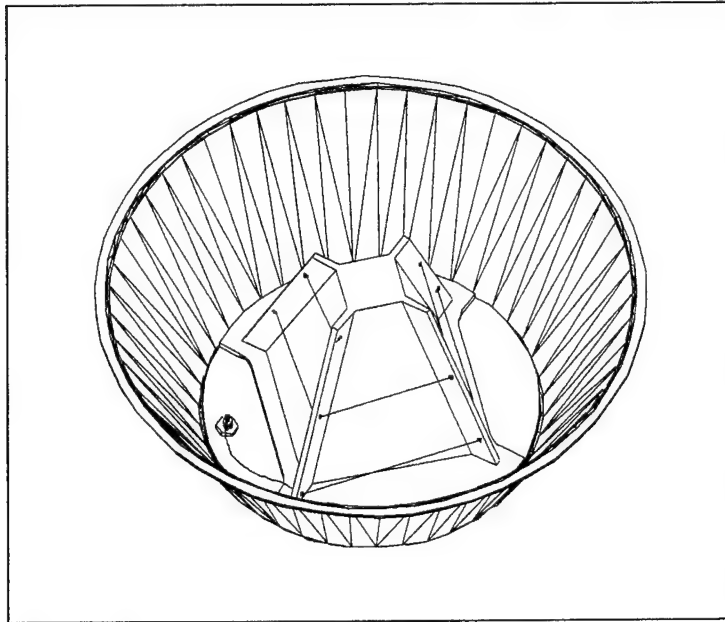


Figure 15, LIMB antenna outline

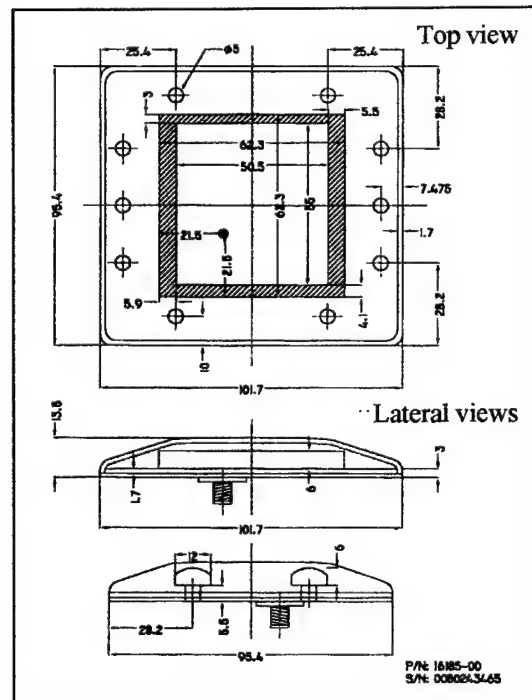


Figure 16, Rectangular patch antenna outline

4.2 SATELLITE MOCKUP MEASUREMENTS.

Different kinds of antennas were installed on the satellite real scale mockup. Antennas installed in the main and propulsion platforms are located among several metallic structures of the different scientific experiments. These close metallic structures and the metallic satellite structure could affect the antenna radiation characteristics. For this reason radiation patterns must be determined with the antenna installed in the satellite mockup, in order to know the metallic structure effects compared to the radiation patterns of the antenna alone.

4.2.1 Radiation patterns.

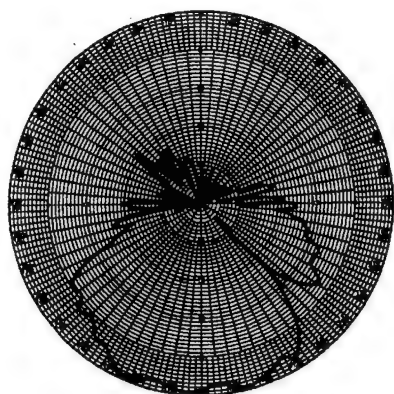
Measurements of radiation patterns have been carried out in the far field. Keeping in mind the far field distance criterium or $R = 2 \cdot D^2 / \lambda$, the minimum measurement distance for the "GPS" band corresponds at a distance $R = 60$ meters.

In this case the maximum satellite dimension is taken into account due to the simulated solar panels. For this reason, the reference antenna was installed at a distance of 80m in order to assure the far field criterium. The reference antenna is of the helical type designed to obtain right circular polarization and its beamwidth is enough to illuminate the satellite mockup. This avoids in part the signal level produced by the terrestrial reflection. This value is considered to be around 20 dB below the direct ray-illuminating signal.

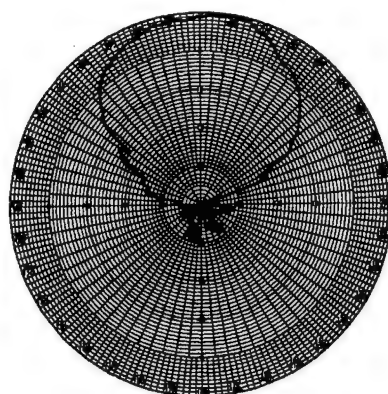
Figure 5 shows an outline of the antenna test range. The location of each antenna in the satellite can be seen in figure 4.

Radiation patterns measured at 1575 MHz, for the GPS antennas installed in the SAC-C satellite mockup are shown in figures 17.

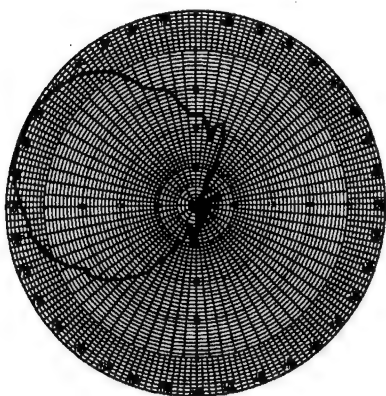
The NADIR and LIMB antennas installed in the SAC-C satellite mockup were reproduced at CITEFA Antennas and Propagation Lab, because only flight antennas were received from JPL and they were tested in radiation patterns, input impedance and gain. These antennas were reproduced for mockup measurements.



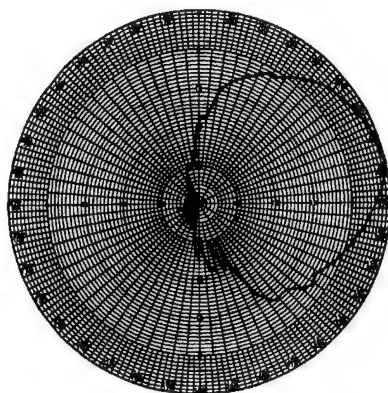
Circular Patch Antenna



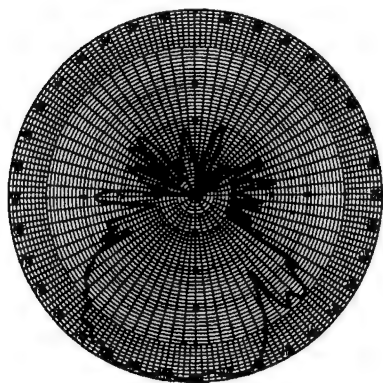
Nadir Antenna



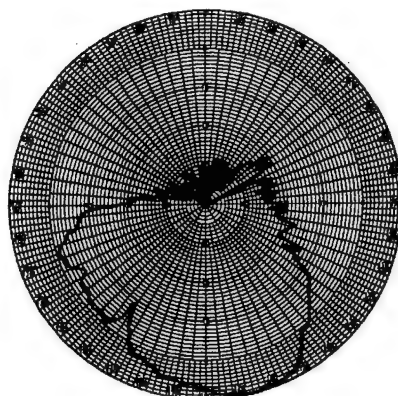
Left side Limb Antenna



Right side Limb Antenna



Rectangular Patch Antenna
Propulsion platform



Rectangular Patch Antenna
Propulsion platform

Figure 17, GPS Antennas radiation patterns

4.2.2 Gain determination.

As it was indicated previously, gain measurements were performed using a spectrum analyzer HP 8563E by means of comparison technique. The comparison antenna is a cylindrical helix whose gain is approximately of 12 dBic.

The measured gain of the GPS antennas are shown in figures 18 to 21. Gain was measured between 1400 to 1700 MHz, to analyze the behavior of this parameter as a function of frequency.

5. CONCLUSIONS.

Measurements carried out for the isolated antennas are inside the specified values.

When the antennas are installed on the satellite mockup the strong influence of the metallic structures surrounding it can be observed. This effect produces an important distortion in the measured radiation patterns. This is evident when a comparison is made with values obtained on the isolated antenna. Similar effect can be observed among gain values measured in the antenna installed in the satellite mockup with respect to those obtained with the isolated antenna.

Although the values obtained for gain and radiation patterns are not optimum, conclusions are that link in this band will be carried out without any problem due to the gain values obtained by measurements that fulfill specifications.

6. ACKNOWLEDGMENTS.

The authors want to express their gratitude to División Antenas and Propagation personnel as well as the Prototype Workshop Department of CITEFA for their support during the development and the measurement of the several prototypes of these antennas.

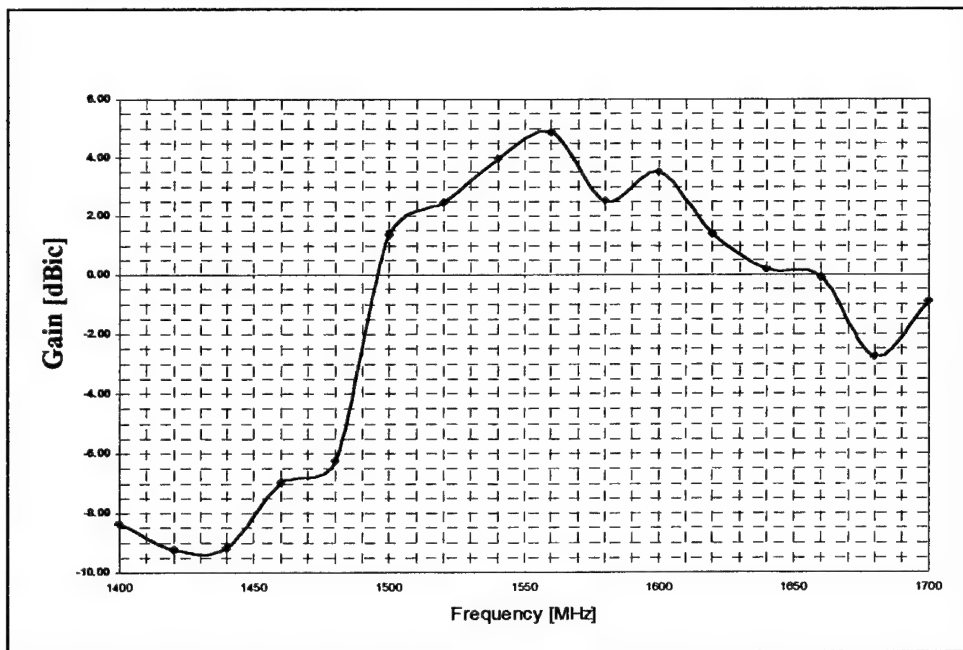


Figure 18, Circular Patch Antenna Gain, placed on SAC-C satellite mockup

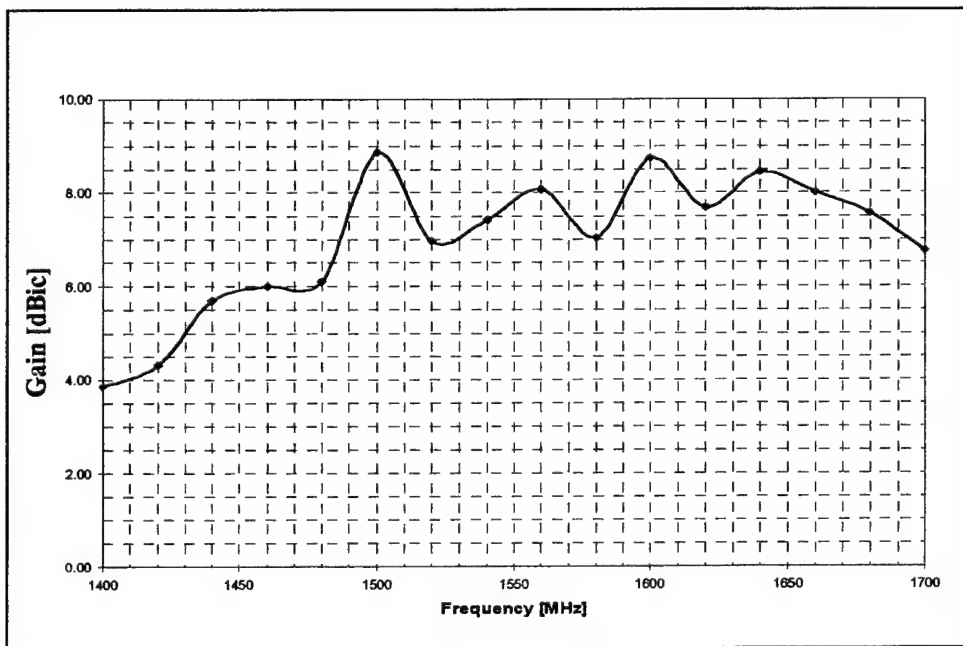


Figure 19, NADIR Antenna Gain, placed on SAC-C satellite mockup

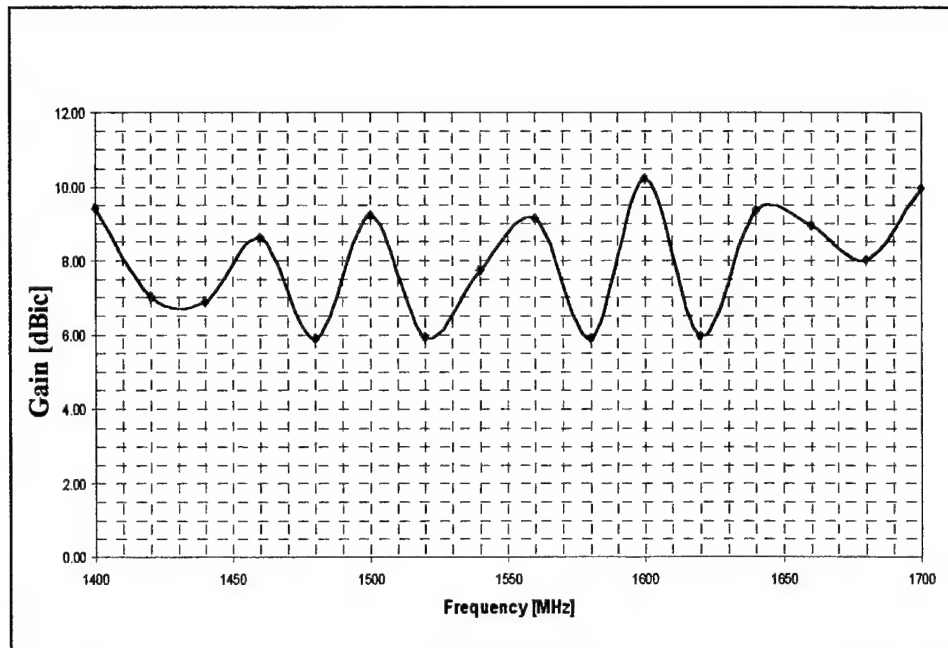


Figure 20, LIMB Antenna, placed on SAC-C satellite mockup

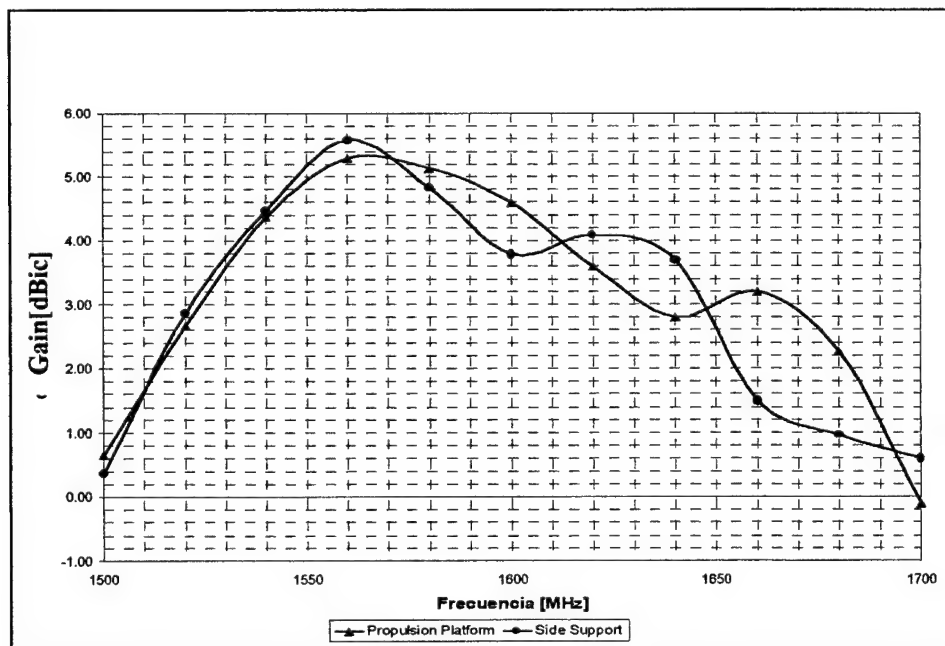


Figure 21, Rectangular Patch Antenna, placed on SAC-Csatellite mockup

7. REFERENCES

- [1] V. Trainotti, N. Dalmas Di Giovanni, J. Skora, D. Schweitzer, "SAC-C Satellite Antennas", Proceedings of the 1998 Antenna Applications Symposium, Allerton Park, Monticello, Illinois, September 16-18, 1998
- [2] V. Trainotti, J. Skora, D. Schweitzer, P. Pérez, "Antenas de Banda "UHF" para el Satélite SAC-C", CITEFA Technical Note N° 814, December 1999
- [3] V. Trainotti, J. Skora, D. Schweitzer, P. Pérez, "Antenas de Banda "S" para el Satélite SAC-C", CITEFA Technical Note N° 811, November 1999
- [4] V. Trainotti, J. Skora, D. Schweitzer, P. Pérez, "Antenas de Banda "X" para el Satélite SAC-C", CITEFA Technical Note N° 813, November 1999
- [5] V. Trainotti, J. Skora, D. Schweitzer, P. Pérez, "Antenas de Banda "GPS" para el Satélite SAC-C", CITEFA Technical Note N° 818, July 2000

ERROR COMPENSATION FOR VERY LARGE INFLATABLE REFLECTOR ANTENNAS

William H. Weedon
Applied Radar, Inc.
79 Timberline Road, Warwick, RI 02886
<http://www.appliedradar.com>

Weng Cho Chew and Tie Jun Cui
Electromagnetics Laboratory and
Center for Computational Electromagnetics
University of Illinois, Urbana, IL 61801

Livio Poles
Air Force Research Laboratory AFRL/SNHA
80 Scott Road, Hanscom AFB, MA 01731

Very large inflatable reflector antennas are currently being investigated for medium earth orbit (MEO) space-based radar. The present concept would utilize a reflector antenna with a 60 meter diameter in order to achieve sufficient aperture and power on target from a low-MEO orbit. These large inflatable reflectors are subject to various mechanical errors and shape deformations which would affect the overall performance of the antenna. The mechanical errors could arise from various sources such as seams in the reflector material fabric, holes in the material fabric caused by micrometeors and resulting in uneven pressure distribution, uneven thermal heating, and deformations induced by the platform thrusters. We discuss various approaches to model the effects of these mechanical errors on the overall performance of the reflector antenna. Methods of compensating for the errors using digital beamforming techniques are also discussed.

1. Introduction

Inflatable reflector antennas [1,2] offer an attractive method for achieving a large antenna aperture for high-gain space-based radar and communications applications. One space-based radar application of interest to the Air Force requires a 60 meter diameter reflector antenna in order to achieve sufficient power on target in a low-MEO orbit. The inflatable reflector antenna is attractive because it has a low weight can be easily transported to space on a rocket or space shuttle in a deflated configuration, and inflated once it is orbit.

There are, however, some disadvantages to using an inflatable reflector, rather than a more rigid construction. Firstly, the reflector must be constantly inflated due to holes arising from micrometeors [1] and other punctures and leaks. These leaks often lead to uneven pressure distribution within the reflector, causing surface errors. Uneven thermal heating due to solar radiation is another source of error that may lead to deformation of the reflector surface. Yet another source of surface error arises due to the various acceleration vectors acting at various portions of the structure due to the attached spacecraft thruster activation. The seams in the reflector surface also deform the surface. Figure 1 illustrates a 60 meter reflector and these various sources of error on the reflector surface.

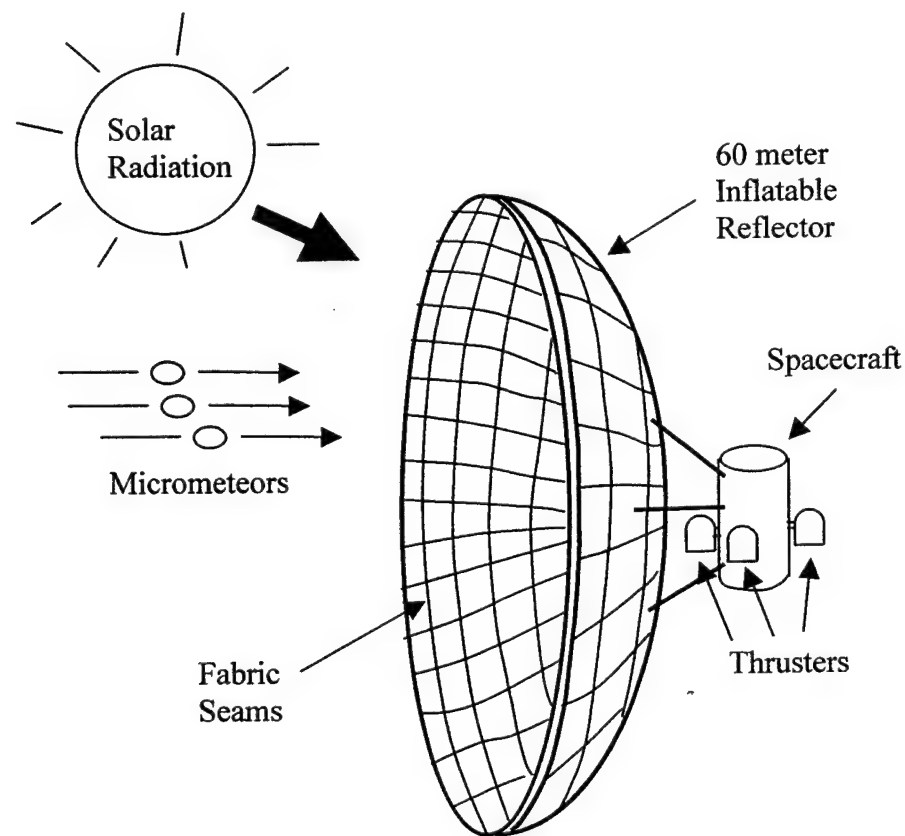


Figure 1: Illustration of a 60 meter inflatable reflector antenna and attached spacecraft showing various sources of reflector surface errors. These errors include spacecraft motion due to activation of spacecraft thrusters, micrometeors which may puncture holes in reflector skin, solar radiation, which induces surface deformations due to uneven thermal heating, and seams in the reflector fabric.

We are concerned here with the effect that these various sources of mechanical error on the reflector surface will have on the overall antenna performance. Depending on the severity of the deformations, the surface errors will have detrimental effects on the antenna main beam and sidelobes. The first stage of our work, therefore, is to model the reflector with the induced surface errors and to get an idea of the antenna performance under various perturbations in the surface.

Assuming that the mechanical surface errors significantly degrade the performance of the antenna, the next question that we wish to address is whether these surface errors can be compensated for using a phased-array feed with transverse equalization. Digital beamforming (DBF) is gaining popularity as a method of forming a phased-array feed, and would be ideally suited for implementing such a transverse equalization procedure. In a practical implementation, the reflector surface errors could be measured in real-time using a raster-scanned laser interferometer located near the feed and used as an input to generate the DBF correction weights.

2. Modeling the Reflector Surface Errors

Independent of the origin of the reflector surface error, whether it be due to thermal effects, leakage or thruster activation, we can model surface errors mathematically as consisting of a "desired" surface, such as a parabolic reflector shape, plus a surface perturbation due to the mechanical errors. The surface perturbations may be modeled as either "continuous" or "segmented". In the continuous case, the surface errors may be modeled mathematically using either a polynomial or superposition of sinusoids. In the segmented case, the panel seams are considered, which may not be modeled using smooth mathematical functions.

We are currently developing a CAD tool which will generate the geometry required to model surface errors in both the continuous and segmented case. This CAD tool will allow the antenna designer or systems engineer to input the antenna geometry and specify various types and magnitudes of mechanical surface errors. The software will then automatically generate an electromagnetic-compatible mesh in order to compute the antenna gain and radiation pattern using a computational electromagnetic field solver.

3. Radiation Pattern Calculations

There are two general methods for evaluating the radiation pattern of a reflector antenna: aperture-field method and current-distribution method. In the first method, one obtains the far field from the field distribution in the aperture plane,

where it assumes that the reflection from the surface forms a planar wavefront. This is true for a paraboloidal reflector fed at its focus point, but otherwise it is not true. The current-distribution method, however, calculates the far field from the currents induced on the reflector surface because of the primary feed of the feed. Therefore, it is a general method and adopted in shaped antennas.

An easy way to obtain the induced current distribution on the reflector is using the physical optics (PO) approximation [3], which gives

$$\mathbf{J} = 2 \mathbf{n} \times \mathbf{H} \quad (1)$$

where \mathbf{H} is the magnetic field produced by the feed, and \mathbf{n} is the normal direction of the surface. From the induced current \mathbf{J} , one easily obtains the far field pattern.

However, it is not accurate to evaluate the current distribution using the PO method. An exact way to obtain \mathbf{J} is solving an electric field integral equation, which numerically leads to a matrix equation. When the electrical size of the reflector is large, it is impossible to solve the matrix equation by using the conventional LU decomposition method, in which the total CPU time is proportional to N^3 and the storage requirement is of order of $O(N^2)$. To solve the large problem accurately, we use the multilevel fast multipole algorithm (MLFMA) [4,5], in which both the CPU time and storage requirement are only of order of $O(N \log N)$. In the examples we provide, we use 6-level MLFMA.

4. Results

We have computed the radiation patterns for a 60 meter parabolic reflector antenna using both the PO and MLFMA technique. Due to present computer resources on our DEC Alpha computer workstation, we have only computed the patterns at 100 MHz to date. At this frequency, the reflector is 20 wavelengths, and the MLFMA computes the patterns using a full 3-D computational EM code. We plan to extend this solution to 1 GHz and above using an SGI Origin 2000 computer. However, at 1 GHz the reflector is 200 wavelengths in diameter, which is near the maximum problem size that may be solved using the MLFMA with present-day computer resources.

The antenna geometry and electromagnetic mesh are currently generated using the IDEAS software package. Although this software does not allow us to specify arbitrary antenna surface errors as discussed previously, we can generate a

circularly symmetric reflector with circularly symmetric surface perturbations. The geometry is generated as

$$z = \begin{cases} x^2/4f, & \text{for } x \in [0,10) \\ x^2/4f + \delta \sin[0.1 \pi (x-10)], & \text{for } x \in [10,20) \\ x^2/4f, & \text{for } x \in [20,30]. \end{cases} \quad (2)$$

where z is the reflector normal, f is the focal length of 20 meters, and x is also in meters. This 2-D geometry is then rotated about the z -axis using IDEAS to generate the 3-D circularly symmetric reflector surface.

Figure 2 shows the radiation pattern for a 60 meter reflector antenna computed at 100 MHz using both the PO and MLFMA algorithms. The input source is a horizontal electric dipole placed at the focus. Clearly, the PO algorithm does not adequately model the radiation pattern. The sidelobe computation is particularly poor, although there is also some error in the computation of the mainlobe beamwidth. Figure 3 shows a comparison of the radiation pattern computed using MLFMA with no surface error ($\delta=0$) and with a surface error of ($\delta=0.1$). Figure 4 shows a similar comparison with ($\delta=0.2$).

5. Conclusions

We discussed the modeling of reflector surface errors on a very large diameter inflatable reflector antenna. Radiation patterns were computed using both the PO and MLFMA techniques. The PO method clearly does not model the antenna sidelobes accurately, which justifies the use of the full-wave MLFMA solution. It is expected that reflector surface errors will manifest themselves primarily in the radiation pattern sidelobes. Therefore, it is imperative that the field solver compute the sidelobes accurately. Unfortunately, the modeling of such a large reflector antenna (200 wavelengths at L-band) is pushing the limits of present-day computer resources and computational EM algorithms. Future work will involve not only the modeling of these reflector antenna surface errors, but schemes to correct for these errors using digital beamforming. We also plan to model more general reflector surface errors.

Acknowledgement:

This work is supported by the US Air Force Research Laboratory AFRL/SNHA, Hanscom AFB, MA under contract number F19628-00-C-0058.

References

- [1] C. G. Cassapakis, A. W. Love and A. L. Palisoc, "Inflatable space antennas: a brief overview," IEEE, p. 453-8, 1998.
- [2] M. Thomas, "Inflatable space structures," IEEE Potentials Magazine, pp. 29-32, Dec. 1992.
- [3] C. A. Balanis, Antenna Theory: Analysis and Design, Second Ed., Wiley, NY 1997.
- [4] J. M. Song and W. C. Chew, "Multilevel fast-multipole algorithm for solving combined field integral equations of electromagnetic scattering," Micro. Opt. Tech. Lett., vol. 10, no. 1, pp. 14-19, Sept. 1995.
- [5] J. M. Song, C. C. Lu and W. C. Chew, "MLFMA for electromagnetic scattering from large complex objects," IEEE Trans. Antennas Propagat., vol. 45, no. 10, pp. 1488-1493, Oct. 1997.

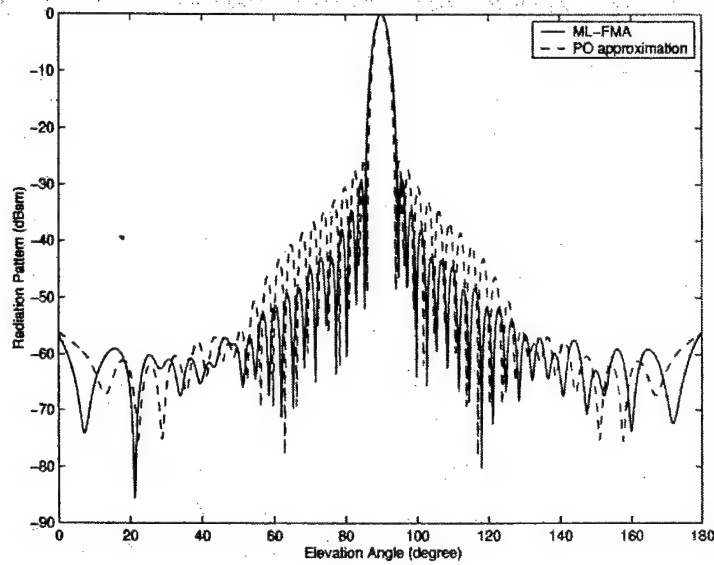


Figure 2: Comparison of PO and MLFMA solutions for a 60 meter parabolic reflector antenna at 100 MHz (200 wavelength diameter) with no surface errors. The PO solution does not accurately model the sidelobes.

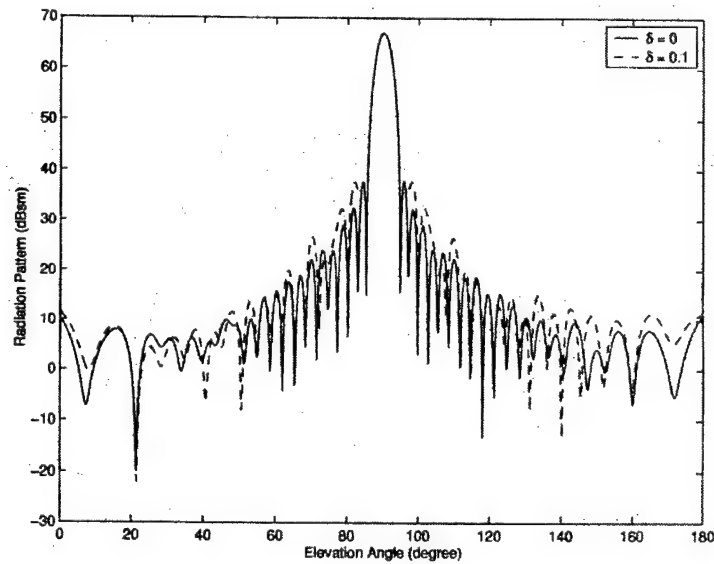


Figure 3: Comparison of 60 meter inflatable reflector with no errors ($\delta = 0$) and reflector with errors ($\delta = 0.1$) in Equation (2). Both solutions computed using MLFMA.

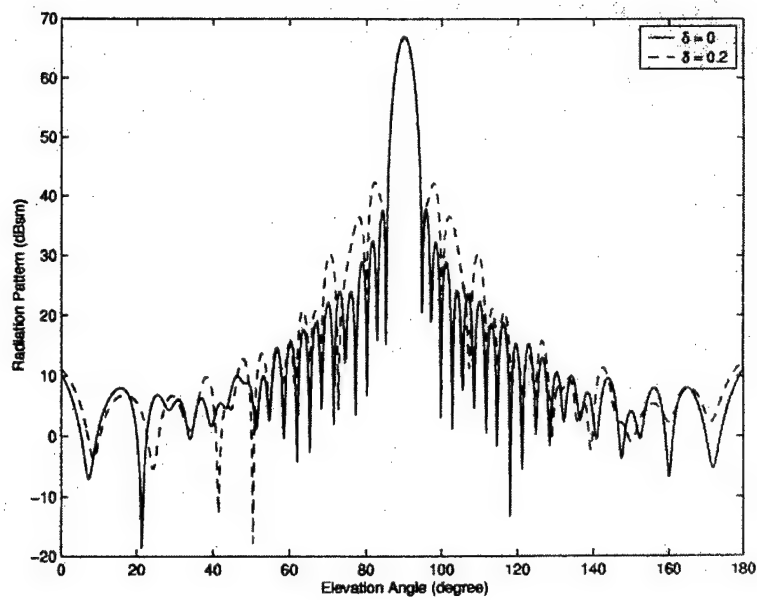


Figure 4: Comparison of 60 meter inflatable reflector with no errors ($\delta = 0$) and reflector with errors ($\delta = 0.2$) in Equation (2). Both solutions computed using MLFMA.

A Dual-Feed REConfigurable Leaky-Wave/Patch APerture

James Sor, Yongxi Qian and Tatsuo Itoh

Department of Electrical Engineering
University of California, Los Angeles
405 Hilgard Ave., Los Angeles, CA 90095, USA

Abstract: A novel dual-feed reconfigurable leaky-wave/patch antenna aperture is presented. The structure consists of two leaky-wave antennas and a patch antenna, all three of which share the same physical aperture. The mode of operation can be reconfigured by turning on or off the appropriate pin diode switches. When the pin diode switches are turned on, the entire aperture is operated as a leaky-wave antenna. Due to the unique dual-feed configuration of the leaky-wave aperture, the antenna's tilted main beam can be steered with high gain symmetrically in either direction. When the pin diode switches are turned off, the reconfigurable aperture is operated as a patch antenna with moderate gain at broadside. The reconfigurable structure cleverly utilizes the field configurations of each aperture's mode configuration to provide maximum isolation between the different ports. Input return loss, antenna gain and radiation patterns of each aperture are consistent with standard leaky-wave and patch antenna characteristics. The dual-feed leaky-wave/patch antenna structure is employed to realize a multi-port reconfigurable leaky-wave/patch antenna aperture. The multi-port structure provides excellent scan coverage through a combination of five separate antennas that share the same radiating aperture.

I. INTRODUCTION

The abundance of antennas in modern radar and communications systems has resulted in an explosion in the number of antennas both on the ground and in orbital space. The need to reduce antenna size has accordingly become more important, especially in payload situations where space comes at a premium. It is highly desirable, therefore, to develop topologies and techniques where a number

of antennas that cover different frequency bands and/or serve different functionalities can share a single physical aperture without sacrificing system performance. It is of no surprise, then, that reconfigurable aperture antennas have garnered increased attention in the literature recently [1] [2] [3].

To address this need, we recently proposed in [4] a reconfigurable leaky-mode/multifunction patch antenna array structure. In this scheme, long leaky-wave apertures form a linear array and can be frequency scanned with high gain (12 dB). Using conventional or MEMS switches, each of the leaky wave apertures can be segmented into several smaller patch antenna apertures, with the mode of operation controlled by the state of the switches. The individual patches can be designed to operate at multiple frequency bands with moderate gain at broadside. In [5] and [6], we demonstrated the viability of this structure through a simplified version of the proposed concept.

In this paper, we extend the reconfigurable leaky-mode/patch aperture concept to realize a multi-port structure, as shown in Fig. 1. In this scheme, two reconfigurable dual-feed leaky-wave antennas are placed perpendicular to each other. The intersection of the two dual-feed leaky-wave antennas forms a patch antenna structure, with the resulting system forming the basis for a multi-port antenna. This reconfigurable multi-port antenna serves three main purposes. First, the structure expands upon our original reconfigurable aperture concept. Specifically, the multi-port antenna structure utilizes five distinct antennas that are physically sharing the same radiating aperture. To the author's best knowledge, this is the greatest number of antennas to all physically share the same radiating aperture. Second, the multi-port aperture demonstrates that each patch antenna can be reconfigured and shared with two degrees of freedom. This extends the functionality of the reconfigurable leaky-wave/patch concept, and can potentially be used to form a full 2D reconfigurable leaky-wave/patch phased array, which is shown conceptually in Fig. 2. Finally, the multi-port antenna demonstrates that each leaky-wave antenna can be reconfigured into a patch aperture at any point along the leaky-wave aperture without sacrificing the performance of either the patch or leaky-wave antenna. This should be distinguished from the test structure we demonstrated in [6], where the patch apertures were placed at the end of the leaky-wave antenna. Here, most of the leaky-mode field has vanished due to radiation.

II. APERTURE DESIGN & OPERATION

The antenna is built on RT/Duroid substrate with permittivity $\epsilon_r = 2.33$ and thickness $t = 31$ mils. The multi-port aperture is a five-port device, with the

first four ports designated as the rotationally symmetric leaky-wave ports and port 5 as the probe-fed patch port. An enlargement of the central patch region is shown in Fig. 3. Eight pin-diode switches separate the central patch structure from the four leaky-wave arms. Shorting vias are used in each of the leaky-wave mode launchers to suppress the undesired fundamental even mode while simultaneously exciting the desired first higher-order odd mode. As a result, each of the leaky-wave arms is intrinsically grounded at DC. Due to the arrangement of the pin-diode switches, only two leaky-wave ports can be turned on at any instant. For example, when a positive bias is fed through the patch antenna port, all the horizontally placed pin-diode switches turn on, while the vertically placed pin-diode switches are off. The opposite occurs when a negative bias is fed through the patch antenna port. As we shall see later, this arrangement intrinsically isolates any two leaky-wave arms that are perpendicular to each other. The pin-diode switches that separate the central patch antenna structure from each of the leaky-wave arms are strategically placed along the edges of the leaky-wave antenna, where the leaky-mode field profile is maximum. This arrangement ensures minimal insertion loss of the leaky-mode when the switches are turned on.

III. RADIATION PATTERNS

The multi-port antenna aperture demonstrates the multi-mode/multifunction characteristics of the reconfigurable leaky-wave/patch aperture concept. Each of the leaky-wave arms provides moderate bandwidth of about 13% when the diodes are switched for leaky-mode operation, as shown in Fig. 4. An inherent trait of leaky-wave antennas is the ability to frequency scan the tilted main beam with relatively high gain (~ 12 dB). This is demonstrated in Fig. 5, where 30° of scan coverage is achieved about the elevation angle in the operating band of the leaky-wave antennas.

When a ground bias is fed through the probe-fed patch port, all of the pin-diode switches are turned off and the multi-port antenna operates solely in the patch mode. This is clearly demonstrated in Fig. 6, where we have achieved an input match of -18 dB at the resonant frequency. It should be noted that the patch antenna was originally designed to operate at 8 GHz. However, due to the combined loading effects of the pin-diode switches and the surrounding leaky-wave antenna metallization, the operational frequency has shifted slightly to 7.77 GHz. Despite the shift in frequency, the measured radiation patterns in Fig. 7 of the patch antenna are consistent with conventional patch patterns, showing only a slight perturbation in the H-plane that is due to the loading effects of the

surrounding metallization and the pin-diode switches. The resonant patch antenna offers broadside coverage with moderate gain, with a front-to-back ratio better than 15 dB.

IV. ISOLATION

An important parameter for any transmitting or receiving system is the isolation between the different ports. This requirement becomes more paramount in the case of the reconfigurable aperture, where one or more antennas are physically sharing the same aperture. The isolation between any two ports is measured by recording the insertion loss with all other ports terminated by 50Ω loads. When the diodes in one direction are turned on, we measure the isolation between two parallel arms. Although a direct patch exists between the input and output ports in this configuration, we should expect good isolation since we expect most of the excited leaky-mode will have been radiated by the time the wave arrives at the output port. The results are shown in Fig. 8, where it is observed the isolation is better than -15 dB in the operating band of the leaky-wave antenna. This level of isolation should drop further as the length of the leaky-wave aperture is increased. Meanwhile, we expect better isolation between perpendicular arms, since the pin-diode configuration utilized never allows a conducting path between perpendicular arms. This is exactly the case as seen in Fig. 9, where isolation is better than -20 dB in the operating band of the leaky-wave antenna. Finally, the most susceptible configuration is between any leaky-wave port and the patch antenna port, since the separation distance is the shortest between these two ports. Nonetheless, we see in Fig. 10 that across the operating band of the leaky-wave arms and in the resonant frequency of the patch antenna, isolation is measured to be better than -15 dB. It should be noted that these isolation values represent the intrinsic isolation of the antenna aperture itself. In system configurations where isolation requirements are much more stringent, additional switches can be utilized at the input ports for better isolation.

V. CONCLUSION

A reconfigurable multi-port antenna aperture utilizing dual-feed leaky-wave/patch antennas has been presented. The unique structure enables excellent coverage through a combination of four scannable leaky-wave antennas plus a resonant patch antenna with broadside coverage, all of which physically share the same radiating aperture. Pin-diode switches enable switching between the different configurations with good isolation characteristics and minimal pattern distortion.

VI. ACKNOWLEDGEMENT

This work was supported by DARPA/SPAWAR under contract N66001-C-99-8638.

VII. REFERENCES

- [1] J. Veihl, R. Hodges, D. McGrath, and C. Monzon, "Reconfigurable aperture decade bandwidth array," *2000 IEEE AP-S International Symposium Digest*, pp. 314-317, Jul. 2000.
- [2] J. H. Schaffner, R. Y. Loo, D. F. Sievenpiper, F. A. Dolezal, G. L. Tangonan, J. S. Colburn, J. J. Lynch, J. J. Lee, S. W. Livingston, R. J. Broas, and M. Wu, "Reconfigurable aperture antennas using RF MEMS switches for multi-octave tenability and beam steering," *2000 IEEE AP-S International Symposium Digest*, pp. 321-324, Jul. 2000.
- [3] A. Fathy, A. Rosen, F. McGinty, G. Taylor, S. Perlow, M. ElSherbiny, "Silicon based reconfigurable antennas," *2000 IEEE AP-S International Symposium Digest*, pp. 325, Jul. 2000.
- [4] Y. Qian, B.C.C. Chang, M.F. Chang and T. Itoh, "Reconfigurable leaky-mode/multifunction patch antenna structure," *Electronics Letters*, vol. 35 (2), pp. 104-105, Jan. 1999.
- [5] B. C. C. Chang, Y. Qian and T. Itoh, "A reconfigurable leaky mode/patch antenna controlled by PIN diode switches," presented at *1999 IEEE AP-S International Symposium Digest*, pp. 2694-2697, Jul. 1999.
- [6] J. Sor, Y. Qian and T. Itoh, "Characterization of a multi-mode microstrip structure for reconfigurable aperture application," *2000 IEEE MTT-S International Microwave Symposium Digest*, pp. 589-592, Jun. 2000.

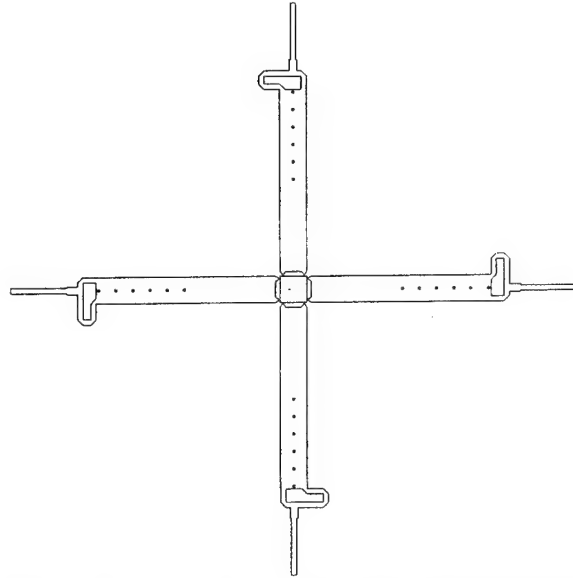


Fig. 1: Mask of the reconfigurable multi-port antenna structure.

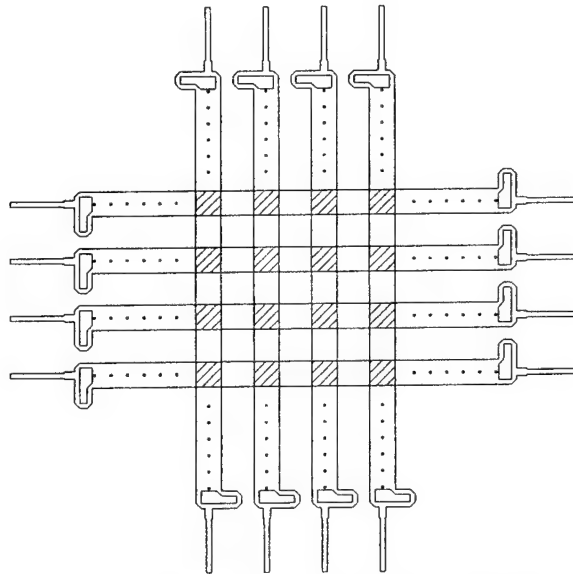


Fig. 2: Proposed 2D reconfigurable leaky-wave/patch array.

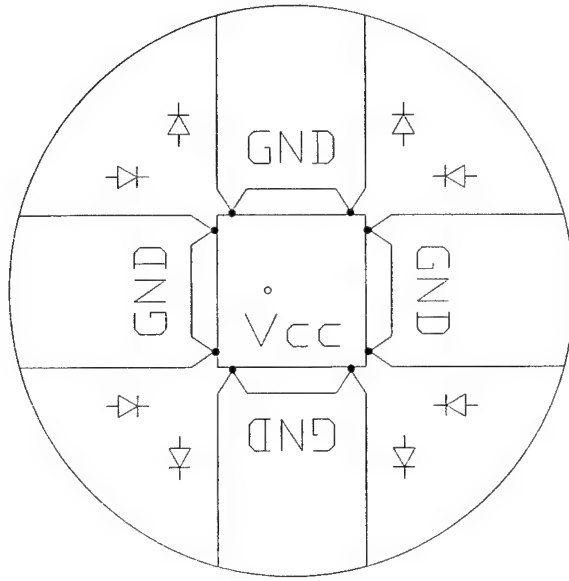


Fig. 3: Enlarged view of central patch area indicating placement and direction of pin diodes.

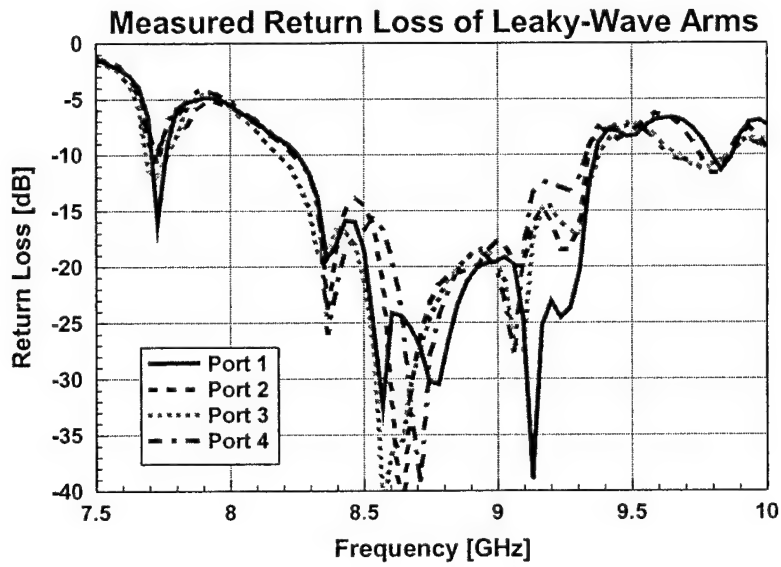


Fig. 4: Measured return loss of each leaky-wave arm of the multi-port aperture.

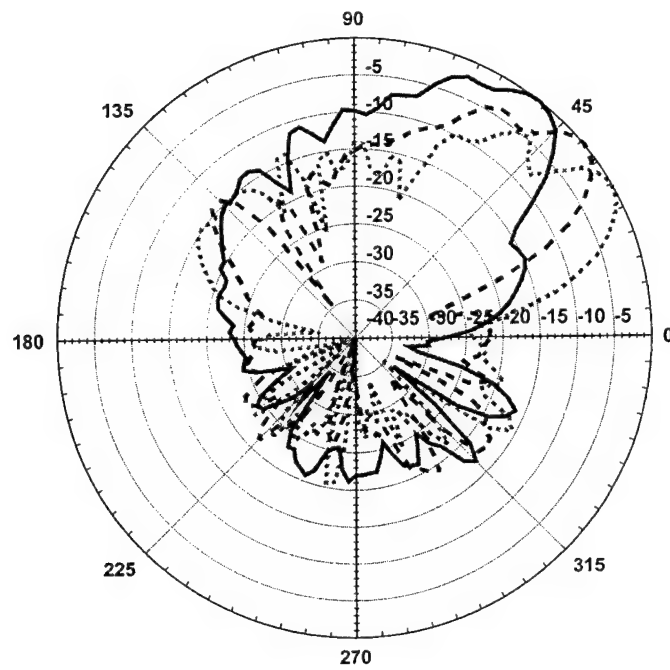


Fig. 5: Frequency scanning with each arm of the multi-port aperture.

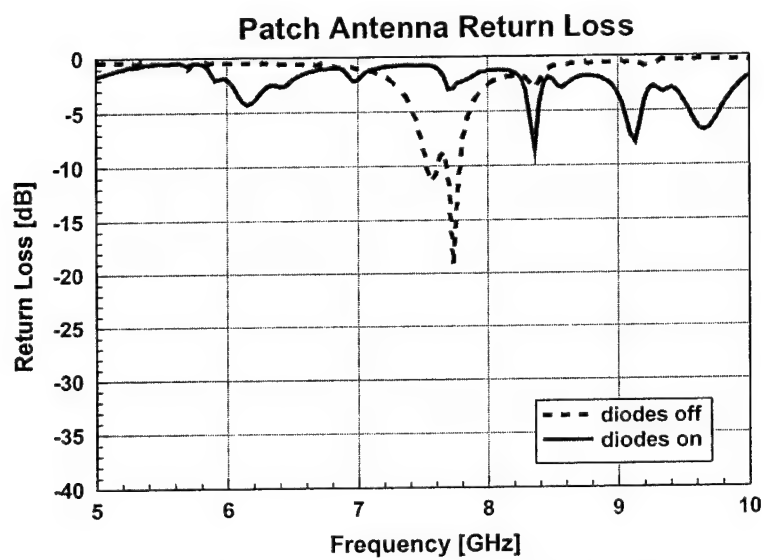


Fig. 6: Measured return loss of probe-fed patch.

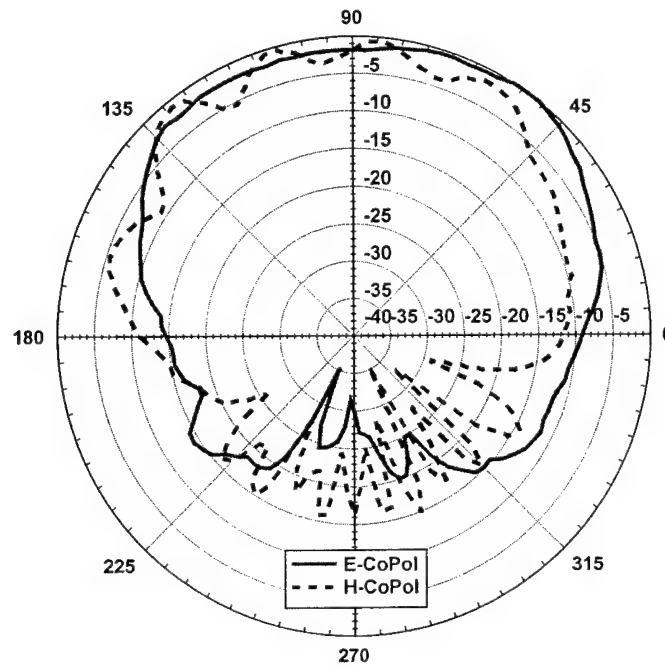


Fig. 7: Measured radiation patterns in the patch mode.

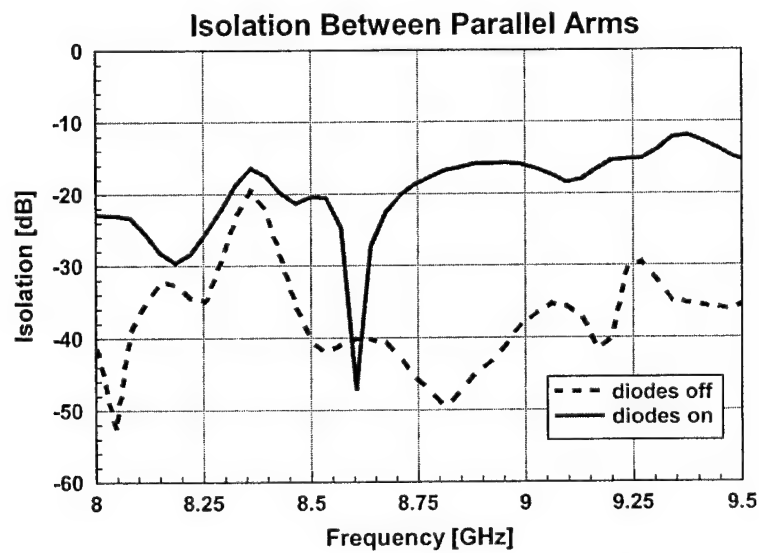


Fig. 8: Measured isolation between parallel arms of multi-port aperture.

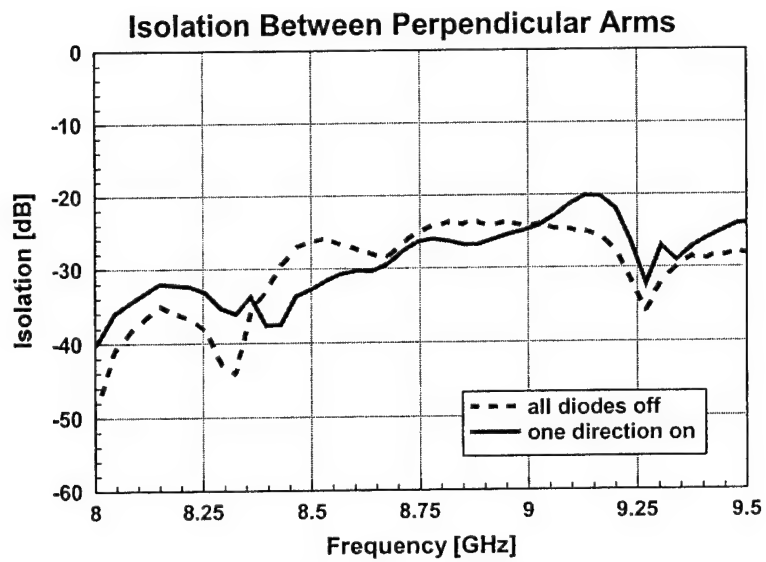


Fig. 9: Measured isolation between perpendicular arms of multi-port aperture.

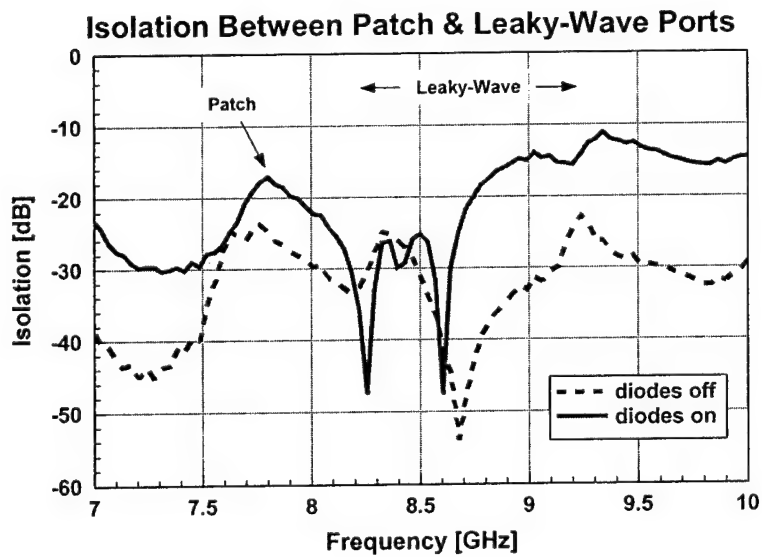


Fig. 10: Measured isolation between patch port and leaky-wave port.

STRIPLINE FEED NETWORKS FOR RECONFIGURABLE PATCH ANTENNAS

William J. Payne and William H. Weedon
Applied Radar, Inc.
79 Timberline Road, Warwick, RI 02886
<http://www.appliedradar.com>

Reconfigurable patch antennas have drawn a lot of attention recently as a paradigm for generating several different antenna array operating modes with a single reconfigurable antenna aperture. Such "operating modes" may consist of various operating frequency bands (e.g. L-band and X-band), polarizations, beampatterns or nulls. Different technologies have been proposed as methods of switching the array elements to the various configurations including MEMS switches, photonic switches, and solid-state switches, including FET switches and PIN diodes. What is often neglected in the reconfigurable antenna design, however, is a practical method of feeding the antenna elements. In this paper, we discuss stripline feed networks that may be used to feed reconfigurable patch antennas, independent of the switching technology used to reconfigure the elements. Simulation and measurement results are presented for Wilkinson power dividers used to distribute the RF energy in a corporate feed network. Blind via transitions are used to transition energy from the feed network to the radiating elements, and results are presented for various cases considered.

1. Introduction

Reconfigurable antennas have gained a lot of attention recently [1-3] as a method of obtaining several operating modes out of a single antenna aperture. Such operating modes may consist of different frequency bands, polarizations, beampatterns, nulls, etc. for which the antenna may be configured using switching elements. Different technologies have been proposed as methods of switching the array elements to the various configurations including MEMS switches, photonic switches, and solid-state switches, including FET switches and PIN diodes. What is often neglected in the reconfigurable antenna design, however, is a practical method of feeding the antenna elements. In this paper, we discuss stripline feed networks that may be used to feed reconfigurable patch antennas, independent of the switching technology used to reconfigure the elements.

Last year [1], we presented simulations and prototype measurement results for a 3x3 array of microstrip patch elements that may be configured to resonate at either L-band or X-band. We also presented a general adaptive reconfigurable feed (GARF) methodology whereby each array configuration would be fed independently using a separate stripline corporate feed. In the current paper, we present simulation and measurement results for stripline Wilkinson power dividers and blind via transitions that may be used both as a basis for the corporate feed network and to transition between the multiple PCB layers.

2. Wilkinson Power Divider Results

An X-band Wilkinson power divider was designed using HFSS, fabricated and tested. Figure 1 shows the CAD model used for HFSS. A termination resistor is shunted across the output arms to reduce mismatch reflections. The device was fabricated using layers of 0.030 inch Rogers 5880. Figures 2 and 3 show the simulation and measured data at X-band. The performance is excellent. A 1-to-4 power divider has also been successfully built and tested at X-band, and will be presented in the oral presentation.

3. Blind Via Vertical Transition Results

Blind via vertical transitions at X-band were also designed, built and tested. Figure 4 shows the HFSS model, and Figure 5 defines the various components of the design. The design started using the coaxial equation relating the center via pin and relief opening to the impedance

$$Z_0 = [138 / \sqrt{\epsilon_r}] \log_{10} (R_r / R_v) \quad (1)$$

where ϵ_r is the relative permittivity of the substrate, R_r is the relief hole radius, and R_v is the via hole radius. This allows us to obtain a course estimates of the relief hole for a particular via size. Next, the design was fine-tuned using HFSS.

The following optimized parameters were obtained from the HFSS simulations:

Thru via diameter= 0.020 in

Relief diameter= 0.070 in

Mode suppression pin diameter= 0.120 in

Figure 6 shows the HFSS results on a Smith chart. Figure 7 shows the corresponding measured data on the Smith Chart. Figure 8 shows the return loss (S11) and insertion loss (S22). The measured data has an insertion loss of about 0.6 dB and an input match of -18.2 dB. Overall, the performance is very good.

4. Conclusions

Wilkinson power dividers and blind via transitions were designed, fabricated and tested for application to reconfigurable patch antennas using stripline technology. The examples presented here were for X-band. Using the GARF feed methodology, a separate feed mechanism uncoupled through switches would be used for the L-band configuration. A similar design procedure could be used to design the L-band transitions and power splitters.

Acknowledgement

This work was supported by the US Air Force Research Laboratory AFRL/SNHA, Hanscom AFB, MA under contract number F19628-99-C-0056.

References

- [1] W. H. Weedon, W. J. Payne, G. M. Rebeiz and J. S. Herd and M. Champion, "MEMS-Switched reconfigurable multi-band antenna: design and modeling," 1999 Antenna Application Symposium, Monticello, IL, Sept. 15-17, 1999.
- [2] DARPA RECAP workshop, McLean, VA Dec. 7-9, 1999 (Various papers).
- [3] J. K. Smith, Organizer, Session on "Reconfigurable Aperture Antennas", IEEE AP-S International Symposium, Salt Lake City, UT, July 16-21, 2000 (Various papers).

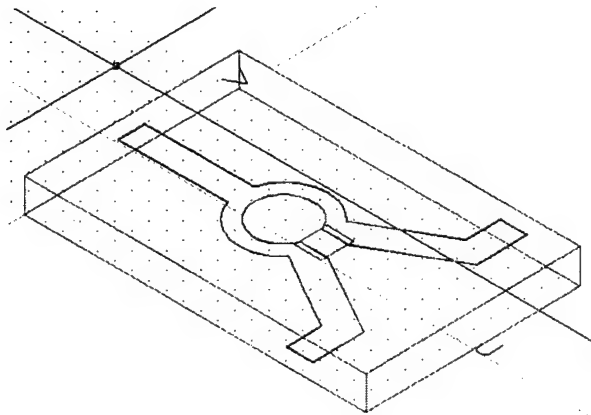


Figure 1: HFSS model for Wilkinson power divider.

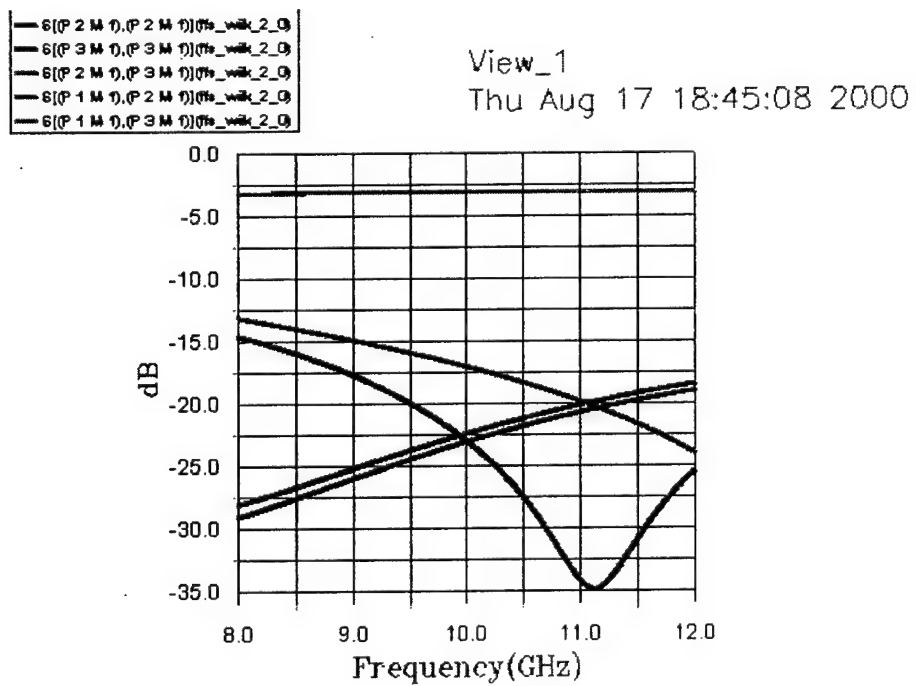


Figure 2: Simulation results for Wilkinson power divider.

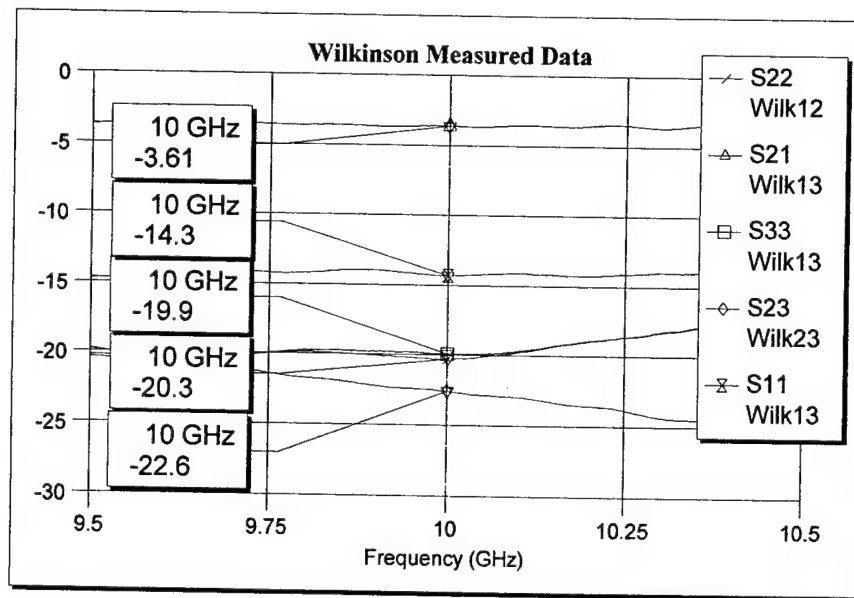


Figure 3: Measured data for Wilkinson power divider.

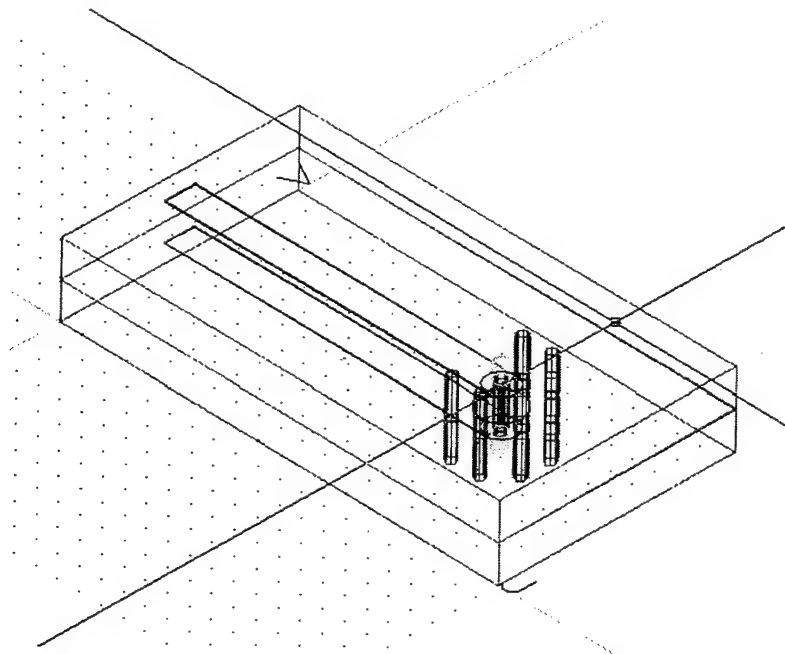


Figure 4: HFSS model of vertical transition

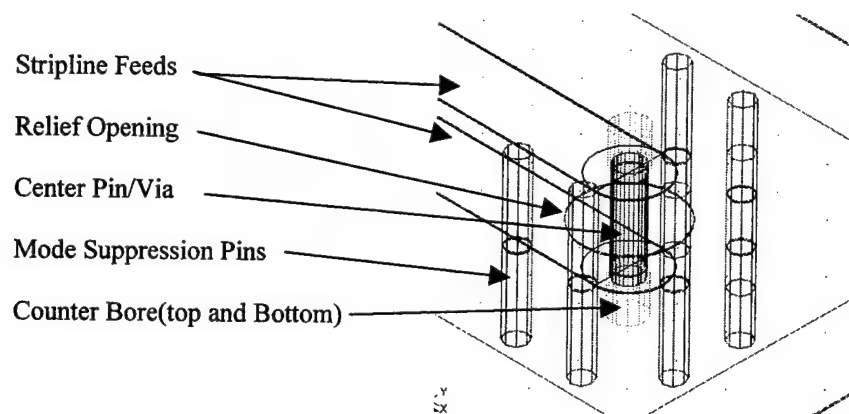


Figure 5: Definition of components in blind via vertical transition.

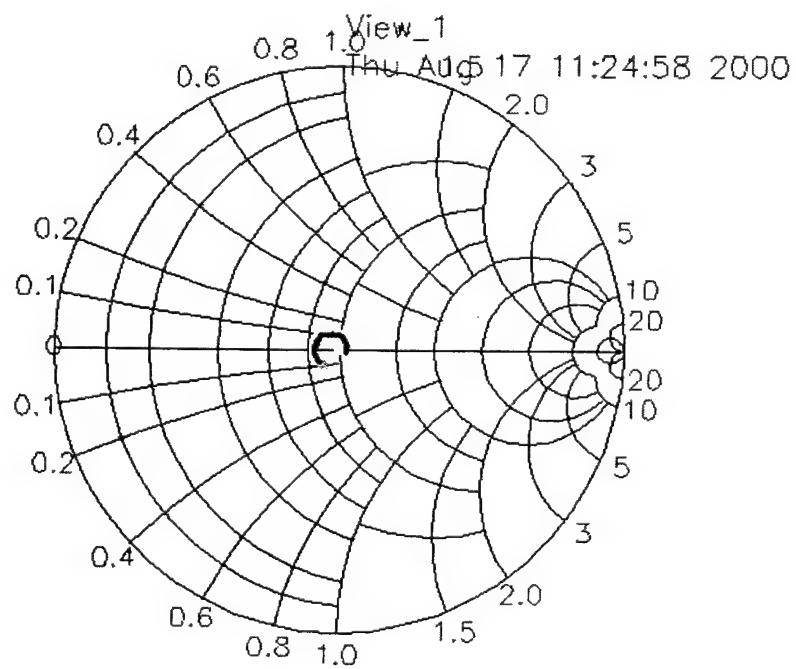


Figure 6: HFSS simulation results for blind via vertical transition.

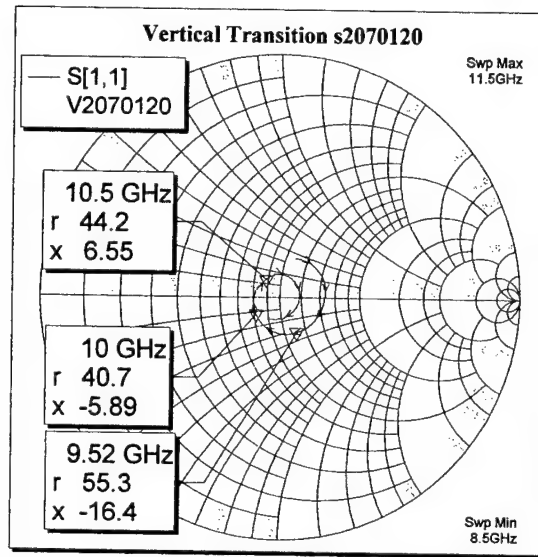


Figure 7: Measured Smith Chart results for blind via vertical transition.

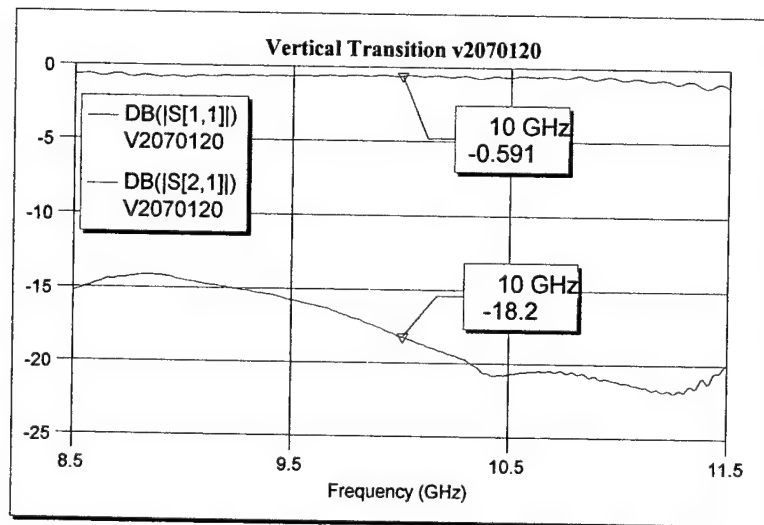


Figure 8: Measured return loss (S11) and insertion loss (S21) results for blind via vertical transition.

PROGRAM TO PLOT TOUCHSTONE® ANTENNA CIRCUIT FILES

W.R. Pickles
U.S. Naval Research Laboratory
Washington, DC 20375

ABSTRACT: It is frequently necessary to build feed networks and power divider networks in the course of designing antennas, particularly printed circuit antennas. Touchstone is an easy-to-use microwave CAD program which is commonly used to design such networks. A program is presented which produces geometric representations of Touchstone circuits in DXF format. The features of the program include: (1) the ability to combine antenna elements or circuit elements analyzed outside of Touchstone into the overall geometrical representation, (2) the ability to combine a large number of line segments into a few polylines, (3) the generation of a new circuit file with a sequentially numbered netlist (when elements are inserted in the middle of a netlist, the node numbering can become confusing), (4) the identification of unused variables, and (5) some syntax error warnings. This program is useful for checking that a circuit is geometrically reasonable, producing artwork that can be sent to circuit etchers with only minor modification, or checking a Touchstone circuit analysis with an electromagnetic solver. This program can simplify the work of an electromagnetic solver by allowing the circuit part of a design to be analyzed in Touchstone and then combined with the antenna portion. The basic requirements for using this program are of course Touchstone and a CAD program that accepts DXF formatted files. The full usefulness of this program is realized when it is used with an electromagnetic solver that accepts DXF input and produces antenna port data in touchstone SNP format. Examples using stripline or microstrip circuits and various radiators drawn from NRL research projects are given.

A companion CD-ROM with the executable code, source code, examples, and a freely available C++ compiler from Cygnus is also provided. The source code is provided so that the user may add to or modify the program, or recompile it with a preferred C++ compiler.

1.0 INTRODUCTION About a decade ago I borrowed a copy of Touchstone from another section at NRL. It did not have any plotting capability, so I wrote a program in Pascal to plot my circuit files. This was fairly simple as I was only using stripline lines, stripline steps, stripline bends, and stripline tees. As my understanding of Touchstone grew I added new features to the plotting program – more elements, equation parsing, and exporting DXF files. Several years ago I rewrote my Touchstone plotting routine in C++.

I have continued to use Touchstone, even as circuit analysis programs with schematic capture have become available, because I appreciate its simplicity. I use Touchstone mostly to design power dividers for arrays, and viewing them with a schematic capture program has seemed awkward to me. If I make one big circuit then it is hard to view it all at once and if I make a lot of small circuits in different files then I still cannot view it all at once. When the price of schematic capture programs is added in, there did not seem to be an advantage for my particular applications. I have run into quite a few engineers who still use Touchstone but Hewlett Packard recently stopped selling it, so as people lose their hardware keys the number of Touchstone users will dwindle.

The name of the program described in this report is TSPLOT32. “TSPLOT” means Touchstone Plot and the “32” indicates that it has been revised thirty two times.

2.0 WHY C++ When I made the switch from MS-DOS to MS-Windows, I found that most of the programs I had written did not access the printer port reliably. In general everything else worked as it had, but a change was necessary because I use the printer for plotting most of the time. I tried out a commercially available C++ compiler and found that it could replace FORTRAN because it handles complex numbers gracefully, it could replace Pascal because it allows easy access to dynamic memory, and if I used the built in debugger it could replace BASIC which I used for its ease of debugging. In addition, C++ facilitates, but does not mandate, object oriented programming. As will be explained in the section “**EXTENDING THE CAPABILITIES OF TSPLOT32**”, this simplifies the maintenance and extension of programs as requirements change.

2.1 FREE C++ COMPILERS A number of C++ compilers can be downloaded for free from the Internet. They are generally command line compilers which means they work in an MS-DOS type environment. However, a number of integrated development environments (IDE’s) are also available free over the Internet. An IDE is a Windows based text editor which has the ability to

invoke the compiler on the program it is processing. TSPLOT32 has been tested with two free compiler-IDE combinations: (1) The GNU Cygwin version 20b compiler and the pcGRASP IDE, and (2) the Borland version 5.5 compiler and the VIDE.

The Cygwin compiler can be downloaded directly from <ftp://sourceware.cygnum.com/pub/cygwin/old/cygwin-b20/>. and the pcGRASP IDE can be downloaded from <http://www.eng.auburn.edu/departments/cse/research/grasp/> after logging in. The Borland version 5.5 compiler can be download from <http://www.borland.com/bcppbuilder/freecompiler/> after logging into the "Borland Community" and VIDE can be downloaded from <http://www.objectcentral.com/downloads.htm>. All of the compiler and IDE files are self extracting. In addition, advice and help files for the Borland-VIDE combination can be found at <http://www.pharo.onlinehome.de/Downloads.html>.

The Cygwin - pcGRASP combination is elegant for its simple setup procedure. If all the defaults are chosen in installation, pcGRASP can be configured for the GNU compiler by going to the *file* menu, choosing the *global preferences* sub-menu, clicking the *C++* tab, scrolling down to *(C++) Cygnus Beta 20* in the *Compiler Environment for C++ Programs* box, and clicking *OK*. That is all there is to do. The Borland-VIDE installation is quite a bit more involved and is different for Windows 98 and Windows NT. However, if you make it through all the wickets you will be rewarded with a compiler that gives better error messages.

3.0 INTRODUCTORY EXAMPLE. A simple example will illustrate most of the features of TSPLOT32. Listing 1 shows part of a Touchstone .ckt file (the entire file, wilkdemo.ckt, is on the companion CD-ROM) for a Wilkinson power divider, with untapered arms for simplicity. Most of the feature of TSPLOT32 will be demonstrated by examining how this file is processed and the final output. First notice that lines 52, 56 and 57 have the declaration *!!ENDS* which looks something like a Touchstone comment and something like a Touchstone element. This is a special non-Touchstone element that has been added to draw perpendicular lines across the circuit, typically at the ends of traces.

When TSPLOT32 opens the file wilkdemo.ckt, it reads through the DIM block, parses the VAR block, parses and evaluates the EQN block, and parses and constructs the circuit elements in the CKT block. When TSPLOT32 gets to line

```

13: VAR
14: w50 = 104
15: w100 = 27
16: wres = 40
17: lres = 40
18: l0 = 100
19: l1 = 750
20: l1a = 100
21: l1b = 312
22: l1c = 256.25
23: l2a = 50
24: l2b = 200
25: l2c = 250
26:
27: Nturns = 1.41421
28: r1 = 200
29:
30: EQN
31: l1d = l1 - l1a - l1b - l1c
32:
33: CKT
34: SSUB ER = 2.2 B = 125 T = 0 RHO = 0
35: SLIN 1 2 W^w100 L^L1a
36: SMITER 23 2 W^w100
37: SLIN 23 34 W^w100 L^l1b
38: SMITER 35 34 W^w100
39: SLIN 35 36 W^w100 L^l1c
40: SMITER 36 37 W^w100
41: SLIN 37 24 W^w100 L^l1d
42: STEE 24 3 4 W1^w100 W2^w100 W3^wres
43: SLIN 4 6 W^wres L^lres
44: SLIN 3 45 W^w100 L^l2a
45: SBEND2 45 46 W^w100 ANG=45 M=0
46: SLIN 46 47 W^w100 L^l2b
47: SBEND2 47 48 W^w100 ANG=45 M=0
48: SLIN 48 5 W^w100 L^l2c
49: DEF3P 1 6 5 arm
50:
51: SLIN 1 2 W^w50 L^l0
52: !!ENDS 1 W^w50
53: S3P 3 4 2 tee4.s3p
54: arm 3 23 13
55: arm 4 24 14 FLIP
56: !!ENDS 13 W^w100
57: !!ENDS 14 W^w100
58: RES 23 24 R^r1
59: XFER 13 5 0 0 N^Nturns
60: XFER 14 6 0 0 N^Nturns
61: DEF3P 1 5 6 tee

```

Listing 1 - Touchstone File for Simple Wilkinson Divider

49, its representation of the circuit in memory looks something what is shown in Fig. 1a. It has constructed all the elements and made note of the nodes to which these elements are connected. At this point it constructs a temporary new three port element called "arm" for use later on.

The execution of TSPLOT32 continues to line 53 which specifies a

Touchstone data file named "tee4.s3p". Touchstone data files do not have any geometric information so TSPLOT32 looks for a DXF file named "tee4.dxf". The DXF file must be formatted in a particular way which will be discussed in the section on "EXTENDING THE CAPABILITIES OF TSPLOT32". Just before TSPLOT32 processes line 61 its internal representation resembles Fig. 1b, and right after, its internal representation resembles Fig. 1c. The next non-blank line TSPLOT32 encounters indicates that it has finished the CKT block, and the representation in Fig. 1c becomes final. At this point TSPLOT32 does five things:

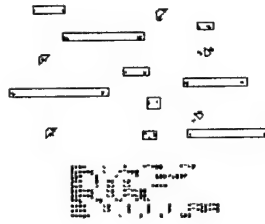


Figure 1a

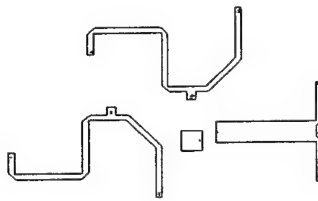


Figure 1b

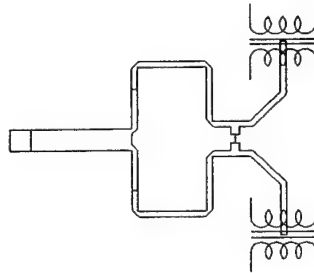


Figure 1c

Figure 1 – Internal Representation of Wilkdemo.ckt by TSPLLOT32 at intermediate stages (a) and (b) and the final output (c).

- 1) It reads the rest of the file and stores the remaining lines as comments.
- 2) It prints all the values from the VAR and EQN blocks to the screen and to a file named wilkdemo_.txt. If any of the variables were not used it prints a warning.
- 3) It generates a DXF file of the circuit named wilkdemo_.dxf and plots a line drawing of the circuit to a HP LaserJet 3¹ printer if it is attached to the line printer port.
- 4) It renumbers the nodes sequentially in the circuit file, and prints the renumbered file to wilkdemo_.ckt.
- 5) If there were any disconnected elements or any nodes that did not have exactly two elements TSLOT32 prints a warning to the screen.

Figure 1c also provides a pictorial representation of the resistors and transformers that were in the circuit. This is for user information only. The resistor and transformer have no geometrical information associated with them so they must be located on the ports or extremities of the circuit.

4.0 CAPABILITIES. TSLOT32 recognizes and plots the stripline and microstrip elements shown in Table 1. These are elements which are used frequently by the author and hence have been debugged through usage.

TSLOT32 recognizes, and in some cases plots, Touchstone elements which are not stripline or microstrip (or coplanar waveguide). These elements are shown in Table 2. The reason these elements are included is that they are used frequently in designing microwave circuits and if they are not recognized they must be removed (or commented out) whenever TSLOT32 is used to process the circuit file. Where possible a graphical representation of these elements is added to the DXF file and the printed drawing.

Several non-Touchstone elements have been added to the repertoire of TSLOT32 elements. These elements must be transparent to Touchstone so they must appear as comments. In order for TSLOT32 to differentiate these special

¹LaserJet 4, 5 and 6 also.

Table 1 – Touchstone Stripline and Microstrip Elements Processed by TSPLOT32

<u>ELEMENT</u>	<u>SYNTAX</u>				<u>COMMENT</u>
Stripline Substrate	SSUB	ER=	B=	T= RHO=	Parameter B used in optimum miter calculations
Loss Tangent	TAND	TAND=			
Stripline Open Circuit With End Effect	SLEF	n1	W=	L=	Capacitor to ground drawn as remainder of end effect
Stripline Open Circuit	SLOC	n1	W=	L=	
Stripline Short Circuit	SLSC	n1	W=	L=	
Stripline Straight Section	SLIN	n1	n2	W= L=	Ground symbol drawn as remainder
Stripline Step	SSTEP	n1	n2	W1= W2=	Optional parameter L causes left offset, R causes right offset, C is centered which is default
Stripline Bend	SBEND	n1	n2	W= ANG=	no miter
Mitered Stripline Bend	SBEND2	n1	n2	W= ANG= M=	
Optimally Mitered Stripline 90° Bend	SMITER	n1	n2	W=	Used SSUB parameter B in calculations
Stripline Curve	SCURVE	n1	n2	W= ANG= RAD=	approximated by many short straight segments
Stripline Tee	STEE	n1	n2 n3	W1= W2= W3=	

Table 1 - Touchstone Stripline and Microstrip Elements Processed by TSPLOT32 (continued)

<u>ELEMENT</u>	<u>SYNTAX</u>						<u>COMMENT</u>
Stripline Cross	SCROS	n1	n2	n3	n4	W1= W2= W3= W4=	
Stripline Coupled Lines	SCLIN	n1	n2	n3	n4	W= S= L=	
Microstrip Substrate	MSUB	ER=	H=	T=	RHO=	RGH=	parameter H used in optimum miter calculations
Microstrip Cover	MCOVER	HC=					
Microstrip Open Circuit With End Effect	MLEF	n1	W=	L=			Capacitor to ground drawn as reminder of end effect
Microstrip Open Circuit	MLOC	n1	W=	L=			
Microstrip Short Circuit	MLSC	n1	W=	L=			Ground symbol drawn as reminder
Microstrip Straight Section	MLIN	n1	n2	W=	L=		
Microstrip Step	MSTEP	n1	n2	W1=	W2=	!L !C !R	Optional parameter L causes left offset, R causes right offset, C is centered which is default
Microstrip Taper	MTAPER	n1	n2	W1=	W2=	L=	
Mitered Microstrip Bend	MBEND	n1	n2	W=	ANG=	M= !G=	Optional parameter G is for specifying CPWG gap. Exercise caution.

Table 1 – Touchstone Stripline and Microstrip Elements Processed by TSPLOT32 (continued)

<u>ELEMENT</u>	<u>SYNTAX</u>					<u>COMMENT</u>
Mitered Microstrip 90° Bend	MBEND2	n1	n2	W=	!G=	Same as above
Optimally Mitered Microstrip 90° Bend	MBEND3	n1	n2	W=		
Microstrip Curve	MCURVE	n1	n2	W=	ANG= RAD=	See SCURVE comment
Microstrip Tee	MTEE	!G1= G2= G3=			n1 n2 n3 W1= W2= W3=	Optional parameters G1, G2, and G3 specify CPWG gaps when used as CPWG Tee. Exercise caution.
Microstrip Cross	MCROS	n1	n2	n3	n4 W1= W2= W3= W4=	
Microstrip Coupled Lines	MCLIN	n1	n2	n3	n4 W= S= L=	
Grounded Coplanar Waveguide	CPWG	n1	n2	W=	G= L= !W1= W2=	Optimal parameter W1 and W2 specify width of lines before and after current line
Touchstone Data File	S[N]P	n1...nN			datafile:s[N]p	datafile stands for user supplied name. N in S[N]P element must match N in ".s[N]p" file extension. A DXF file with name datafile.dxf must reside in same directory

Table 2 – Touchstone Elements Processed by TSPLOT32 that are not from Stripline or Microstrip families.

<u>ELEMENT</u>	<u>SYNTAX</u>	<u>COMMENT</u>
Matched Load	SMATCH n1	
Short Circuit	SHOR n1	Ground symbol drawn as reminder
Resistor	RES n1 n2 R= !W= G=	Optional Parameters W and G used for chip resistors on coplanar waveguide. W is width of resistor, G is space to ground plane.
Gain (Loss) element	GAIN n1 n2 A= S= F=	Draws gain element as reminder
Ideal Transformer	XFER n1 n2 n3 n4 N=	Draws transformer as reminder. n3 and n4 usually set to 0 when transforming port impedances.

Table 3 – Graphical non-Touchstone Elements Processed by TSPLOT32.

<u>ELEMENT</u>	<u>SYNTAX</u>	<u>COMMENT</u>
Close Trace End	!!ENDS n1 W=	Tells TSPLOT32 draw perpendicular line of length W across circuit trace at node n1
Close Coplanar Waveguide Trace Ends	!!CPEND n1 W= G=	Tells TSPLOT32 to draw perpendicular lines across the two gaps with width G of a coplanar waveguide with a width of W.
Coplanar Waveguide Step	!!CPSTP n1 W1= W2= G1= G2=	Draws a sloped step from CPWG with parameters W1, G1 before node n1 to CPWG with parameters W2, G2 after node n1. The width of the step from end to middle is set by parameter cpfmin in on line xx of TSPLOT32. Total length of step is 2*cpfmin. Gentle steps facilitate analysis with method of moments codes.
Debug Coplanar Step	!!DEBUG	Used to debug coplanar waveguide steps. !!CPSTP and CPWG draw lines to slightly overshoot desired length. Then TSPLOT32 oks for intersection and trims line lengths to intersection. !!DEBUG stops the trimming process to help locate CPSTP parameters that may be incorrectly specified.

graphical elements from other comments, they begin with a double comment character "!!". The special graphical elements are listed in Table 3. TSPLOT32 generates polylines² from the outlines of all the elements in the circuit it is interpreting. In the course of generating polylines, TSPLOT32 attempts to minimize the number of segments without changing the outline of the circuit in any way. If TSPLOT32 finds three consecutive points that are collinear it eliminates the middle point, leaving one long segment. This might happen, for example, if the circuit had a 50Ω stripline 10 mils long followed by a 50Ω stripline 500 mils long. TSPLOT32 would make one segment 510 mils long. This feature is especially useful if the DXF output of TSPLOT32 is used as the input for a method of moments electromagnetic solver. Short segments in DXF polyline are difficult for method of moments solvers to analyze. Also, in the course of making a digital representation of the circuit elements, and moving them to the element with matching node numbers, digitization errors can occur. When TSPLOT32 joins two line segments or attempts to eliminate intermediate collinear points, it does not test for absolute equality but rather looks for approximate equality. The parameter which controls the degree of approximation is named "ERR" and is defined on line 29 of the program. The user can change this parameter; of course TSPLOT32 must be recompiled after any code is changed.

Often TSPLOT32 is able to generate a single closed polyline for the circuit if there are no parallel coupled lines in the circuit. The pseudo-element "!!ENDS" from Table 3 is required to accomplish this because TSPLOT32 does not add perpendicular lines across the ends of circuit traces. The polylines generated by TSPLOT32 are useful in at least three ways:

- 1) As mentioned previously, they facilitate the importation of Touchstone files to method of moments codes.
- 2) Often if TSPLOT32 is not able to join two segments that should be joined, it is indicative of an error in the circuit. An example of this would be two different width traces that abut each other without an intervening SSTEP or MSTEP statement.
- 3) The closed polylines can facilitate the preparation of circuit etching files.

²The term polyline is an AutoCAD feature. It refers to a sequence of line segments, not necessarily collinear, joined end to end to form a single entity in an AutoCAD drawing. The author has recently seen the term used in contexts that had no immediate connection to AutoCAD, though it does not yet merit an entry in the dictionary.

When circuits are etched they must be made slightly oversized to account for the conductor edges being undercut by the etchant. The DXF files generated by TSPLOT32 can be read back into AutoCAD and offset by the amount of the expected edge undercutting.

TSPLOT32 generates DXF files that have four layers. The first layer, "0", is where most circuit traces are drawn. The second layer, "1", is reserved for the outer lines that represent grounded coplanar waveguide traces. The outer lines are put on a separate layer from the inner lines to facilitate drawing vias in AutoCAD. This is done by reading the DXF file into AutoCAD, offsetting the lines on layer 1 by the distance to the vias, using the divide feature to draw points at regular intervals along the offset line, setting AutoCAD to snap to points, and then copying vias to each point. Layer "2" is reserved for circles, and layer "3" is reserved for non essential features such as the resistor and transformers shown in Fig. 1c.

5.0 RESTRICTIONS. TSPLOT32 only recognizes a subset of Touchstone microstrip and stripline elements which is shown in Table 1. The section on "**EXTENDING THE CAPABILITIES OF TSPLOT32**" shows how to add subroutines to handle new elements.

TSPLOT32 does not recognize the Touchstone line continuation character "&".

TSPLOT32 reads but does not process the DIM block in Touchstone files.

TSPLOT32 assumes that all length dimensions are in mils and all angular dimensions are in degrees. The length dimensions in DXF files must be interpreted from context. The dimensions in DXF files produced by TSPLOT32 are interpreted as having units of inches. Similarly, when TSPLOT32 reads a DXF file it interprets it as having units of inches.

The Touchstone stripline and microstrip couplers, SCLIN, and MCLIN have four optional parameters which designate the widths of the lines adjoining the couplers. These are used to maintain the proper spacial relationship between cascaded coupler sections. TSPLOT32 does not recognize these four optional parameters.

TSPLOT32 does not recognize the artwork replacement parameters used by Touchstone for resistors, capacitors, inductors, via pads, etc. When TSPLOT32 uses DXF for output or input, it expects AutoCAD version 12 DXF.

Version 12 DXF output by AutoCAD 14 is acceptable for input, and AutoCAD version 13 DXF may work. The DXF format changed extensively with AutoCAD 14 and it is completely unusable by TSPLOT32 for input. However, AutoCAD 14 has no problem reading DXF from any earlier version of AutoCAD.

6.0 EXTENDING THE CAPABILITIES OF TSPLOT32 The capabilities of TSPLOT32 may be extended in two ways; (1) by supplying Touchstone with an S-parameter data file for an element that is not in its library and supplying TSPLOT32 with a specially formatted DXF file for the same part, and (2) by adding code to TSPLOT32 for an element which is in the Touchstone repertoire, but which has not been implemented yet. The former method affords great flexibility in the variety of geometries that may be accommodated, while the latter method is much easier than it sounds because of the object oriented nature of C++.

6.1 DXF FORMAT RULES FOR EXTERNALLY ANALYZED CIRCUITS. In describing the process of making a drawing and exporting it in DXF format it will be assumed that the reader is using AutoCAD 14. There are many drawing CAD packages on the market so it is impossible to make generalizations about them all. When making the drawing, keep the following points in mind:

- 1) TSPLOT32 interprets all the dimensions in Touchstone circuit files as having units of mils, and all dimensions in DXF files as having units of inches. The circuit files could just as well have units of millimeters if the DXF file have units of meters.
- 2) TSPLOT32 transfers only the polylines and circles that it finds in the input DXF file to its output representation.
- 3) TSPLOT32 needs to determine the location of each microwave port in the input DXF file. This is done by drawing points in the exact center of each port.
- 4) TSPLOT32 needs to correlate the port numbers with the locations of the ports. This is done by drawing the points designating ports in the order they are numbered. AutoCAD 14 lists drawing objects in DXF files in the order in which they are drawn.

- 5) TSPLIT32 needs to determine the orientation of each port. This is done by drawing line segments from the points designating the ports into the interior of the port. These line segments must be perpendicular to the planes of the ports.

The tee used in Listing 1 will be analyzed as an example. The AutoCAD drawing used to generate the DXF file is shown in Fig. 2. The first step is to draw the polyline segments ABC, DEFGHI, and JKL. If a drawing already exists that was used in an electromagnetic solver, it will work. However, be sure that all

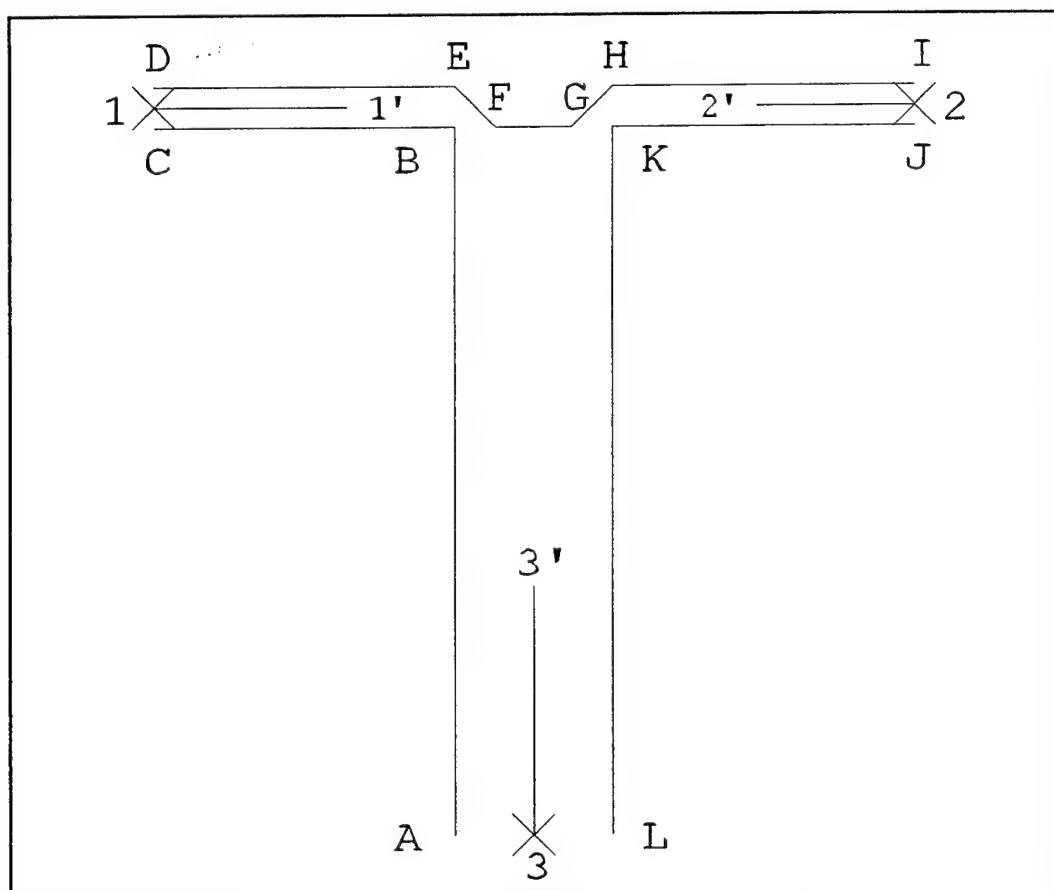


Figure 2 – Format of DXF for Tee in Listing 1.

segments which you want to include are converted to polylines. If the drawing has polyline segments closing off the ports at CD, IJ, and LA they will be imported by TSPLIT32 if not removed. The next step is to designate the location of the ports at points 1, 2, and 3. In AutoCAD 14 the easiest way to do this is to turn off all

snap functions, select draw point, and when it prompts you for a location, type 'cal. When AutoCAD prompts you for an expression, type $(end+end)/2$ and snap on points C and D. Do the same for points 2 and 3, snapping on points I & J, and L & A. The last step is to draw the segments 1-1', 2-2', and 3-3' which designate the orientation of the ports. In AutoCAD 14, the easiest way to do this is to set the snap mode to node, and turn ortho mode on. Then draw lines from points 1, 2, and 3 into the interior of the tee. The conversion is done. Save the file, export it as an AutoCAD version 12 DXF file with the same name root as the corresponding Touchstone data file, and put it in the same directory as the circuit file and the Touchstone data file. When TSPLOT32 encounters the statement specifying the Touchstone data file it will automatically open the corresponding DXF file.

6.2 ADDING CODE TO TSPLOT32 FOR NEW TOUCHSTONE ELEMENTS. TSPLOT32 has been written in C++ which is an object oriented language. Object oriented means that you specify certain data sets and functions to operate on those data sets, and the compiler figures out from context which functions and data go together. An example from FORTRAN can help illustrate this point. In FORTRAN there are four or more numeric data types: integer, real, double precision, and complex. Each of these data types has an absolute value function: IABS(), FABS(), DABS(), and CABS(), respectively. Older FORTRAN compilers required the programmer to call the correct absolute value function for the data type used. More modern compilers allow the programmer to use a generic ABS() function, and the compiler figures out which form to actually call. With FORTRAN, the ability to choose which type of built-in functions to call for built-in data types is done as a convenience to the programmer. In C++, the ability of the compiler to call user specified functions for user specified data based on context is an important feature of the language.

In the FORTRAN example just discussed, the generic type for integer, real, double precision, and complex is "number", so they all share enough in common that ABS() makes sense for each. In TSPLOT32 the generic type is "Touchstone circuit element". All Touchstone elements as they are processed by TSPLOT32 have a number of properties in common, and this has been addressed in the body of the program. All that is necessary to add a new Touchstone element to TSPLOT32 is for the user to supply the code which makes the new element different from all the others, and the code to recognize the new element.

C++ has a construct called a "class" in which data and functions that operate on them are defined simultaneously. The functions which are defined in

C++ are functionally the same as what would be defined in C, Pascal, or FORTRAN, but in those languages the programmer has to somehow mark data as to what it represents and at various stages in the program check that mark to see what subroutine to use. With C++ all the code relating to a specific data type is defined in one place, and the compiler takes care of executing the appropriate code at the appropriate time.

The procedure for adding the code for a new Touchstone Element to TSPLOT32 has several steps:

- 1) Draw a picture of the element with dimensions given in terms of Touchstone parameters. Draw node 1 so that it is centered at the origin, and points in the direction of 180° . Refer to the Touchstone Circuit Element Catalog[1][2] for a precise explanation of geometrical relationships.
- 2) Write algebraic equations relating the positions and orientations of the other elements to the position of node 1 and the parameters of the element.
- 3) Write algebraic equations relating the positions of vertices in the outline of the element to the position of node 1 and the parameters of the element.
- 4) Find the code for an element that is similar to the element being added, and copy it. Systematically go through the code and change the name of variables that refer to the old element to names that refer to the new element. This is not required since the variables are local, but helpful to keep attention focused on the new element.
- 5) Modify the old code where possible and add new code as necessary to describe the new element in TSPLOT32.
- 6) Add the new code into TSPLOT32 between the class definitions for two other Touchstone elements. The section of TSPLOT32 which contains these definitions is between lines 2076 and 3869.
- 7) Go to the part of TSPLOT32 that parses the CKT block and add the lines that will allow it to recognize the new element. This is almost entirely a cutting and pasting operation.
- 8) Save the modified program with a new name, e.g. TSPLOT33. This

insures a return path to a working version of the program.

9) Compile and test the new program.

This process will be illustrated by modifying the code for SLIN, a stripline straight section to obtain the code for MBEND2, a simple mitred microstrip line. Fig. 3 shows the SLIN and MBEND2 elements and the algebraic relationships between the element parameters, and the coordinates of the vertices and nodes in the elements. The code in TSPLOT32 which refers specifically to SLIN begins on line 2263 and extends to line 2284, and this is shown in Listing 2.

```
2263:   class slin: public nport{
2264:       realNum w, l;
2265:   public:
2266:       slin(GNList &slinlist, TVList &rList, char *linstr,
           int ln=0 ): nport( 2,
2267:           slin list, rList, linstr, ln) {
2268:           for (int i=1; i<=2; i++) pGblNArray[i] =
           slinlist.pFindMatch(pstr, LinNum());
2269:           checkParamStr( "W", w, rVList);
2270:           checkParamStr( "L", l, rVList);
2271:           locNArray[1].abs_set_x_y_theta(0,0,180);
2272:           locNArray[2].abs_set_x_y_theta(1(),0,0);
2273:           newline();
2274:           pAddToBack(0,w()/2);
2275:           pAddToBack(1(),w()/2);
2276:           newline();
2277:           pAddToBack(0,-w()/2);
2278:           pAddToBack(1(),-w()/2);
2279:       }
2280:       void ckt_Prt_1(ostream &rs) {
2281:           rs << "  SLIN      " << pGblNArray[1]->getNum() << ss
2282:               << pGblNArray[2]->getNum() << ss << "W" << w
2283:               << ss << "L" << l << '\n'; }
2284:   };
```

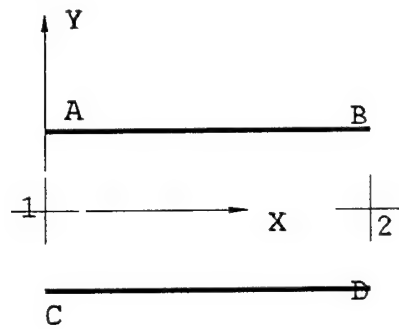
Listing 2 - Code in TSPLOT32 referring to SLIN element.

The first step is to designate a new class mbend2:

```
class mbend2: public nport {
```

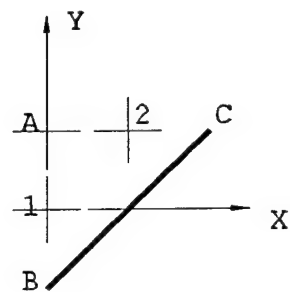
The next step is to declare the Touchstone parameter for Mbend2, namely w.

```
realNum w;
```



2: $X=L$ $Y=0$ $\text{THETA}=180^\circ$
 A: $X=0$ $Y=W/2$
 B: $X=L$ $Y=W/2$
 C: $X=0$ $Y=-W/2$
 D: $X=L$ $Y=-W/2$

(a) SLIN dimensions



2: $X=W/2$ $Y=W/2$ $\text{THETA}=90^\circ$
 A: $X=0$ $Y=W/2$
 B: $X=0$ $Y=-W/2$
 C: $X=L$ $Y=W/2$
 D: $X=L$ $Y=-W/2$

(b) MBEND2 dimensions

Figure 3 – SLIN and MBEND2 Dimensions in terms of Touchstone Parameters

“realNum” is a special type created for TSPLOT32 which has all the properties of a real number plus the ability to read itself from and write itself out to a Touchstone file. This means that if a realNum is associated with optimization limits, it keeps track of those limits, and prints them out to the renumbered file when required. However, since a realNum is not a true C++ real variable it must be followed by parenthesis when used in an algebraic statement. The next line should be copied exactly:

```
public:
```

Line 2266 and 2267 should be copied directly, replacing the characters “slin” with “mbend2” wherever they appear.

```
mbend2(GNList &mbend2list, TVList &rList, char *linstr, int
      ln=0 ): nport( 2, mbend2list, rList, linstr, ln) {
```

The “2” which appears immediately after the characters “nport (” specifies that MBEND2 has two ports and would be changed if the number of ports was being changed. Line 2268 reads the nodes in and stores them in a list. “slin” must be changed to “mbend2” producing:

```
for (int i=1; i<=2; i++) pGblNArray[i]
    =mbend2list.pFindMatch(pstr, LinNum());
```

Line 2269 can be copied directly because both SLIN and MBEND2 have a parameter “w”.

```
checkParamStr( "W", w, rVList);
```

MBEND2 does not have any more parameters. Line 2271 specifies the position and orientation of node 1 and is copied directly:

```
locNArray[1].abs_set_x_y_theta(0,0,180);
```

By referring to Fig. 3 it can be seen that node 2 is at location $x=w/2$, $y=w/2$, and the outward normal points in the direction of 90° . Line 2272 is modified accordingly:

```
locNArray[2].abs_set_x_y_theta(w()/2,w()/2,90);
```

TSPLOT32 stores polylines internally as a sequence of x-y coordinates designating the vertices. SLIN has two polylines and SBEND2 has one. The programmer

notifies TSPLIT32 that another polyline is coming with the statement "newline();" and adds vertices with the pAddToBack(x, y) statement. Referring to lines 2273 to 2275 of Listing 2 and to Fig. 3, it can be seen that the one polyline in MBEND2 is created with:

```
newline();
pAddToBack(0,-w()/2);
pAddToBack(w(),w()/2);
```

This creates a segment from $x=0$, $y=-w/2$ to $x=w$, $y=w/2$. This completes the code which reads in the nodes and element parameters, and creates the internal data representation of MBEND2. It is closed off with a right brace:

```
}
```

The next section of code, lines 2280 to 2283, is the subroutine which prints SLIN out to a renumbered circuit file. In C++ input and output devices are called streams. The operator which sends data to a stream is called the inserter operator and is designated by "<<". The stream and each of the items being sent to it are separated by the inserter operator. The inserter does not add any spaces so they must be included explicitly in a quoted string or with the variable ss which represents four spaces. The inserter operator does not send carriage returns either so they must be specified explicitly with '\n'. With these guidelines in mind, the print function for SLIN can be copied without much change. "SLIN" is changed to "MBEND2" and reference to parameter "L" is erased giving:

```
void ckt_Prt_1(ostream &rs) {
    rs << " MBEND2 " << pGblNArray[1]->getNum() << ss
    << pGblNArray[2]->getNum() << ss << "W" << w << '\n';
}
```

The section of code called "class mbend2" is closed off with a right brace and a semicolon:

```
};
```

The code created here can be compared to the code for MBEND2 which begins on line 3205 of TSPLIT32. The code in TSPLIT32 is the same except that it has been modified to accept an optional coplanar waveguide parameter G which specifies the width of the gap. The coplanar code is fairly transparent so a comparison should be easy.

There is still one little programming chore to do. All the code that has been written for MBEND2 so far tells TSPLOT32 what to do once it has recognized MBEND2 in the CKT block of a Touchstone file. TSPLOT32 also needs to be modified to recognize MBEND2 in the first place. This is done between lines 4402 and 4557. The section of code for SLIN begins on line 4430 and is shown in Listing 3.

```
4430:  else if (!strcmp( elmstr, "SLIN")) {
4431:      slin *slin1 = new slin(nodList, VList, pexpstr, ln);
4432:      cktList_1.pAddToBack(slin1);
4433:  }
```

Listing 3 - Code to recognize Touchstone SLIN element

Lines 4402 to 4557 is a chain of if statements, so all that needs to be done is to copy the SLIN link in the chain, paste it somewhere in the chain between two links, and change the characters "slin" to "mbend2" everywhere in the new link as shown below:

```
    else if (!strcmp( elmstr, "MBEND2")) {
        mbend2 *mbend21 = new mbend2(nodList, VList, pexpstr, ln);
        cktList_1.pAddToBack(mbend21);
    }
```

For comparison, the code which is already in TSPLOT32 to recognize MBEND2 may be found beginning on line 4518.

6.3 C++ HELP Numerous reference on C++ are available in bookstores and libraries, but "Thinking in C++" by Bruce Eckel[3] is one of the best. It is also available for free on the Internet in HTML or PDF format[4]. The first four chapters provide sufficient knowledge to get started modifying TSPLOT32.

7.0 RUNNING TSPLOT32 The procedure for running TSPLOT32 will be described with reference to using the pcGRASP - GNU combination. The steps are as follows:

- 1) Choose pcGRASP from the START->Programs selection of Windows 9x or Windows NT. If you have placed the pcGRASP icon on your desktop you can click on it.
- 2) pcGRASP has been designed to work with several different languages, so it must be informed what type of file it is opening. In pcGRASP choose the

“file” menu, “open” sub-menu, and select “C++”; an open file dialog box appears. Navigate to the directory which contains TSPLLOT32 and the Touchstone circuit file you want to plot. Open TSPLLOT32. Note that pcGRASP adds many little figures and lines to the file. These marks may be turned off by selecting the Remove CSD button near the top left of the screen.

- 3) Compile TSPLLOT32 by clicking the Compile and Link button. It can be identified by the icon with two arrows pointing down to a sheet of paper. Alternatively, it should be the fourteenth button over from the left. If TSPLLOT32 has already been compiled and linked this step may be omitted.

N.B. The GNU compiler had its origin on UNIX systems, so it is still semi-case sensitive with respect to file names, while Windows is case insensitive. TSPLLOT32 should have a file extension of “.cpp” but sometimes Windows changes it to “.CPP”. The GNU compiler will produce strange error messages to the effect that the file format is not recognized. This may be corrected by invoking Windows Explorer, clicking on TSPLLOT32.CPP and changing the file extension to small letters.

- 4) Run TSPLLOT32 by clicking on the run button. The run button is the sixteenth button over from the left and has a down arrow in its icon.
- 5) TSPLLOT32 is a console mode program so the MS-DOS window appears with a message prompting the user for the Touchstone file name without the “.ckt” extension. TSPLLOT32 prints out messages about its progress, and prompts the user for acknowledgment several times before it finishes. This is done because there are number of problems which can occur such as improper Touchstone syntax, or being unable to find an input DXF file, and it is helpful to know where in the process the problem occurred.
- 6) In principal, once a program has been compiled, there should be no need to use the compiler or the IDE again. However, pcGRASP loads a dynamic link library which TSPLLOT32 uses, so TSPLLOT32 must be run from pcGRASP even if it is not re-compiled again.

8.0 EXAMPLES The predecessor of TSPLLOT32 was developed to plot the power divider design for a broadband array of dual flared notches[5]. The power divider which was designed to cover a three to one bandwidth, is shown in Fig. 4.

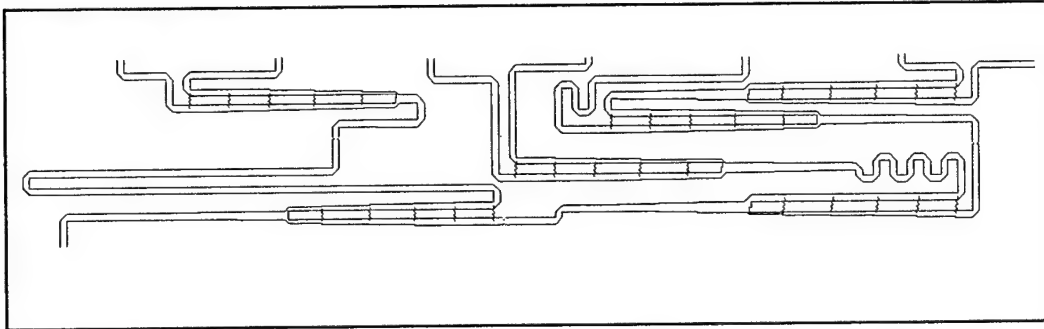


Figure 4 – Seven way power divider designed for Wideband Array of Dual Flared Notch Elements as plotted by TSPLOT32.

The Touchstone circuit file may be found on the accompanying CD-ROM and is named 7_way.ckt. The circuit file as it exists in 7_way.ckt was much too large to be analyzed with the MS-DOS version of Touchstone. Rather each tee in the circuit was analyzed separately, and then all were combined for the purpose of plotting. The entire circuit was analyzed with the current version of Touchstone in preparation for this report and the amplitudes of the outputs were found to match the design levels closely. However, the phases of the outputs were poorly matched. This agrees with measurements as extensive trimming was required to get the phases matched. It is also worth noting that TSPLOT32 is much easier to modify than its predecessor. When a new element was added to the old plotting program, it was necessary to modify the code in about a dozen different places. TSPLOT32 requires changes in only two places.

Fig. 5 shows a six way power divider implemented in coplanar waveguide, and the Touchstone file for it is named 6_way.ckt on the accompanying CD-ROM. TSPLOT32 was modified to optionally plot microstrip tees and bends as coplanar tees and bends. This capability was mentioned earlier but not discussed at length because the results were mixed. The input was well matched, and the outputs of the center four ports tracked closely. However the two outside ports varied from the others markedly. The relative amplitude of the outside ports varied from 0.2 dB at 1 GHz to 0.8 dB at 4 GHz and the relative phase varied from 10° to 40° over the same frequency span. The experience with this design prompted the addition of the DXF input capability to TSPLOT32 so that coplanar waveguide tees and bends can be analyzed with a method of moments program and imported to Touchstone.

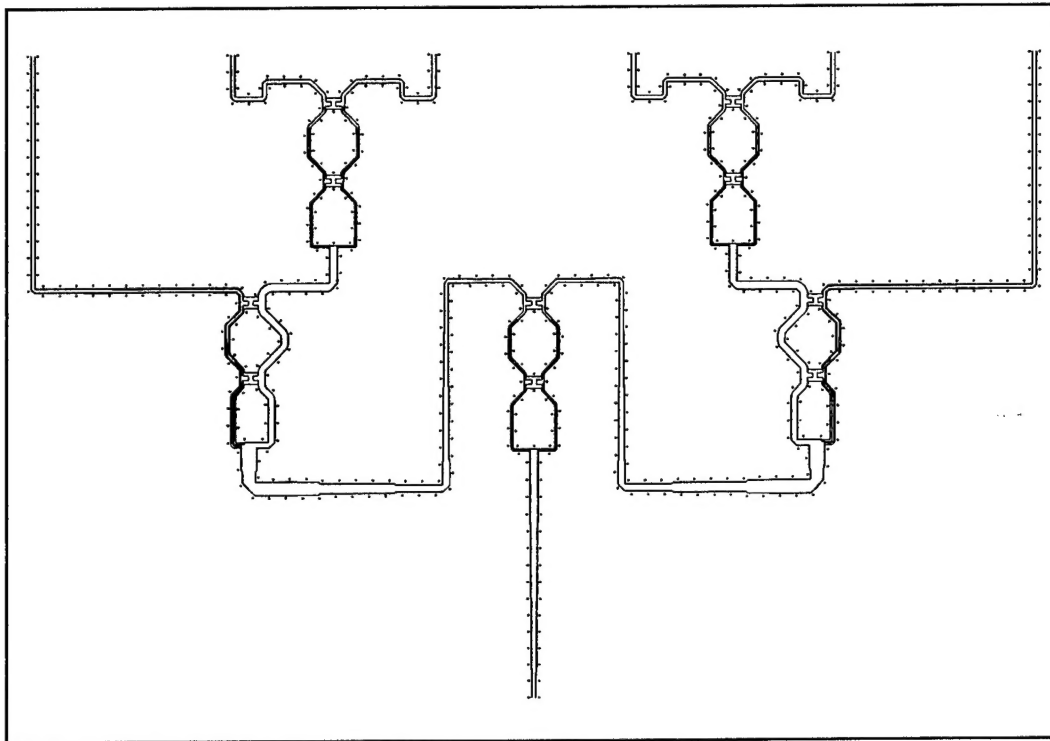


Figure 5 – 6 way coplanar waveguide power divider. The output from TSPLOT32 has been edited with AutoCAD to add vias to ground plane, and to finish details around resistor contact pads.

Fig. 6 shows a stripline cavity-slot antenna which was inspired by the design of Clouston and Evans[6]. Their design featured a cavity that was twice as wide as the one shown in Fig 6. with feeds on each side of the slot that were 180 degrees out of phase. Thus they had a plane of anti-symmetry through the center of their slot. In an effort to save space their design was cut in half with an electric wall through the center of the slot, and with some adjustment of dimensions satisfying results were obtained.

The cavity is constructed with plated through vias connecting the top and bottom grounds. The radiating slot is etched on one long side of the cavity and the stripline feed comes in from the opposite side. The feed is connected to the top ground plane only by a plated through via, and the impedance is adjusted by moving the via position towards or away from the slot. Series stubs to increase the bandwidth are located just outside the cavity.

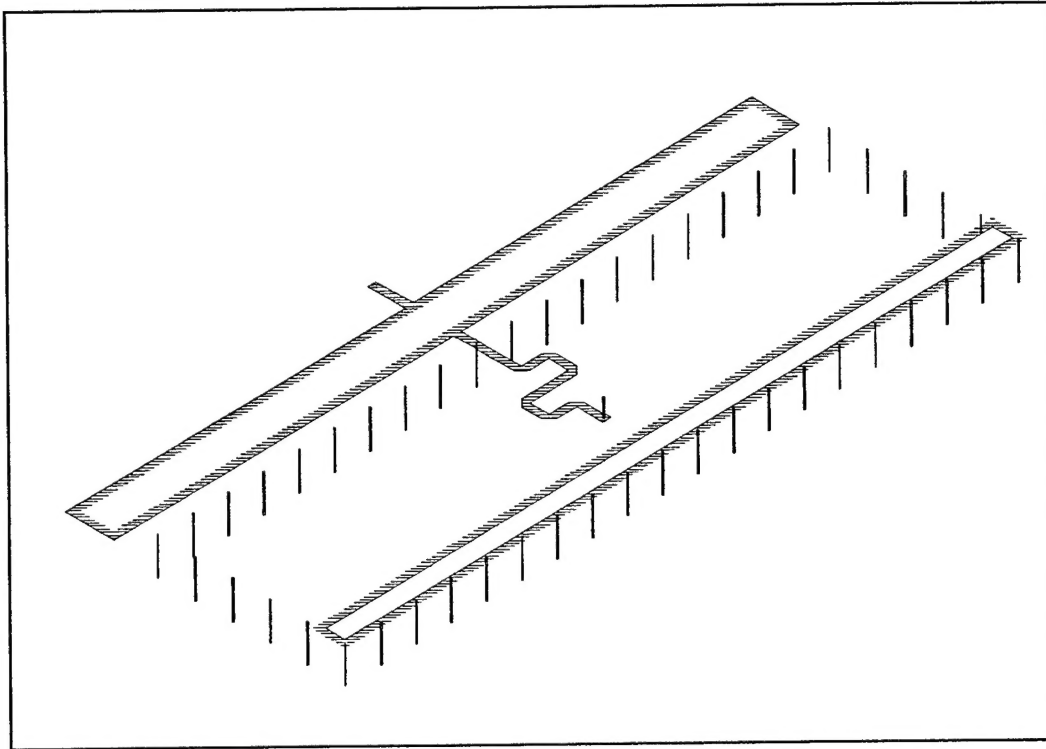


Figure6 – Isometric View of stripline slot antenna.

The slot is capacitive below resonance and inductive above resonance, while the stubs are just the opposite. The combination of the slot and the stubs increases the bandwidth. It is found that the bandwidth can be increased further by modifying the dimensions of the slot so that it never achieves a perfect match, tending more to the capacitive side of the Smith chart. Similarly the optimum matching stub tends to the inductive side of the chart. The design process for this antenna was begun by analyzing a series of unmatched slots using a method of moments code. Impedance data for each design was exported to a Touchstone data file, and the Touchstone optimizer was used to design the matching network. Then TSPLIT32 was used to convert the composite design back into DXF format. Finally the DXF file was fed back into the method of moments code for fine tuning. Figure 7 illustrates this concept. The files for this example can also be found on the CD-ROM: umslot.dxf is the DXF file for the unmatched slot. Umslot.s1p is the Touchstone data for the unmatched slot which was generated by the method of moments program. Matchslt.ckt is a Touchstone circuit file which combines the matching network with umslot.s1p. Finally mslot.dxf is the DXF files for the slot antenna after it has been tuned with the method of moments code.

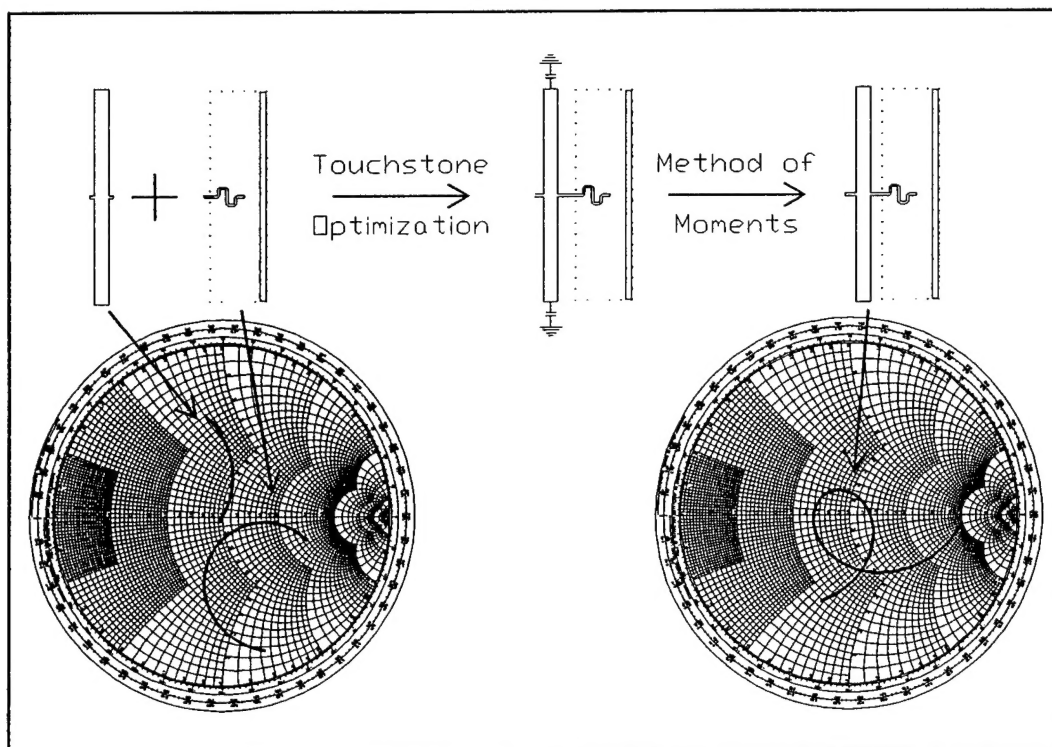


Figure 7 – Conceptual sequence to increase bandwidth of stripline slot antenna. Start with slot analyzed alone, add stubs, do course optimization with Touchstone, and do fine tuning with method-of-moments program

9.0 CONCLUSION A report on a program to generate DXF files from Touchstone Data files has been presented. Source code for the program has also been presented. Although this report is intended to serve as a manual for both using and modifying the program, it is assumed the reader has access to the Touchstone manuals. Several examples from NRL research projects have been presented to illustrate the use of the program.

Hewlett Packard discontinued selling Touchstone in the last year. However, Touchstone retains a loyal following for its simplicity and accuracy in analyzing linear passive microwave circuits. It is hoped that this program will be helpful to the community of Touchstone users.

10.0 ACKNOWLEDGMENTS Prof. Walter Kahn conceived the stripline slot radiating element and provided insight and guidance as the design progressed.

The code in TSPLIT32 which parses the equations in the EQN block of Touchstone circuit files was adapted from: Herbert Schildt, *Schildt's Expert C++*, Berkely, CA :Osborne McGraw-Hill, 1996.

Several mathematical subroutines in TSPLIT32 were adapted from: Namir C. Shamma, *C/C++ Mathematical Algorithms for Scientists and Engineers*, New York: McGraw-Hill, 1995.

11.0 REFERENCES

[1] Touchstone/DOS Reference, Version 3.0, Westlake Village, CA: EESof, 1991.

[2] HP-EESof Microwave & RF Circuit Design Circuit Element Catalog, Palo Alto, CA: Hewlett Packard, 1994.

[3] Bruce Eckel, *Thinking in C++*, 2nd Ed., Upper Saddle River, NJ: Prentice Hall, 2000

[4] Bruce Eckel, *Thinking in C++*, 2nd Ed.,
<http://www.bruceeckel.com/ThinkingInCPP2e.html>

[5] W.R. Pickles and J.B.L. Rao, "Broadband Array Antenna of Dual Flared Notch Elements", Antenna Applications Symposium, Robert Allerton Park, University of Illinois, September 1992.

[6] E. N. Clouston and S. Evans, "A Triplate Stripline Slot Antenna Developed For Time-Domain Measurements on Phased Arrays", *IEEE Ant. Propagat Int. Symp. Dig.*, vol. 1 , pp. 312-315, 1988.